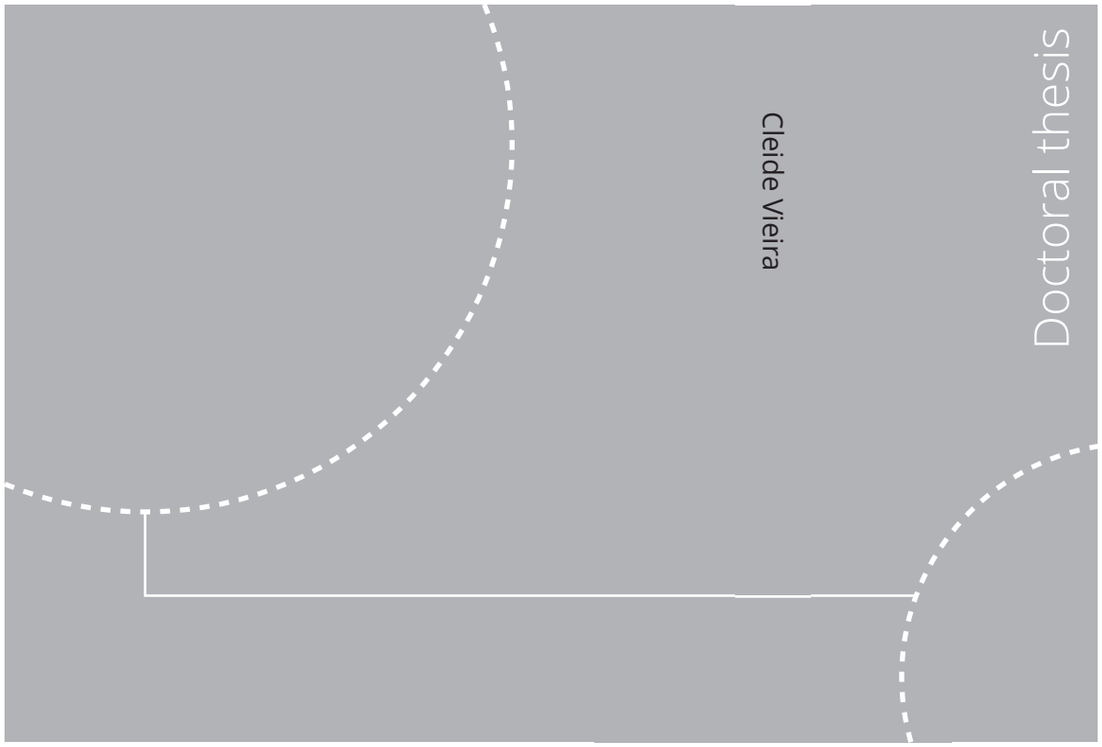

Doctoral theses at NTNU, 2020:340

Cleide Vieira

Modelling and Experimental Study on the Production of Gas Wells with Associated Liquid

ISBN 978-82-326-5026-2 (printed ver.)
ISBN 978-82-326-5027-9 (electronic ver.)
ISSN 1503-8181

NTNU
Norwegian University of
Science and Technology

Doctoral theses at NTNU, 2020:340

NTNU

NTNU
Norwegian University of
Science and Technology
Thesis for the degree of
Philosophiae Doctor
Faculty of Engineering
Department of Geoscience and Petroleum

NTNU
Norwegian University of
Science and Technology

Cleide Vieira

Modelling and Experimental Study on the Production of Gas Wells with Associated Liquid

Thesis for the degree of Philosophiae Doctor

Trondheim, November 2020

Norwegian University of Science and Technology
Faculty of Engineering
Department of Geoscience and Petroleum

NTNU
Norwegian University of
Science and Technology

NTNU
Norwegian University of Science and Technology

Thesis for the degree of Philosophiae Doctor

Faculty of Engineering
Department of Geoscience and Petroleum

ISBN 978-82-326-5026-2 (printed ver.)
ISBN 978-82-326-5027-9 (electronic ver.)
ISSN 1503-8181

Doctoral theses at NTNU, 2020:340

PRINTED IN NORWAY
NO - 1598

NORDIC SWAN ECOLABEL
Printed matter
2041 0731

Printed by Skipnes Kommunikasjon AS

Abstract

Once a gas field is developed liquid production may start and persists sometime during the production life of most dry gas wells. This liquid could be condensate, water or both, resulting from condensate dropout due to reduction of pressure or water breakthrough. Liquids can accumulate in the wellbore if the liquid fraction increases or if gas rates decrease (e.g. with depletion) and are not able to carry liquids to surface. This phenomenon is known as liquid loading and can cause further reduction of gas rates due to excessive back-pressure on the formation and erratic production. To effectively plan and design a gas well that will eventually produce liquid, it is essential to be able to accurately predict the onset of liquid loading.

In this thesis, several aspects on gas flow with associated liquid in upward inclined pipes have been studied. Experimental and numerical work have been carried out, with the following goals: (a) improve the understanding of the effect of liquid viscosity and inclination on flow map, liquid loading onset and post-loading behaviour. (b) quantify accuracy of existing liquid loading onset models using laboratory and literature data and development of an improved model with more predictability. (c) evaluate the behaviour of existing liquid loading onset models when the droplet fraction is taken into account. (d) quantify the variability in the onset rates predicted by several onset criteria and pressure drop models.

Several experimental tests were performed and data acquired for three different fluid systems (air-water, air-Exxsol D80 and air-mixed oil) and wide range of pipe inclinations. The experimental data was compared against numerical models to quantify their accuracy in predicting the flow pattern transition between annular and slug flow.

In general, the liquid droplet-based models considered underestimated the critical gas velocity while the models based on liquid film were more conservative. Moreover, liquid film models have better accuracy than liquid droplet models. The commercial transient simulator (OLGA 7.3) did not capture properly the influence of viscosity nor predicted transitions for pipe inclinations lower than 60° from horizontal. The model of Shekhar et al. (2017) had the best accuracy from all models considered.

Including the entrainment of droplets in the gas core in liquid film models improved modestly their accuracy when predicting the experimental data and data reported in the literature.

The new liquid loading onset model developed in this work is based on the model of Barnea (1986) and uses the liquid holdup in the momentum equation instead of assuming an uniform film thickness. The model successfully reproduces the experimental data and

literature data, with a higher accuracy than the model of Shekhar et al. (2017). Therefore, it represents a significant improvement and contribution of the present work.

Finally, the numerical study performed on a synthetic vertical well shows that the loading criteria and pressure drop model used affect considerably the onset rate predicted. The variation in the gas liquid loading onset rate is considerable. In general, when the gas rate is lowered below the liquid loading onset rate, the wellbore transitions rapidly from unloaded to fully loaded, except for one of the models studied.

Preface

The work presented in this dissertation was performed at the Norwegian University of Science and Technology (NTNU) between January 2016 and December 2019. It was part of a joint academic project sponsored by Norad (through EnPe), headed by Eduardo Mondlane Univeristy (UEM) and NTNU. I am indebted to the sponsors for financing the three and half year of my doctoral work.

My supervisor throughout present thesis has been Associate Professor Milan Stanko whom I thank for his advice and for giving me the opportunity and motivation to undertake this work. No less important was the support from Professor Pål Skalle who was of important help throughout the dissertation edition.

I would like to express special thanks to Professor Ole-Jørgen Nydal for taking interest in this thesis, allowing me to use the Multiphase Flow laboratory to perform the experimental work and to Professor Zhilin Yang for his advises and the experience transferred in the workshops for the Multiphase Flow group meeting. To the amazing team of the Energy and Process Engineering Department Martin Bustadmo and Stein Skånoy and Per Bjørnaas; without them it would have been a lot more difficult to finish this work.

I would like to thank the staff of the Department of Geoscience and Petroleum (IGP) for all the support provided and for creating an enjoyable working atmosphere.

I am deeply grateful to my colleagues and friends Alberto, Oscar, Xiyang and Lahiru not just for their support, guidance and technical discussions, but also for the refreshing coffee breaks, pizza dinners and their friendship that were essential to keep me going.

Last but not least, I am hugely grateful to my family (Rosalina, Shaimin, Marlon, Karla, Luan, Rafaella) and boyfriend Tomáš O.P.L.T for their unconditional support, love and encouragement which have been a vital ingredient to my success.

- Muito Obrigado -

Contents

List of Tables

List of Figures

Nomenclature

Latin letters

A	Pipe cross section area, $[m^2]$
D	Pipe diameter, [m]
dp/dx	Pressure gradient, [Pa/m]
E	Droplet entrainment, [-]
f	Friction factor, [-]
g	Gravity acceleration, $[m/s^2]$
H_L	Liquid holdup, [-]
h_L	Liquid level, [-]
p	Pressure, [Pa]
p_{wf}	Bottom flowing pressure [Psia]
p_{wh}	Wellhead pressure [Psia]
Re	Reynolds number, [-]
S	Wet perimeter, [mm]
v_{sg}	Superficial gas velocity, [m/s]
v_{sl}	Superficial liquid velocity, [m/s]

Greek letters

α	In-situ volume fraction of gas
β	Half of angle confirmed by liquid wetted periphery in stratified flow, [°]
δ	Film thickness, [m]
μ	Viscosity, [cP]
Φ	Pipe circumferential, [°]
ρ	Density, $[kg/m^3]$
σ	Surface tension, [N/m]
τ	Shear stress, [Pa]
θ	Pipe angle from horizontal, [°]

Subscripts

atm	atmospheric
g	gas
i	interfacial
l	liquid
s	superficial
avg	average

max	maximum
min	minimum
NS	no-slip

Abbreviations

Calc	Calculated
CV	Control valve
DQA	Data acquisition system
elmag	Electromagnetic
Exp	Experimental
FH	From horizontal
FR	Flow Regime
FRM	Flow regime maps
ID	Inner diameter
LL	Liquid loading
Obs	Observed
std	Standard deviation
STP	Standard Temperature and Pressure
VBA	Visual Basic for Applications
WGR	Water-gas ratio

Chapter 1

Introduction

1.1 Background

Production of natural gas is becoming more and more attractive, mainly due to the environmental footprint, which is relatively small compared to oil and coal production. Advances in engineering practices in unconventional gas fields (e.g. shale fields in U.S) and large offshore gas discoveries in countries like Mozambique and Tanzania have sparked interest of many oil companies in developing projects in such fields. Besides production of natural gas, these wells also produce liquids, such as condensate and water, in moderate amounts, but if accumulated in the wellbore, it can hinder the wells productivity.

At early production, the gas flow rate is high enough to carry any existing co-produced liquid out of the well, which makes the well produce at stable condition. However, at some later period in the life of the well, as reservoir pressure declines, the gas production rate drops as well as its capacity of lifting any liquid to the surface. Under such conditions, non-removed liquid accumulates in the wellbore, leading to a phenomenon commonly known as liquid loading. If not counteracted, the accumulated liquid creates a back-pressure against the formation, leading to increased resistance along the gas production pathway, causing further accumulation of liquid, a reduction of the natural flow of gas from the reservoir to the surface, and eventually a premature abandonment of the well. This leads to economic losses due to reduction in hydrocarbon sales and to increase of operational expenses. For many years research in this area was aiming at accurately predicting the onset of liquid loading, to predict when the problem might arise, so that corrective and preventive measures could be taken well in advance. Hence, many models have been proposed for liquid loading predictions in gas wells. A standard model extensively used to predict the onset of liquid loading is based on the "critical velocity" concept.

The critical gas velocity concept assumes that most of the liquid phase is distributed as droplets dispersed in the gas. When the gas velocity is equal to the critical velocity, the liquid phase is moving neither upward nor downward. When the gas velocity falls below the critical gas velocity, the liquid will start to accumulate in the wellbore and gas production becomes erratic.

The ultimate goal of present research work is to contribute to improving current onset of liquid loading criteria and modelling practices. To reach this goal a comprehensive understanding of the liquid loading multiphase flow phenomenon using experimental and numerical modelling studies was conducted. Experimental data acquired at the Multiphase Flow laboratory at NTNU were used to evaluate applicability of existing theoretical models and to validate the new proposed model.

1.2 Objectives

The primary objective of this work was to improve the understanding of liquid loading of gas-liquid flow in deviated pipes by performing experimental work and data analysis of information available in the literature. The specific objectives of this work were:

- Perform experimental investigation on multiphase flow mechanics related to gas-liquid flow in inclined pipes using water, light oil and viscous oil.
- Build a numerical model to compare the experimental data and data in the literature against numerical models available in the public domain.
- Quantify the accuracy and deficiencies of existing liquid loading onset models.
- Investigate the effect of entrainment droplets in the gas core in the existing liquid film models.
- Develop a new model for prediction of the onset of liquid loading in inclined pipe.
- Analyse and quantify liquid accumulation along the wellbore vs. gas flow rate, considering several onset criteria and pressure drop models.

1.3 Contributions

During the research period several contributions were made, in terms of modelling work and experimental work. This work's contributions include:

- Multiphase lab upgrades related to start-up and shutting-down procedures, and the modification of existing experimental facility, by:
  - Installing and calibrating appropriate instrumentation to measure pressure gradient covering the whole range of pipe inclination tested.
  - Installing high-speed camera and lighting (LED panel) to enable a better visualization of the flow present in the pipe.
- Experimental data acquisition on gas-liquid two-phase flow in upwards inclined pipe by investigating :
  - Effect of liquid viscosity on the flow pattern transition in an inclined pipe.
  - The effect of fluid type, inclination angles and flow rates on the liquid loading deposition mechanism.

- Theoretical investigation on the applicability of available models for the prediction of:
  - Flow pattern transition in inclined pipe.
  - Liquid loading deposition mechanism in inclined pipe.
- Numerical analyses on existing dynamic multiphase flow simulator to quantify the accuracy and deficiencies of the simulator on the prediction of:
  - Flow pattern transition in inclined pipe.
  - Liquid loading deposition mechanism in inclined pipe.
- Development and validation of a new model for prediction of the onset of liquid loading in inclined pipe.

1.4 Research overview

The work performed in this research was partly experimental and partly numerical. A test matrix (see Section 3.4) was designed and executed to support the study of flow regime transition model and onset of liquid loading in gas-liquid flow in inclined pipes.

The diagram presented in Figure 1.1 summarises the activities of the research work, where the major activities encompassed literature survey, experimental and flow simulation. Experimental data were compared with results from existing numerical models and from a commercial transient simulator.

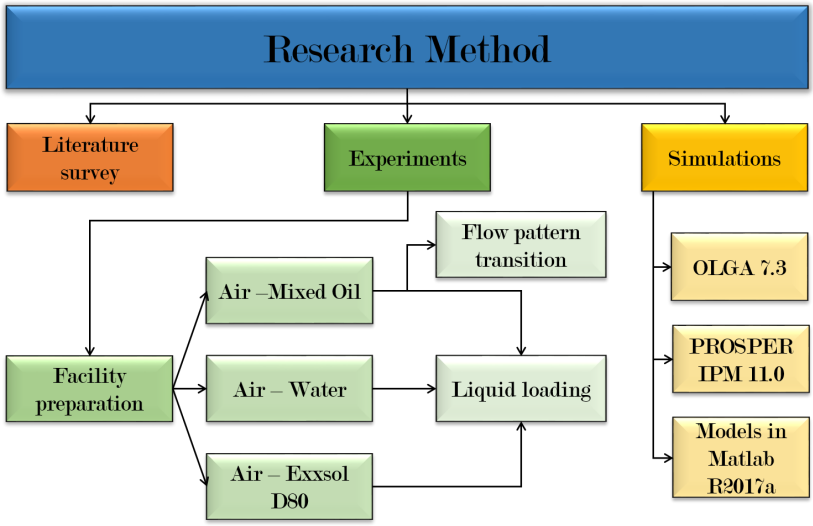

Figure 1.1. Research activity overview

At the beginning of the research project, a careful and detailed literature survey on topics related to liquid loading and two-phase gas-liquid multiphase flow in upward inclined pipes were carried out.

The experimental stage started with facility preparation, which gradually included improvements of instrumentation, updating the acquisition system and familiarisation with laboratory equipment handling, such as start-up; testing; shutdown and safety procedures. Later on, numerical studies were performed, where acquired data was used for evaluation of existing methods.

1.4.1 Thesis structure

Five chapters and three appendices define the dissertation subdivisions. The chapters cover the following topics. Theoretical background on diverse aspects within the research topic. Experimental work procedures and techniques. Results of different evaluations. Conclusions and recommendations of further work.

Thus, Chapter 2 gives a general review of the most relevant theories and concepts available in the literature on experimental and analytic studies related to the scope of the thesis. Chapter 3 provides a detailed description of the experimental procedures, test section, data acquisition and processing methods as well as of the instrumentation, which might be useful as basis for future experiments in similar or distinct work. Chapter 4 presents the results and the discussion on validation of the model found in the literature with the data acquired. Chapter 5 concludes the work, and recommends further studies.

1.4.2 Paper list

This PhD work has produced the following publications:

- **Paper 1 (Conference paper, published):** Vieira, C., Kallager, M., Vassmyr, M., Forgia, N., Yang, Z., 2018, Experimental investigation of two-phase flow regime in an inclined pipe, 11th North American Conference on Multiphase Production Technology, Banff, Canada, 6-8 June 2018
- **Paper 2 (Conference paper, published):** Vieira, C., Stanko, M. 2019, Applicability of models for liquid loading prediction in gas wells, 81st SPE Europec featured at 81st EAGE Conference and Exhibition, London, 3-6 June 2019
- **Paper 3 (Conference paper, published):** Vieira, C., Stanko, M. 2019, Effect of droplet entrainment in liquid loading prediction, 19th international conference on multiphase production technology. France, Cannes, 5-7 June 2019
- **Paper 4 :** Vieira, C., Stanko, M., Oplt, T., An improved model to predict liquid loading onset in inclined pipes considering a non-uniform liquid wall film.
  Draft paper to be submitted to the Journal of Natural Gas Science and Engineering

Chapter 2

Review of inclined gas-liquid flow

For several years, efforts have been directed towards improving the understanding of multiphase flow complexity, as well as to develop technical solutions for handling and controlling flow behaviour. Basically, multiphase flow refers to the physical phenomenon with two or more phases flowing in a pipe. In multiphase flow, the phases exhibit different distribution configurations in the pipe depending on the characteristics of the system, the properties of the fluid and operational conditions. The geometrical configurations are called flow patterns or flow regimes. Determination of flow regime in multiphase flow analysis is a major challenge, and pressure drop, holdup and phase velocities are strongly dependent on flow pattern (Shoham, 2006). Two-phase flow can be characterised as liquid-liquid or gas-liquid system, where the first case means that the two liquids are immiscible. Three-phase flow is normally characterised by liquid-liquid-gas systems. Gas-liquid two-phase flow can occur in various industrial fields such as chemical and nuclear reactors in a wide range of engineering applications. In the petroleum industry, this type of flow can occur during production and transportation of oil and gas, in production tubing, in flow-lines and in processing plants. For instance, in gas wells, the decline of pressure and temperature during long-term production could lead to condensation of liquid from the gas, thereby creating a complex two-phase flow system that must be studied in detail. Gas wells have in general drawn much attention among researchers regarding their behaviour, especially for the phenomenon called liquid loading.

The literature review deals with gas-liquid two-phase flow in upward inclined pipe. The review presented in this section is limited to gas dominated flows with low liquid content, for which annular flow and transition to intermittent flow (slug or churn flow) are the dominant flow regime of interest. Other flow patterns were also explored. A summary of all the most relevant studies are presented in Table 2.1 and Table 2.2 at the end of the Chapter.

2.1 Flow pattern maps in inclined pipe

For many years the flow pattern classification in two-phase gas-liquid flow have been a topic highly subjective to lack of agreement among investigators, due to complex patterns that is usually classified individually by visual observations, videos and photos of the flow. For the industry this has been a disadvantage, since different visual interpretations were reported under identical flow conditions. Therefore, many empirical correlations to classify and identify the flow patterns quantitatively were proposed.

Nowadays, with exploration into deep water from central installations, production wells tend to be highly deviated wells with inclinations between 10° to 85°. For inclined wells little information is available and most of the existing correlations have not been successful in predicting their flow behaviour. Normally, pipe with a low upward inclination angle from horizontal can present considerable higher gravitational pressure gradient than the frictional pressure gradient. If not well predicted this difference can have a considerable impact on the designing of field processing equipment such as gas-liquid separators. Therefore, accurate prediction of flow behaviour is required.

Several authors have proposed flow regime maps from experimental work and developed empirical correlations for flow pattern predictions for different conditions for either horizontal or vertical pipe: Kosterin (1949), Baker (1953), Eaton et al. (1965), Aziz and Govier (1972), Taitel and Dukler (1976) and Weisman and Kang (1981) (cited in Shoham (2006)). Studies on gas-liquid two-phase flow for inclined pipe began in the mid 1970's, when Singh and Griffith investigated slug flow at small upward inclination angles using air and water and developed simple correlations for pressure drop and liquid holdup. Beggs and Brill (1973) developed a correlation for pressure gradient prediction in two-phase flow that could be applied to the entire range of inclination angles. Taitel and Dukler (1976) proposed a physical model that predicted flow regime transitions in horizontal and near horizontal (±10°) gas-liquid flow. They compared the experimental flow pattern transition presented by Mandhane et al. (1974) with their own model prediction.

In 1980 Barnea et al. published flow regime maps from experimental measurements performed for air-water upward and downward system in ±10° inclined pipe. The data was compared with the Taitel and Dukler (1976) model which led to the conclusion that the model was applicable to ±10° inclination with good accuracy. Weisman and Kang (1981) conducted experiments on flow pattern transition during co-current gas-liquid flow in vertical and upwardly inclined pipe. The collected data were used to develop an improved dimensionless correlations of flow pattern boundaries. They concluded that the effect of the inclination angle in upward co-current flow was not very significant on the flow regime boundary.

Shoham (1982) attempted to define an acceptable set of flow patterns over the entire range of inclination angles, namely horizontal flow, upward/downward inclined flow and upward/downward vertical flow. He classified two-phase flow into four main regions: **Stratified**, subdivided into stratified-smooth (SS) and stratified-wavy (SW); **Intermittent** with elongated-bubble (EB), slug (SL) and churn (CH) flow; **Annular** with annular (A) and annular-wavy (WA) and **Dispersed-bubble** or **Bubble** region. Figure 2.1 and 2.2 present an example and illustration of flow regime maps classification for two-phase

flow in inclined pipes.

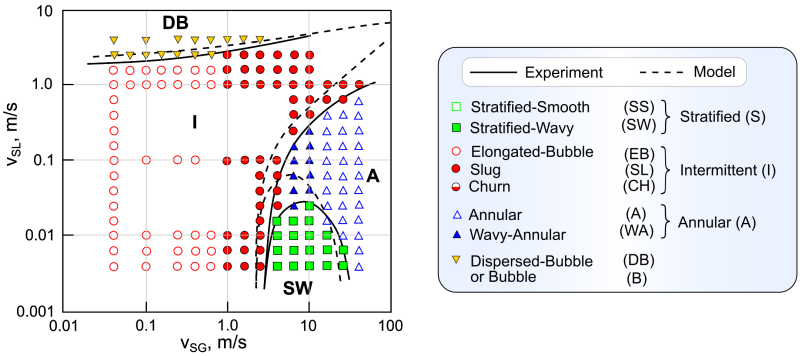

Figure 2.1. Example of flow pattern maps classification for air-water flow at standard temperature-pressure (STP) in 2.54 cm 0.25° upward inclined pipes. Adapted from Shoham (2006)

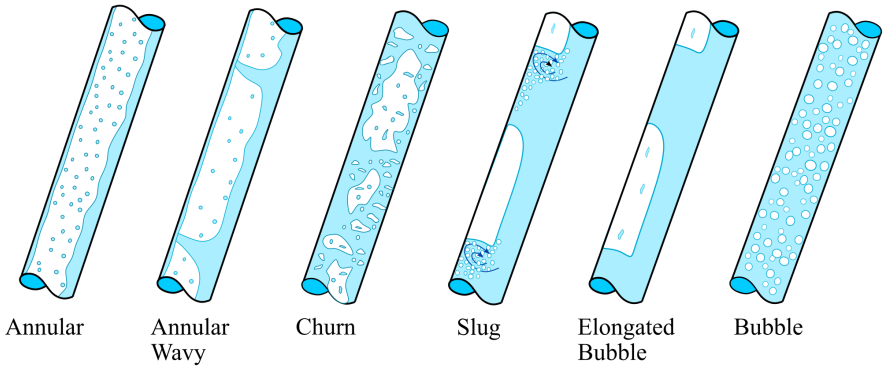

Figure 2.2. Flow regime maps for gas-liquid flow in inclined pipes. Adapted from Shoham (2006)

Stratified flow is characterised by phase segregation due to gravity, where liquid flows at the bottom of the pipe and the gas on the top. Stratified flow is mainly present in horizontal pipes at relatively low pipe inclination angles. It also occurs at low gas and liquid flow rates. Stratified wavy flow is identified in the presence of stable waves formed at the interface, while stratified smooth is defined when the gas-liquid interface is smooth. Stratified smooth flow can occur in upward inclination less than 0.25° (Barnea et al., 1980*b*).

Intermittent flow is normally characterised by alternate flow of liquid and gas, where liquid fill the entire pipe cross-sectional area while the gas flows as gas pockets. The flow might also contain a stratified liquid layer flowing at the bottom of the pipe, in case of low inclination. In vertical pipes the gas phase flows as large bullet-shaped bubbles known as "Taylor bubble". The bubble diameter is almost equal to the pipe diameter. In the case of churn flow the liquid phase flows with an oscillation motion while flowing upwards. This flow pattern occurs at high gas flow rates and is similar to slug flow but much more

chaotic and the Taylor bubble breaks slowly up into dispersed bubbles. At relatively low gas rates, the flow is calmer and elongated-bubble can occur.

Annular flow is characterised by the presence of a high velocity gas core, which might contain dispersed liquid droplets and is surrounded by thin annular liquid film that flow along the pipe wall. For vertical flow, the thickness of the liquid film is approximately uniform. For horizontal and slightly inclined pipes the liquid film at the bottom of the pipe is usually thicker than the top, depending of the gas and liquid flow rates. At lower gas flow rates, annular wavy flow is identified at the bottom of the pipe, while aerated unstable waves are swept around the pipe which can make the flow appear both stratified wavy and slugging.

Dispersed-bubble flow is defined as the flow were the gas phase is distributed as discrete bubbles within the continuous liquid phase. In this flow regime the phases move at almost the same velocity as a result of high liquid flow rates.

Barnea et al. (1985) reported a new set of experimental data covering inclinations ranging from 0° to 90°. They modified and extended the model of Taitel and Dukler (1976) and Taitel et al. (1980) to provide mechanistic models for flow pattern transition boundaries estimations over the entire inclination range. Stanislav et al. (1986) reported flow patterns, pressure gradients and liquid holdup for a two-phase flow using air and oil. The data was compared to Taitel and Dukler's theory and Nicholson et al. (1978) intermittent flow model and showed a good agreement. Afterwards, Barnea (1987) proposed a unified model to predict the steady-state transition boundaries for the whole range of pipe inclinations through equations and dimensionless maps, that incorporated the effect of flow rates, fluid properties, pipe size and pipe inclination. The model was an extension of the suggested model by Barnea (1986) where the transition from annular to intermittent flow and from dispersed bubble flow were suggested and previously published by Barnea et al. (1982*a*,*b*, 1980*b*, 1985). The validation of Barnea model was performed using experimental data from Shoham (1982). Gokcal et al. (2008) experimentally studied the effect of high viscosity liquid on the flow pattern for oil-gas flow in horizontal pipe. Later Jeyachandra et al. (2012) extended the study using slightly inclined pipe (±2° from horizontal). They reported flow pattern and pressure drop. The results were then used to evaluate different flow pattern maps and two-phase flow correlations. They also confirmed the observations of Kokal and Stanislav (1989*b*), who claimed that pressure gradients were flow pattern dependent.

The present thesis focuses on the transition mechanism from annular to intermittent flow and will use as a starting point the model described by Barnea (1986). Other flow types, such as stratified, dispersed bubble and elongated bubble, will only be briefly described. A detailed description of the annular-intermittent transition mechanism is presented in Appendix B.1.

2.1.1 Pressure gradient

Pressure gradient in two-phase flow is of particular interest to many industries. In the petroleum industry for instance, pressure gradient prediction is important during system design. Compared to single phase flow, pressure gradient in two-phase flow is more com-

plicated and difficult, due to the complexity of the flow.

Several studies on the determination of pressure gradient in two-phase flow have been performed for horizontal and vertical pipes (Baker, 1953; Flanigan, 1958; Dukler et al., 1964*a*,*b*; Orkiszewski, 1967; Aziz and Govier, 1972 and Shoham, 2006). Orkiszewski (1967) for instance, developed a pressure drop prediction scheme for vertical pipes based on an identification of the flow pattern and application of selected mechanistic and empirical methods of individual flow patterns. Shoham (2006) presented total pressure gradient for different flow patterns in vertical and horizontal pipes. He used data reported by Aziz and Govier (1972) for a 25 mm inner diameter pipe with air-water at standard conditions.

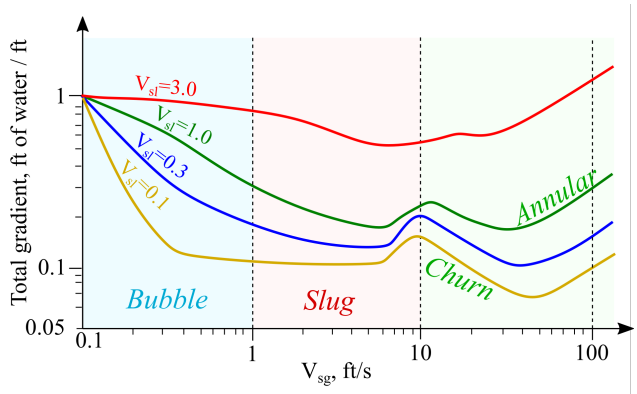

Figure 2.3. Pressure gradient vs. superficial gas velocity in vertical flow. Adapted from Shoham (2006)

Figure 2.3 presents pressure gradient dependence on flow pattern for vertical flow, at constant superficial liquid velocity. As can be seen, for low superficial gas and liquid velocities, the flow is bubble flow, exhibiting high pressure gradients. This is due to high liquid content present in the pipe, which results in high gravitational pressure gradient. Keeping the superficial liquid velocity constant, as the superficial gas velocity increases, total pressure gradient reduces and the flow pattern become intermittent flow. The increase of gas flow rate leads to a reduction of liquid content, resulting in lower gravitational pressure drop. On the other hand, frictional pressure gradient effect is not high since moderate superficial gas velocity is encountered in intermittent flow. Thus, total pressure gradient exhibits a minimum value, which is the sum of the gravitational and frictional gradient. At further increase of superficial gas velocity, the flow pattern becomes annular and total pressure gradient rises due to high frictional pressure gradient. However, these proposed correlations were not corrected for inclined flow.

In 1973 Beggs and Brill published a correlation for prediction of pressure drop when gas, liquid or both are flowing in a pipe. The development of the correlation was based on horizontal pipe and then extended to cover the whole range of inclination pipe. For pressure drop prediction the correlation often checks for flow regime that would occur if the pipe were horizontal. Afterwards the liquid holdup is corrected for other inclination angles, though inclination correction factors differs for each flow regime.

Gray (1978) developed a correlation for pressure drop for vertical gas wells producing

free water and/or condensate. In the petroleum industry Gray's correlation have been widely used for pressure loss predictions along the wellbore, especially for gas well with low liquid fraction. The correlation was based on the mechanical energy balance, where the pressure loss was a result of hydrostatic head, frictional head loss and acceleration. A detailed description of Equation 2.1 is presented in Appendix B.2.

$$\frac{dp}{dx} = \underbrace{\frac{g\overline{\rho}}{144g_c}}_{\text{Gravity}} + \underbrace{\frac{2f\rho_{NS}v_m^2}{144g_cD}}_{\text{Friction}} + \underbrace{\rho_{NS}v_m\frac{dv_m}{dz}}_{\text{Acceleration}} \tag{2.1}$$

2.2 Liquid loading

Most mature gas wells eventually enter into a period when start experiencing a period where the flow rate of the produced gas is not sufficient to carry all the co-produced liquid to the surface. Under this condition, the non-produced liquid accumulates at the wellbore, resulting in reduction of the gas production or even causing a premature abandonment of the well. This phenomenon is often defined as liquid loading. The co-produced fluid can be free liquid flowing from the reservoir and/or condensate and water that drop out of the gas due to pressure and temperature reduction along the tubing.

Figure 2.4 illustrates gas well behaviour with time once the reservoir pressure depletes.

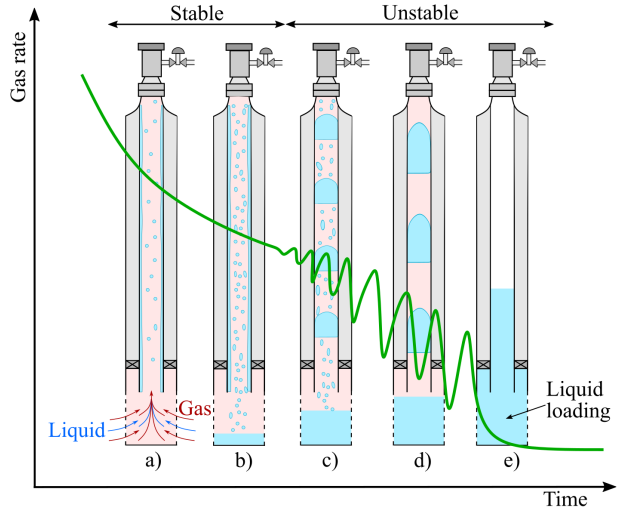

Figure 2.4. Production profile for gas wells experiencing liquid loading. Adapted from Fernandez et al. (2010)

At the beginning of the production, reservoir pressure is sufficiently high to achieve gas production rates that can transport any co-produced liquid phase that might exist to the surface, which makes the well produce at stable condition (annular flow regime). The liquid phase is normally transported as droplets entrained in the gas core and/or as film attached to the pipe wall.

As the pressure in the reservoir goes down, the gas rate drops as well as its capacity of lifting the liquid, reaching a critical gas rate. At the critical gas rate, liquid present in the wellbore starts to flow counter-current and accumulates in the bottom of the production tubing. This situation is followed by the start of intermittent flow pattern present in some parts of the tubing, leading to an unstable production condition. Liquid loading typically starts occurring at the bottom-hole, where pressure is maximum and gas velocity is minimum, or close to the wellhead, where the temperature is lower and liquid content is maximum. The accumulated liquid creates a back-pressure against the formation resulting in a further reduction of gas production and premature abandonment of the well due to further accumulation of the liquid.

To counteract liquid loading and to maintain production, deliquification methods such as gas lift, plunger lift, production cycling, down-hole pumps, etc, are typically installed in these wells. The operator must make an accurate prediction of the onset of liquid loading to support the choice of the method to be used to prevent the well from abandonment. Despise the extensive availability of models used for predicting the behaviour of such wells, the basic flow mechanism is not accurately accounted for by current models. This is due to lack of experimental data, especially for wells with inclined sections.

Several researchers (Vitter Jr, 1942; Jones, 1946; Duggan, 1961 cited by Turner et al., 1969; Guo et al., 2005 and Chupin et al., 2007) have suggested different methods, correlations based on field and experimental data, equations from physical properties to determine when the liquid starts to accumulate in the well. Almost all these analyses indicated the existence of two physical models for liquid removal in gas wells (see Figure 2.5): (a) liquid is transported as droplets entrained in the high velocity gas core and (b) liquid is transported as film moving along the walls of the pipe.

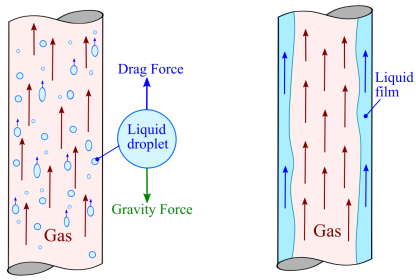

Figure 2.5. Illustrative diagram of liquid transportation in gas well

2.2.1 Liquid droplet model

The liquid droplet entrained model, also known as liquid droplet reversal, assumes that the falling of liquid droplets present in gas core is the main cause of liquid loading. Turner et al. (1969) proposed an equation that calculates minimum gas velocity necessary to lift the largest droplet present in gas core. When the gas velocity in the tubing drops below this minimum gas velocity, liquid loading will likely occur. The equation was developed based on drag and gravity forces that act on the falling liquid droplet. Turner's equation for critical superficial gas velocity (m/s):

$$v_{g,min} = 6.556\left[\frac{\sigma(\rho_l - \rho_g)}{{\rho_g}^2}\right]^{1/4} \tag{2.2}$$

To match their field data during model validation the original coefficient was corrected by 20%. Therefore, the value of 5.463 was changed to 6.556.

Many researchers made refinements and modifications to Turner et al. (1969) droplet model to better match different sets of data with varying degrees of success (Coleman et al., 1991; Nosseir et al., 1997; Li et al., 2001; Wang et al., 2010 and Sutton et al., 2010). Modification were addressed on the shape of the liquid droplet, adjustment of the equation coefficient value and effect of flow condition among others.

The Turner et al.'s equation has been widely used in the petroleum industry as a primary method to predict liquid loading in gas well, but it was not long before the need of predicting the phenomenon in deviated wells came up. Thus, the droplet model was modified to include the effect of inclination. Flores-Avila et al. (2002) proposed a new droplet model based on the Turner et al. model. They adapted to field units and included a coefficient to account for well deviation angle. Flores's equation for critical superficial gas velocity (m/s):

$$v_{g,min} = 14.27\left[\frac{\sigma(\rho_l - \rho_g)}{K_d\cos(\alpha){\rho_g}^2}\right]^{1/4} \tag{2.3}$$

$$K_d = 4\left[\frac{24}{N_{Re}} + \frac{4}{N_{Re}^{0.468}} + 0.5\right]$$

where, α is the deviation angle from vertical, K_d is the drag coefficient that corresponds to the Reynolds number at flowing condition of the continuous phase as suggested by Nosseir et al. (1997).

In 2008 Belfroid et al. studied the effect of pipe inclination angle on the droplet model prediction. Plotting the critical gas velocity, a function of inclination angle using data from Van't Westende (2008), presented in Figure 2.6, they observed that as the inclination angle changed downwards from vertical, the critical gas velocity increased, reaching a maximum value.

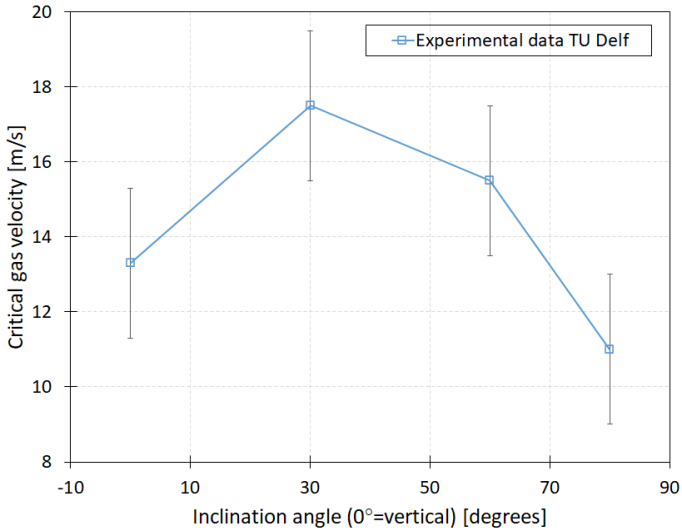

Figure 2.6. Critical gas velocity vs. inclination angle (Belfroid et al., 2008)

The behaviour was then related to the decrease of gravitational forces perpendicular to the flow and increase of film thickness along the full circumference of the tubing. To account for the effect of inclination angle on the critical gas velocity prediction they proposed a new droplet model. The proposed model resulted from a combination of Fiedler and Auracher (2004) model with the conventional Turner equation. Belfroid's equation for critical superficial gas velocity (m/s):

$$\dot{m}_{g,min} = \left(3.1A\sqrt{\rho_g}(g\sigma(\rho_l - \rho_g))^{1/4}\right)\frac{(\sin 1.7\theta)^{0.38}}{0.74} \tag{2.4}$$

where $\dot{m}_{g,minx}$ is the minimum gas mass flow rate [kg/s], ρ_g and ρ_l the gas and liquid density [kg/m^3], σ the surface tension [N/m] and θ the inclination angle refereed to horizontal (where $\theta = 0°$).

Recently, Wang et al. (2016) performed an experimental study on air-water flow system in coiled pipes with 30 mm and 40 mm inner diameter at an inclination angle of 15° to 76° from horizontal. Based on the experimental data, they proposed a modification on Belfroid et al. (2008) model to include the effect of pipe diameter on the prediction of critical gas velocity. Wang's model for critical superficial gas velocity (m/s):

$$v_{g,min} = (5.13\ln D - 14.1)\left[\frac{\sigma(\rho_l - \rho_g)}{{\rho_g}^2}\right]^{1/4}\frac{(\sin 1.7\theta)^{0.38}}{0.74}\frac{1}{\ln\left(45.6v_{sl}^2 - 9.5v_{sl} + 3.1\right)} \tag{2.5}$$

Even though the droplet model is simple, easy to use and tune, there is some field and experimental evidence that shows limited predictability (Guo et al., 2005; Zhou and Yuan, 2009; Veeken et al., 2010; Yuan, 2011 and Shekhar et al., 2017).

2.2.2 Liquid film model

The liquid film model also known as liquid-film-reversal model assumes that liquid is transported as film moving along the walls of the conduit while the gas core flows in the centre. The liquid accumulation in the well starts when the liquid film can no longer be lifted to the surface. Turner et al. (1969) on basis of field data analyses, concluded that liquid film does not represent the controlling liquid transport mechanism. To identify when the liquid film is no longer lifted to the surface, approach was proposed based on pressure gradient measures and flow regime transitions.

Zabaras et al. (1986) conducted an experimental study on the film flow for vertical upwards concurrent annular gas-liquid flow, where instantaneous local film thickness, wall shear stress and pressure gradient were measured. They concluded that at low gas flow rates the film motion is controlled by a switching mechanism. This switch mechanism was designated as churn flow, that is coupled to the instability of the liquid film due to decreasing of both film-thickness and the interfacial friction. Several subsequent authors have shown that liquid loading is accompanied by flow regime transition from annular flow to slug or churn flow (intermittent flow). The annular-intermittent transition model of Barnea (1986, 1987) is widely used for the onset of liquid loading in deviated pipes (see Appendix B.1). The model assumes no variation in film thickness around the pipe for all inclination angles.

In 1994 Paz performed experimental and theoretical investigation on two-phase annular flow focused on the effect of inclination angle on the liquid film thickness distribution in the circumferential of the pipe. They observed that as the pipe inclination approaches horizontal conditions liquid phase tends to accumulate at the bottom of the pipe. This results in a thicker liquid film at the bottom and a thinner film at the top (Figure 2.7). They concluded that inclination angle strongly affects the liquid film thickness (δ) proving Barnea's assumption wrong.

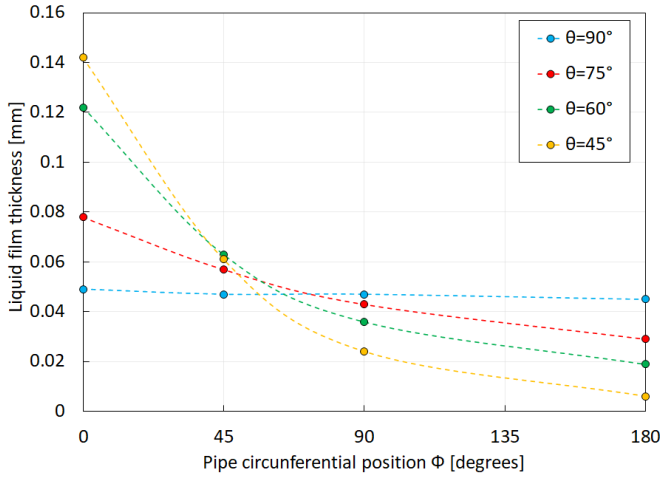

Figure 2.7. Liquid film thickness distribution around the pipe circumference (Φ=0° at the bottom of the pipe) for v_{sg}=18.29 m/s, v_{sl}=0.0124 m/s, different pipe inclination (θ=90° is vertical) observed by Paz (1994)

Recently, Luo et al. (2014) published a correlation that took into account the non-uniform film thickness (Equation 2.9) and used Barnea (1986) methodology to predict the onset of liquid loading, i.e., annular-intermittent transition. They used Fore et al. (2000) interfacial friction factor correlation (Equation 2.6) instead of Wallis (1969) (Equation B.12).

$$f_i = 0.005 \left\{ 1 + 300 \left[\left(1 + \frac{17,500}{Re_g} \right) \widetilde{\delta_L} - 0.0015 \right] \right\} \tag{2.6}$$

The new correlation was developed by comparing a uniform and non-uniform film thickness model shown in Figure 2.8. For the case of uniform film thickness they approximated the area of the film to the area of an expanded rectangle, while for non-uniform case the film was approximated to a trapezoid (see Equation 2.7) that was used in the work of Barnea (1986).

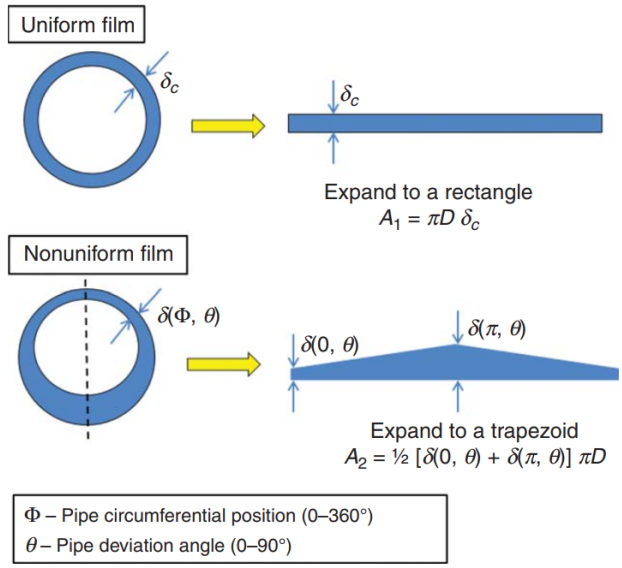

Figure 2.8. Schematic of uniform and non-uniform liquid film thickness. Taken from Luo et al. (2014)

$$A_1 = \pi D \delta_c \qquad A_2 = \frac{1}{2} \left[\delta(0,\theta) + \delta(\pi,\theta) \right] \pi D \tag{2.7}$$

where D is the pipe diameter, δ_c is the constant film thickness, $\delta(0,\theta)$ is the film thickness at the top of the pipe and $\delta(\pi,\theta)$ is the film thickness at the bottom of the pipe. Considering, A_1 equals A_2, constant film thickness was expressed as

$$\delta_c = \frac{1}{2} \left[\delta(0,\theta) + \delta(\pi,\theta) \right] \tag{2.8}$$

For film distribution along the pipe circumferential position for different pipe deviation they proposed the following empirical equation

$$\delta(\phi,\theta) = (1 - \alpha\theta\cos\phi)\,\delta_c \tag{2.9}$$

$$\alpha = \begin{cases} 0.0287 & 0 \leq \theta < 30 \\ 0.55\theta^{-0.868} & 30 \leq \theta \leq 90 \end{cases}$$

To incorporate the equation for the variation of film thickness due to pipe inclination into Barnea's model, the film thickness ($\widetilde{\delta_l}$) that satisfy Equation B.14 is considered to be δ_c, and the new film thickness is assumed to be corrected for inclined pipe.

Later, Shekhar et al. (2017) proposed a new set of empirical correlations keeping the same concept of film thickness variation with pipe inclination (Equation 2.10). They used the same criterion as developed by Barnea (1986), except they assumed that in inclined pipe the liquid loading onset would begin when the liquid film at the bottom of the pipe starts falling back.

$$\delta(\phi,\theta) = \left[1 - \left(\frac{1 - e^{-0.088\theta}}{1 + e^{-0.088\theta}}\right)\cos\theta\right]\widetilde{\delta}_{avgL} \tag{2.10}$$

To calculate the critical gas velocity, they estimate the maximum film thickness for required shear stress given by Equation B.8, and then converted the film thickness using the relation given in Equation 2.11. Thereafter, their corrected $\widetilde{\delta_{avgL}}$ is substituted back on Barnea (1986) Equation B.8, for determination of the critical superficial gas velocity.

$$\widetilde{\delta_{avgL}} = \frac{1}{2}\left(1 + e^{-0.088\theta}\right)\widetilde{\delta_{max}} \tag{2.11}$$

In addition, they modified Wallis (1969) (Equation B.12) interfacial friction faction (f_i) and proposed a correlation that is dependent on the inclination angle (Equation 2.12).

$$f_i = 0.005\left\{1 + \left[340\,(1 + \cos\theta)\,\widetilde{\delta_{avgL}}\right]\right\} \tag{2.12}$$

The validation of the new model was performed though the use of data from Alsaadi (2013) and Guner (2012), which have shown an improvement on the prediction of onset of liquid loading.

Along with the concept of film fall reversal due to switch mechanism, nodal analysis concept was taken as a new criterion to predict of onset of liquid loading. The nodal analysis concept suggests that once the pressure drop in the production tubing decreases reaching a minimum pressure liquid starts to accumulate at the wellbore.

Zabaras et al. (1986) through experimental data observed that the pressure drop displays a minimum as the gas flow rate is reduced for a given constant liquid flow rate. They related the minimum pressure with a dimensionless gas velocity $v_g^* = 1.06$ where,

$$v_g^* = v_g \times \rho_g^{1/2} \left[gD(\rho_l - \rho_g) \right]^{-1/2} \tag{2.13}$$

This behaviour was earlier observed by Hewitt et al. (1965), who reported $v_g^* = 1.12$ as mentioned on Zabaras et al. (1986).

This behaviour of the pressure drop was accompanied with the annular-intermittent flow transition. Erratic behaviour of the flow (intermittent flow) was observed on the left region of the minimum pressure point, while on the right region a more stable flow (annular flow) was dominant. Figure 2.9 illustrates the gas well pressure behaviour vs gas velocity.

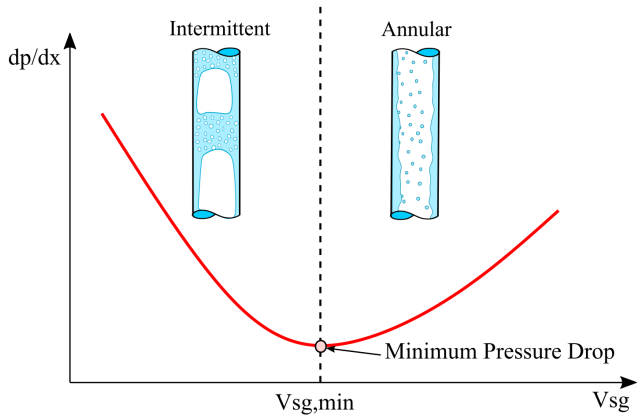

Figure 2.9. Schematic of the total pressure gradient on vertical pipe observed. After Zabaras et al. (1986)

Afterwards, researchers like Kelkar et al. (2013), Sarica et al. (2013), Luo et al. (2014) and Waltrich et al. (2015) started to use the concept of minimum pressure to define the initiation of liquid loading.

Tables 2.1 and Table 2.2 below show a summary of most relevant works within, gas-liquid two-phase flow and liquid loading. Information such, year of publication, purpose of the work and flow conditions were also presented in the tables.

Table 2.1. Experimental studies on upwards gas-liquid two-phase flow

Source	**Meas.**	**Test fluid**	v_{sg}**(m/s)**	v_{sl}**(m/s)**	**ID(mm)**	θ **(deg.)FH**	**Purpose**
Singh and Griffith (1970)	dP/dx, void fraction	air–water	-	-	5.9, 20.9, 27, 34.7, 40.6	5, 10, 15	simple model of two-phase slug flow in inclined pipes is proposed
Beggs and Brill (1973)	dP/dx, H_L	air–water	0 – 98	0 – 3.7	25.4, 38.1	±90, ±85, ±75, ±55, ±35, ±20, ±15, ±10, ±5, 0	empirical model for pressure drop and liquid holdup calculation
Barnea et al. (1980*b*)	FRM	air–water	0.03 – 26	0.003 – 2.5	25.5	0, 0.25, 2, 10	evaluate the performance of Taitel and Dukler (1976) model
Shoham (1982)	FRM	air–water	0.03 – 26	0.003 – 2.5	25, 51	15, 20, 30, 50, 70, 80, 85	effect of pipe inclination on flow pattern transition
Barnea et al. (1985)	FRM	air–water	0.03-26	0.003-2.5	25, 51	0 – 90	extend model to predict flow pattern for entire inclination range
Stanislav et al. (1986)	dP/dx, H_L, FRM	air–oil	0.1 – 30	0.05 – 4	25.8	0, 1, 5, 9	evaluate the performance of Taitel and Dukler (1976) and intermittent flow model
Kokal and Stanislav (1989*a*,*b*)	dP/dx, H_L, FRM	air–ligh oil	0.1 – 30	0.05 – 4	25.8, 51.2, 76.3	0, ±1, ±5, ±9	proposed a new model for flow pattern transition and compared data with Taitel and Dukler model
Gokcal et al. (2008)	dP/dx, H_L, FRM	air–oil	0 – 20	0.01 – 1.75	50.8	±2	effect of viscosity on flow pattern, pressure drop and liquid holdup
Jeyachandra et al. (2012)	dP/dx, FRM	air–oil	0 – 10	0.01 – 1.75	50.8	±2	effect of viscosity on flow pattern

Table 2.2. Studies on liquid loading on upward two-phase gas dominant flow

Source	**Meas.**	**Test fluid**	v_{sg}**(m/s)**	v_{sl}**(m/s)**	**ID(mm)**	θ **(deg.)FH**	**Purpose**
Zabaras et al. (1986)	dP/dx, δ, τ_w	air-water			50.8	90	introduced a switch mechanism concept
Flores-Avila et al. (2002)	H_{L0}	air–water	0.34–11.46		154.1	15, 30, 50, 70, 90	modified Turner's equation to account pipe deviation
Van't Westende (2008)	dP/dx	dry air–water	10–40	0.01, 0.02, 0.04, 0.08	50	90	investigate the dispersed-phase
Yuan (2011)	dP/dx, H_L, $v_{g,min}$	air–water	10–35	0.005–0.1	76.2	60, 75, 90	explored the mechanisms of liquid loading and investigated the effect of well deviations
Alsaadi (2013)	dP/dx, H_L	air–water	2 – 40	0.01 – 0.1	76.2	2, 5, 10, 20, 30	evaluate the effect of deviation angle and liquid flow rates on critical gas velocity
Sarica et al. (2013)	dP/dx, H_L, $v_{g,min}$	air–water	10 – 35	0.005 – 0.1	76.2	60, 75, 90	evaluate the minimum velocity with the deviation angle
Kelkar et al. (2013)	dP/dx, H_L, $v_{g,min}$	air–water	10 – 30	0.01–0.05	51, 102	90	study the effect of pipe diameter in liquid loading
Waltrich et al. (2015)	dP/dx, H_L,T	air–water		0.15–0.3	50(PVC)	90	evaluate available liquid loading prediction models
Guner et al. (2015)	dP/dx, H_L, $v_{g,min}$	air–water	1.5–40	0.01, 0.05, 0.1	76.2	45, 60, 75, 90	compare available model used to predict the liquid loading

Chapter 3

Experimental methodology

Experiments were carried out at the Multiphase Flow Laboratory located in the department of Energy and Process Engineering at NTNU in Trondheim, Norway. The laboratory facility consists of several flexible test sections and mini loops, that have been extensively used to generate multiphase flow experimental data for diverse conditions. Three-phases; water, oil and air, can be simultaneously circulated. The infrastructure includes fixed elements such as flow meters, control valves, pumping system, mixing sections, separator and tanks, allowing fluid supply and operational condition control. All lab instrumentation are connected to a data acquisition system and controlled by a main program written in LabView® where output signals are provided. For this research work the inclined test section was used for further investigation on the effect of pipe inclination on the multiphase flow systems and on liquid loading phenomena.

3.1 Experimental setup

Figure 3.1 presents a schematic representation of the inclined facility, showing the main single phase flow lines and equipment installed in the inclined test section. The inclined test section comprises of a 60 mm inner diameter, approximately 7 m long inclined transparent acrylic pipe, leaning on a steel beam connected to a lift mechanism, which allows the section to be easily adjusted to a desired inclination angle by using a connected lift handle. The test section inclination range spans vary from 0° to 90° (referenced to horizontal). However, the range of variation of inclination angle was limited because the structure that supports the steel beam had a maximum of 78° predetermined inclination due to safety. The section had two possible mixing sections for liquid and gas. One located before the test section pipe (mix point1) where gas and liquid phases flowed together through a flexible pipe before entering the test section. When the second mixing section was used (mix point2), the phases flowed separately through the flexible pipes and were mixed at the bottom of the test section. The second mixing section was preferred, to avoid flow instabilities and transients caused by the flexible pipe. After entering the mixing section the fluids flowed through the test section to a separator located at the top of the pipe where the air was vented to the atmosphere while water and/or oil passed into a secondary separator and finally fell back into the main separator at the basement. To improve the separation of oil and water the main separator contained mesh coalescers.

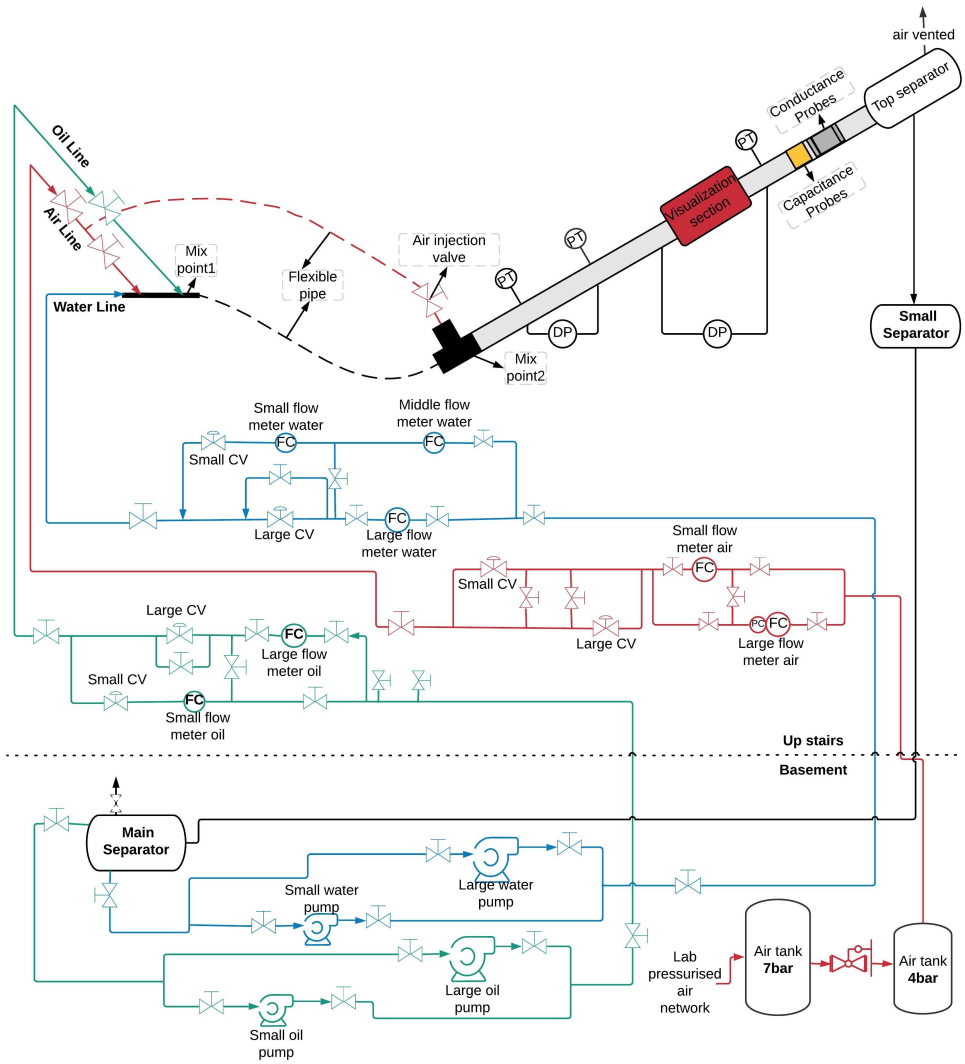

Figure 3.1. Sketch of the inclined test section at NTNU

3.1.1 Fluid system

Experiments were carried out using mineral oil and water as liquid phase and compressed air as gas phase. Air was supplied at 7 bar by the pressurised air network of the building and reduced to operational pressure of approximately 4 bar. A ball valve was installed on the air line inlet allowing a direct control on gas injection in the test section. Oil and water were supplied through individual lines by the pumping system and stored in the main separator located in the basement of the laboratory. To visually discriminate oil and water a dye that gave a yellow-green colour (fluorescein sodium $C_{20}H_{10}Na_2O_5$) was added to the water.

Two distinct mineral oil were used in the experimental campaigns, Exxsol D80 and mixed oil. Diaz (2016) who had performed experimental tests previous to this research, reported that the mixed oil present in the main separator was a combination of 5600 litres of Nexbase 3080 (79% by volume) diluted with 1500 litres of Exxsol D80 (21% by volume). Prior to a new experimental campaign samples of the liquid were taken from the flow loop separator. Fluid properties are summarised in Table 3.1.

Table 3.1. Liquid and gas properties @ 1 atm and 20°C

Phase	Fluid	Density [kg/m^3]	Viscosity [cP]	Surface tension [mN/m]
Liquid	Mixed oil	840.1	25	28
	Exxsol D80	802.6	1.8	24.9
	Water	997.9	1.1	60
Gas	Air	1.2	0.018	-

Laboratory temperature variation was monitored during the experiments using a thermocouple. From one experiment to the other, the temperature was around 20°C with a variation of ±3°C.

Oil and water densities were measured by filling a pycnometer with known volume and then weighting it on a precision scale. Considering air as an ideal gas, the density was determined by the ideal gas law equation.

Oil and water dynamic viscosity were measured using a rotational rheology meter (model Ares-G2- from TA Instruments). The rheology meter used determines the viscosity by measuring the shear stress between the plate and the fluid while varying the shear rate. The effect of pressure on viscosity was neglected. The effect of temperature in the fluid viscosity could also be estimated by using a heating plate. Figure 3.2 shows the variation of the fluid viscosity with temperature at atmospheric pressure. Due to the difference on the fluids viscosity range secondary axis was used for water and Exxsol D80 measurements.

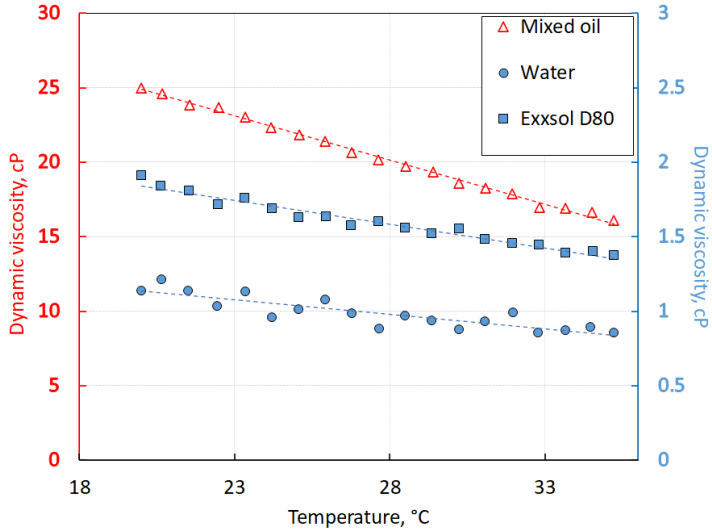

Figure 3.2. Dynamic liquid viscosity variation with temperature

It can be seen from Table 3.1, that the water present in the flow loop exhibited a slightly higher viscosity than pure water. This might be due to emulsification with oil present in the separator. The effect of temperature on the working liquid viscosity was estimated using Lewis-Squire correlation (Equation 3.1) from Chupin (2003):

$$\mu_l{}^{-0.2661} = \mu_K{}^{-0.2661} + \frac{T - T_K}{233} \tag{3.1}$$

where μ_K is the measured liquid viscosity in cP at $T_K = 293.15K$, T and T_K are in K, μ_l and μ_K in cP. Considering a temperature variation of $\pm 3°C$ in the lab, the variations in mixed oil viscosity, water viscosity and Exxsol D80 viscosity did not exceed $\pm$3cP, $\pm$0.06cP and $\pm$0.1cP respectively.

Oil and water surface tension were measured with a drop shape analyse tensiometer (model DSA100 from Krüss) using the Pendant drop method. Pendant drop method measures the surface tension or interfacial tension from the shadow image of a drop suspended from a needle in a bulk liquid or gas phase. Figure 3.3 shows the measurement of surface tension, where air drop is suspended in Exxsol D80.

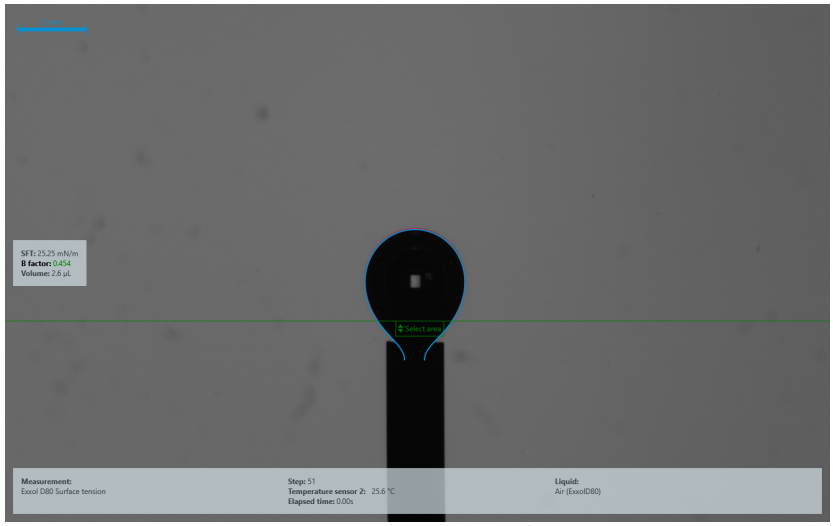

Figure 3.3. Drop shape analysis for liquid surface tension measurement

After the test, the tensiometer outputs gave a report where a mean value for the surface tension was displayed. From Table 3.1 it is possible to see that the surface tension of water is lower compared with pure water (typically 72 mN/m), probably due to a contamination by surface active agents coming from either the oil or small organisms living in the water.

3.2 Instrumentation

3.2.1 Flow rate measurements

The multiphase laboratory was equipped with six flow meters. For each flow line (oil, water and air) two flow meters were connected as shown in Figure 3.1. The selection of the flow meter was dependent on the experiments to be conducted. Table 3.2 summarises the specifications of the flow meters including the operating range and accuracy.

Table 3.2. Flow meter specifications

Fluid	**Model**	**Type**	**Range**	**Accuracy(±)**
Air	MicroMotion CMF025 Elite	Coriolis	0.12 - 80 kg/h	0.5%
	Endress & Hauser Prowir 77W	Vortex	0 - 85 l/h	1%
Oil	Micromotion F025	Coriolis	100 - 1000 kg/h	0.15%
	Micromotion F025	Coriolis	1000 - 5000 kg/h	0.15%
Water	Endress & Hauser Promag 33	Elmag	0.053 - 0.987 l/s	0.5%
	Fisher-Porter COPAXM Series	Elmag	0.83 - 10 l/s	0.5%

In case of air flow rate measurement, the Coriolis meter provides a direct measurement of the mass flow rate, while the vortex meter located on the high-pressure side of the facility gives a volumetric flow rate. Pressure readings from a pressure transducer (p_{vortex}) located next to the vortex meter was used to estimate the superficial gas velocity using Equation 3.2.

$$v_{g,atm} = \frac{1}{A} q_{vortex} \frac{p_{vortex}}{p_{atm}} \tag{3.2}$$

where A is the pipe cross section of the test section.

3.2.2 Pressure gradient measurements

Pressure gradient was obtained from the measurement of two differential pressure transmitters (DPT) and three absolute pressure sensors. Instrument specifications are given in Table 3.3

Table 3.3. Specifications of the pressure sensors

Instrument tag	DPT 4.02	DPT 4.03	PT 4.08	PT 4.11	PT 4.12
Serie type[a]	Fuji FKCW22	Fuji FKCW22	Aplisens	Aplisens	Aplisens
Range limit[bar]	±0.06	±0.06	1 – 1.4	0 – 1	0 – 1
Serie type[b]	Aplisens 2000ALW	Fuji FHCW22	Keller	Keller	Keller
Range limit[kPa]	±50	± 64	0 – 200	0 – 200	0 – 200

[a]Sensor used in experimental campaign: February 2017 to July 2017

[b]Sensor used in experimental campaign: March 2017 to December 2018

The pressure sensors were connected to the test section through pressure taps (see Figure 3.4) glued on the outside wall of the pipe at specified location (see Figure 3.5). The absolute pressure sensors were connected to the upper wall pressure taps while differential pressure cells were connect to the bottom through small impulse nylon tubes (6 mm inner diameter) filled with a known fluid to avoid that bubbles trapped in the nylon lines could damp the pressure signal. The DPT were fixed separately to the pipe section to avoid vibration error due to high values of gas velocity used during the experiments.

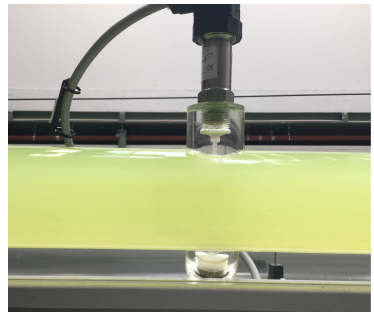

Figure 3.4. Pressure tap glued to the test section

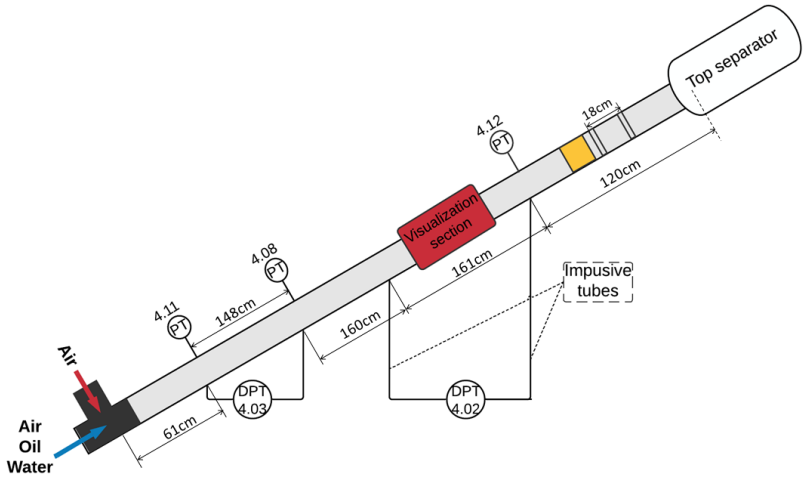

Figure 3.5. Schematic diagram of the instrumentation implemented in the test section. This diagram provides an overview of the instrumentation installed and position of each instrument

Each pressure transducer was calibrated individually and showed very good linearity, as presented in Figure 3.6.

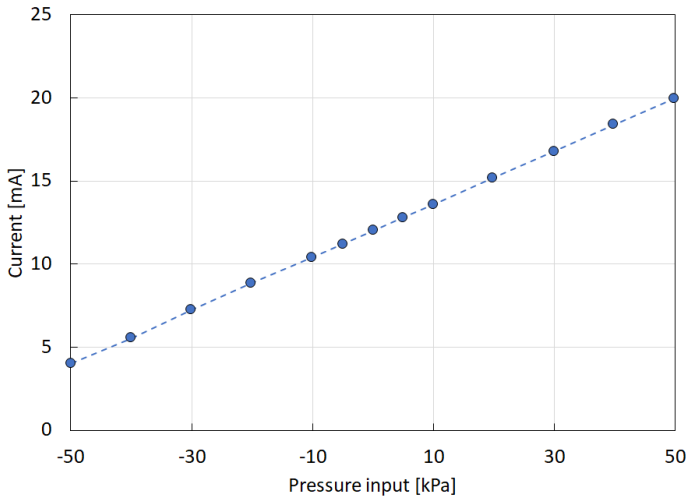

Figure 3.6. Example of calibration results for one of the pressure transducers

Besides the individual calibration, daily verification was performed prior to the experiments to ensure acceptable accuracy on the pressure gradient measured. For the absolute pressure sensors, the test section was fully filled with water which would be flowing for at least 15 minutes to ensure no bubble were present in the test section and on the pressure taps. After 15 minutes pumping the system was stopped and pressure recorded for each absolute pressure sensor. The recorded pressure was then compared with the hydrostatic pressure determined by Equation 3.3.

$$p_{PT,i} = p_{atm} + \rho_{l,pipe} g \Delta h_{PT,i} \tag{3.3}$$

where p_{atm} is the atmospheric pressure, $\rho_{l,pipe}$ is the liquid density present in the pipe section, g is the acceleration of gravity and $\Delta h_{PT,i} = \sin\theta L_{PT,i}$ is the height of the water column above each corresponding pressure sensor.

Figure 3.7 shows the result of daily verification for different pipe inclinations used in the research work. Measured pressure values exhibit a good match with the calculated hydrostatic pressure.

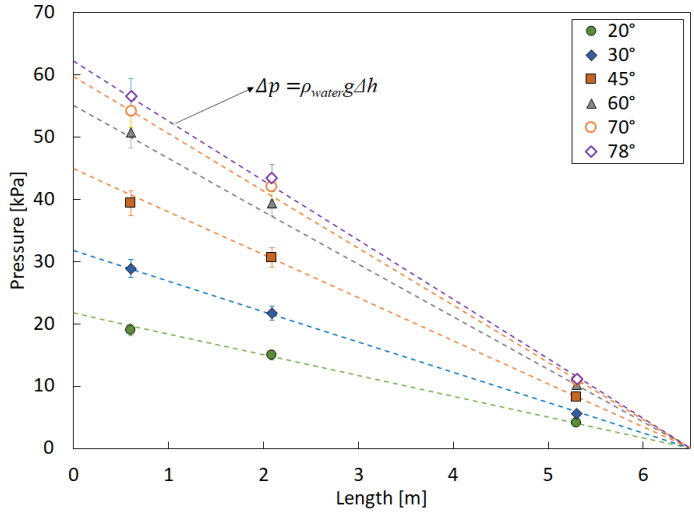

Figure 3.7. Daily calibration verification results for the absolute pressure transducers for different pipe inclinations

As the pipe section is tilted from horizontal position, static pressure is added to the pressure measured by the differential pressure. This pressure comes from the liquid inside the impulse tubes which connected the pressure taps with the differential cells. So, for the differential pressure transmitter the pressure was recorded when the pipe section was empty, and the impulsive tubes were filled with a known liquid. The recorded data was then compared with a pressure gradient determined by Equation 3.4.

$$\Delta p_{DPT,i} = \rho_{l,it} g \sin\theta L_{DPT,i} \tag{3.4}$$

where $\rho_{l,it}$ is the known liquid density inside the impulse tubes, $L_{DPT,i}$ is the distance between the high to the low pressure side of the differential pressure transmitter.
Figure 3.8 shows the result of daily verification for the differential pressure transmitter for different pipe inclination. Measured pressure gradient presented a good match with the calculated.

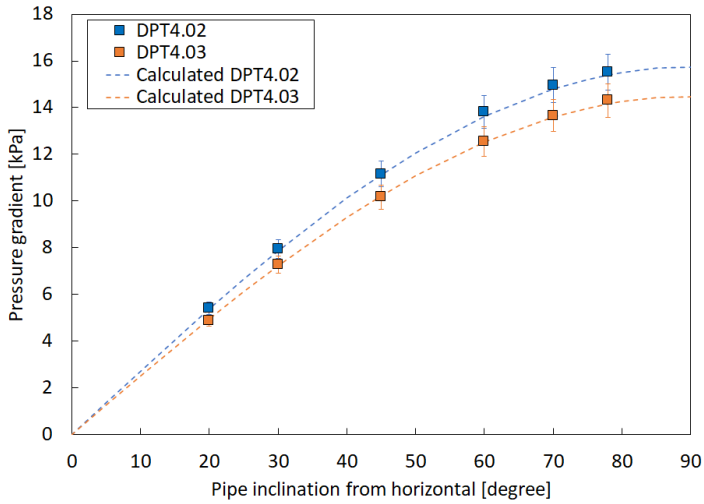

Figure 3.8. Daily calibration verification results for the differential pressure transmitter for different pipe inclinations - impulsive tubes filled with water

The pressure gradient measured during the experimental work had to be corrected for the additional hydrostatic pressure difference in the tubes. Thus, the values of Figure 3.8 were subtracted from the pressure readings coming from the differential transmitters. In order to improve the accuracy of the measurements, the set of pressure range for the DPT was defined for each pipe inclination based on the hydrostatic pressure created by the liquid in the impulsive tubes.

3.2.3 Liquid holdup measurements

Liquid holdup was measured experimentally by using electrical impedance probes. This method is also known as electrical conductivity and capacitance probes and it is widely used in research due to simplicity of installation and low cost. The idea behind the electrical probes is to place an electrical field in the pipe perimeter and measure the response of the impedance between the electrodes, which can be related to the liquid faction inside the pipe. The impedance probe type is normally selected depending on the working fluid.

For conductance probes, in order to measure the conductivity of the fluid inside the pipe, electrodes were fixed to the inner wall of the pipe (Figure 3.9). Thus, a continuous phase is required by this technique in order to conduct electricity and should be in contact with the wall. The capacitance probe does not require a conductive continuous phase and can therefore be placed in the outer part of the pipe (Figure 3.10). On the present work for oil-gas two-phase flows the capacitance was used since oil exhibits dielectric properties. For water-gas two-phase flows conductance probes was used since water is a conductor.

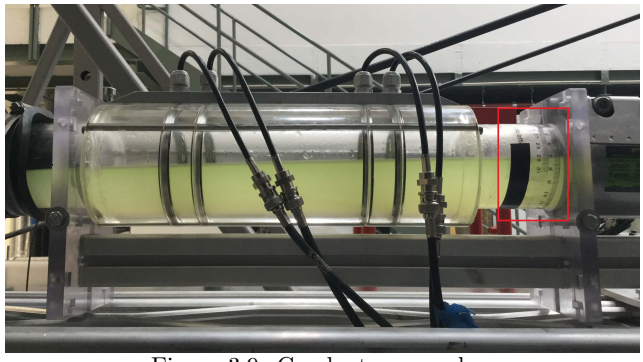

Figure 3.9. Conductance probes

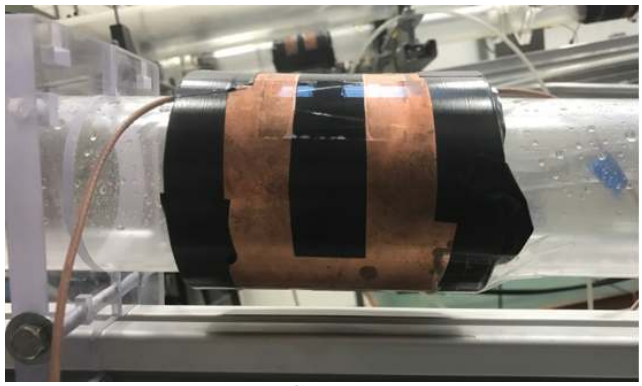

Figure 3.10. Capacitance probes

The capacitance and conductance probes were provided by the multiphase laboratory at NTNU and have previously been successfully used in the experiments of Johansen (2006) and Diaz (2016) experiments. The capacitance probe consisted of a cooper or aluminium foil wrapped around the perimeter of the pipe. The inner strips on the foil, acted as the electrodes, while the outer acted as the active guard. To avoid external interference from the surroundings, the sensor was covered by an outer cooper foil. While the conductance probe consisted of a pair of metallic rings annealed in the pipe inner wall with the same inner diameter as the pipe. Figure 3.9 shows two pair of conductance rings, which gave separated signal.

Each conductance probe and the capacitance installed in the test section should be calibrated prior to the experiments. High sensitivity to environmental conditions could change the reference values and lead to higher error in the holdup measurements.

The calibration of the instruments consisted of filling the pipe while in horizontal position with a known liquid level and read the voltage. Simultaneously, the wetted perimeter was measured by a scale strip wrapped around the external wall of the pipe next to the instruments as shown in Figure 3.9. For the case of conductance probe the signal from the electrodes was collected by two coaxial cables that were connected to an amplifier, sampled by DAQ card and then logged by a computer using a LabView program made specifically for operations involving the rig in the laboratory.

Liquid holdup was then calculated from the horizontal stratified flow through relations below:

$$\begin{aligned} \beta &= \frac{S_L}{r} \\ X &= r\cos\left(\frac{\beta}{2}\right) \\ A_L &= \frac{\beta}{2}r^2 - Xr\sin\left(\frac{\beta}{2}\right) \\ H_L &= \frac{A_L}{A} \end{aligned} \quad (3.5)$$

where, S_L is the wetted perimeter measured, r pipe radius, β angle of the sector and h_L liquid level, which are defined in Figure 3.11.

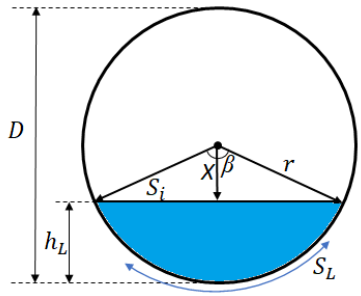

Figure 3.11. Geometrical parameters for stratified flow used on probes calibration

Maximum and minimum voltages were recorded in order to have updated reference values of full and empty pipe. The reference values were then used to normalise the voltage signal through Equation 3.6

$$V^* = \frac{V - V_{min}}{V_{max} - V_{min}} \quad (3.6)$$

After calculating the holdup and normalising the voltage a calibration curve was plotted for both instruments. An example of the calibration S-curve for one capacitance and conductance ring are presented in Figure 3.12.

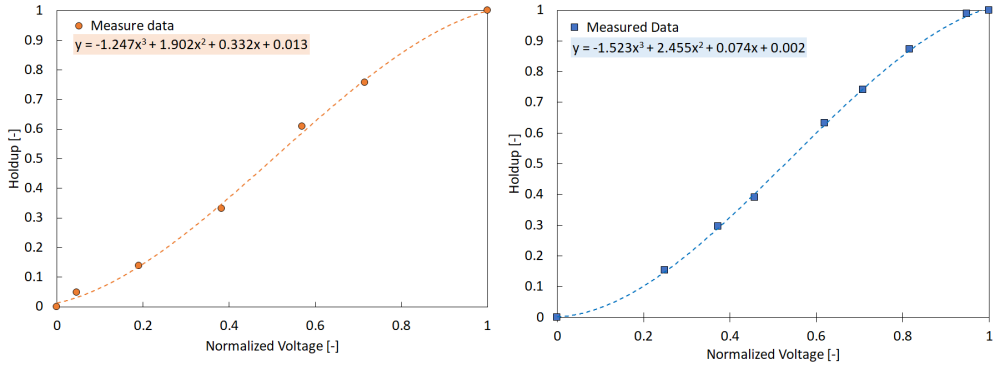

(a) Conductance (b) Capacitance

Figure 3.12. Calibration S-curve for the impedance probes

The fitting equation were then used to relate the instruments output signal with the fraction of liquid present in the pipe. The calibration was performed with the test section in horizontal position due to the inability of having stratified flow in inclined pipe. Thus, the calibration S-curves could eventually be a source of error when used in experiments with inclined pipe.

3.3 Flow pattern classification and detection of liquid loading onset

Recognition of flow pattern and onset of liquid loading was made by visual observations, pictures and video recordings on the flow loop. For flow pattern classification three synchronised GigE cameras model Basler acA640 with maximum resolution of 659x494 pixels in black and white were used. The videos were recorded at 120 frames per second and simultaneously recorded, registered, saved using a program written in LabView for the acquisition system. The program allowed to choose between saving the recording in frames, as a video, or both and stopping the video simultaneously for all the cameras. The location of the cameras varied for different pipe inclination depending on the accessibility of the test section. Thus, for some inclinations it was not possible to have a clear picture of the flow pattern present in the test section. The criteria established to classify the flow pattern for two-phase flow in this study is shown in Figure 3.13. Stratified-wavy (SW), elongated-bubble (EB), cap-bubble (CB), slug (SL), churn (CH) and annular (AN) flow patterns were observed. Discriminating between annular, churn and stratified wavy using visual inspection was sometimes challenging. Other researchers might end up with a slightly different flow pattern map for the same conditions and fluids. The flow pattern present in the test conditions was decided after circulating for a long time (15 minutes), to avoid errors due to transient phenomena.

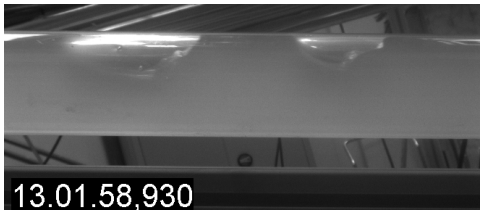

(a) Cap-bubble flow

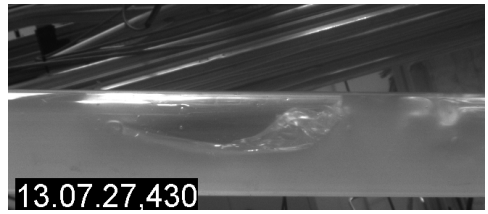

(b) Elongated-bubble flow

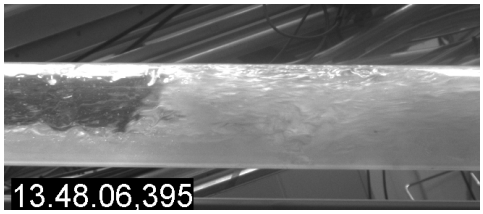

(c) Slug flow

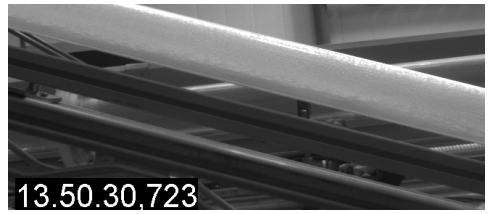

(d) Stratified-wavy flow

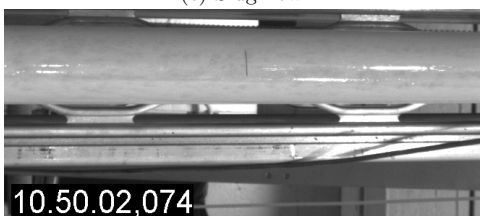

(e) Churn flow

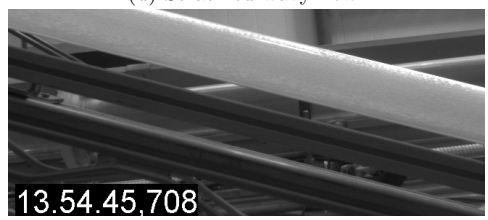

(f) Annular flow

Figure 3.13. Classification criteria for flow patterns

For onset of liquid loading identification, a high-speed camera model GoPro Hero 6 Black® was installed in the test section. The videos were recorded at 120 frames per second in 1920 x 1080 pixels resolution and simultaneously recorded, stored, saved using a camera application installed in the computer. Pictures and videos were recorded through a visualisation section approximately 4 m above the test section entrance. Due to quick transition from annular to intermittent flow, time signals from pressure sensors and conductance probe rings were also used as an extra support on the identification of onset of liquid loading. Figure 3.14 shows a time series of the pressure sensor when transitioning from annular to slug flow.

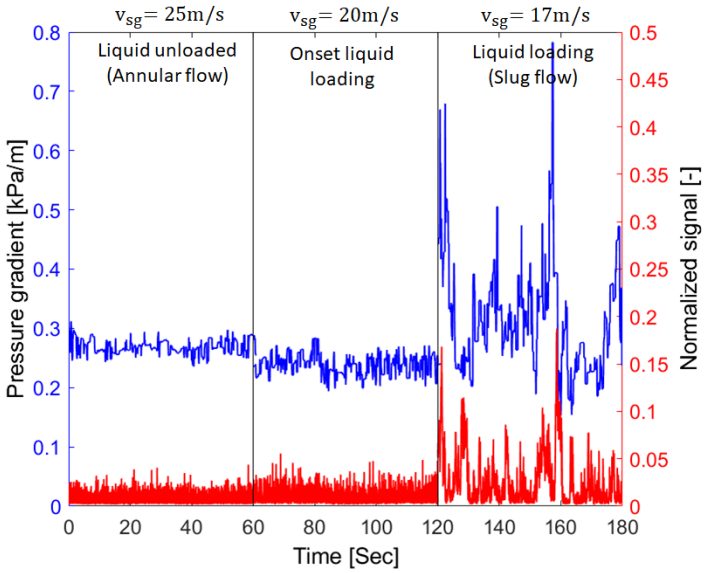

Figure 3.14. Output signal of the differential pressure cell and conductance probes when reducing step-wise the gas rate (air-water system θ=30°, v_{sl}=0.01m/s)

It's clear that at full annular flow (stable flow) the amplitude of the pressure fluctuations was smaller than when the slug flow was present (initiation of liquid loading). At slug flow the larger amplitude was due to the instability of the flow, which led to accumulation of liquid in the test section.

For the conductance probe, the holdup values were very small when the flow pattern was annular flow, but increased and fluctuated significantly when the flow pattern changed to slug flow. This technique for flow pattern identification using conductivity probes was suggested earlier by Barnea et al. (1980*a*).

Visually experimental results for the liquid loading were subdivided in three groups; Loaded for cases were the flow was defined as full intermittent (slug flow), onset liquid loading (*Onset LL*) when the liquid started to move counter-current to the gas flow direction and Unloaded for cases were annular flow was visible.

3.4 Experimental conditions

Experiments were conducted for air-water, air-Exxsol D80 and air-mixed oil two-phase flow systems, where several combinations of pipe inclination, superficial velocity of liquid and superficial velocity of gas were tested. Preliminary experiments were performed to define the test matrix, considering the limitations on the availability of the liquid volume present in the main separator, pump capacity and flow meters range.

3.4.1 Air-water system

For air-water system inclination angles of 20°, 30°, 45°, 60°, 70° and 78° (from horizontal), superficial liquid velocities of 0.01, 0.02, 0.05, 0.1 and to 0.2 m/s, and superficial gas velocities ranging from 60 to 3 m/s, were tested. The matrix was defined to investigate the effect of pipe inclination on liquid loading onset by decreasing gas flow rate.

3.4.2 Air-Exxsol D80 system

Air-Exxsol D80 system experiments were possible only for inclination angles of 30°, 45° and 60° (from horizontal), due to excessive fog created by oil particles, which affected air extraction system and the laboratory fire alarm. Superficial velocity of liquid and gas varying from 0.01 to 0.2 m/s and 50 to 5 m/s, respectively, were tested. Prior tests were performed for each selected inclination in order to identify possible experimental matrix that covers annular to intermittent transition.

3.4.3 Air-mixed oil system

To investigate the effect of pipe inclination and fluid viscosity on the flow pattern transition boundary, several combinations of pipe inclination and fluid velocities were tested. For every inclination 10°, 15°, 20°, 25°, 30°, 45°, 60°, 70° and 78° (from horizontal), combinations of superficial liquid and gas velocity (v_{sl} and v_{sg}) varied from 0.1 m/s to 1.2 m/s, and 0.14 m/s to 32 m/s, respectively.

3.5 Experimental procedure

In this thesis different two-phase flow measurements have been performed, all with the objective of studying the effect of pipe inclination on the flow regime map and on the onset of liquid loading. For the experimental execution a necessary start-up it was recommended by NTNU to test the instrumentation to avoid large uncertainties during the measurements, and to meet some safety requirements. Procedures to prepare the facility for the experiment, are described in Appendix A.

Start-up and daily calibration the experiments were conducted as follows:

1. Start the water/oil pump and open the control valve through LabView. The opening percentage on the control valve and pump frequency determined the liquid flow rate.
2. Set the desired liquid flow rate and circulate the liquid in the section for at least 5 minutes, until no bubble can be seen flowing.
3. With the air injection valve closed, open the air control valve allowing the air to fill the flexible hose (red coloured flexible pipe in Figure 3.1).
4. Set the desired air rate using the air injection valve.
5. Wait for the two-phase flow in the test section to become stable. The waiting time vary from one experiment to the other.

6. Once stable conditions are reached log the data from the instruments in LabView for at least 5 minutes.
7. Capture the high-speed videos and pictures necessary for the visual observation and support for decision making.
8. Insert logged data for flow rates, pressure drop, temperature and probes signal in Excel template containing needed adjustments to the data.
9. Repeat these steps for different gas and liquid flow conditions and pipe inclinations.

3.5.1 Data processing

All laboratory instruments, such as flow meters, control valves, pumps, pressure sensors, thermocouples and probes, can be remotely supervised by a program in LabView. The instruments are wired to a central cabinet where their output signal is converted into voltage signal. The voltage is further directed to an external data logging instrument from which it is digitised and sent to the main lab computer. One generated file contained low and high-speed data recorded at rates of 20 Hz and 2000 Hz respectively.

In order to process high volume of collected experimental data, processing tools were developed using Excel and Matlab program. For each type of data, the processing tool was developed to read the file and calculate the average measurement over the recorded period of two minutes. The tool provided a time-efficient method on the data processing. In addition, they were used to check and identify if the test condition needed to be repeated, while the experiment was running.

3.6 Measurement results

In this section the acquired experimental results are presented. The measured data includes flow pattern map, pressure gradient and liquid holdup.

The objective of the experimental test campaigns was to acquire data-sets to evaluate the applicability of the existing methods used on the prediction of liquid loading onset in an inclined pipe and to proposed possible improvements. Therefore, the main flow regime studied was annular flow and transition to intermittent flow (slug or churn flow). In addition, experimental data was acquired to study the effect of viscous fluid on the flow regime maps for two-phase flow in an inclined pipe. The measurement results are presented in Tables C.2.1, C.2.2 and C.2.3 in Appendix C.

3.6.1 Air-mixed oil system

3.6.1.1 Flow regime transition

Figures 3.15a–3.15i shows the flow pattern maps observed during the experiments performed to evaluate the flow pattern boundary transition for a two-phase flow system when a viscous fluid and inclined test section was used.

Overall, six flow regimes, namely stratified-wavy, elongated-bubble, cap-bubble, slug, churn and annular flow pattern were observed during the experiments. From the classification presented in Figure 2.2 stratified-smooth and dispersed-bubble flow regime were not experimentally identified, due to minimum pipe inclination tested and limitation of the liquid volume available in the laboratory respectively. In Barnea et al. (1985) stratified-smooth flow pattern could be observed only for inclination angles less than 0.25°, which was not the case of pipe inclination tested in this work. Experimentally, churn flow has a similar behaviour as the one verified by Barnea et al. (1985) where the first appearance of this pattern occurred at 70° inclination (Figure 3.15h).

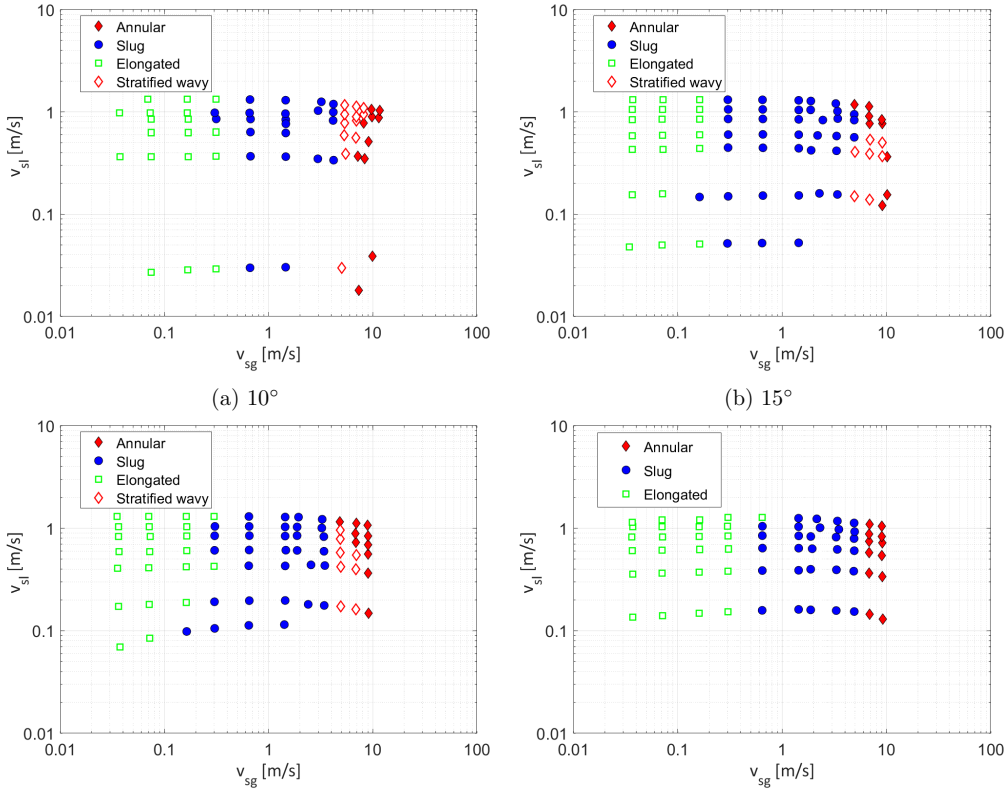

(a) 10° (b) 15°

(c) 20° (d) 25°

Figure 3.15. Experimental tests on flow pattern transitions for air-mixed oil system for different inclination angles (from horizontal)

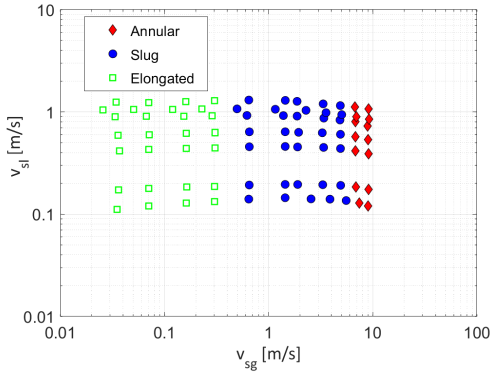

(e) 30°

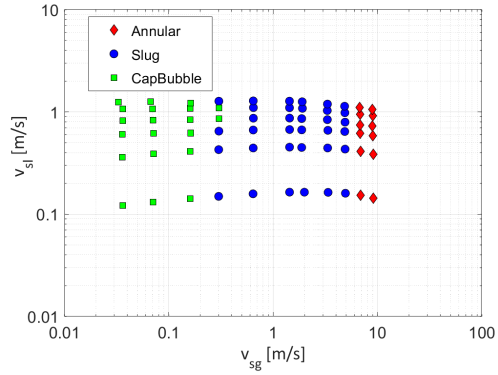

(f) 45°

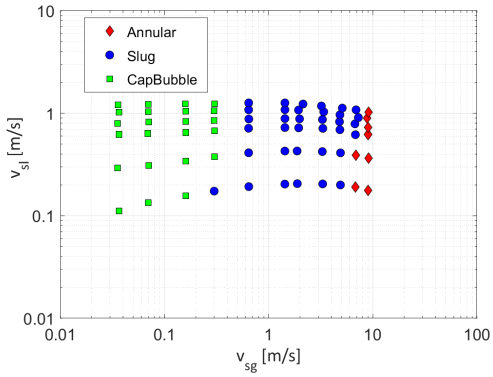

(g) 60°

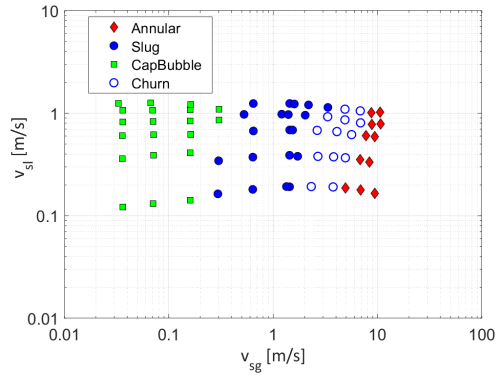

(h) 70°

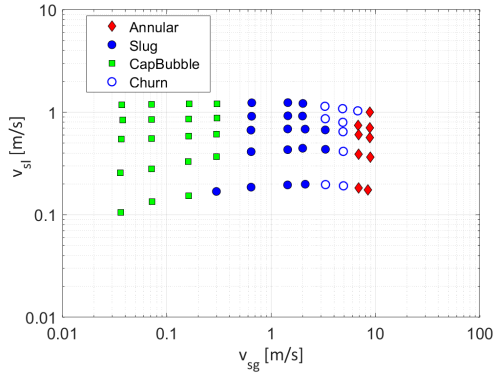

(i) 78°

Figure 3.15. *(cont.)* Experimental tests on flow pattern transitions for air-mixed oil system for different inclination angles (from horizontal)

Stratified-wavy flow was not observed for inclinations above 20°, which is similar to what was observed by Barnea (1987).

Barnea et al. (1985) and Barnea (1987) observed that elongated-bubble disappeared, and cap-bubble flow took place at angles above 30° for upward inclined pipe, this was also observed experimentally. Slug and annular flow were observed for the entire range of

pipe inclinations. Higher superficial gas velocity was not possible due to safety reasons of the laboratory since a viscous fluid was being used. At high gas flow rates, small oil particles would create a fog ambient in the lab with would activate the fire alarm.

3.6.1.2 Pressure gradient

Figures 3.16a–3.16g presents change in pressure gradient vs. superficial gas velocity, given a constant superficial liquid velocity for pipe inclination, tested for air-mixed oil flow system. Differential pressure transducers were used to measure the pressure drop in the test section, where the output signal was processed and corrected for the added static pressure using Equation 3.4 where $\rho_{l,it}$=840 kg/m^3.

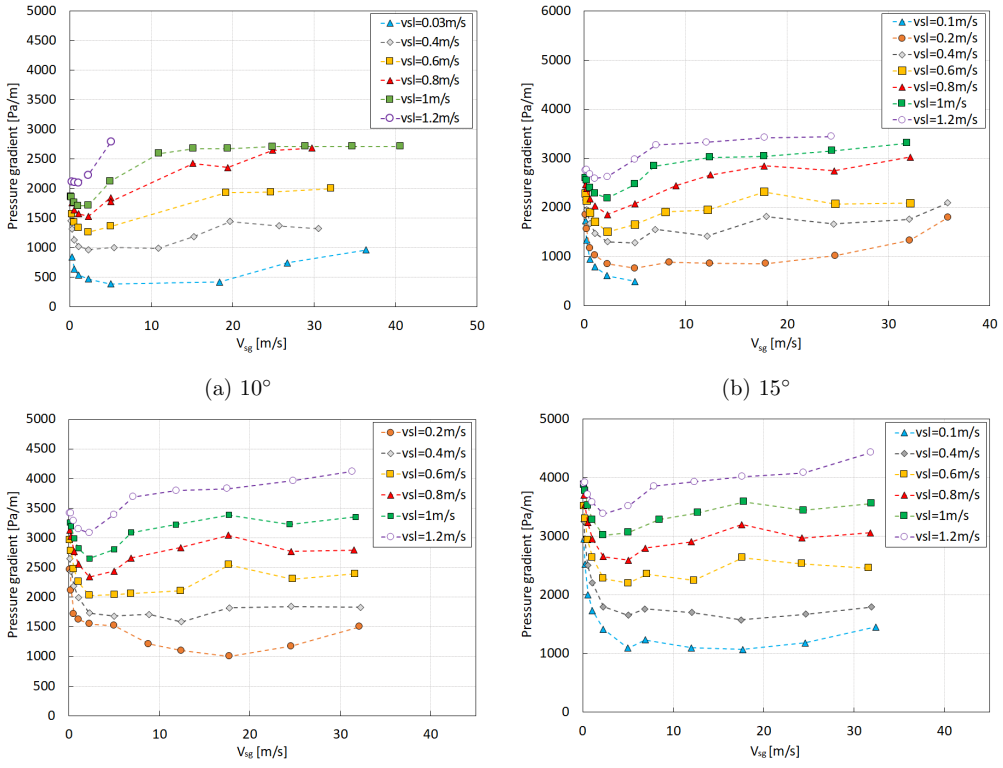

(a) 10° (b) 15°

(c) 20° (d) 25°

Figure 3.16. Pressure gradient variation vs. superficial gas velocity for air-mixed oil system at STP conditions for different inclination angles (from horizontal)

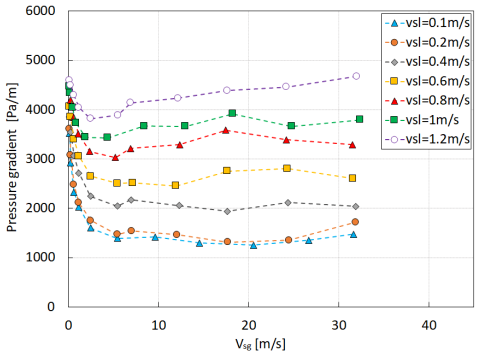

(e) 30°

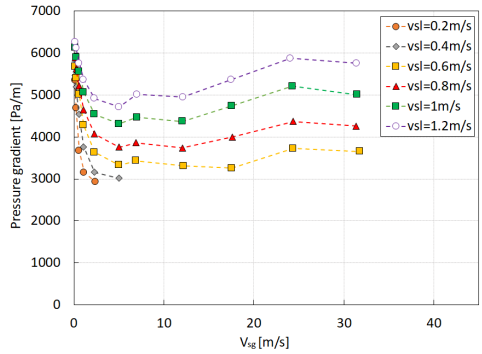

(f) 45°

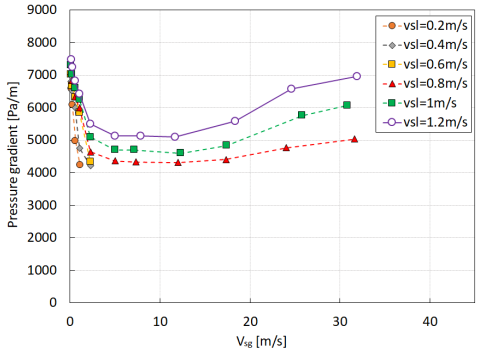

(g) 60°

Figure 3.16. *(cont.)* Pressure gradient variation vs. superficial gas velocity for air-mixed oil system at STP conditions for different inclination angles (from horizontal)

For some pipe inclinations such as 10°, 45°, 60°, 70° and 78° at given liquid flow rate, total pressure drop to be measured was out of the calibration range of the used differential pressure transmitters. Thus, the measurement could not be considered accurate and was therefore not plotted.

Overall, it was observed that the pressure drop response depended on the flow pattern present in the test section as well as with the pipe inclination. For low gas and liquid superficial velocities were bubble flow (elongated and cap) was identified, the pressure drop curve reaches a minimum point. This minimum is due to large liquid holdup that occurs in bubble flow, which results in a large gravitational pressure gradient, and due to low friction pressure gradient because of the low velocities (Shoham, 2006).

3.6.1.3 Liquid holdup

Figures 3.17a–3.17h present the liquid holdup vs. superficial gas velocity given a constant superficial liquid velocity pipe inclination tested for air-mixed oil flow system.

For each data set, the average voltage was converted to the normalised signal and used as input in the S-curve (Figure 3.12b) which the liquid holdup was calculated.

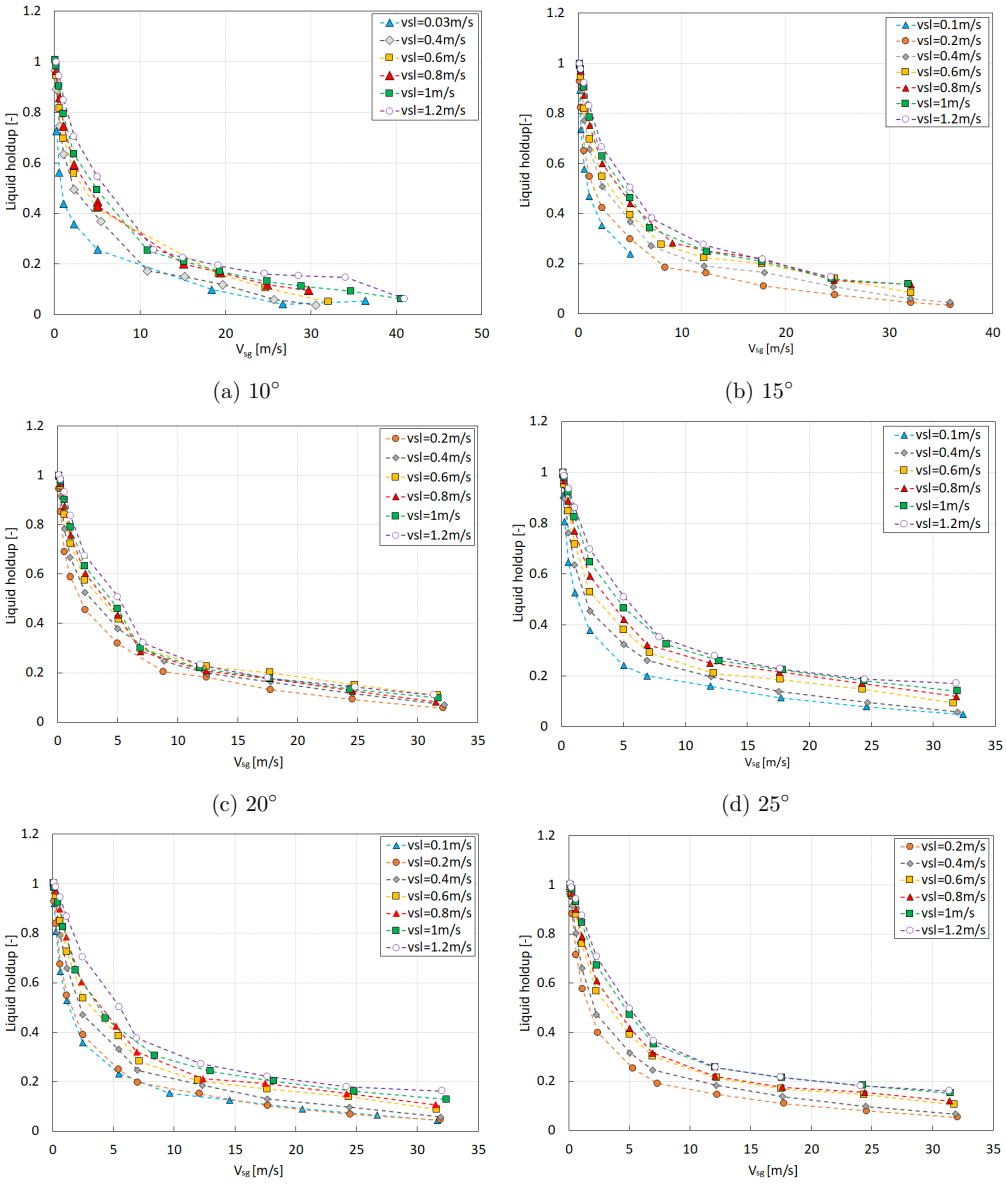

(a) 10°

(b) 15°

(c) 20°

(d) 25°

(e) 30°

(f) 45°

Figure 3.17. Liquid Holdup vs. superficial gas velocity for air-mixed oil system at STP conditions for different inclination angles (from horizontal)

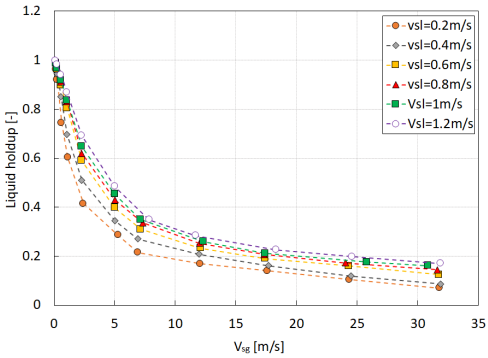

(g) 60°

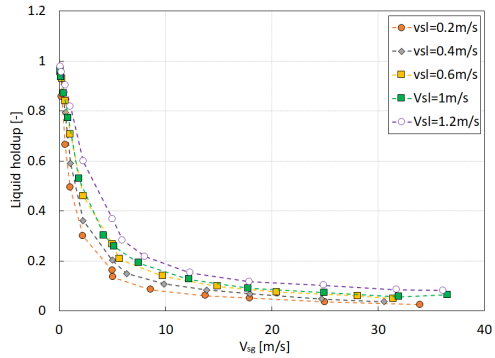

(h) 70°

Figure 3.17. *(cont.)* Liquid Holdup vs. superficial gas velocity for air-mixed oil system at STP conditions for different inclination angles (from horizontal)

Overall, the change in flow pattern and pipe inclination had no significant impact on the liquid holdup behaviour with superficial gas velocity as observed in Figure 3.17.

3.6.2 Air-water system

Result from experiments performed for air-water flow system are presented in this subsection. The experiments were aimed to evaluate the annular-slug transition boundary for inclined test section. Thereafter liquid loading was related to flow pattern transition.

3.6.2.1 Flow regime transition

Observed flow pattern transition from slug to annular flow and the onset of liquid loading is presented in Figure 3.18.

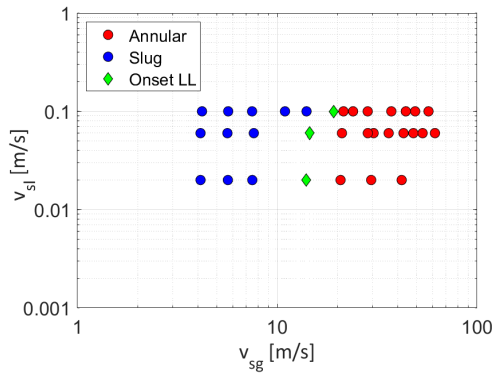

(a) 20°

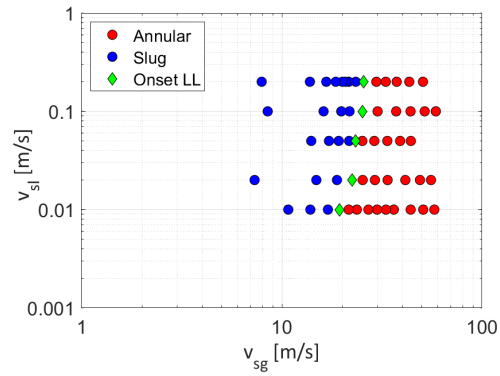

(b) 30°

Figure 3.18. Experimental tests on transition boundary of annular-slug for air-water system at STP condition for different inclination angles (from horizontal)

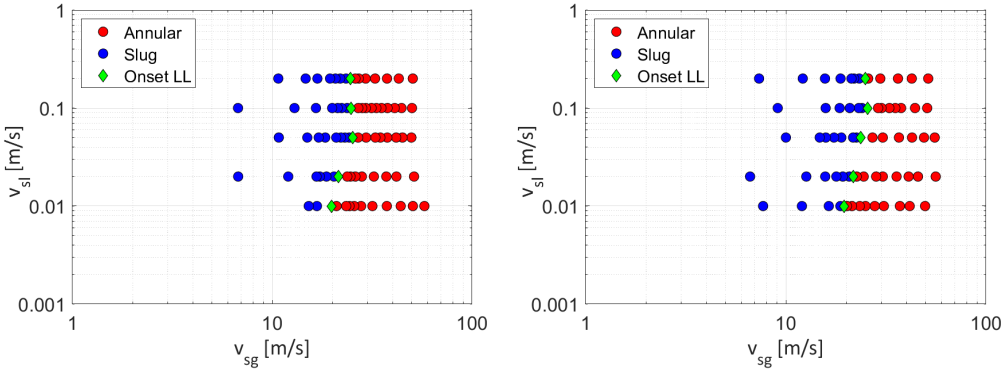

(c) 45°

(d) 60°

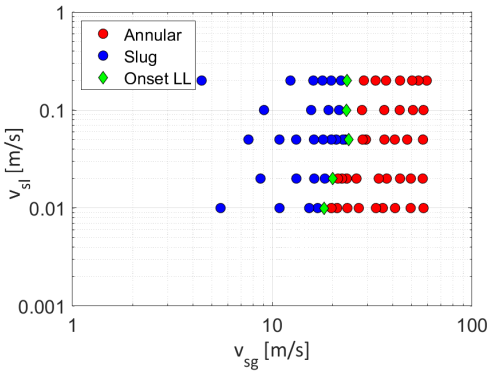

(e) 70°

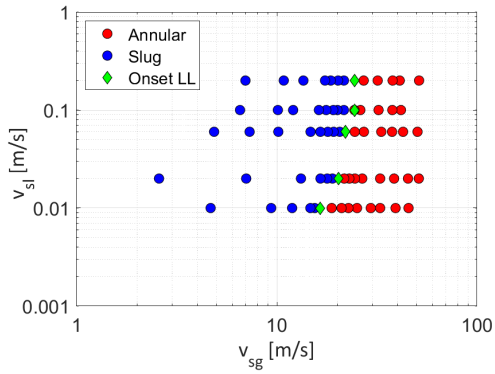

(f) 78°

Figure 3.18. *(cont.)* Experimental tests on transition boundary of slug-annular for air-water system at STP condition for different inclination angles (from horizontal)

For this experimental study, a refined interval was used so that the transition from annular to slug could be identified. In addition, slow motion video was recorded and used in the identification. For a constant superficial liquid velocity, the reduction of superficial gas velocity was irregular, since the valve controlling the gas injection into the test section was operated manually.

3.6.2.2 Pressure gradient

Figures 3.19a–3.19f shows the change in pressure gradient vs. superficial gas velocity for all the pipe inclinations for air-water flow system.

For all the pipe inclination, measured pressure gradient reached a minimum. To the left of the minimum, Shoham (2006) explained that the reduction of pressure drop can be due to the fact that with the increase of the gas flow rate, the liquid holdup reduces, resulting in a lower gravitational pressure gradient and that the velocities encountered in slug flow are not high enough to cause high frictional pressure gradient. To the right of the minimum in the curve the friction component of the pressure gradient starts to be dominant increasing the pressure drop.

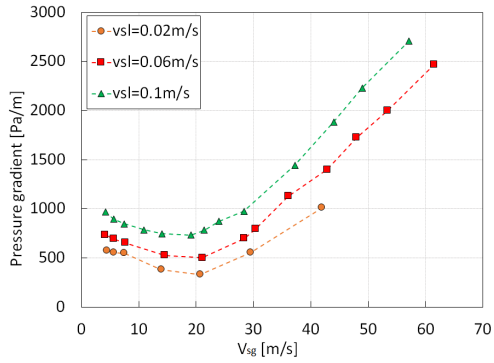

(a) 20°

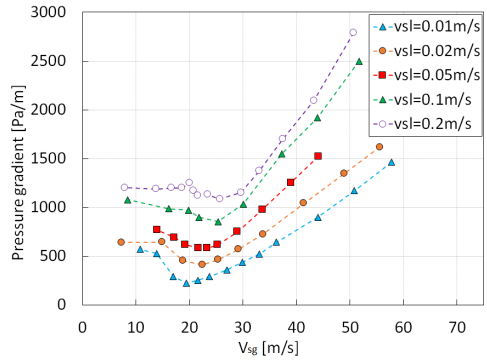

(b) 30°

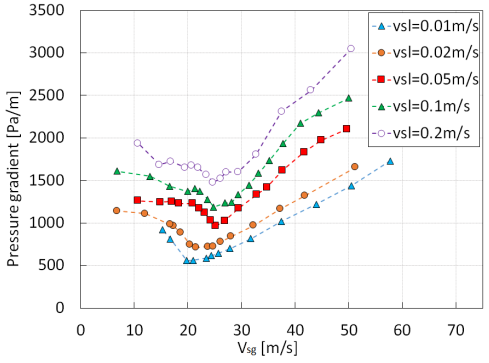

(c) 45°

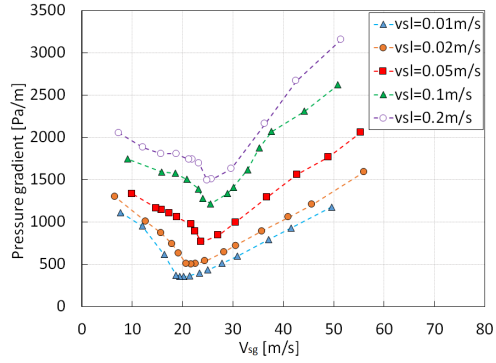

(d) 60°

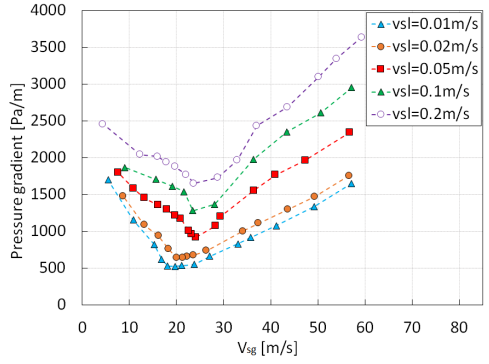

(e) 70°

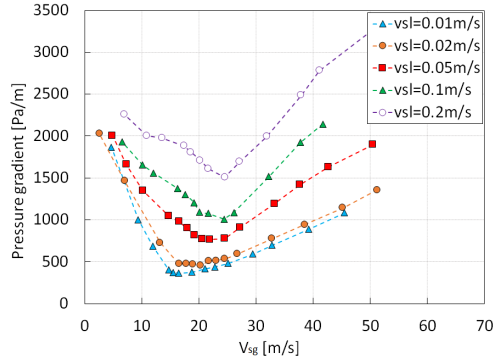

(f) 78°

Figure 3.19. Pressure gradient variation vs. gas superficial velocity for air-water system at STP conditions for different inclination angles (from horizontal)

3.6.2.3 Liquid holdup

Figures 3.20a–3.20f presents the liquid holdup vs. superficial gas velocity for air-mixed oil flow system, for a given constant superficial liquid velocity and pipe inclinations. Liquid holdup at flow regime transition was calculated with the average values and the S-curve of the impedance probe (Figure 3.12a).

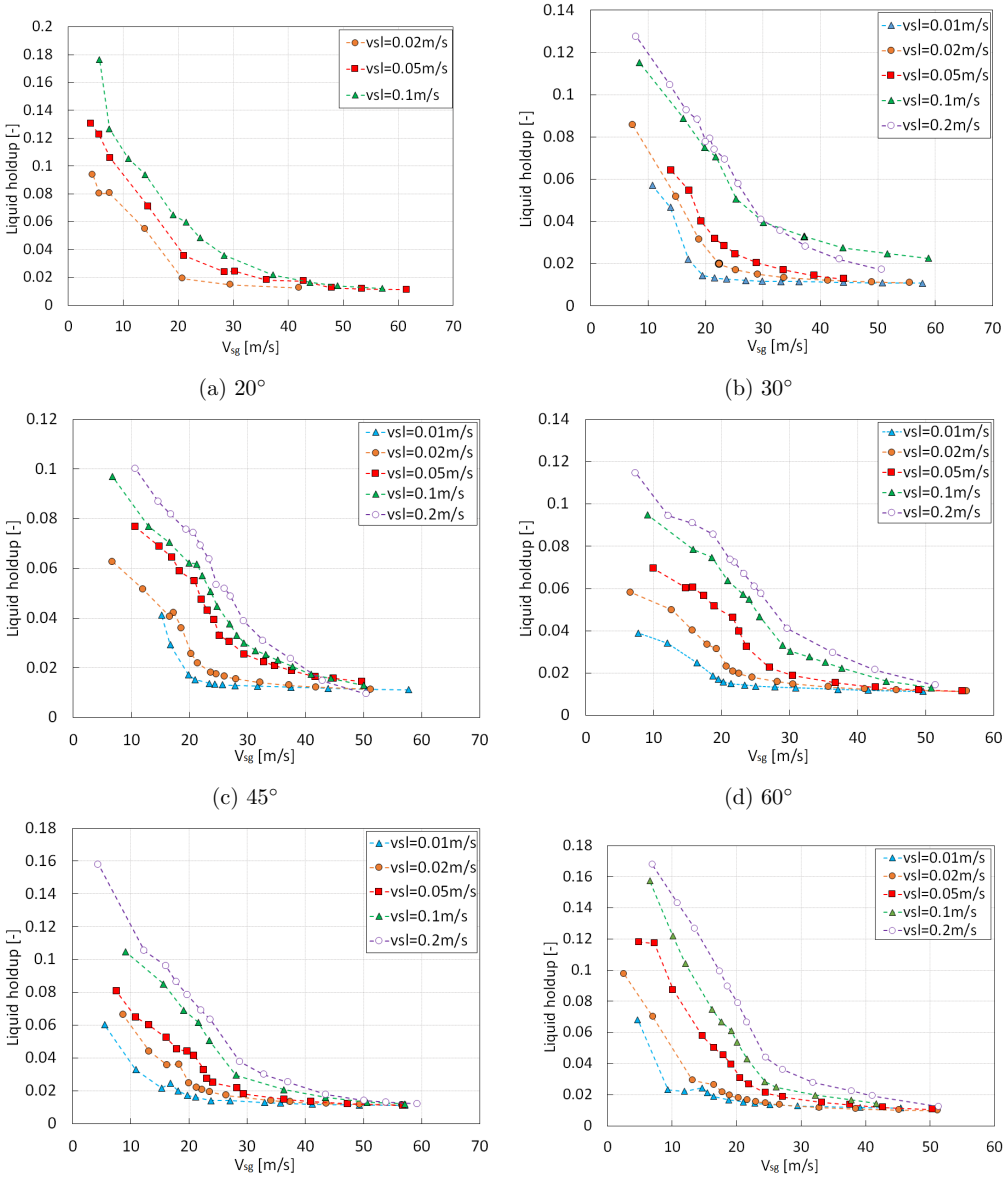

(a) 20° (b) 30°

(c) 45° (d) 60°

(e) 70° (f) 78°

Figure 3.20. Liquid holdup vs. gas superficial velocity for air-water system at STP conditions for different inclination angles (from horizontal)

3.6.3 Air-Exxsol D80 system

Result from experiments preformed for air-Exxsol D80 flow system are presented in this subsection. The experiments were performed aimed to evaluate the annular-slug transition boundary for inclined test section. The acquired data would then be compared with air-water experimental results to evaluate the effect of liquid viscosity on the annular-slug transition. Liquid loading study was also performed for this set of data.

3.6.3.1 Flow regime transition

Flow pattern transition from slug to annular flow observed experimentally is presented in Figure 3.21.

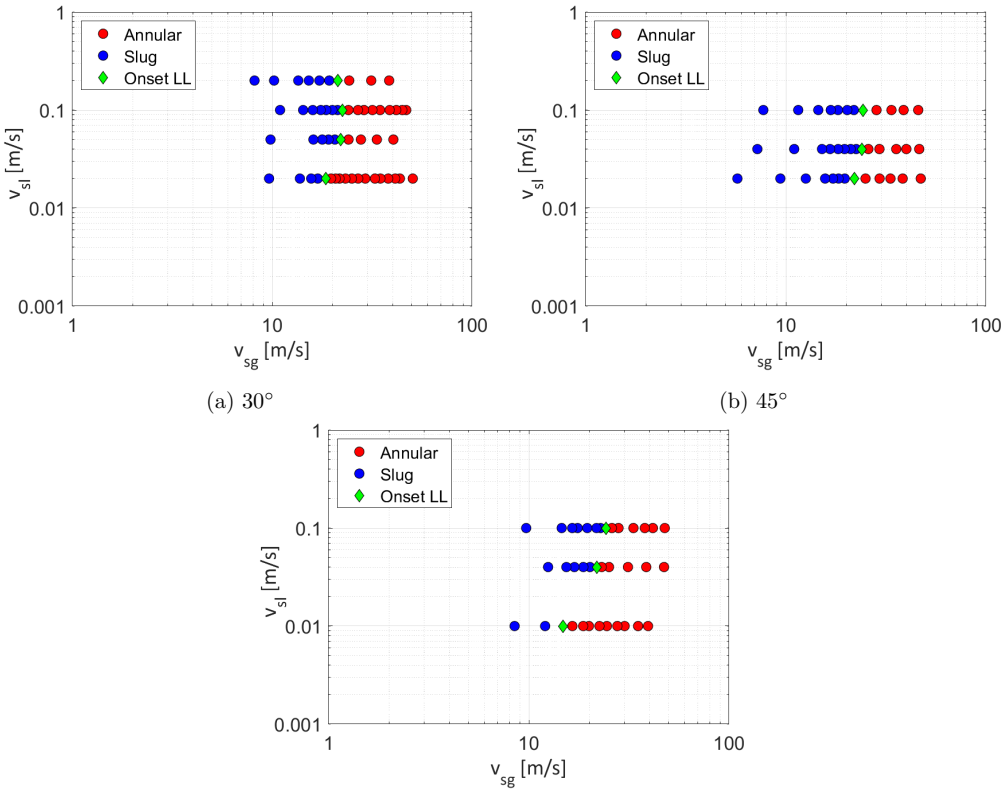

(a) 30°

(b) 45°

(c) 60°

Figure 3.21. Boundary of slug-annular transition for air-Exxsol D80 system for different inclination angles (from horizontal)

The interval of variation of superficial gas and liquid velocity are not equally distributed for tested pipe inclinations, due to insufficiency of liquid available in the lab and to manual injection of the gas flow into the test section.

3.6.3.2 Pressure gradient

Figure 3.22 shows the change in pressure gradient vs. superficial gas velocity for all tested pipe inclinations for air-Exxsol D80 flow system.

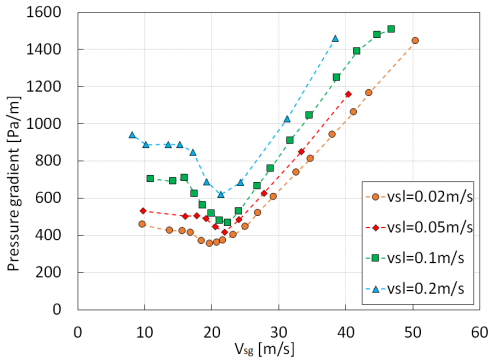

(a) 30°

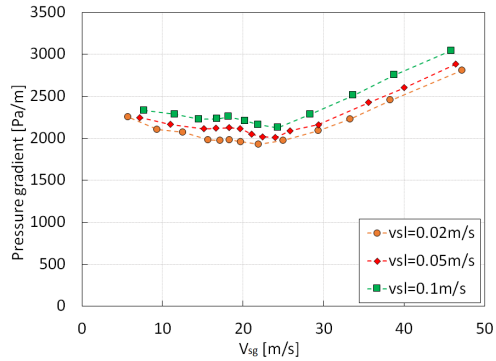

(b) 45°

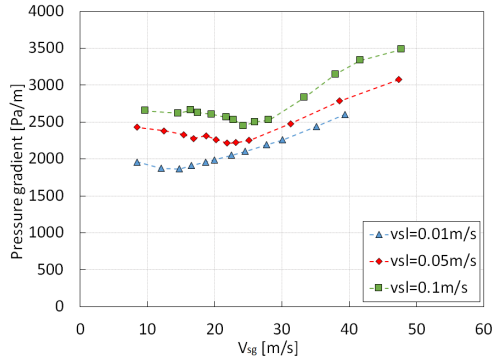

(c) 60°

Figure 3.22. Pressure gradient variation with gas superficial velocity for air-Exxsol D80 system at STP conditions for different inclination angles (from horizontal)

It can be observed that as in air-water system, the pressure gradient reached a minimum value as the superficial gas velocity reduced, which meant an increase in liquid content inside the pipe section.

Liquid holdup was not measured for this experimental campaign due to poor quality of the values measured by the capacitance probes.

Chapter 4

Numerical study on two-phase gas-liquid flow

In this chapter the data acquired for two-phase gas-liquid flow inclined pipe were analysed and compared against models available in the literature, as well as a dynamic simulator. The goal of the present studies was to:

- Investigate the effect of viscous fluid on flow regime map for inclined pipe.
- Evaluate the accuracy of models available in the literature used for prediction of the onset of liquid loading by comparing them against experimental data.
- Investigate the effect of entrainment droplets in gas core in liquid film models.
- Develop a new liquid loading onset model with more predictability.
- Quantify the variability of gas liquid loading onset rates, for different loading criteria and pressure drop.

4.1 Effect of fluid viscosity on two-phase flow in inclined pipe

From literature survey presented in Section 2.1 and summarised in Table 2.1, it was observed that most experimental studies on two-phase flow pattern for inclined section were carried out using water as liquid phase. Few researchers such as Stanislav et al. (1986) and Kokal and Stanislav (1989*a*,*b*) performed experiments for slightly inclined pipe (maximum 9° inclination) using viscous liquid (7 mPa.s and 6.5 mPa.s). Other examples are Gokcal et al. (2008) and Jeyachandra et al. (2012) who performed experiments with higher liquid viscosity, ranging from 0.585 Pa.s to 0.181 Pa.s, in lower pipe inclination (±2° from horizontal). Therefore, the availability of data to evaluate the performance of multiphase flow models on flow pattern predictions for viscous liquid is limited.

The experimental work carried out in this thesis and presented in Section 3.6.1 was used to evaluate the performance of the unified model proposed by Barnea (1987) and the dynamic multiphase flow simulator (OLGA® 7.3 - hereafter referred to as OLGA).

Barnea (1987) model was chosen to be evaluated being the most used model for flow pattern predictions. Pressure gradient values from OLGA simulations for a certain liquid velocity and different pipe inclinations were compared with pressure gradient acquired experimentally.

4.1.1 Flow pattern

Experiments were performed in a steady-state conditions according to methodology presented in section 3.5. The flow regimes observed experimentally were:

- stratified-wavy flow (SW);
- elongated-bubble flow (EB);
- cap-bubble flow (CB);
- slug flow (SL);
- churn flow (CH;
- annular flow (AN).

A complete flow regime mapping such as the example shown in Figure 2.2 was not possible to achieve, due to limitations of the laboratory facility, such as pump capacity, volume of liquid available in the main separator and limited range of flow meters.

The identification of flow regime present in the pipe was sometimes questionable due to visual similarity of some regimes, for example the case of stratified-wavy to annular flow transition for low inclination angles, and churn to annular flow transition for high inclination angles. This brought some uncertainty into flow pattern classification in present study.

Figures 4.1a–4.1i show flow pattern boundaries obtained from the transition model of Barnea (1987) (solid lines), OLGA (discontinuous line) and the data measured in the present work (colour points).

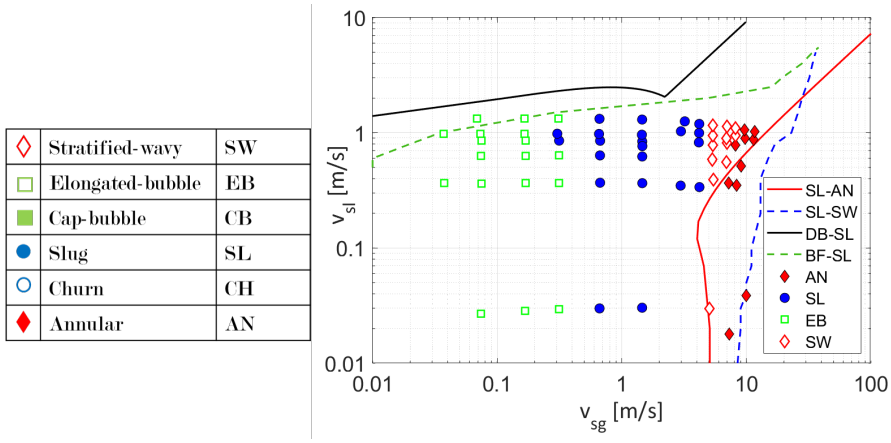

(a) 10°

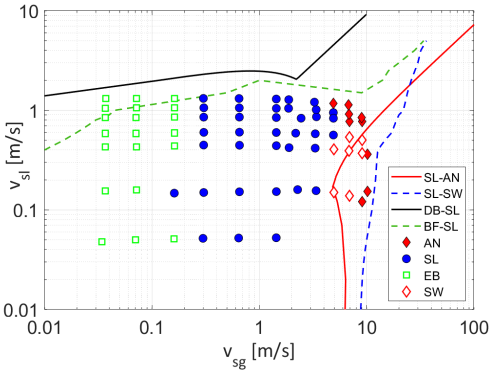

(b) 15°

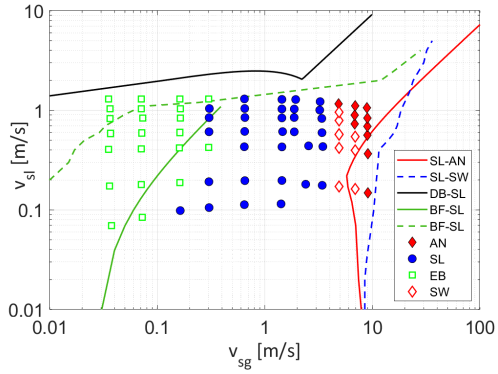

(c) 20°

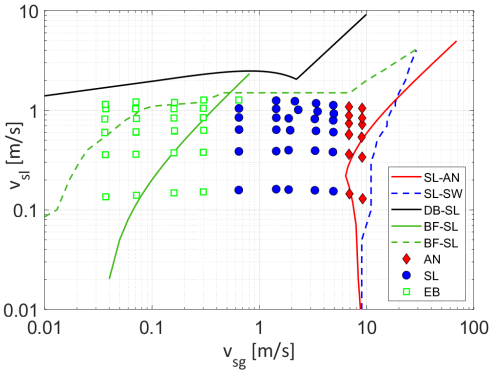

(d) 25°

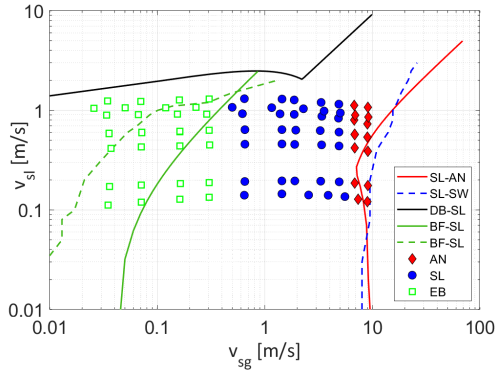

(e) 30°

Figure 4.1. Experimental flow pattern vs. Barnea (1987) model (——) and OLGA simulation (- - - -) for air-mixed oil system in upwards inclined pipes

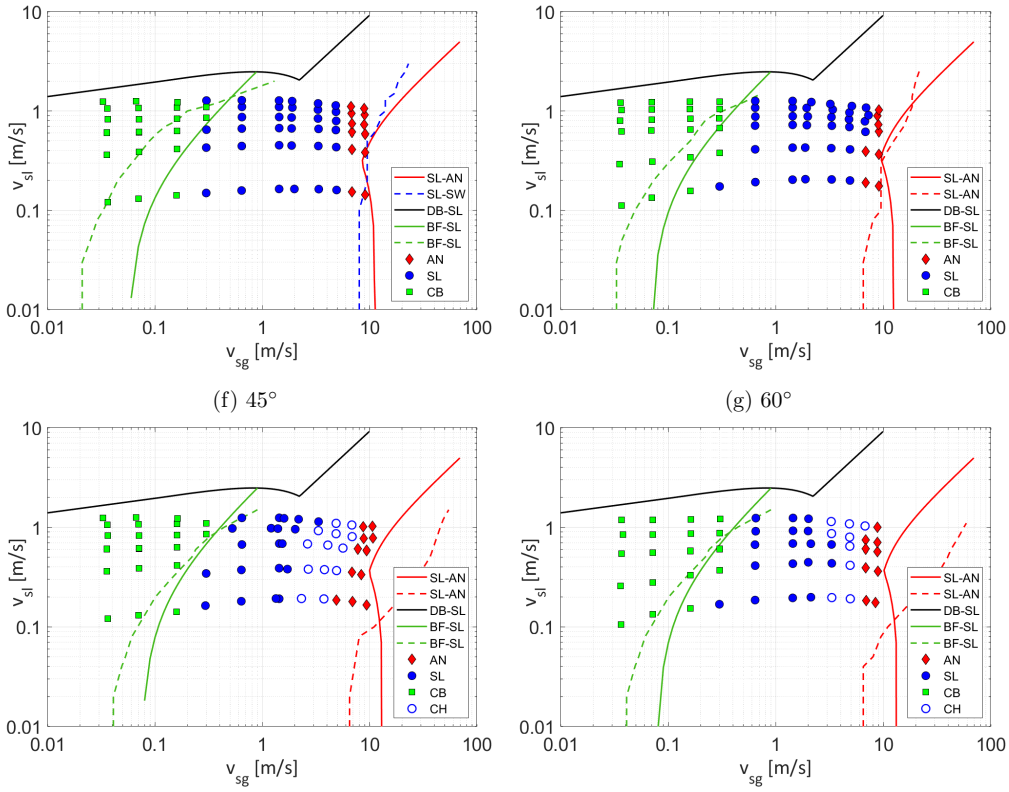

(f) 45° (g) 60°

(h) 70° (i) 78°

Figure 4.1. *(cont.)* Experimental flow pattern vs. Barnea (1987) model (——) and OLGA simulation (- - - -) for air-mixed oil system in upwards inclined pipes

It was mentioned in Section 2.1 that Shoham (1982) classified two-phase flow into four main regions: *Stratified*, subdivided into stratified-smooth and stratified-wavy; *intermittent*, with elongated-bubble, slug and churn flow; *annular*, with annular and annular wavy and finally *dispersed bubble* region (see Figure 2.1). However, In OLGA (according to Bendiksen et al. (1991)) the flow regime identification is based on two flow regime classes, namely *distributed* and *separated*. The distributed class is where the contribution of bubble and slug flow are present, while the separated class include stratified either as smooth or wavy and annular flow. Therefore, OLGA only distinguishes between four flow regimes: stratified, bubble, slug and annular.

Starting from stratified region, it is notable in Figures 4.1 that stratified-smooth flow could neither be observed experimentally nor predicted numerically due to 10° being the minimum inclination angle tested. Barnea et al. (1985) stated that such flow regime would be possible to observe for inclination angles less than 0.25°. Stratified-wavy flow (SW) on the other hand was shown to increase when pipe diameter increased and reduced as the upward inclination increased. Experimentally the SW was not observed for inclinations greater than 20°. However, an transition region predicted by the model was expected to appear, yet could not be displayed on the plot due to the minimum liquid velocity used in this study. In Barnea (1987) model the transition region appeared at low inclination

angles, liquid velocity ranging from 0.001 to 0.01 m/s. It should be mentioned that due to differences in naming between annular-wavy and stratified-wavy, the stratified-wavy to annular transition region was not clear, which mean that experimentally flow pattern could be misinterpreted.

The OLGA simulation results indicated that for inclination angles lower than 60° stratified-wavy to slug flow transition was predicted instead of annular to slug flow as experimentally observed or predicted by the model. Bendiksen et al. (1991) explained that the transition between stratified and annular flow is based on wetted perimeter, where annular flow can appear when the wetted perimeter becomes equal to the film inner circumference, i.e., when the wave height reaches the top of the pipe. The average wave height may be obtained by assuming that the mass flow forces in the gas balance the gravitational and surface tension forces (Bendiksen et al., 1991).

Experimentally, through visual inspection, it was observed that for lower pipe inclinations high gas velocities was required in order to see an uniform liquid film around the pipe. Barnea et al. (1980*b*) mentioned that annular flow regime could be classified as annular-wavy which is characterised by an unstable liquid film wave around the pipe circumference.

For the intermittent region, it was observed experimentally and confirmed from the data published by Barnea et al. (1985) that the elongated-bubble flow area is reduced with increasing pipe diameter and inclination angles. In elongated-bubble flow the gas phase had a smooth bullet-formed shape, while the liquid phase did not contain any dispersed bubble and the flowing of the fluid was slowly approaching slug flow. For inclinations above 30°, small bubbles flowing at the top of the pipe were observed and classified as cap-bubble flow. The appearance of small bubbles were due to the air injection point, that protrudes into the test section (see Figure 3.1), which was located at the top of the test section. Barnea et al. (1985) and Barnea (1987) observed that for inclinations above 30°, elongated-bubble disappeared and dispersed flow took place. Therefore, for low gas and liquid velocity and high inclinations, a cap-bubble was identified instead of dispersed-bubbles.

Churn flow in the experimental data had a similar behaviour as the one verified by Barnea et al. (1985), where the first appearance of this pattern occurred at 70° inclination (Figure 4.1h). In Barnea et al. (1985) the range of v_{sl} at which churn flow was observed, increased with pipe diameter. Thus for the test section diameter and liquid velocity test it was possible to experimentally observe churn flow.

Slug flow was observed through all the tested inclination angles, and transition to annular flow occurred at high gas velocities. The tested gas velocity was lower than the boundary velocity required for numerical and simulated slug-annular flow transition (SL-AN) as shown in Figure 4.1. In OLGA for instance SL-AN transition was observed only for inclinations above 60° as explained previously. Simulations were performed for 30° pipe inclination, aiming to estimate at which gas velocity annular flow could be found. However, no transition could be found, even for gas velocities above 200m/s (see Figure 4.2).

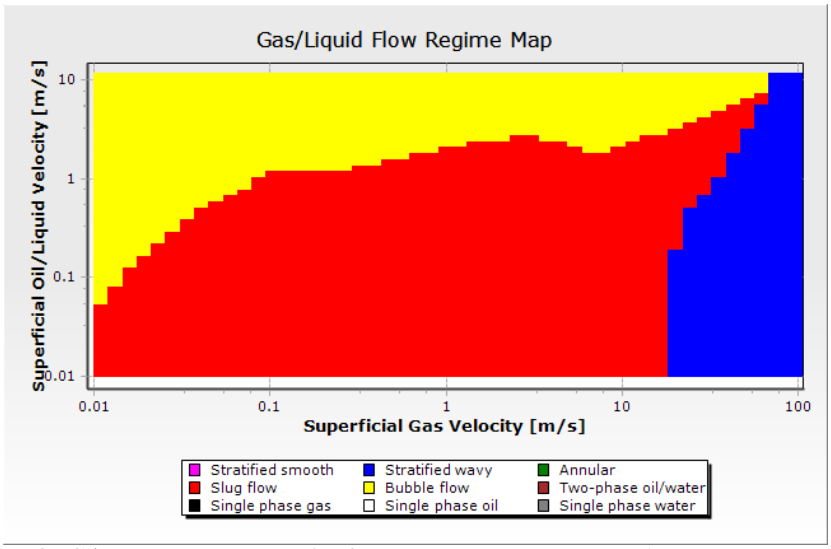

Figure 4.2. OLGA simulation results for flow pattern transition in 30° upward inclined pipe for air-mixed oil system at STP condition

For high liquid velocities the dispersed-bubble region was not achieved experimentally since available liquid volume was limited by the capacity of the main separator. Dispersed-bubble to slug transition (DB-SL) predicted through the Barnea's model was located above the maximum applicable liquid velocity, which showed good agreement with observations. Barnea (1987) defined the bubble flow region for low liquid and gas velocities and high inclination angles instead of dispersed-bubble flow. Experimental data for inclination angles above 60° showed good agreement with predicted bubble to slug flow transition (BF-SL). In OLGA, the BF-SL transition curve moved downwards to the right as the inclination angle increased, hence the experimental bubble flow region was better represented by inclination above 30°. This conclusion was based on the fact that cap-bubble flow existed in the dispersed-bubble region.

Overall, the flow pattern map for viscous fluid predicted using Barnea (1987) unified model presented a good agreement with the experimental data. Most the flow pattern regions identified experimentally could also be identified by the model with acceptable accuracy, except for annular flow. It seemed to be too offset from the numerical and simulated results. OLGA did not manage to reproduce satisfactorily the experimental flow pattern map measured.

4.1.2 Pressure gradient

Pressure gradients in two-phase flow are more complicated and difficult to predict compared to single phase flow. As mentioned in Section 2.1.1, pressure gradients are strongly dependent on flow pattern. This was also observed experimentally, where for a certain flow regime present in the pipe section, recorded pressure drop and capacitance presented different readings. Figures C.1 to C.6 present total pressure drop and capacitance probe signal against superficial gas velocities at given constant superficial liquid velocity for different pipe inclination angles.

Figure 4.3 presents measured pressure gradient compared to OLGA simulations, given a constant superficial liquid velocity, varying superficial gas velocities and pipe inclinations.

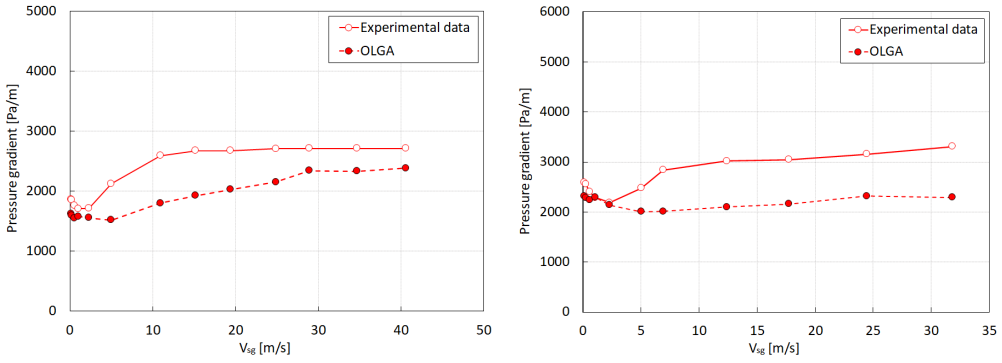

(a) 10°

(b) 15°

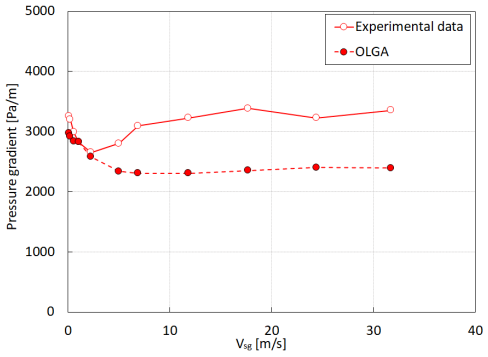

(c) 20°

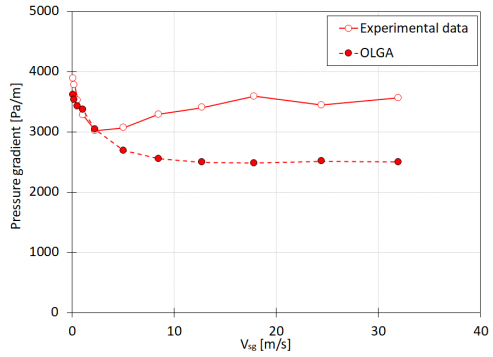

(d) 25°

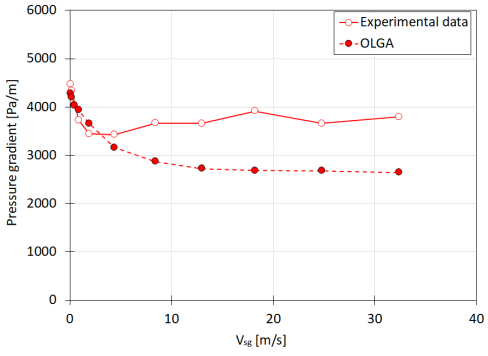

(e) 30°

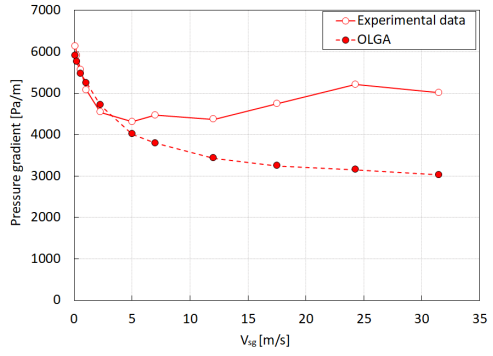

(f) 45°

Figure 4.3. Recorded pressure gradient in upward inclined pipes compared to OLGA simulation for v_{sl}=1m/s

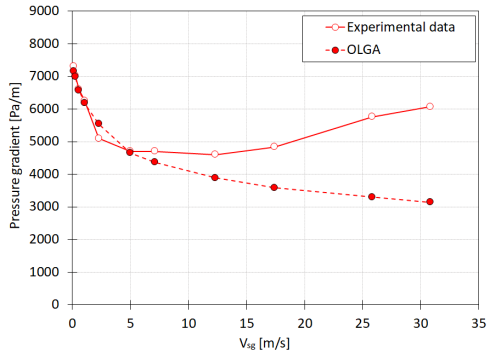

(g) 60°

Figure 4.3. *(cont.)* Recorded pressure gradient in upward inclined pipes compared to OLGA simulation for v_{sl}=1m/s

Experimentally, it was observed that for a given constant superficial liquid velocity as gas velocity increases, total pressure gradient reached two minimum points in the curve. For lower values of superficial gas velocity the minimum was reached during the transition between bubble to slug flow and at high gas velocities on intermittent to annular flow transition. Bubble flow can exist at low superficial gas and liquid velocities, exhibiting high gravitational pressure gradient due to high liquid content. As superficial gas velocities increases up to moderate values towards the slug flow or intermittent region, the liquid content reduces, resulting in lower gravitational pressure drop. Simultaneously, frictional pressure gradient increases leading to a minimum pressure gradient. Further increase of superficial gas velocity causes the existence of annular flow, where frictional losses are more dominant.

Figure 4.3 have shown that both experimental and the simulation results presented a similar trend. However, there was a significant discrepancy at high superficial gas velocities. A reason for these discrepancies could be due to the difference between the flow regimes predicted in OLGA compared to the regimes experimentally observed. At high superficial gas velocity OLGA predicted slug or stratified-wavy flow, while stratified-wavy or annular flow were observed. For superficial gas velocities above 5 m/s OLGA underestimated the total pressure drop compared to measured total pressure drop.

In order to quantify how the measured data differ from the OLGA simulation, experimental and calculated results were compared and presented in Figure 4.4

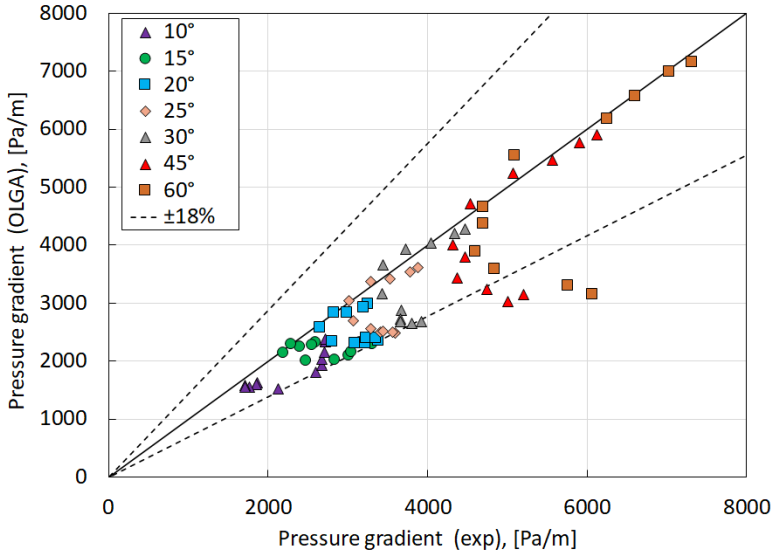

Figure 4.4. Comparison of measured pressure gradient with OLGA values for all pipe inclinations at constant v_{sl}=1m/s

Figure 4.4 shows that most values predicted with OLGA are within ±18% error with respect to the measured data values except for some data point for 45° and 60° inclinations due to the large gap on high gas velocities previous presented in Figures 4.3f and 4.3g.

4.2 Applicability of existing models for liquid loading prediction

The literature review in Section 2.2 revealed that most of the proposed models for onset of liquid loading prediction were empirical correlations developed based on field and experimental data. Therefore, it is expected that such models will perform good for operational conditions close to the conditions for which the correlations are derived, but it could exhibit significant deviations for conditions different from those. Hence, each model provided different indications on the critical gas velocity at which the onset of liquid loading might exist.

The goal of this section is to quantify and evaluate the performance of the available models used for liquid loading onset prediction. Prediction results from the most relevant and currently used models, such as droplet model by Turner et al. (1969) and Belfroid et al. (2008), along with liquid film models by Barnea (1986), Luo et al. (2014) and Shekhar et al. (2017) and results from a dynamic simulator (OLGA), were evaluated through comparison with experimental data acquired in this work.

Model performance was quantified by calculating an absolute error for each data point, following a calculation of relative error by using Equations B.30 and B.31, respectively. Relative errors were presented as bar plot and summarised in Tables B.3 and B.4.

4.2.1 Air-water system

Discrete data points representing the critical gas velocity ($v_{sg,critical}$) at which the onset of liquid loading occurs were taken from the experimental data presented in Section 3.6.2.1.

Figures 4.4a–4.4f presents the measured critical gas velocity plotted in logarithmic scale with the models and OLGA predicted transition boundary values for critical gas velocity. Prediction from liquid film model were shown as continuous lines and the prediction from liquid droplet models as well as OLGA were shown as dashed lines.

In addition, to represent the variability of the measured critical gas velocity, an error bar was added to the data points (Onset LL) where the right length of the horizontal error bars represented the last full stable production (annular flow) and left length the first full unstable production (slug flow), both flows were identified by visual inspection.

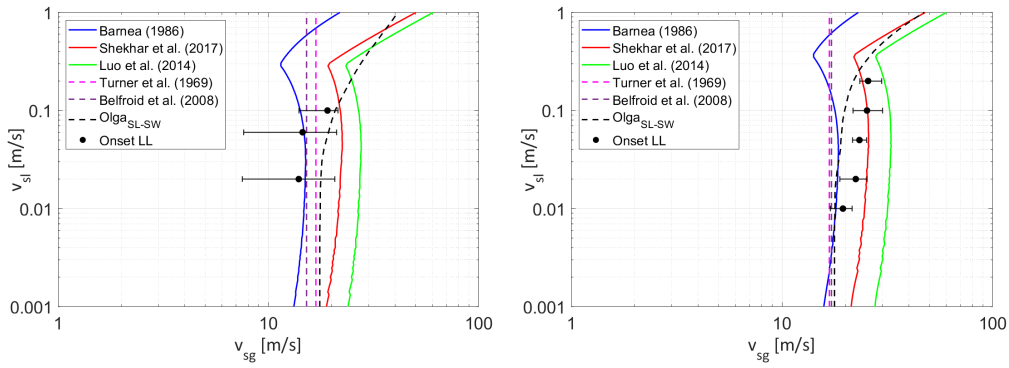

(a) 20°

(b) 30°

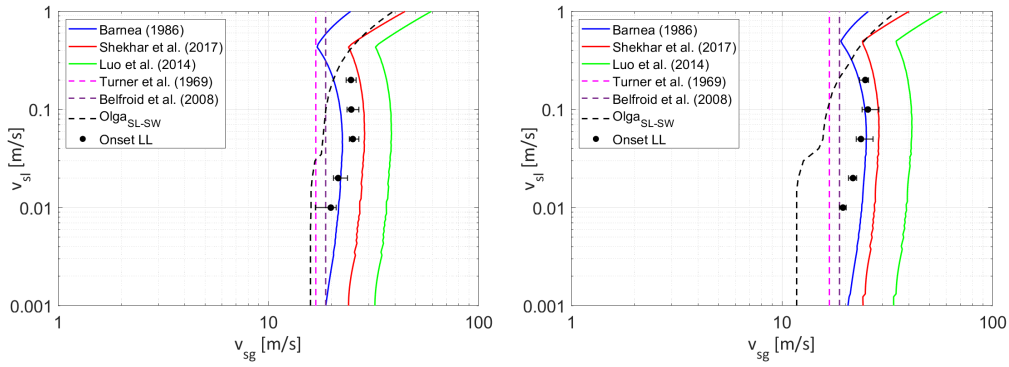

(c) 45°

(d) 60°

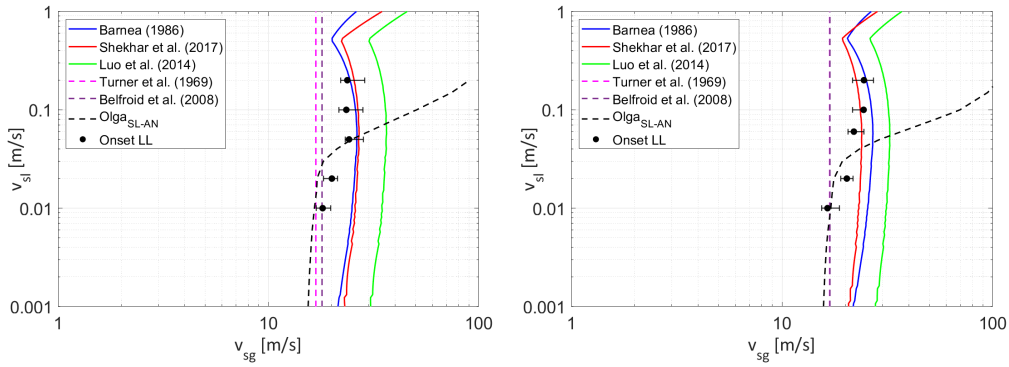

(e) 70°

(f) 78°

Figure 4.4. Comparison between experimental data, models prediction and OLGA results for an inclined pipe and air-water system at STP condition

In general, the proposed liquid film models represented the critical gas velocities measured experimentally better than the liquid droplet model and OLGA simulations results. The poor performance of Turner et al. liquid droplet model could be related to the fact that no inclination effect or liquid film was taken into consideration during critical gas velocity prediction. However, for the model proposed by Belfroid et al. (2008) in which

pipe inclination effects were considered, also performed poorly. This revealed that liquid droplet model may not be a good approach to predict the onset of liquid loading in inclined pipes.

Among all the liquid film models evaluated in this study it was consistently found that the model proposed by Luo et al. (2014) had a poor performance. Such deficiency was also highlighted by Shekhar et al. (2017). To overcome this problem Shekhar et al. (2017) corrected the Luo et al. (2014) model and proposed a new set of equations. The performance of the models proposed by Barnea (1986) and Shekhar et al. (2017), on the other hand, was similar, except for inclination angles lower than 45°, in which the models predicted poorly for the annular-slug transition line.

Regarding OLGA simulation, it was mentioned in Section 4.1.1 that flow regime transition distinguished between four main regions: stratified (smooth or wavy), annular, slug and bubble flow. In this study, the identification of annular-to-slug flow transition was desired, and such transition occurred only for inclination angles greater than 60°. For lower inclinations annular-to-stratified-wavy transition was predicted instead. Figure 4.4a to Figure 4.4c showed that the transition line predicted by the simulator was close to the experimental data, even-though slug to stratified-wavy was estimated. It is worth mentioning that for lower pipe inclination annular flow could also be classified as stratified-wavy or annular-wavy. Visual classification during the experiments to differentiate between those flows was challenging, thus only annular flow was presented.

An error quantification was performed by estimating relative errors between measured and calculated critical gas velocities. Figure 4.5 presents the relative error for each tested pipe inclination.

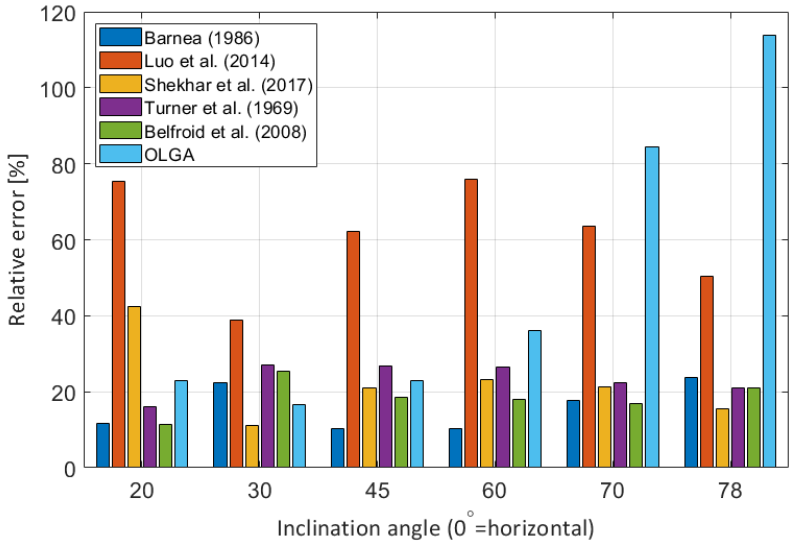

Figure 4.5. Comparison between experimental data with models prediction for all inclined pipe tested of air-water system at STP condition

From Figure 4.5 we can confirm the visual observation previously discussed. Among the evaluated liquid film models, Luo et al. (2014) presented higher relative error for all the pipe inclinations. In case of OLGA, the relative error tended to increase with increasing pipe inclination, reaching higher values for inclination greater than 60°. This could be due to the fact that at higher inclinations the predicted transition from annular-slug flow at moderate superficial liquid velocity were given at very high superficial gas velocities. This behaviour was not experimentally observed for inclinations where annular-stratified wavy transition was predicted.

For liquid droplet models it was observed that the error calculated with the prediction from Belfroid et al. (2008) model, did not present a wide range of variation with increase of inclination and in some cases where close to the liquid film model error. The same was not observed for Turner et al. (1969) model where the relative error appeared mostly to be higher than the liquid film model.

In general, liquid film models from Barnea (1986) and Shekhar et al. (2017) presented relative lower errors compared to the rest of the evaluated models. It was expected that the Shekhar et al. (2017) model would present better performance for lower inclination compared to Barnea (1986) model, since the model took into account the effect of enlarged film thickness at the bottom of the pipe. However, such behaviour was not observed.

To evaluate further the performance of the models, especially for Barnea (1986) and Shekhar et al. (2017), every individual observed onset LL data point was plotted against predicted results, as shown in Figure 4.6, and relative errors using all data points for every inclination was estimated and presented in Table 4.1.

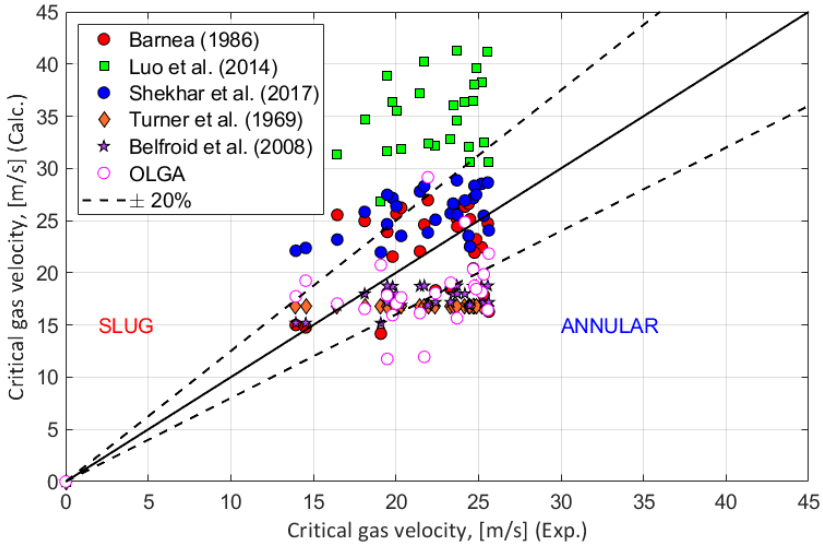

Figure 4.6. Comparison between experimental data vs. predicted results for air-water systems

Table 4.1. Model prediction error using all the data measured experimentally for air-water system

model	**number of data correctly predicted**	$err_{rel}(\%)$
Barnea (1986)	17/28	16.9
Luo et al. (2014)	28/28	60
Shekhar et al. (2017)	25/28	20.9
Turner et al. (1969)	3/28	23.8
Belfroid et al. (2008)	3/28	19.0
OLGA	10/28	54.7

In Figure 4.6 the 45° line in the plot represents the annular-slug transition boundary. This boundary divides the plot into an unloaded region which is the lower part (full annular flow) and a loaded region (full slug flow). The onset LL data points corresponded to the stage at when the unstable flow started to be visible. Therefore, the model's prediction values were considered to be accurate if the data point fell close to the 45° line or into the slug region. For liquid film models most of the data point fell above the line, except the model of Luo et al. (2014) which overestimate the transition. On the other hand, the liquid droplet model and OLGA seemed to underestimate the critical gas velocity during the transition.

After close analyse of the performance of Barnea (1986) and Shekhar et al. (2017), it can be seen on Figure 4.6 and Table 4.1 that Shekhar et al. (2017) shows a good match for the numbers of data correctly predicted (25 out of 28 correct predictions). However, it present a higher relative error (20.9%) compared to 16.9% given by Barnea (1986) predictions.

Overall for air-water systems the predictions of liquid loading onset in inclined pipes were better predicted by the liquid film model proposed by Barnea (1986) followed by the model of Shekhar et al. (2017).

4.2.2 Air-Exxsol D80 system

Experiments were performed for air-Exxsol D80 system to evaluate the performance of models used on prediction of liquid loading in gas wells. It is important to mention that most of the liquid loading models presented earlier were developed and evaluated for experimental data acquired for air-water flow systems. Discrete data points representing the critical gas velocity at which the onset of liquid loading exists were taken from the experimental data presented in Section 3.6.2.2.

Figures 4.7a–4.7c presents the measured critical gas velocity plotted in a logarithmic scale with the models and OLGA predicted transition boundary values for critical gas velocity. Prediction from liquid film model is shown as continuous lines and the prediction from liquid droplet model as well as OLGA are shown as dashed lines.

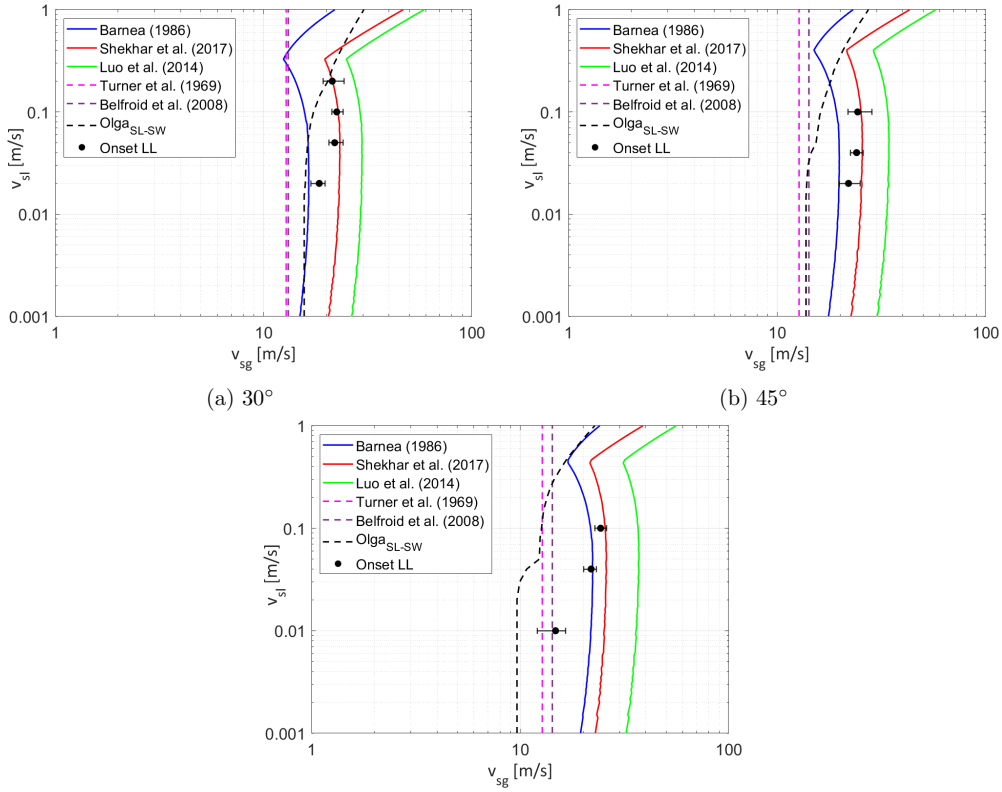

(a) 30°

(b) 45°

(c) 60°

Figure 4.7. Comparison between experimental data, models prediction and OLGA results an inclined pipe and air-Exxsol D80 system at STP condition

In general, the same behaviour as seen in air-water systems (Figure 4.4) was observed. The liquid film models gave a good agreement with the experimental critical gas velocities, while the liquid droplet by Turner et al. (1969) and Belfroid et al. (2008) models and OLGA under-estimated the critical gas velocity for all the inclination angles.

The predictions using the model of Luo et al. (2014) overestimated the critical gas velocity. On the other hand, the models proposed by Barnea (1986) and Shekhar et al. (2017) showed a reasonable match with the experimental data. However, considerable difference between annular-slug flow transition predicted by the models was detected for 30° pipe inclination.

Regarding OLGA simulation results, annular to stratified-wavy flow transition was observed for all pipe inclinations. Figure 4.7a showed that the predicted transition line was near the experimental data. Similar behaviour was observed for air-water system (Figure 4.4).

To evaluate the model's performance quantitatively, relative errors were estimated using measured and calculated critical gas velocities. Figure 4.8 presents the relative error for each pipe inclination.

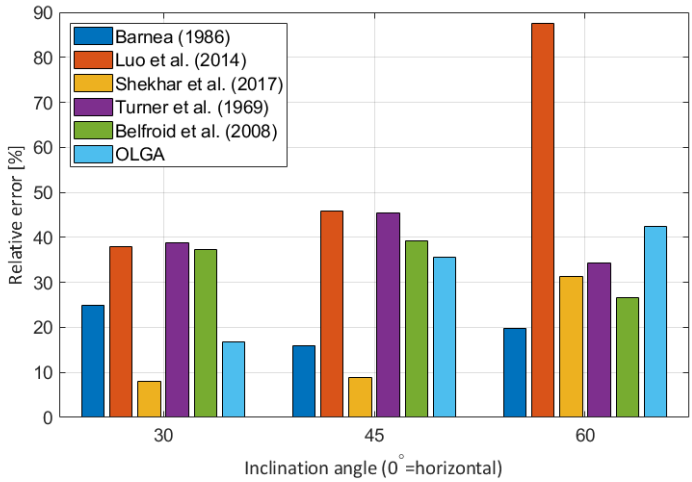

Figure 4.8. Comparison between experimental data with model predictions for all pipe inclinations for air-Exxsol D80 system at STP conditions

From Figure 4.8 we can confirm the visual observations discussed previously. Among the evaluated liquid film models, Luo et al. (2014) presented higher relative error for all pipe inclinations. For OLGA the relative error tended to increase with increasing inclination, reaching the highest values for 60° inclination.

Liquid droplet models exhibited higher relative error when compared to the liquid film models.

It is known that the model of Shekhar et al. (2017) was proposed to account for the inclination effect on the film thickness, which at the bottom of the pipe increases with decreasing inclination. Analysing the error for 30° and 45° inclinations, Shekhar et al. (2017) model provided a better prediction, which might be due to the fact that for such inclination the film thickness had high influence on the critical gas velocity estimation.

To get a better interpretation of the model's performance, for every individual observed onset of LL, data points were plotted against predicted results, as shown in Figure 4.9 and the relative error, using all data points for every inclination, was estimated and presented in Table 4.2

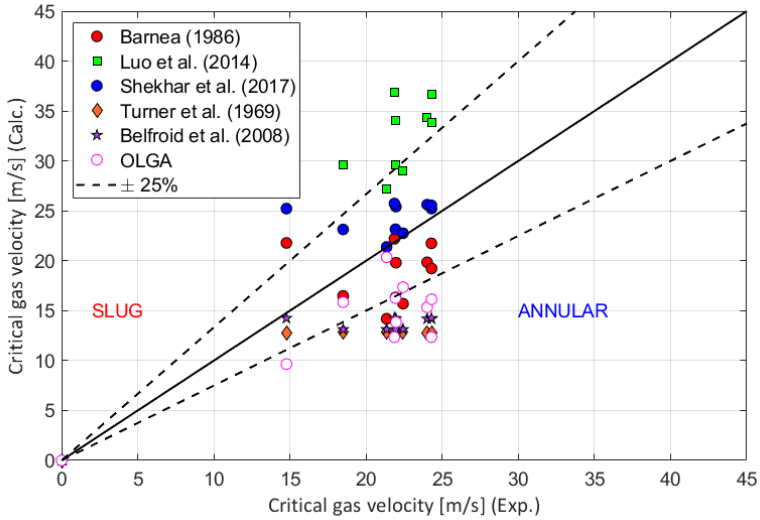

Figure 4.9. Comparison between experimental data vs. predicted results for air-Exxsol D80 system

Table 4.2. Model prediction error using all the data measured experimentally for air-Exxsol D80 system

model	**number of data correctly predicted**	$err_{rel}(\%)$
Barnea (1986)	2/10	20.8
Luo et al. (2014)	10/10	55.2
Shekhar et al. (2017)	10/10	15.2
Turner et al. (1969)	0/10	39.4
Belfroid et al. (2008)	0/10	34.7
OLGA	0/10	30.1

In Figure 4.9 the 45° line represents the annular-slug transition boundary. It can be seen that for liquid film models most data fall on the slug region except for the Barnea (1986) model. Although Luo et al. (2014) model predicted that the pipe will be in unstable flow, the values over-estimate the critical gas velocities, which is not the case for Shekhar et al. (2017); all the data points are close to the 45° line and having a variation of approximately 25%. For liquid droplet models and the OLGA simulator all the data points fell into the annular region, which did not made the predictions accurate.

Table 4.2 shows a good match for number of data correctly predicted (10 out of 10 correct predictions) for Shekhar et al. (2017) when compared to Barnea (1986) (2 out of 10 correct predictions) as well as the relative error of 15.2% estimated from the Shekhar et al. (2017) model, which proved to be the lowest error.

Overall, for air-Exxsol D80 system, the predictions of onset of liquid loading in inclined pipes were better interpreted by the liquid film model proposed by Shekhar et al. (2017), especially for pipe inclinations lower than 45°.

4.2.3 Air-mixed oil system

Experiments were performed for air-mixed oil systems to evaluate flow regime mapping for two-phase flow system in inclined pipes when high viscosity fluid (32cP) was used. Since flow pattern was the primary goal of the experimental study, an accurate annular-slug flow transition boundary was not covered. Therefore, slug flow and annular flow data were used to create an annular-slug transition region (shown in yellow in the plot below). Discrete data points representing both flows were taken from the experimental data presented in Section 3.6.2.3.

Figures 4.10a–4.10f presents the experimental data in logarithmic scale with the models predicting transition values for critical gas velocity. Prediction from the liquid film model were shown as continuous lines while prediction from the liquid droplet models were shown as dashed lines.

In the study performed in Section 4.1 it was observed that the Barnea (1986) model showed a good agreement with the data for the flow pattern mapping prediction. However, an additional study to evaluate Barnea (1986) model on predicting the annular-slug transition was performed, and likewise for models proposed by Luo et al. (2014) and Shekhar et al. (2017).

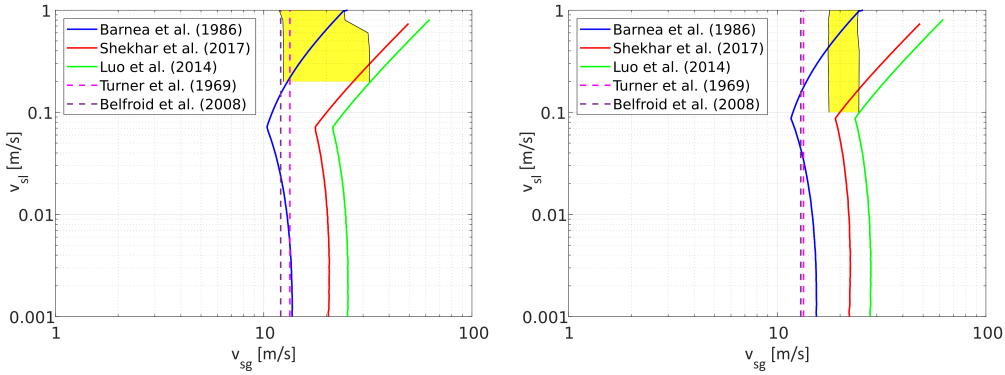

(a) 20° (b) 25°

Figure 4.10. Comparison between experimental data and models prediction results for an inclined pipe and air-mixed oil system at STP condition

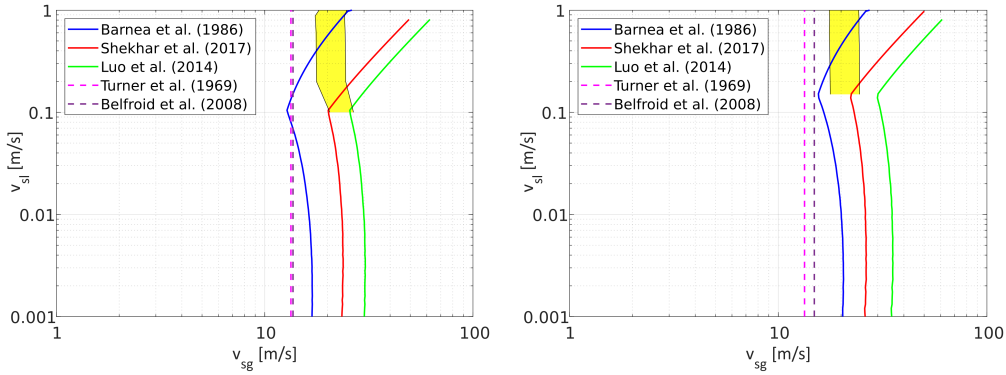

(c) 30° (d) 45°

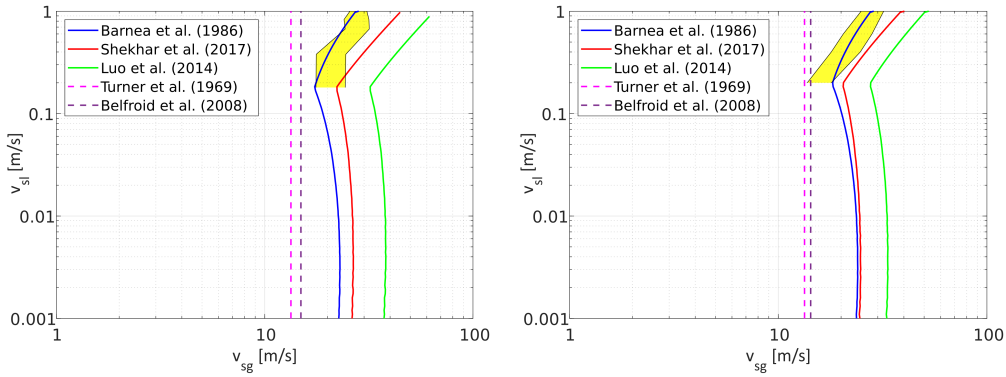

(e) 60° (f) 70°

Figure 4.10. *(cont.)* Comparison between experimental data and prediction model results in inclined pipes and air-mixed oil system at STP condition

Figure 4.10a through Figure 4.10f shows the comparison between the experimental data for air and viscous oil with the models. To evaluate the models, the transition line predicted by the models were compared with the transition area, i.e., if the transition line from the model is located in the transition region it means that the model had a better chance of predicting the correct critical gas velocity.

It can be observed from Figure 4.10 that the Barnea's model predicted better than the Shekhar et al. (2017) and Luo et al. (2014) model, since the annular-slug flow transition boundary line passed through a larger part of the region.

4.3 Effect of entrainment on the annular-slug flow regime transition for liquid loading prediction

In section 4.2 it was shown that the onset of liquid loading was better predicted when liquid film models were used. However, literature review in Section 2.2.2 revealed that all the liquid film models were developed based on the assumption that the liquid present in the well was only transported in the film, neglecting the droplets entrainment in the gas core. This assumption could overestimate the film thickness and therefore affect the prediction of critical gas velocity for a gas well with risk of liquid accumulation.

The objective of the present section was to evaluate the effect of droplet entraiment in liquid film models for the prediction of liquid loading in gas wells. Thus, an empirical equation that takes into account the fraction of liquid droplet entering the gas core (E) i.e, liquid transported as droplets was added to the model. The model proposed by Barnea (1986), Luo et al. (2014) and Shekhar et al. (2017) were evaluated. A study done by Enos (2018) on the evaluation of the model to predict liquid loading have shown that an equation proposed by Oliemans et al. (1986) predicted better the fraction of droplet entering the gas core. Oliemans et al. (1986) empirical correlation was developed from a regression analysis using the Harwell data bank. The correlation model proposed was:

$$\frac{E}{1-E} = 10^{-2.52}\rho_l^{1.08}\rho_g^{0.18}\mu_l^{0.27}\mu_g^{0.28}\sigma^{-1.80}D^{1.72}v_{sl}^{0.70}v_{sg}^{1.44}g^{0.46} \tag{4.1}$$

where E is the fraction of liquid droplet entering the gas core. The exponent values in Equation 4.1 were chosen such that the right-hand side of the equation formed a dimensionless group. The parameters were compiled both for the whole Harwell data bank and for subgroups after dividing the data bank into a number of intervals based on the film Reynolds number (Oliemans et al., 1986).

Experimental data acquired in present work and in field data from Turner et al. (1969), Belfroid et al. (2008) and Veeken et al. (2010) were used to evaluate the ability of the liquid film models to predict the onset of liquid loading, considering and neglecting the entrainment of droplets in the gas core. The absolute error for every individual well or data point was estimated by Equation B.30 and then the relative error was estimated for the whole set of data by Equation B.31. For the case of experimental data, the relative errors were presented as bar plot (summarised in Tables B.1 and B.2) while for field data the results were presented in tables.

In addition, for a better interpretation on the model's performance, assuming droplet entraiment, for every individual observation, the critical gas velocity was plotted against predicted results.

4.3.1 Experimental data evaluation

Experimental data for the onset of liquid loading transition for air-water and air-Exxsol D80 system, were used to evaluate the liquid film model when droplet fraction was considered. Section 4.2.1 states that models proposed by Barnea (1986) and Shekhar et al. (2017) could correctly predict the onset of liquid loading for air-water two-phase flow in inclined pipes. While Section 4.2.2 have shown that in air-exxsol D80 two-phase flow in inclined pipes, the onset of liquid loading was better predicted by the Shekhar et al. (2017) model. Overall, it is observed that the model proposed by Luo et al. (2014) overestimates the annular-slug flow transition for all inclinations in both systems.

Figure 4.11 and Figure 4.12 presents the relative error between measured and calculated critical gas velocity with and without droplet entrainment in gas core, estimated for all pipe inclinations for air-water and air-exxsol D80 system, respectively.

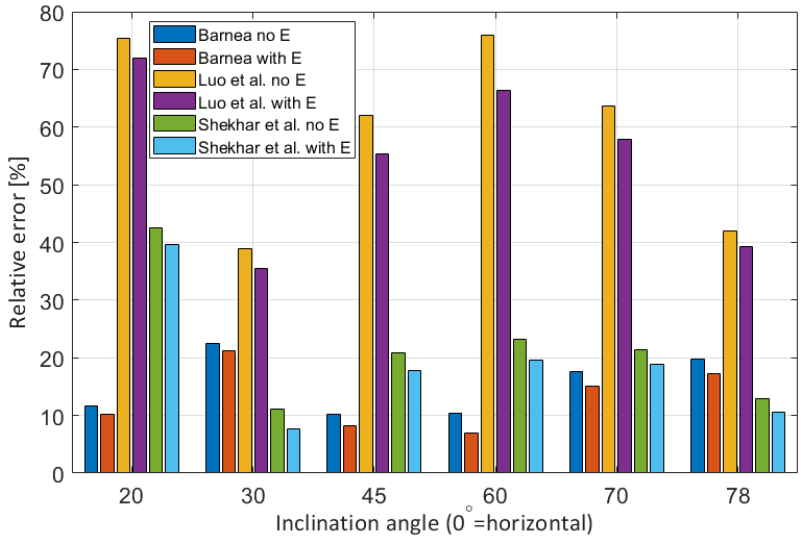

Figure 4.11. Comparison between experimental data with liquid film models prediction with and without entrainment for air-water system at STP conditions

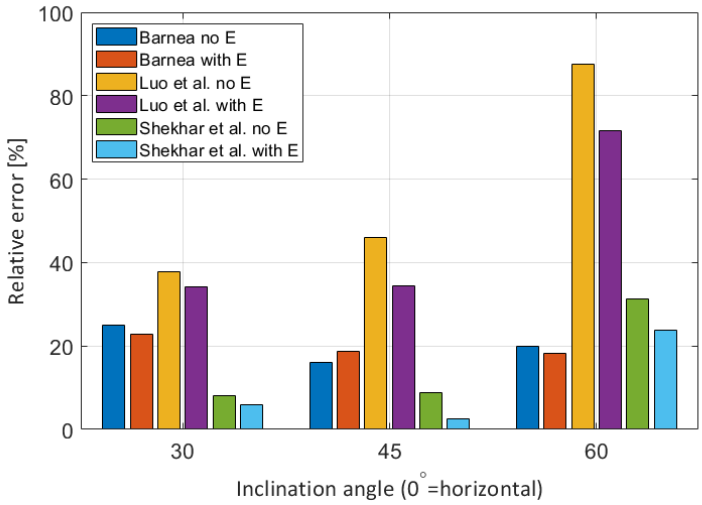

Figure 4.12. Comparison between experimental data with liquid film models prediction with and without entrainment for air-Exxsol D80 system at STP conditions

Overall, the model including the entrainment in the liquid film model improved the prediction of the flow pattern transition by presenting lower relative error compared to the liquid film model that neglected the presence of liquid in form of droplet in the gas core.

From Figure 4.11 it is observed that for 45° inclination Shekhar et al. (2017) model without (no E) droplet fraction, predicted the critical gas velocities with 20.9% relative error versus 14.4% for prediction with droplet fraction (with E). For higher inclinations the relative error reduced substantially.

In Figure 4.12 the relative error was estimated for 45° pipe inclination, and exhibit the same behaviour; the error reduced from 8.8% to 3.4% when Shekhar et al. (2017) model was used. Likewise, for 60° pipe inclination the relative error reduced from 31.2% to 20.7%.

It was observed that for higher pipe inclinations, there was an insignificant difference between the relative error for liquid film models predicting the onset of liquid loading taking into account the liquid entrained in gas core as droplet. This could be related to the rates of droplet deposition and droplet entrainment, being equal at steady-state condition as stated on Shoham (2006).

Figure 4.13 and 4.14 present every individual observed critical gas velocity plotted against the results from the model's prediction with and without droplet entrainment.

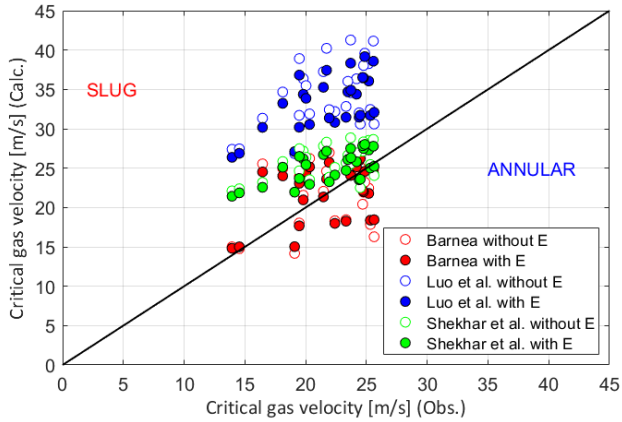

Figure 4.13. Experimental data vs. predicted results for air-water system

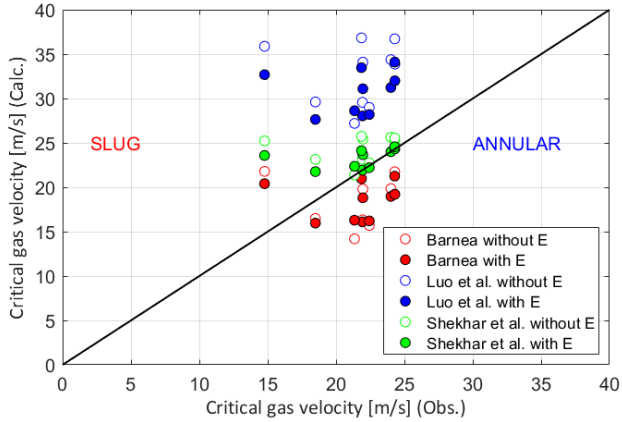

Figure 4.14. Experimental data vs. predicted results for air-Exxsol D80 system

The 45° line in the plot represent the annular-slug transition boundary. This boundary divides the plot into unloaded region at the lower part (full annular flow) and loaded region (full slug flow). The critical gas velocity data points were measured when the unstable flow started to be visible. Therefore, the model's prediction values are considered to be accurate for data point close to the 45° line or in the slug region. It can be seen that for Shekhar et al. (2017) and Luo et al. (2014) models, most of the data points fall above the line. However, Luo et al. (2014) seems to overestimate the transition. On the other hand, the Barnea (1986) model seem to underestimate the critical gas velocity at which the onset of liquid loading was observed. Predicted results seems to be closer to the 45° line when the empirical correlation for the liquid droplet fraction was used.

A relative error using all data points for every tested pipe inclination for air-water and air-Exxsol D80 system were estimated and presented in Table 4.3. A close analysis of the performance between Barnea (1986) and Shekhar et al. (2017) show that for air-water system both models show a good match with the data by presenting similar relative error.

Table 4.3. Model prediction (With E) relative error using all the data measured experimentally for air-water and air-Exxsol D80 system

	Air-Water		**Air-Exxsol D80**	
model	**data correctly predicted**	$err_{rel}(\%)$	**data correctly predicted**	$err_{rel}(\%)$
Barnea (1986)	16/28	14.0	1/10	20.3
Luo et al. (2014)	28/28	54.5	10/10	45.5
Shekhar et al. (2017)	24/28	17.9	5/10	10.3

However, Shekhar et al. (2017) presented higher number of data correctly predicted (24 out of 28 correct predictions). Comparing with Table 4.1, the relative error of Shekhar et al. (2017) reduced from 20.9% to 17.9%. For air-Exxsol D80 system a good agreement with the data was estimated for Shekhar et al. (2017) model, were 5 out of 10 data were correctly predicted and the relative error proved to be the lowest.

Overall, the Shekhar et al. (2017) model predicted better the liquid loading phenomenon in inclined pipes for air-water and air-Exxsol D80 system when liquid droplet fraction was taken into account.

4.3.2 Field data evaluation

Three different sets of field data were used to evaluate the importance of droplet entrainment for predicting the onset of liquid loading.

The first field data used in the study was the one published by Veeken et al. (2010). They published data from 67 gas wells from North Sea that were starting to experience liquid loading. The gas wells had tubing diameter from 2–6 inches and included vertical and inclined pipe geometry (0° to 64° inclination angles from vertical). The liquids produced were condensate and water. Liquid gas ratio was assumed to be 5 bbl/MMcf in the calculation as recommended by Luo et al. (2014). In their paper the reported test gas rate was converted to superficial gas velocity.

Figure 4.15 to 4.17 observed gas velocities of Veeken et al., 2010 were compared with critical gas velocities predicted by Barnea (1986), Luo et al. (2014) and Shekhar et al. (2017) models, with and without the correlation of liquid droplet fraction present in the gas core. The 45° line in the plot represent the unload and loaded transition boundary. Veeken et al. (2010) reported the gas rate after the onset of liquid loading, which means that all the data should be located slight above the 45° line (loaded region) in the plot of calculated critical gas velocity and the observed critical gas velocity.

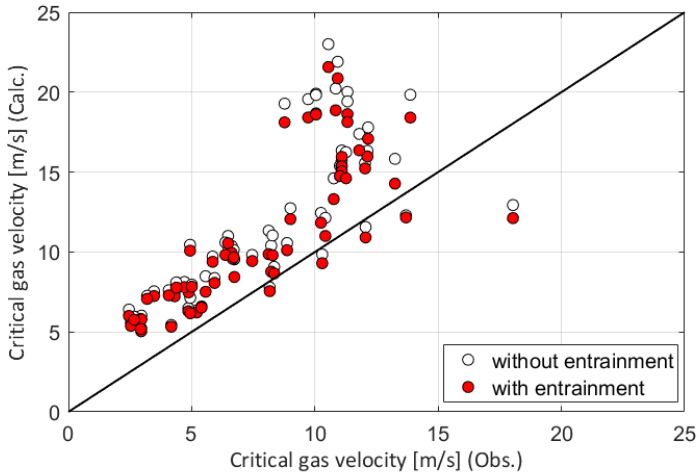

Figure 4.15. Veeken et al. (2010) data vs. the Barnea (1986) model prediction

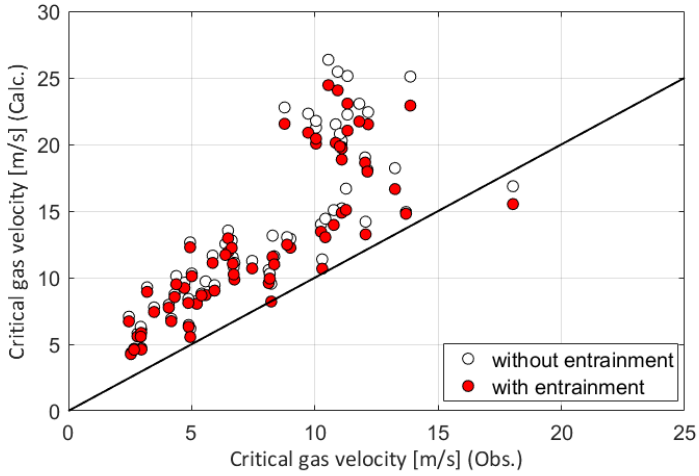

Figure 4.16. Veeken et al. (2010) data vs. the Luo et al. (2014) model prediction

Table 4.4. Critical gas velocity prediction for Veeken et al. (2010) data

	No Entrainment		**Entrainment**	
model	**well correctly predicted**	$err_{rel}(\%)$	**well correctly predicted**	$err_{rel}(\%)$
Barnea (1986)	62/67	59.07	62/67	51.28
Luo et al. (2014)	66/67	78.84	65/67	69.82
Shekhar et al. (2017)	57/67	35.73	54/67	32.56

It can be seen that most of the wells were in the loaded region. It is also observed

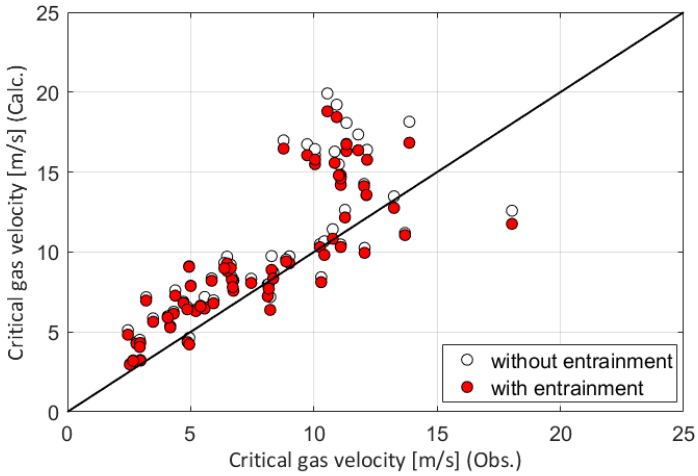

Figure 4.17. Veeken et al. (2010) data vs. the Shekhar et al. (2017) model prediction

that when droplet entrainment was considered during critical gas velocity prediction, the results were close by the 45° line, suggesting that the well had just started to load.

For an ideal model, the points have to be slightly above the 45° line and the relative error as low as possible. From Table 4.4 result, it is clear that Shekhar et al., assuming entrainment, exhibits the best result, although the number of wells predicted correctly is almost the same.

The second field data used for model evaluation was the wells published by Belfroid et al. (2008). They published data for two gas wells. Both wells had an inclined pipe geometry of 40° (from vertical). One well had a tubing diameter of 0.112 m and observed critical gas rate of 90 000 Sm^3/d, and the other well 0.074 m tubing diameter and 45 000 Sm^3/d critical gas rate. Calculations were performed using data given in their publications. As the wells were also reported at critical condition, the predicted results were expected to be above the 45° line, as seen in Figure 4.18. Like for the Veeken et al. (2010) data, Table 4.5 shows that critical gas velocity prediction improved by showing smaller relative error when the model assumed droplet entrainment.

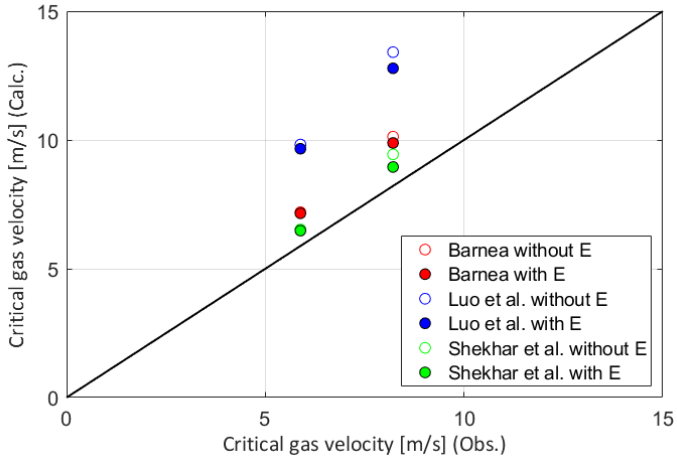

Figure 4.18. Belfroid et al. (2008) data vs. liquid film models prediction

Table 4.5. Critical gas velocity prediction for Belfroid et al. (2008) data

	No Entrainment		**Entrainment**	
model	**well correctly predicted**	$err_{rel}(\%)$	**well correctly predicted**	$err_{rel}(\%)$
Barnea (1986)	2/2	22.82	2/2	20.95
Luo et al. (2014)	2/2	65.10	2/2	59.9
Shekhar et al. (2017)	2/2	12.91	2/2	9.56

The third field data set used for evaluation of the model was the wells production data published by Turner et al. (1969). They published field data for 90 gas wells, where 37 were experiencing liquid loading and 53 were producing at stable conditions, meaning no liquid accumulation in the wellbore (unloaded). All the wells were vertical (0° inclination angle). Gas rate tested and reported by Turner were converted to superficial gas velocities, which were then used to compare with calculated critical gas velocity using the model with and without entrainment. The comparison was performed for every individual well, as shown in Figures 4.19 to 4.21.

When the calculated velocity was higher than the observed, the well was considered loaded. If the calculated critical gas velocity was lower than the observed, the well was defined as unloaded. In case of unloaded wells, the well data were located slightly below the 45° line in the plot. It can be seen that for Turner et al. (1969) field data, entrainment fraction of droplets did not influence the prediction of critical gas velocity. This behaviour could be explained by the observations given by Shoham (2006) that, the film thickness variation result in variation of the deposition and the entrainment rate. Since the published well had vertical geometry, film thickness was considered constant, therefore deposition and entrainment was considered constant.

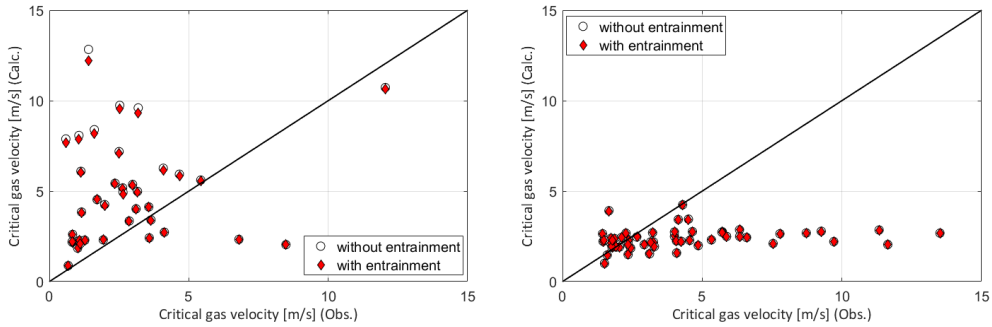

(a) Loaded wells (b) Unloaded wells

Figure 4.19. Turner et al. (1969) data vs. Barnea (1986) model prediction

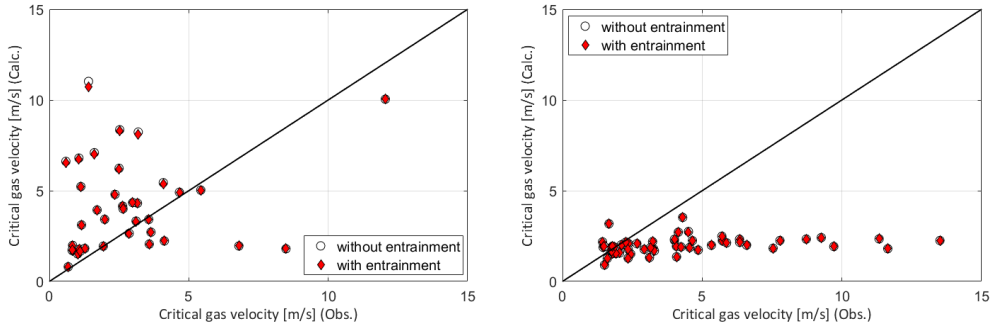

(a) Loaded wells (b) Unloaded wells

Figure 4.20. Turner et al. (1969) data vs. Luo et al. (2014) model prediction

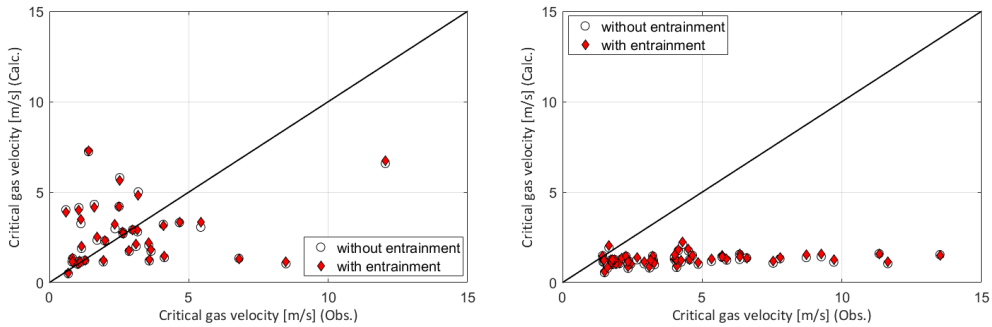

(a) Loaded wells (b) Unloaded wells

Figure 4.21. Turner et al. (1969) data vs. Shekhar et al. (2017) model prediction

For all models the prediction of unloaded wells was conservative i.e., the well data were located below the 45°-line. However, the relative error was highest in the case of Luo et al. (2014) and Shekhar et al. (2017) as shown in Table 4.6. Although the film

thickness correlation was introduced in both models to account for the effect of inclination, no improvement was observed. To mention that the interfacial friction factor suggested by both researchers influence on the prediction by overestimating the critical gas velocity in gas well with a vertical geometry. On the other hand, Barnea (1986) model showed better prediction in both number of wells and in percentage deviation.

Table 4.6. Critical gas velocity prediction for Turner et al. (1969) data

Well at loaded condition				
model	**no Entrainment**		**Entrainment**	
	well correctly predicted	$err_{rel}(\%)$	**well correctly predicted**	$err_{rel}(\%)$
Barnea (1986)	31/37	176.72	31/37	172.54
Luo et al. (2014)	28/37	137.39	28/37	135.93
Shekhar et al. (2017)	20/37	78.09	20/37	77.27
Well at unloaded condition				
Barnea (1986)	41/53	42.03	40/53	42.07
Luo et al. (2014)	46/53	44.29	46/53	44.28
Shekhar et al. (2017)	51/53	60.64	51/53	58.90

Overall, it was observed that for deviated wells, Shekhar et al. (2017) model presented a good agreement with tested gas velocities. On the other hand, the model failed to predict the gas velocity for stable production gas wells with vertical geometry.

4.4 Effect of liquid film distribution on the determination of liquid loading onset

Many investigators have proposed models consisting of correlations based on field and experimental data, equations from physical properties, aiming at predicting when liquid accumulation in the wellbore would start to be a problem in a gas well. Most models are often inaccurate for estimating the liquid loading onset when used at different conditions for which the models were evaluated. Most of these models assume that the liquid removal in gas wells resulted from liquid being transported as droplets entrained in the gas core (liquid droplet models) or as liquid film attached to the pipe wall (liquid film models). Earlier studies performed in this thesis have revealed that liquid film models presented a better prediction of liquid loading onset.

The liquid film model, also known as liquid film reversal, assumes that liquid is transported as film moving with the gas along the wall of the conduit and liquid accumulation occurs once the film flows counter-current to the gas core. The model was developed based on empirical correlations and mechanistic modelling of multiphase flow in pipe.

As mentioned in Section 2.2.2, several researchers relate the onset of liquid loading with the flow regime transition from annular to intermittent flow. Most of this research followed after the work performed by Zabaras et al. (1986), who concluded that at low gas flow rates the film motion was controlled by a switching mechanism coupled to the instability of the liquid film due to decreasing of both film-thickness and the interfacial friction. Thereafter, the two-phase flow annular to slug transition model, started to be used for predictions of the critical gas velocity for example the model proposed by Barnea (1986).

The annular-slug transition boundary model proposed by Barnea (1986) has been widely used and related to liquid loading onset predictions. The model was developed to cover the transition boundary for whole range of pipe inclinations, assuming that liquid film thickness distribution around the pipe is constant. Details of the model derivation are presented in Appendix B.1.

Recently, the Barnea (1986) model have been improved by Shekhar et al. (2017) by taking into account non-uniform film thickness distribution due to pipe inclination. The changes were proposed after the results of Paz (1994) who proved that pipe inclination had an effect on the liquid film thickness distribution (Figure 4.22).

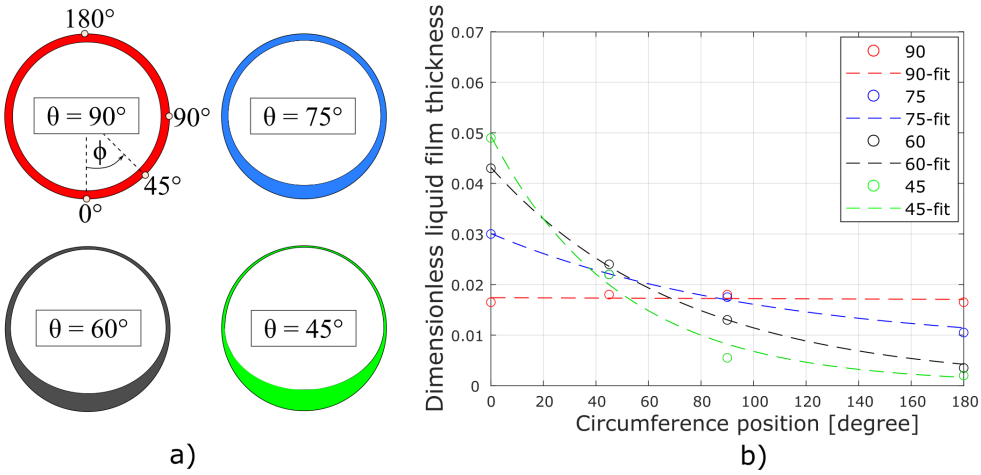

Figure 4.22. Illustration of liquid cross-section for various inclinations a) and for liquid film distribution fitting (Paz (1994), v_{sl}=0.006 m/s, v_{sg}=18.29 m/s) b)

The prediction of annular-slug transition boundary by Barnea (1986) is based on estimation of uniform liquid film thickness ($\widetilde{\delta_L}$) that satisfies the interfacial shear stress at given superficial liquid velocity (Equation B.8). Then the value is used to determine the critical superficial gas velocity. Shekhar et al. (2017) based their model following the same criterion. However, they assumed that the critical film thickness occurred at the bottom of the pipe, i.e., the liquid loading would begin when the thicker film at the bottom can no longer be carried by the gas phase. Thus, they estimated the maximum film thickness that satisfied the required shear stress (Equation B.8) as ($\widetilde{\delta_{max}}$), and used a relation (Equation 2.11) to convert into $\widetilde{\delta_{avgL}}$. The corrected value was then used back in Barnea (1986) equation (Equation B.8) for determination of the critical superficial gas velocity.

It is worth to mention that Equation B.8 was derived assuming uniform film thickness (Figure B.3 and Equations B.7).

Although the Shekhar et al. (2017) model was proposed to take into account the non-uniform film thickness, it still calculates critical superficial gas velocity to uniform liquid film thickness concept by using the equation provided by Barnea (1986). Thus, in this research work a new approach was suggested, assuming liquid loading would start at a position in the pipe of maximum liquid film thickness (δ_{maxL}), and that the maximum liquid film thickness would be one that satisfy Equation B.8 similar to Shekhar et al. (2017). However, in contrast to them, the model predicts the critical superficial gas velocity by employing liquid holdup ($H_L = A_L/A$) caused by non-uniform liquid film thickness distribution due to pipe inclination in the momentum balance equation instead of the liquid thickness directly. The momentum balance equation for gas-liquid two-phase flow (Equation B.3) can then be re-written as

$$\tau_i S_i \left(\frac{1}{H_L} + \frac{1}{(1-H_L)} \right) - gA(\rho_l - \rho_g)\sin\theta - \tau_{wl}\frac{S_L}{H_L} = 0 \tag{4.2}$$

The model is based on Paz's measured circumferential film thickness for various in-

clinations and liquid velocities v_{sl}. Film thickness distribution changes with decreasing inclination from uniform to non-uniform, when thickness at the top of the pipe becomes thinner, while thickness at the bottom increases (Figure 4.22a). The dimensionless liquid film thickness at several angular positions (ϕ) in the pipe cross section was computed from measured values by Paz (1994) and plotted versus pipe inclination angle (θ) for different liquid superficial velocities. The data was fitted to an exponential function (Equation 4.3)

$$\widetilde{\delta_L}(\phi, \theta) = ae^{(-b\phi)} + c \tag{4.3}$$

The function was numerically integrated in ϕ in order to obtain the area under the curve, which represents the cross-sectional area of liquid in the pipe from position 0° to 180° (Figure 4.22b). The same analysis was performed for the other liquid velocities of similar behaviour as shown in Figs. B.7 through B.11.

The liquid holdup was calculated from the cross section area occupied by the liquid estimated above, and plotted versus the maximum dimensionless liquid film thickness (occurring at the bottom of the pipe), presented in Figure 4.23.

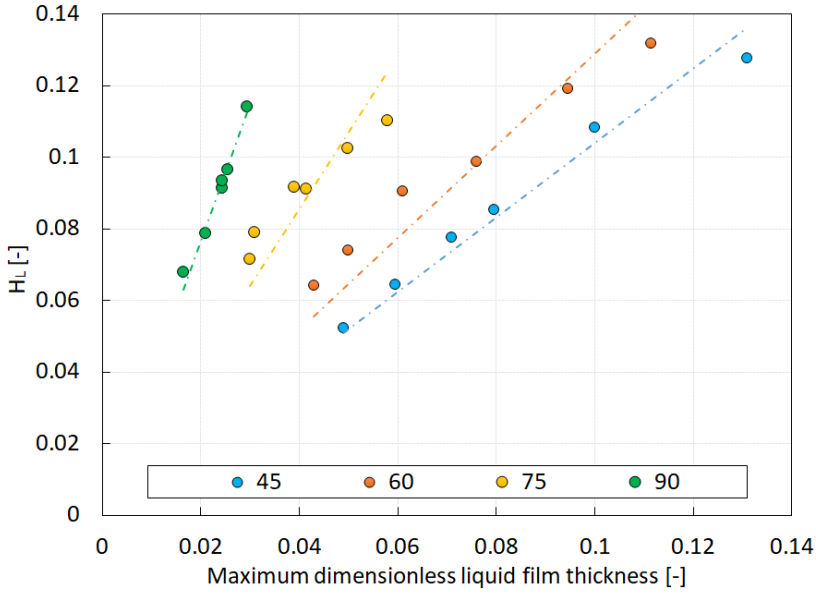

Figure 4.23. Liquid holdup vs. maximum dimensionless liquid film thickness (measured at the bottom of the pipe)

There is a fairly linear relationship between these two variables, thus the liquid holdup can be used to determine the maximum film thickness and can be described by a simple linear function of the single variable **a**.

$$H_L = a\widetilde{\delta_{maxL}} \tag{4.4}$$

The slope of the fitting lines (**a**) increases with increasing pipe inclination (θ). Both of these variables were plotted in Figure 4.24.

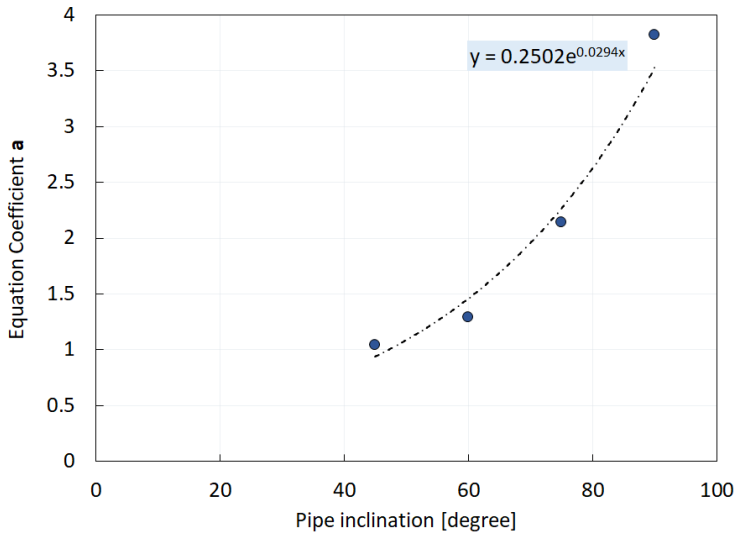

Figure 4.24. Estimation of liquid holdup equation vs. pipe inclination (from horizontal)

As it can be seen, the coefficient a increases exponentially with increasing pipe inclination and their relationship is described by:

$$a = 0.25e^{0.0294\theta} \tag{4.5}$$

The change of liquid area (liquid holdup) due to pipe inclination also causes a change in the perimeter of the liquid-gas interface (S_i). From the functions created by fitting the Paz (1994) data, the perimeter S_i was computer from Equation 4.3 and plotted against liquid holdup (Figure 4.25). Equation 4.6 is proposed to fit the data.

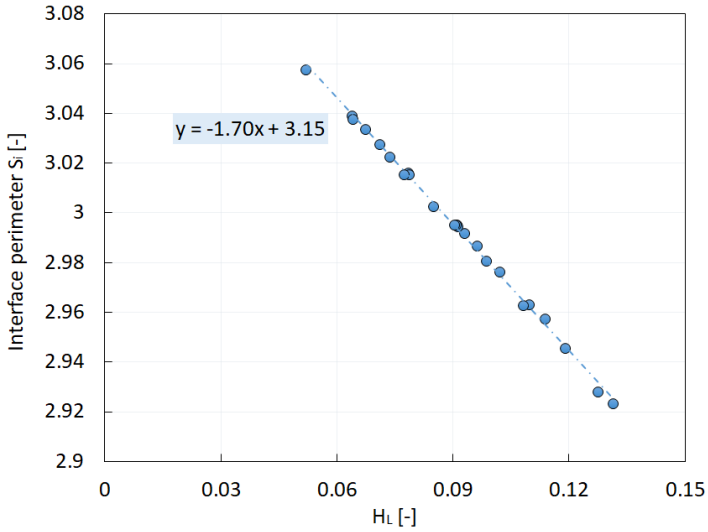

Figure 4.25. Estimation of interface perimeter against liquid holdup

$$S_i = (\pi - 1.7H_L)D \tag{4.6}$$

The perimeter of the wall-liquid interface was calculated by $S_L = \pi D$ and wall shear stress by Equation 4.7, which was related to the local liquid velocity at the bottom of the pipe, similar to what is presented by Barnea (1986).

$$\tau_{wl} = \frac{1}{2}C_l\rho_l\left(\frac{\rho_l D v_{sl}}{\mu_l}\right)^{-n}\frac{v_{sl}^2}{4\left(\widetilde{\delta_{maxL}} - \widetilde{\delta_{maxL}}^2\right)} \tag{4.7}$$

where C_l and n are constants in the friction factor correlation, where $C_l = 0.046$, $n = 0.2$ for turbulent liquid film and $C_l = 16$, $n = 1$ for laminar liquid film.

Substituting the relationship of S_L, S_i, H_L and the wall shear stress expression into Equation 4.2 and solving for interfacial shear stress yields

$$\tau_{i,liquid} = \frac{\tau_{wl}\dfrac{S_l}{H_L} + gA(\rho_l - \rho_g)\sin\theta}{S_i\left[\dfrac{1}{H_L} + \dfrac{1}{(1-H_L)}\right]} \tag{4.8}$$

Then the supplied interfacial shear stress provided by gas-phase was estimated by Equation 4.9

$$\tau_{i,gas} = \frac{1}{2}f_i\frac{\rho_g v_{sg}^2}{(1 - 2\widetilde{\delta_{maxL}})^4} \tag{4.9}$$

In addition, a new equation for calculating the interfacial friction factor developed based on the experimental data of Paz (1994) data was proposed. The steps used for the development are presented below:

1. Calculate the liquid friction factor using Equation B.5.
2. Calculate the liquid cross section area by multiplying liquid holdup (Figure 4.23) with pipe area.
3. Calculate liquid shear stress (τ_{wl}) using Equation B.4 where the actual liquid velocity was estimated using Equation B.6.
4. Determine pressure drop from Equation 4.10. The equation was obtained by adding the momentum equation of liquid (Equation B.1) with the gas core (Equation B.2)

$$-\frac{dp}{dL}A = g(A_l\rho_l + A_g\rho_g)\sin\theta + \tau_{wl}S_l. \tag{4.10}$$

5. Determine the interface shear stress using either Equation B.1 or Equation B.2
6. Calculate the interface friction factor

$$f_i = \frac{2\tau_i}{\rho_g v_g^2} \tag{4.11}$$

where $v_g = v_{sg}\dfrac{A}{(1-A_l)}$

7. Plot the relation interfacial friction factor given in terms of dimensionless parameter $\boldsymbol{I}$ against liquid holdup (H_l)

$$I = \frac{f_i}{\sin\theta f_g} \tag{4.12}$$

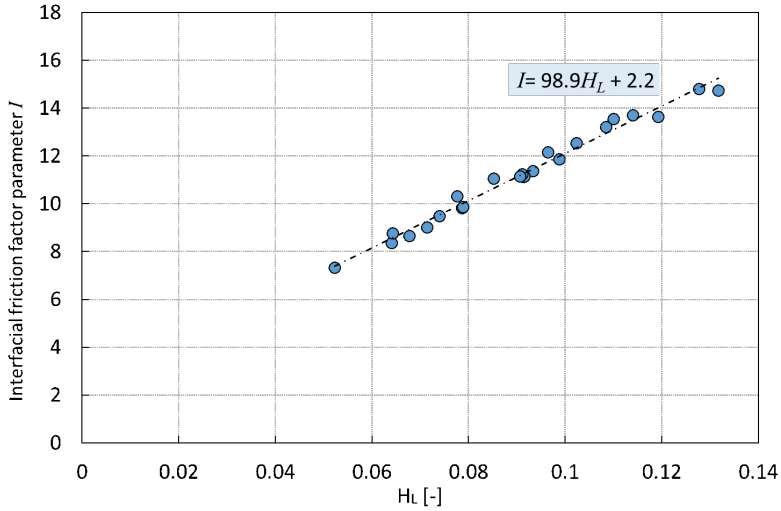

Figure 4.26. Interface friction factor relationship with the liquid holdup estimated from Paz (1994) data

From Figure 4.26 the new interfacial friction factor is determined by:

$$f_i = f_g(98.87H_L + 2.2)\sin\theta \tag{4.13}$$

Here the superficial gas friction factor (f_g) was assumed to be 0.005 and the pipe inclination (θ) is expressed in radians.

Using the experimental data of Paz (1994), interfacial friction factor was estimated using the new proposed correlation (Equation 4.13), Wallis (1969) (Equation B.12), Fore et al. (2000) (Equation 2.6) and Shekhar et al. (2017) (Equation 2.12). The comparison is presented in Figure 4.27.

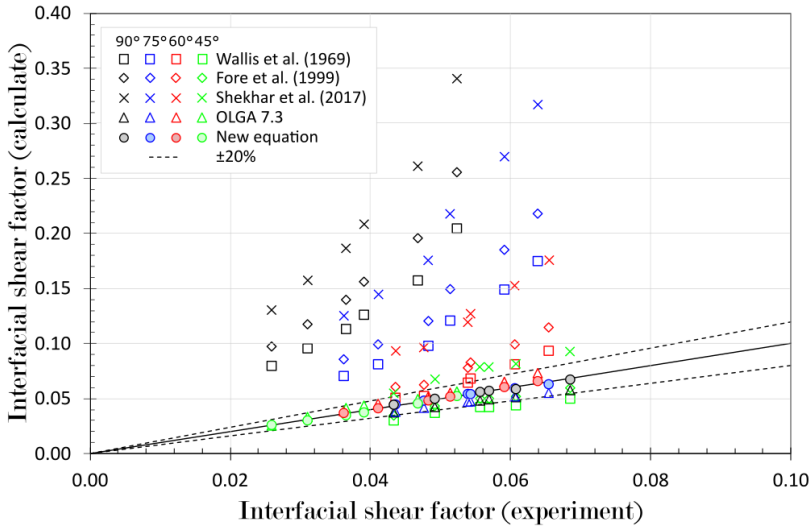

Figure 4.27. Comparison of interfacial friction factor estimated from experimental Paz (1994) data with Wallis (1969), Fore et al. (2000), Shekhar et al. (2017) and OLGA prediction values of interfacial friction factor

It can be seen that for inclination above 45°, equations proposed by Wallis (1969), Fore et al. (2000) and Shekhar et al. (2017), overestimate the interfacial friction factor. On the other hand, OLGA predicted values close to the experimental estimation, similar to the new equation predictions.

Figure 4.28 shows an overall flow chart for the annular-intermittent transition boundary (critical gas velocity) for inclined pipe. Critical gas velocity is first determined from on the input parameters. Then the momentum and continuity equation is used to calculate the hydrodynamic behaviour of the two-phase flow.

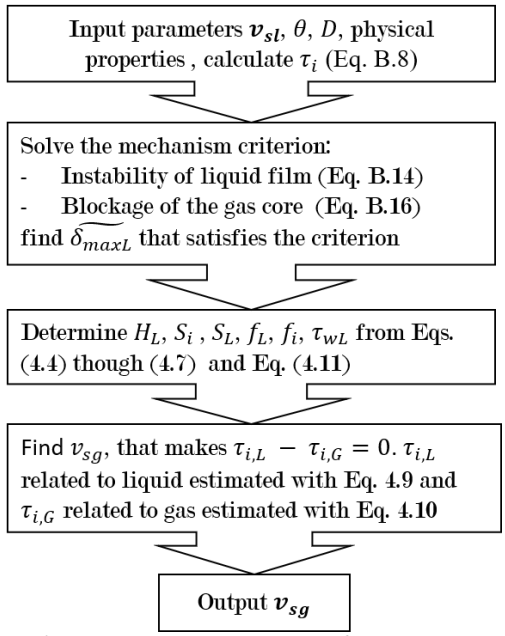

Figure 4.28. Flow chart for calculating annular-slug flow transition boundary calculation

4.4.1 Model validation

Experimental critical gas velocities acquired for air-water and air-Exxsol D80 system (Section 3.6.2 and 3.6.3 respectively) were used to evaluate the applicability of the proposed model on the prediction of liquid loading in gas wells.

Figures 4.29a–4.29f, discrete experimental points from air-water system were plotted on logarithmic scale with the continuous-line representing the annular-slug transition boundary for the new model. The transition estimated with the models of Barnea (1986) and Shekhar et al. (2017) are also plotted using dashed-lines.

Figure 4.30a–4.30c presents the same analysis where air-Exxsol D80 discrete data point were used instead.

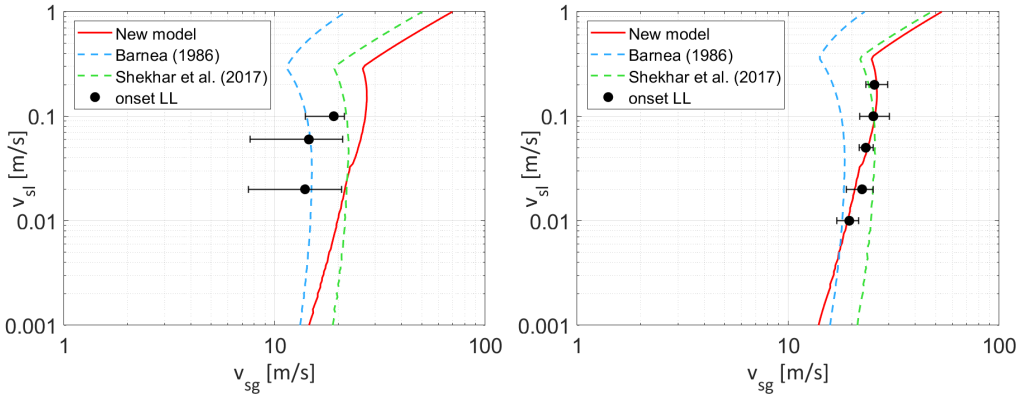

(a) 20°

(b) 30°

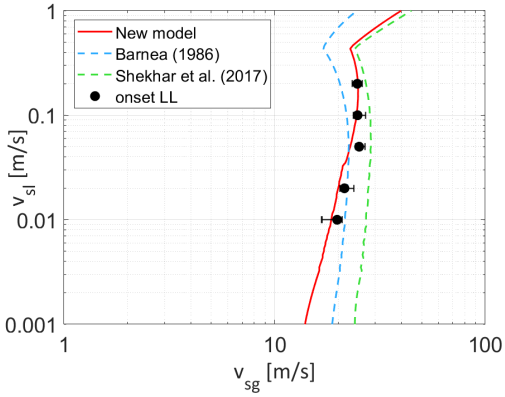

(c) 45°

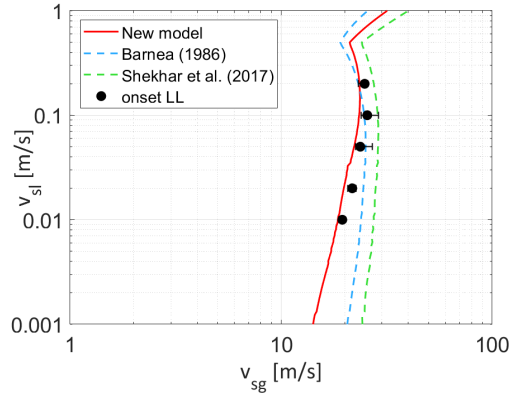

(d) 60°

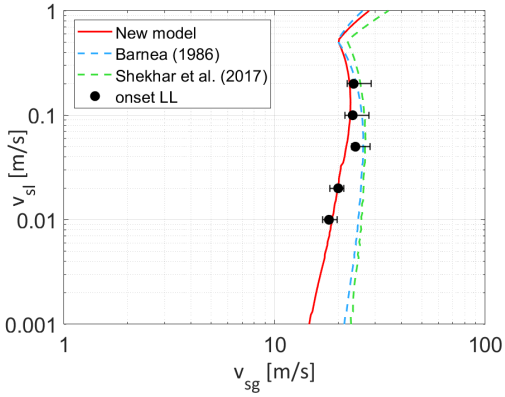

(e) 70°

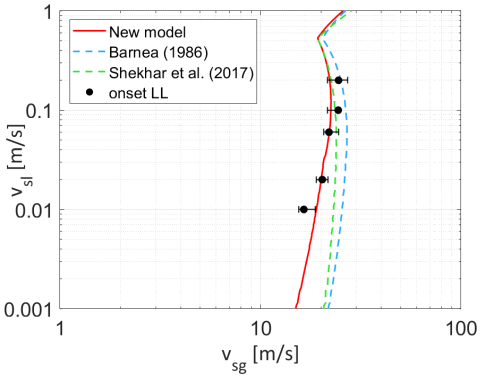

(f) 78°

Figure 4.29. Comparison between experimental data and the transition boundary prediction by the new model, the model by Barnea (1986) and the model by Shekhar et al. (2017), for air-water system at STP condition

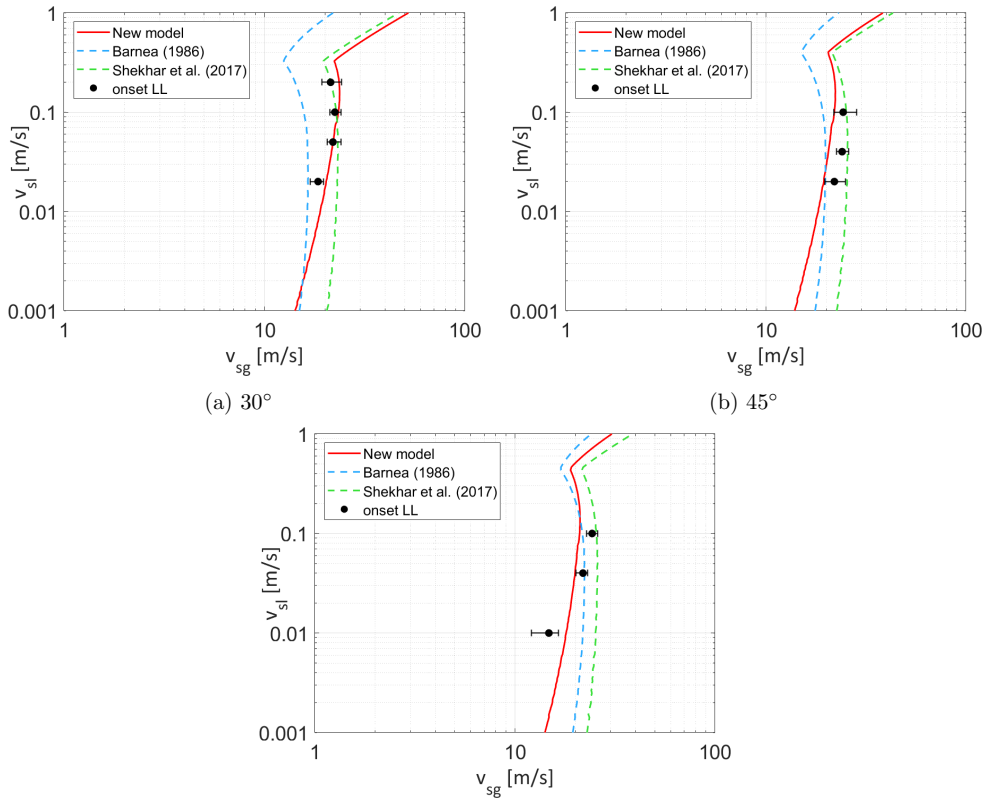

(a) 30°

(b) 45°

(c) 60°

Figure 4.30. Comparison between experimental data and the transition boundary prediction by the new model, the model by Barnea (1986) and the model by Shekhar et al. (2017) for air-Exxsol D80 system at STP condition

The agreement between the predictions using the new model and experimental measurements is fairly good for most cases. This could indicate that the model is generic and can be extrapolated to other operational conditions different than the ones from which it was derived (experimental data of Paz (1994)). However, the model has poor performance for the lowest inclination in air-water flow (Figure 4.29a). This could be because the data of Paz does not include inclinations below 45°. Figure 4.29b and 4.30a shows that even though the pipe inclination is below 45°, the model agreed with the experimental measurements. This could be due to the fact that at 30° inclination the conditions are not significantly different as presented in 45° (Figure 4.22a). However, for an inclination of 20° the difference might be significant as the liquid film might not reach the top of the pipe.

Figure 4.31 shows the comparison between every individual observed critical gas velocities predicted by the present model and the measured data.

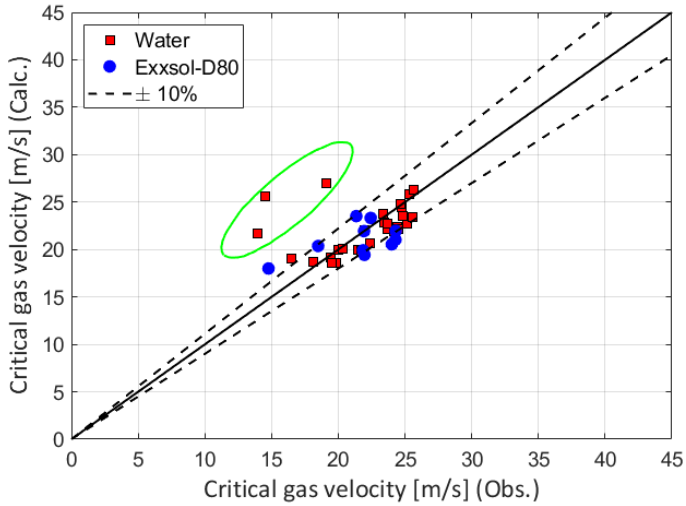

Figure 4.31. Comparison between experimental data vs. predicted values by the new model

In Figure 4.31 the 45° line in the plot represents the annular-slug transition boundary. It can be seen that the predicted critical gas velocities lays close to the line, having a variation of approximately 10%. It was also noticed that the model overestimates the values for the critical gas velocity at 20° pipe inclination (points surrounded by the green ellipse).

Table 4.7 presents the relative error calculated for each pipe inclination and using all the data points for air-water and air-Exxsol D80 system, respectively.

Table 4.7. Relative error for the air-water and air-Exxsol D80 system

	Air-Water	**Air-Exxsol D80**
pipe inclination[°]	$err_{rel}(\%)$	$err_{rel}(\%)$
20	57.50	-
30	3.22	6.10
45	4.91	11.85
60	6.68	14.73
70	4.14	-
78	7.01	-
all data	10.8	10

Comparing the results presented in Table 4.7 for air-water system its was possible to see that the new model had an improvement on prediction of critical gas velocity with an average accuracy for all inclinations of 10.8% against the 20.9% from Shekhar et al. (2017) and 16.9% from Barnea (1986) (see Table 4.1). For air-Exxsol D80 a similar trend is observed, the new model has a lower error of 10% against 15.2% and 20.8%, for Shekhar et al. (2017) and Barnea (1986) respectively (see Table 4.2).

To evaluate further the performance of the new proposed model, experimental data publish by Guner (2012) on two-phase air-water system was used. He performed experiments in 3-in ID pipe at inclination angles of 90°, 75°, 60° and 45° from horizontal, using superficial liquid velocity of 0.01, 0.05 and 0.1 m/s and superficial gas velocity ranging from approximately 40-2m/s.

The set of discrete data points define by (Guner, 2012) as the onset of film reversal, complete film reversal (critical v_{sg}) and no loading were used. The complete film reversal data points were used as the left length of the horizontal error bars while the no loading as the right length the first full unstable production.

Figure 4.32a to 4.32d shows the comparison of the discrete data with the prediction from the new model, Barnea (1986) and Shekhar et al. (2017).

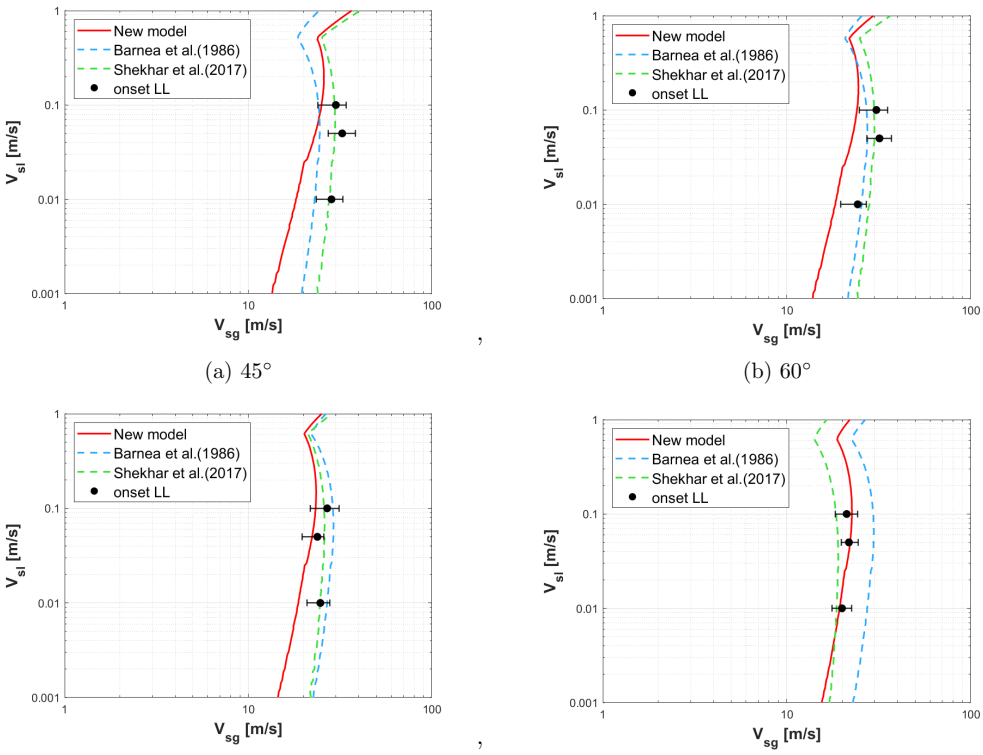

(a) 45° , (b) 60°

(c) 75° , (d) 90°

Figure 4.32. Comparison between Guner (2012) experimental data and the transition boundary prediction by the new method, Barnea (1986) and Shekhar et al. (2017)

Overall, the agreement between the prediction using the new model and Guner (2012) experimental data is fairly good for most cases. However, comparing to Shekhar et al. (2017) model performance the new model predicted poorly with more than 25% of error (Figure 4.33).

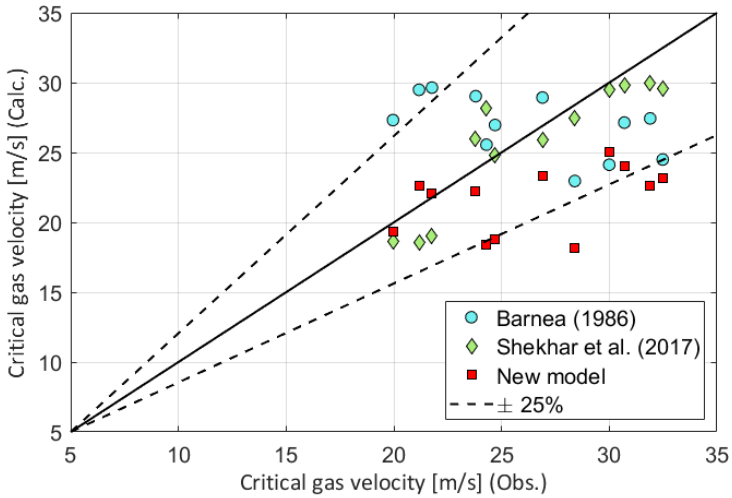

Figure 4.33. Comparison between Guner (2012) experimental data vs. predicted values by the new model, Barnea (1986) and Shekhar et al. (2017)

It is worthwhile to mention that the same set of data was published by Guner et al. (2015), where the values of critical superficial gas velocity are the same as the values presented earlier as loaded conditions, past the onset point. The author has therefore assumed that the values published are the critical onset velocities, but if otherwise, results will vary.

Application to field data

Field data previously studied on section 4.3.2 was used to evaluate the performance of the new method for the prediction on liquid loading onset.

Analysis of the field data revealed that for a accurate prediction, the model required an upwards adjustment of approximately a factor of 0.4 on the interfacial friction factor for cases of low liquid holdup. Therefore, a coefficient was added to Equation 4.13 resulting in Equation 4.14

$$f_i = \ 0.4 f_g (98.87 H_L + 2.2) \sin\theta \quad H_L < 0.05 \tag{4.14}$$

When this modification is introduced, the prediction accuracy for the datasets described above worsened from 10% to 50% relative error. However, the model prediction is conservative (i.e. lower critical gas velocities are predicted) see Figure 4.34). A similar behaviour was observed when applied for Guner (2012) experimental data (Figure 4.35).

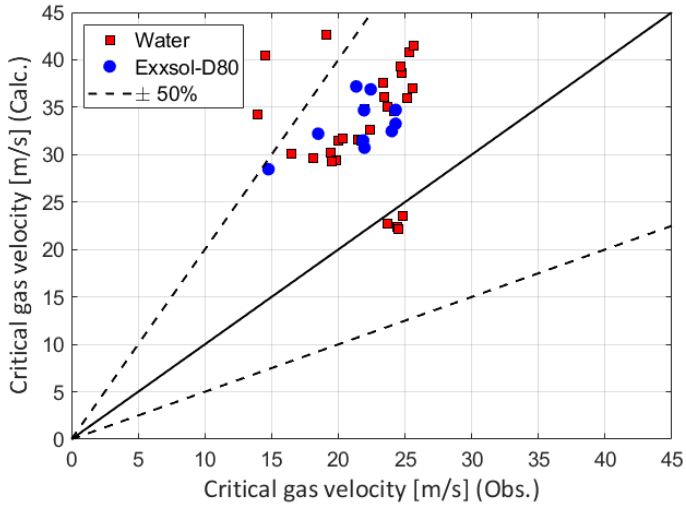

Figure 4.34. Comparison between experimental data vs. predicted values by the new model with adjustment factor

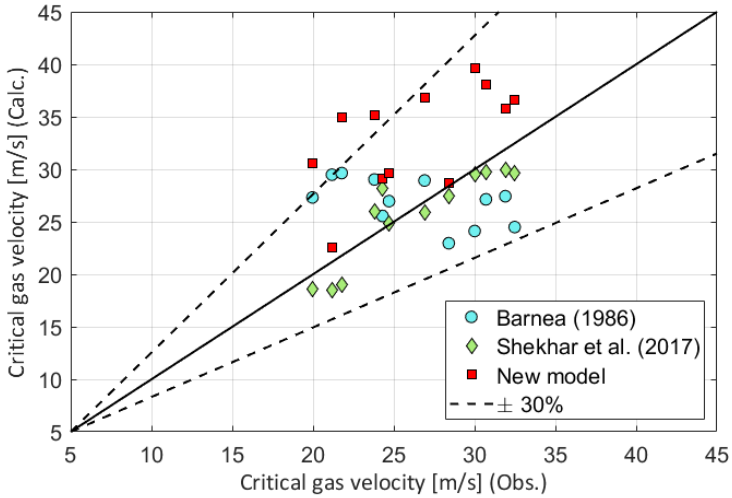

Figure 4.35. Comparison between Guner (2012) experimental data vs. predicted values by the new model with adjustment factor

In Figure 4.36 through Figure 4.39, measured field data were plotted in a 45° line plot and compared with the new model prediction and for the other studied models.

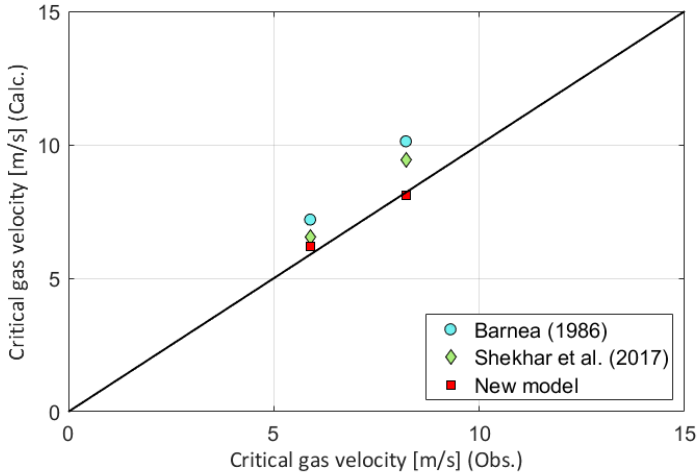

Figure 4.36. Comparison between Belfroid et al. (2008) data vs. predicted values from new model

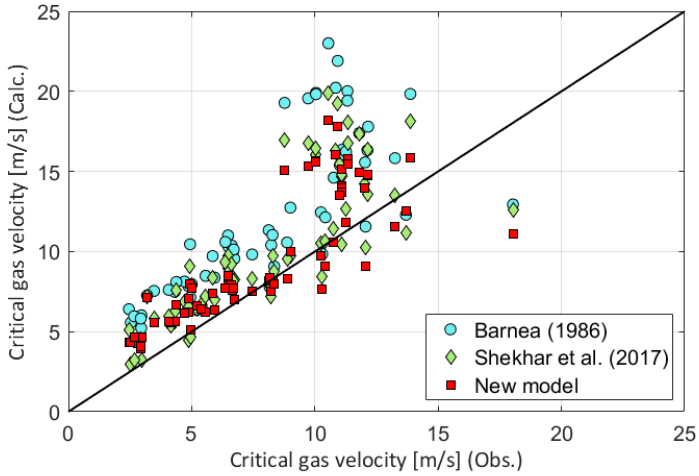

Figure 4.37. Comparison between Veeken et al. (2010) data vs. predicted values from new model

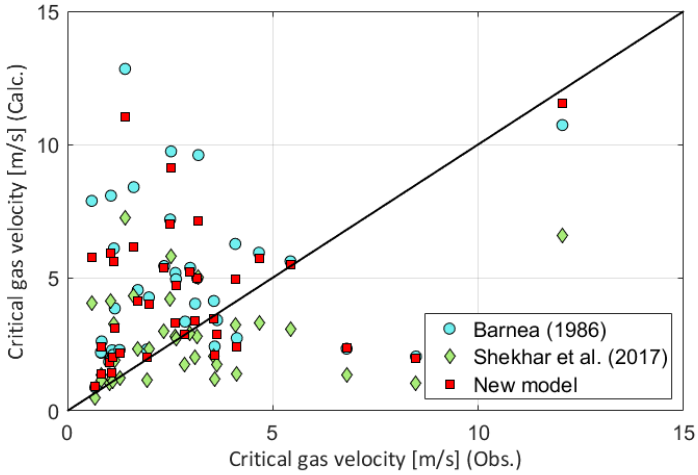

Figure 4.38. Comparison between Turner et al. (1969) data (loaded) vs. predicted values from new model

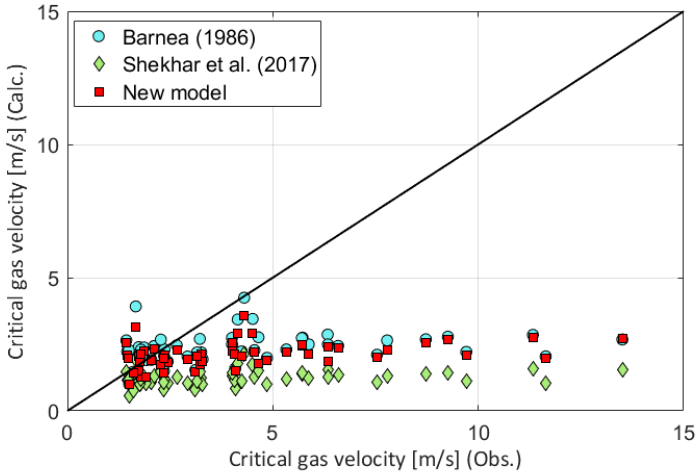

Figure 4.39. Comparison between Turner et al. (1969) data (unloaded) vs. predicted values from new model

The new model exhibits a slightly better prediction when compared to Barnea (1986) and Shekhar et al. (2017) by given the prediction results close to the actual measured gas velocity, i.e., more data points were close to the 45° line. Although, the suggested model performed well, it is recommended as further and future work to investigate methods to verify the applicability of the equations developed (and improve them if necessary) with experimental data for other pipe diameter, test fluids and extended liquid holdup ranges.

Overall, the new proposed model performed better for our experimental data when compared against models of Barnea (1986) and Shekhar et al. (2017), and similar was for the field data, which constitutes an improvement.

4.5 Study on liquid accumulation along the wellbore

In the previous sections the analysis of the liquid loading onset was performed considering one location in the pipe. However, in reality a well is a long pipe of a few thousand meters divided in several sections. Thus, there are some spatial aspects of liquid loading that are important to look into, namely:

- The changes of superficial velocities of gas and liquid along the wellbore will cause liquid loading to have its onset usually in one location. Then as gas rate is reduced further, there will be other locations in the well that will start also to experience loading. Therefore, a study was performed to evaluate how does the wellbore transitions from unloaded to fully loaded and quantify the increase in pressure drop and the fraction of the wellbore that is loaded.
- Additionally, a comparison between different liquid loading criteria such as droplet model (Turner et al., 1969), film model (annular to slug transition) and minimum in the pressure drop curve were performed. This with the objective to quantify the variability in the critical gas rate values predicted with different criteria.

Due to the fact that it was not feasible to do field testing on this issue, numerical study was performed. To carry out the pressure drop study in the tubing as a function of gas rate, three numerical simulators were employed a dynamic flow simulator (OLGA), a well performance simulator tool (PROSPER) and Gray (1978) (model described in Appendix B.2) pressure correlation, programmed in Excel VBA. The reason of choosing the models and simulation listed was such that OLGA is able to capture and model flow transients, if any. PROSPER on the other hand is a steady state tool commonly used by the industry for liquid loading studies, as well as Gray correlation. To determine either or not a point on the wellbore is experiencing liquid loading three methods were used:

- The gas velocity (actual) was compared against the critical gas velocity computed with Turner et al. correlation (Equation 2.2).
- The flow pattern was checked, if different than annular flow, the point is considered to be loaded.
- The minimum pressure drop in the vertical performance lift curve was identified.

The study case consist of a vertical 1.625-inches inner diameter gas well, 3468 ft long production tubing, with constant wellhead pressure of 25 psia and temperature of 100°F. Dry gas and free water were used as fluid which entered at the same point at the bottom of the well. Figure 4.40 shows the schematic of the simulated well.

Gas rates ranging from 0.00625 to 1.5 MMscf/d and water-gas ratio (WGR) of 1, 16.67, 100 and 300 stb/MMscf, estimated from a constant flow rate of 15 Mscf/d, were simulated. Results obtained from the simulators were bottom flowing pressure (p_{wf}), wellbore pressure profile, fluid properties and superficial velocities.

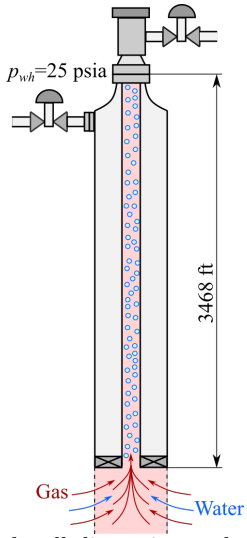

Figure 4.40. Simulated well dimension and operational conditions

To simplify the simulations and to remove the effect of the formation temperature distribution, isothermal ambient conditions were assumed. However, due to the Joule-Thomson effect and the pressure drop experienced by the fluid, the fluid exhibited a temperature variation along the wellbore.

The change in pressure influenced some of the fluid properties such as gas density and surface tension. Therefore, a curve of surface tension and gas density varying with pressure at constant temperature was obtained from the PVT file in OLGA (Figure 4.41 and 4.42). A fitting equation was determined and used to correct the value of surface tension for all the simulated scenarios.

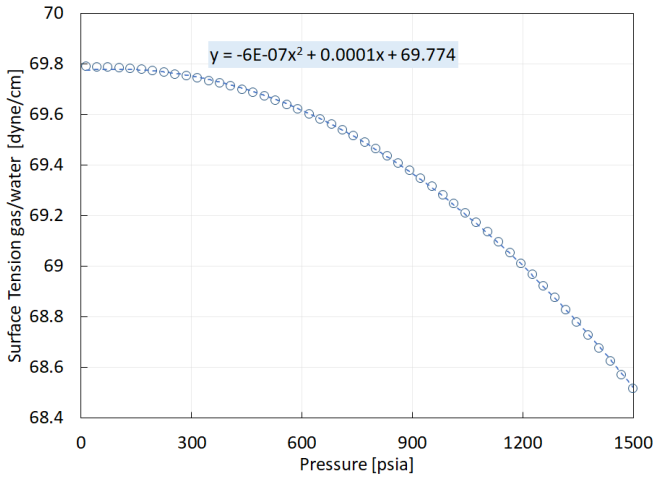

Figure 4.41. Surface tension as function of pressure from OLGA at 100°F

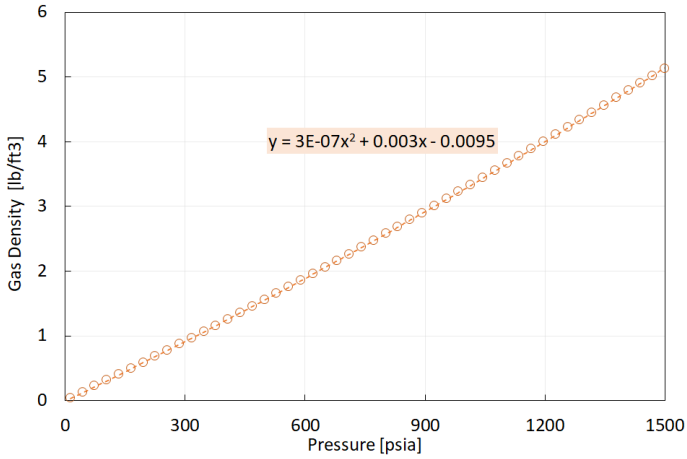

Figure 4.42. Gas density as function of pressure from OLGA at 100°F

4.5.1 Simulation results

In this section the simulation results are presented. Figure 4.43 to Figure 4.45 presents the bottom flowing pressure varying with gas flow rate obtained from Gray (1978), OLGA and PROSPER at constant wellhead pressure and various gas rate and water-gas ratio.

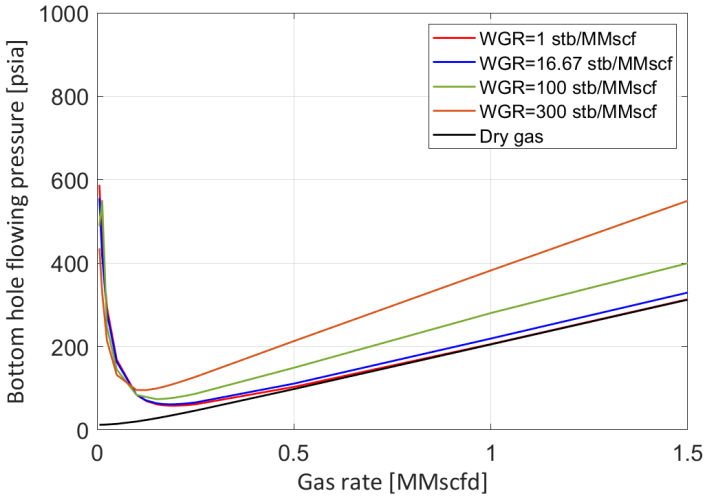

Figure 4.43. Pressure drop for vertical well with 1.625-inches inner diameter using Gray correlation model

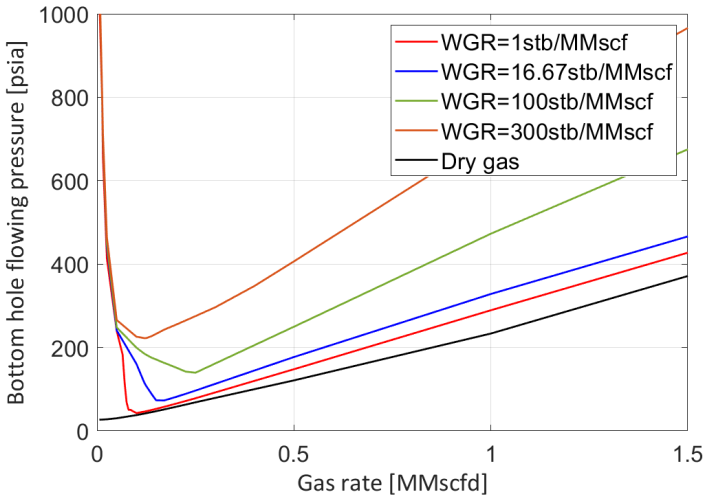

Figure 4.44. Pressure drop for vertical well with 1.625-inches inner diameter using OLGA model

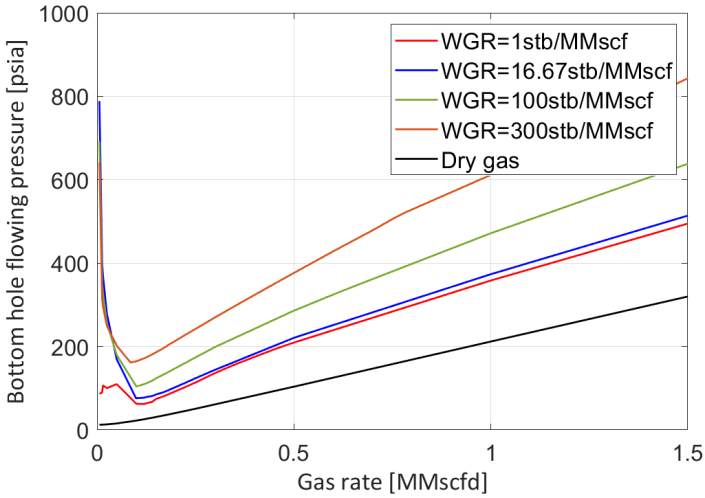

Figure 4.45. Pressure drop for vertical well with 1.625-inches inner diameter using PROSPER model

Overall, the curves presented in Figure 4.43–4.45 show a similar behaviour. As the gas flow rate decreases the bottom hole flowing pressure (p_{wf}) decreases until a minimum pressure point. A further decrease of gas flow rate the p_{wf} increases rapidly, where the curves tend to overlap. For the case of pressure predicted by OLGA (Figure 4.44) the minimum pressure point exhibits a sharp curvature at the minimum pressure point and below those rates, the curves tend to overlap. This could be due to limitation of the PVT data table inserted in the simulator that does not allow simulations to continue at very low gas flow rates. When using PROSPER, it was noticed that, for WGR=1 stb/MMscf, for low gas rates, the curve has different trends depending on the model employed. This

is shown in 4.46 where the vertical lift performance curve is estimated using 4 models, VBA, Gray, GRE models and Petroleum Experts (PE). VBA and GRAY are the model described by Gray (1978). GRAY refers to the results obtained with PROSPER and VBA the results obtained with Excel. PE uses the Gould et al. flow map and various flow regimes model, while GRE is a model developed in house research by petroleum experts, result of several models including Gray (1978) correlation.(Experts, 2019)

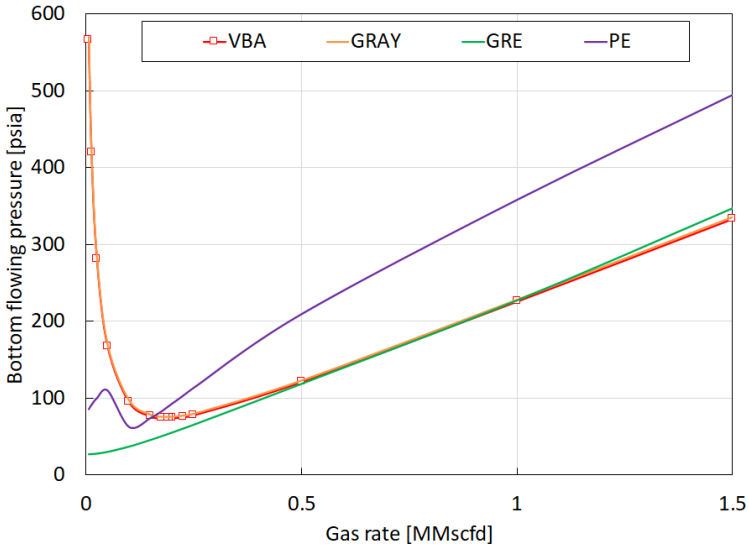

Figure 4.46. Relationship between bottom hole pressure and gas flow rate for different tubing flow correlation for WGR=1 stb/MMscf

Such difference on the vertical lift performance curve predicted by PROSPER was reported by Nymoen (2017). He stated that Gray correlation cannot be used to calculate the static pressure. since with reduction of the gas flow rate the in-situ volume fraction of gas, α, (see Equation B.20) approaches zero, meaning that the gravitational component approaches the liquid density, which could overestimate the pressure drop in gas wells. He also mentioned that the problem could be solved by using the no-slip density (Equation B.28) on the determination of the gravitational component instead of the average density.

Gray and VBA present the same results as expected since is the same model. GRE as mention in the simulator is the modification of PE which is a correlation result of the combination of several existing correlations. In the present study the PE correlation was used. It is also worth to mention that the vertical lift relationship curve predicted by PROSPER was also dependent of the version of the simulator.

For each gas flow rate given a constant WGR, wellbore pressure profile was determined. Figure 4.47 shows the wellbore pressure profile calculated by the models. In order to obtain pressure at different locations, the wellbore was divided into section. The number of wellbore section varied according to the models used. In the case of PROSPER for example the maximum number of section was 14, which was automatically estimated. OLGA and Gray's for instance was 50 since the number of sections could be manually introduced prior to the calculations.

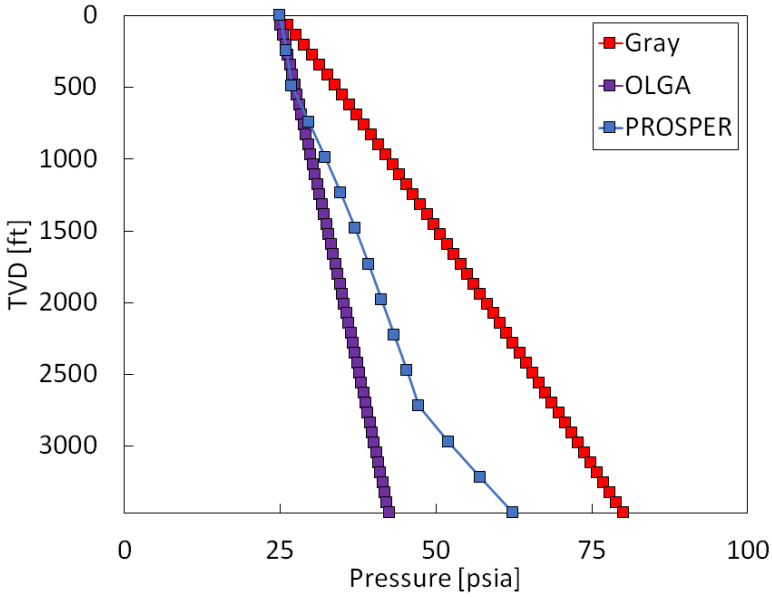

Figure 4.47. True vertical Depth (TVD) vs. wellbore pressure profile for Gray correlation, OLGA and PROSPER for WGR=1 stb/MMscf and v_{sg}=0.1 MMscfd

After the wellbore pressure profile was calculated, three criteria/methods used on the identification of liquid loading onset such as 1. droplet model from Turner et al. (1969), 2. film model (annular to slug transition) and 3. minimum pressure in the vertical lift performance curve were evaluated.

From the Excel VBA (Gray correlation) only the droplet and minimum pressure critical gas flow rate were estimated.

In this study the liquid loading accumulation in all the simulated scenarios start at the bottom of the well, because the local superficial gas rate is smallest at that point due to high pressure.

Figure 4.48 present the vertical lift performance relationship curves and in addition each curve present the critical gas flow rate determine by the different methods. The critical gas flow rates were determined as follow:

- Droplet model:when the local superficial gas velocity was lower than the superficial gas velocity determined ($v_g < v_{gc}$).
- Film model: when the flow pattern at the bottom of the well was different than annular flow.
- Minimum pressure: rate at which the vertical performance lift curve displaced a minimum.

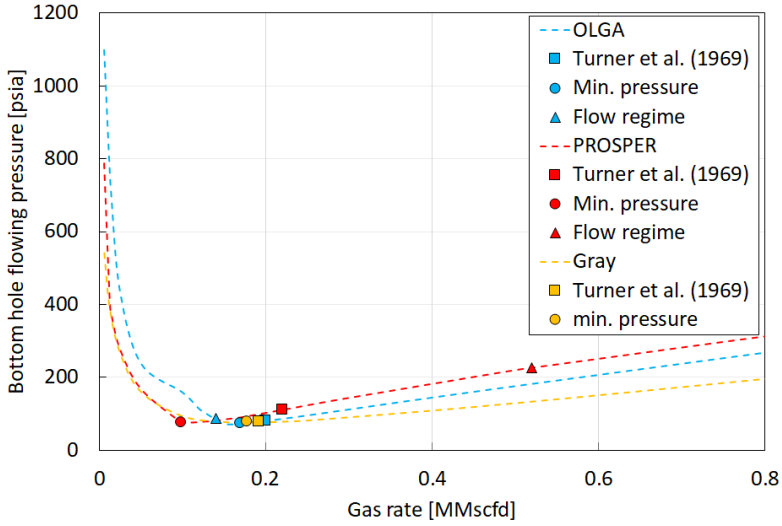

Figure 4.48. Simulation results on liquid loading onset using three different criteria given WGR=16.7 stb/MMscf and constant wellhead pressure of 25 psia

Tables 4.8 to 4.10 presents the critical gas rate for the onset of liquid loading predicted using the different methods for the three models. Additionally, the table present the average gas rate (q_{avg}), standard deviation (std) and a spread band (s) for the predicted gas flow rate. The spread band (Equation 4.15) was calculated using the difference between the maximum and minimum predicted critical gas rate divided by the average gas flow rate.

$$s = \frac{Max - Min}{Average} \tag{4.15}$$

Table 4.8. Liquid loading onset gas flow rate predicted using Gray model for the different methods

WGR	**Liquid loading onset rate**				
stb/MMscf	Turner	$p_{wf,min}$	q_{avg}	std	s
1	0.19	0.19	0.19	0.02	0.03
16.67	0.19	0.18	0.18	0.04	0.08
100	0.22	0.14	0.18	0.20	0.39
300	0.27	0.11	0.19	0.43	0.87
Total,avg	-	-	-	-	0.34

Table 4.9. Liquid loading onset gas flow rate predicted using OLGA model for the different methods

WGR	**Liquid loading onset rate**					
stb/MMscf	Turner	$p_{wf,min}$	FR	q_{avg}	std	s
1	0.15	0.10	0.10	0.11	0.2	0.6
16.67	0.18	0.17	0.14	0.16	0.10	0.2
100	0.25	0.25	0.23	0.24	0.05	0.1
300	0.40	0.12	0.50	0.34	0.47	1.1
Total,avg	-	-	-	-		0.47

Table 4.10. Liquid loading onset gas flow rate predicted using PROSPER model for the different methods

WGR	**Liquid loading onset rate**					
stb/MMscf	Turner	$p_{wf,min}$	FR	q_{avg}	std	s
1	0.21	0.12	0.50	0.28	0.6	1.38
16.67	0.22	0.10	0.52	0.28	0.63	1.51
100	0.29	0.10	0.64	0.34	0.66	1.58
300	0.36	0.09	0.78	0.41	0.70	1.70
Total,avg	-	-	-	-	-	1.54

General a consistently observation was noticed, for all the Gray and OLGA models the prediction of critical gas flow rate by Turner et al. (1969) gave the most conservative, the minimum pressure is the most optimistic (with the lowest bound) and the flow regime is always in between. While for PROSPER the flow regime transition have shown to be the most conservative having the highest critical gas flow rate.

From Tables 4.8 to 4.10 prediction given by Gray and PROSPER models, the critical gas rate increased with increase of WGR when Turner et al. (1969) criteria was used and reversed scenario was seen for the nodal analysis method (minimum pressure in the curve). On the other hand, OLGA predictions did not show a consistent trend when using the minimum pressure criteria as the other models. This could be due to errors when the simulator extrapolated the original PVT table used in the simulations. The average critical gas flow rate estimated from the simulator prediction have shown to increase with increase of WGR and PROSPER model presented standard deviation values above 50% for all the cases. The higher standard deviation is due to the critical gas flow rate values predicted by the flow regime transition criteria. Considering the spread error a similar behaviour as the standard deviation was observed, where the spread increased when WGR increased and PROSPER had the highest spread error.

Overall the models presented quite different standard deviation for a given WGR and constant wellhead pressure. This could mean that, the liquid loading onset rate is dependent not only on the onset criteria employed but also on the pressure drop model.

A study was performed to evaluate how does the wellbore transitions from unloaded to full loaded and to quantify the fraction of the wellbore that is filled with liquid. To identify the status of a well at certain location, the actual superficial gas velocity calculated by the models was compared with the critical gas velocity predicted by Turner criteria and the

critical gas velocity at which the annular-slug flow transition was identified. If the critical gas velocity was higher than the actual superficial gas velocity then at that location the well was considered to be loaded. Figure 4.49 present progression of liquid accumulation in the wellbore as the gas flow rate decreases.

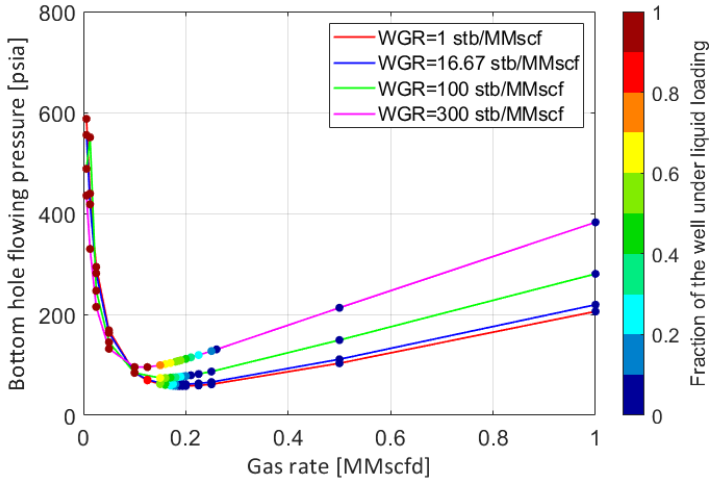

Figure 4.49. Wellbore transition from unloaded to fully loaded for several gas flow rates and WGR estimated by Gray correlation model using Turner equation criteria

It can be observed that once the onset of liquid loading is reached, if the gas rate further decrease the well loads up rapidly. As the water-gas ratio increases the critical gas flow rate also increases.

During the simulation in OLGA it was noticed that the onset of liquid loading along the wellbore could be identified by using the pressure profile chart and flow regime (Figure 4.50).

WGR=16.7 stb/MMscf
q_g=0.125 MMscfd

Well Depth [ft]	Pressure [psia]	Flow Regime [-]
0	25	AN
69	25.4	AN
139	26.2	AN
208	27	AN
277	27.8	AN
347	28.6	AN
416	29.4	AN
485	30.2	AN
555	30.9	AN
624	31.7	AN
694	32.4	AN
763	33.2	AN
832	33.9	AN
902	34.6	AN
971	35.4	AN
1040	36.1	AN
1110	36.8	AN
1179	37.5	AN
1248	38.2	AN
1318	39	AN
1387	39.7	AN
1456	40.4	AN
1526	41.2	AN
1595	41.9	AN
1665	42.7	AN
1734	43.4	AN
1803	44.2	AN
1873	45	AN
1942	45.8	AN
2011	46.7	AN
2081	47.6	AN
2150	48.7	AN
2219	49.9	AN
2289	51.5	AN
2358	53.9	SL
2427	56.9	SL
2497	59.9	SL
2566	63	SL
2636	66.1	SL
2705	69.2	SL
2774	72.4	SL
2844	75.6	SL
2913	78.8	SL
2982	82.0	SL
3052	85.3	SL
3121	88.6	SL
3190	92.0	SL
3260	95.4	SL
3329	98.8	SL
3398	102.2	SL
3468	105.7	SL

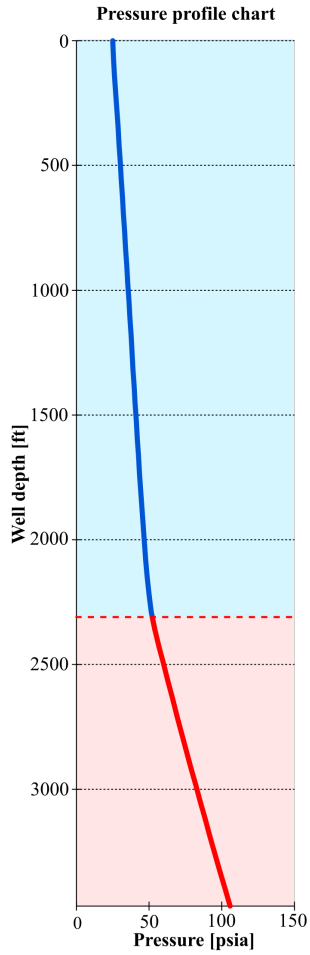

Figure 4.50. Wellbore transition from unloaded to full loaded for several gas flow rates, WGR=300 stb/MMscf estimated by all models using Turner and Flow regime criteria

The pressure profile chart in Figure 4.50 shows the pressure drop per meter across the well bore for the case with 0.125 MMscf gas flow rate and 16.7 stb/MMscf of water-gas ratio, where liquid loading was identified. The pressure profile shows a significant increase in the slug region (0.047 psia/ft) compared to the annular region (0.012 psia/ft). This can be considered as an anticipation of the slug behaviour, where an increase of both the gravity and frictional pressure drop was observed.

Gas rate versus fraction of well filled with liquid were plotted in order to have a better understanding of how the liquid accumulates in the wellbore as the gas flow rate reduces, using the different model and onset prediction criteria. Results are shown in Figure 4.51 to Figure 4.54.

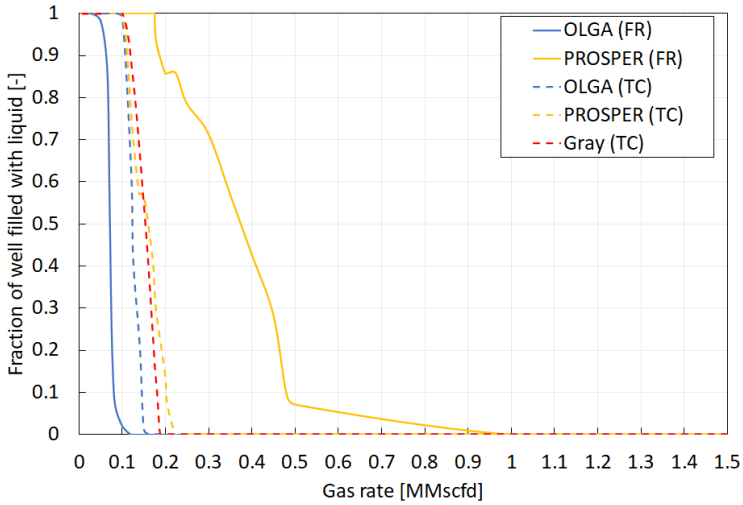

Figure 4.51. Wellbore transition from unloaded to full loaded for several gas flow rates, WGR=1stb/MMscf estimated by all models using Turner and Flow regime criteria

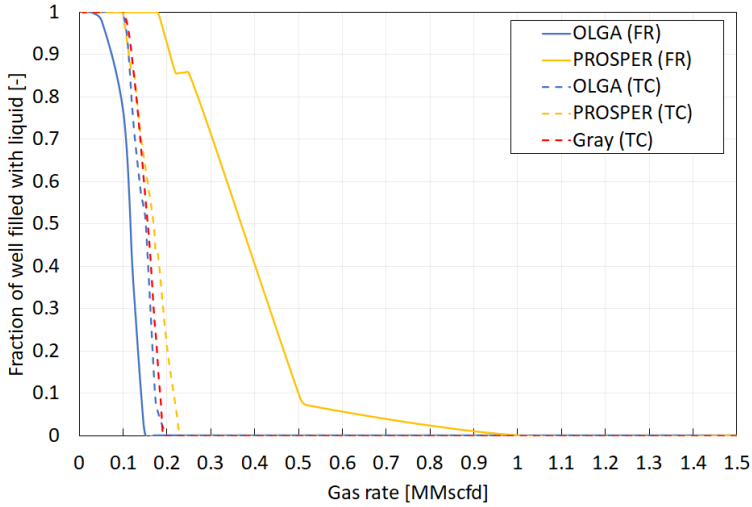

Figure 4.52. Wellbore transition from unloaded to full loaded for several gas flow rates, WGR=16.7stb/MMscf estimated by all models using Turner (TC) and Flow regime (FR) criteria

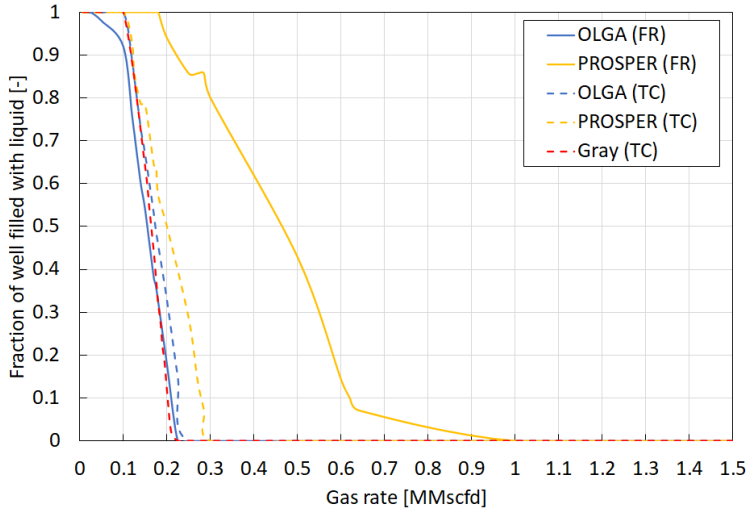

Figure 4.53. Wellbore transition from unloaded to full loaded for several gas flow rates, WGR=100stb/MMscf estimated by all models using (TC) and Flow regime (FR) criteria

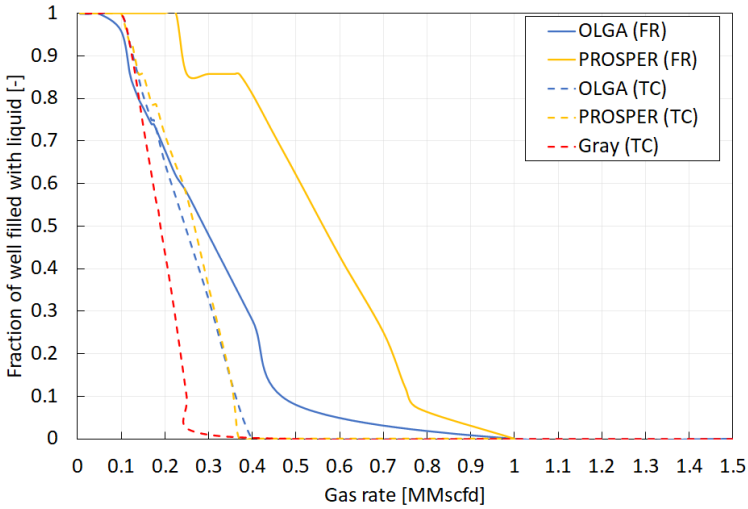

Figure 4.54. Wellbore transition from unloaded to full loaded for several gas flow rates, WGR=300stb/MMscf estimated by all models using (TC) and Flow regime (FR) criteria

For all the simulated scenarios PROSPER results have shown to be more conservative when flow regime transition criteria is used. On the other hand the Turner criteria have shown to have a similar shape for all the models, except for WGR=300 stb/MMscf, where the predicted results were more optimistic, i.e, gave later predictions. To mention that Gray model was not tested for water ratios above 5 bbl/MMcf, which could underestimate pressure predictions for WGR=300 stb/MMscf. Overall, it could be observed that as the onset of liquid loading is identified, an exponential increase of liquid on the wellbore is expected as the gas flow rate keeps reducing.

Chapter 5

Conclusion

5.1 Conclusions

The following conclusions can be drawn from the results obtained in this research:

i. Effect of fluid viscosity on two-phase flow in inclined pipe

An experimental study on the effect of fluid viscosity on flow pattern mapping for two-phase flow in an inclined pipe has been conducted. Observed flow patterns were compared with flow pattern transition modeled by Barnea (1986) and a commercial transient simulator (OLGA 7.3). From the work presented, the following conclusions were derived:

- Most of the flow pattern regions observed by Barnea et al. (1980*a*), Barnea et al. (1980*b*), Barnea et al. (1985) and Barnea (1987) were observed experimentally also in present study.
- The unified model for flow pattern transition proposed by Barnea (1987) predicted satisfactorily the experimentally measured flow pattern map of the two-phase system with viscous fluid as liquid phase at all tested pipe inclinations.
- In general, flow pattern maps predicted with OLGA 7.3 were not in good agreement with measured data. OLGA 7.3 patterns were similar for the slug flow at 70°–78°, but failed on the prediction of slug-annular transition flow for inclinations below 60°.
- Total pressure gradient agreed quite well with the predicted total pressure gradients from OLGA 7.3 for all tested inclination angles.

ii. Applicability of existing models for liquid loading prediction

An experimental study on the applicability of available models to predict important parameters during gas production in inclined wells has been conducted. From the work presented, the following conclusions were derived:

- Models based on droplet model underestimate the annular-slug flow pattern transition for all inclination angles.

- OLGA 7.3 does not predict the transition of intermittent (slug) to annular flow for inclinations lower than 60°. Instead the software predicts a transition slug to stratified-wavy flow.
- Overall, the Luo et al. (2014) model overestimated the transition of intermittent to annular flow, thus giving a worse performance for the liquid film model group of approximately 60% relative error.
- On air-water and air-Exxsol D80 the model presented by Shekhar et al. (2017) performed well at inclinations lower than 60°, where the effect of film thickness was more relevant.
- For high liquid velocities the Barnea (1986) model gave a better prediction than the Shekhar et al. (2017) model for two-phase flow with viscous liquid for all the inclinations.
- The observed critical gas velocity for viscous oil was lower compared to other fluids.
- OLGA 7.3 transition gas velocities, presented a good agreement with the experimental data for pipe inclination lower than 45° despite the fact that slug-stratified wavy flow was predicted instead of slug-annular transition.
- The relative error in OLGA 7.3 tended to increase with increasing pipe inclination.

iii. Effect of entrainment on the annular-slug flow regime transition for liquid loading prediction

In this study, field and experimental data on the onset of liquid loading and flow pattern transition were compared with the liquid film model, and was used for predicting critical gas velocity in gas well. The standard liquid film models assume negligible entrainment. Therefore, the present work was performed considering entrainment on the liquid film model on the prediction of critical gas velocity. From the work performed and presented the following conclusions were derived:

- The predictability of the Shekhar et al. model (2017) of the laboratory data air-water and air-Exxsol D80 system improved when liquid droplet entrainment is included.
- Luo et al. model (2014) overestimated the annular-slug transition boundary flow for all cases studied, consequently also the critical gas velocity for liquid loading predictions.
- Adding an empirical correlation to account for the liquid droplet fraction in the liquid film model by Barnea (1986) and Shekhar et al. (2017) improved the prediction of liquid loading onset for all the analysed data, giving results close to the actual velocity present in the well and observed experimentally.
- In the case of vertical gas wells, droplet entrainment did not have any effect on the critical gas velocity prediction. This was most probably due to the fact that the film thickness is constant at such geometries and the variation of the deposition or entrainment rate in the gas core is negligible.

- Luo et al. (2014) and Shekhar et al. (2017) did not predicted the critical gas velocity satisfactorily in vertical pipes.

iv. Effect of film distribution on the determination of onset of liquid loading

A new model for estimating the onset velocity of liquid loading in inclined pipes in presented based on the flow pattern transition from annular to intermittent flow. Model correlations were developed using published by Paz (1994). The new method was developed using the same guidelines as the models proposed by Barnea (1986) and Shekhar et al. (2017). The distinctive features of the new model are:

(a) The method is suitable for inclined pipes, the effect of pipe inclination on the liquid film thickness varies as the inclination changes and liquid loading initiates at position in the pipe with maximum film thickness, similarly to the approach proposed by Shekhar et al. (2017). However, the critical superficial gas velocity is predicted by employing liquid hold-up variation caused by non-uniform film distribution in the pipe circumference.

(b) A new interfacial friction factor equation was developed, which account for the liquid hold-up variation due to pipe inclination.

- Stated modifications were achieved with an accurate predictions of critical gas velocities as function of pipe inclination, showing a better agreement when compared to those of other methods proposed in the literature.
- The proposed method was tested against experimental data for which it proved to have a good agreement. An experimental data published by Guner (2012) was used for validation of the model. It was shown that the new model was conservative but predicted the values within the rage of transition determined on his experiment.
- Evaluating the new model against field data from Belfroid et al. (2008), Veeken et al. (2010) and Turner et al. (1969), it was observed that for a better prediction it was necessary with an upwards adjustment of the proposed interface friction factor.

v. Study on liquid accumulation development along the wellbore

A numerical study of three models evaluated the wellbore transitions from unloaded to fully loaded, and quantified the increase in pressure drop and the fraction of wellbore that was filled with liquid, by using several onset liquid loading criteria. From the work presented the following conclusions were derived:

- The criteria of estimating the onset of liquid loading using the nodal analysis (minimum pressure in the curve) concept, liquid-droplet reversal and flow regime transition did not match.
- In all cases the rate at which the critical velocity was reached increased when the water-gas ratio increased.

- For all the scenarios calculated through Gray and OLGA models, the result of critical gas flow rate by Turner et al. (1969) gave the most conservative, the minimum pressure was the most optimistic (with the lowest bound) and the flow regime was always in between. While for PROSPER the flow regime transition proved to be the most conservative having the highest critical gas flow rate.
- The models presented quite different standard deviation for a give WGR and constant wellhead pressure. This could mean that the uncertainty in the liquid loading onset depends on the transition criteria and the pressure droplet model employed.
- After the identification of onset of liquid loading, the wellbore transition from unloaded to fully loaded happened rapidly when the Turner et al. criteria (1969) was used for all the models.
- Flow regime criteria is more conservative than Turner et al. (1969) for both OLGA and PROSPER.
- As the onset of liquid loading is identified, an exponential increase of liquid on the wellbore is expected as the gas flow rate keeps reducing.

5.2 Recommendations for future research

The following recommendations can be made for further work on the topic of onset of liquid loading in gas well for inclined pipe:

- Focus on evaluating Barnea (1987), Shekhar et al. (2017) and the new model on two-phase flow system with viscous liquid for a wide range of pipe geometries.
- Further improvement of the closure relationships is needed for the new model to give better predictions of gas-liquid flow behaviour for lower pipe inclinations.
- Consistent test data from experiments on multiphase flow over large ranges of relevant parameters are needed in order to derive better rules and/or methods to improve the predictive ability of the models on liquid loading onset for gas wells.
- Evaluate experimentally the behaviour of the liquid loading onset at three-phase flow conditions.
- Model the on role of the formation interaction with the near-wellbore in the onset of liquid loading.

References

Alsaadi, Y. (2013), Liquid loading in highly deviated gas wells, Master's thesis, University of Tulsa.

Aziz, K. and Govier, G. W. (1972), 'Pressure drop in wells producing oil and gas', *Journal of Canadian Petroleum Technology* **11**(03), 38–48.
URL: *https://doi.org/10.2118/72-03-04*

Baker, O. (1953), Design of pipelines for simultaneous flow of oil and gas, *in* 'Fall Meeting of the Petroleum Branch of AIME', Society of Petroleum Engineers, Dallas, Texas, pp. 1–16.
URL: *https://doi.org/10.2118/323-G*

Barnea, D. (1986), 'Transition from annular flow and from dispersed bubble flow—unified models for the whole range of pipe inclinations', *International journal of multiphase flow* **12**(5), 733–744.
URL: *https://doi.org/10.1016/0301-9322(86)90048-0*

Barnea, D. (1987), 'A unified model for predicting flow-pattern transitions for the whole range of pipe inclinations', *International Journal of Multiphase Flow* **13**(1), 1–12.
URL: *https://doi.org/10.1016/0301-9322(87)90002-4*

Barnea, D., Shoham, O. and Taitel, Y. (1982*a*), 'Flow pattern transition for downward inclined two phase flow; horizontal to vertical', *Chemical Engineering Science* **37**(5), 735–740.
URL: *https://doi.org/10.1016/0009-2509(82)85033-1*

Barnea, D., Shoham, O. and Taitel, Y. (1982*b*), 'Flow pattern transition for vertical downward two phase flow', *Chemical Engineering Science* **37**(5), 741–744.
URL: *https://doi.org/10.1016/0009-2509(82)85034-3*

Barnea, D., Shoham, O., Taitel, Y. and Dukler, A. (1980*a*), 'Flow pattern characterization in two phase flow by electrical conductance probe', *International Journal of Multiphase Flow* **6**(5), 387–397.
URL: *http://dx.doi.org/10.1016/0301-9322(80)90001-4*

Barnea, D., Shoham, O., Taitel, Y. and Dukler, A. (1980*b*), 'Flow pattern transition for gas-liquid flow in horizontal and inclined pipes. comparison of experimental data with theory', *International Journal of Multiphase Flow* **6**(3), 217–225.
URL: *https://doi.org/10.1016/0301-9322(80)90012-9*

Barnea, D., Shoham, O., Taitel, Y. and Dukler, A. (1985), 'Gas-liquid flow in inclined tubes: flow pattern transitions for upward flow', *Chemical Engineering Science* **40**(1), 131–136.
URL: *https://doi.org/10.1016/0009-2509(85)85053-3*

Beggs, D. H. and Brill, J. P. (1973), 'A study of two-phase flow in inclined pipes', *Journal of Petroleum technology* **25**(05), 607–617.
URL: *https://doi.org/10.2118/4007-PA*

Belfroid, S., Schiferli, W., Alberts, G., Veeken, C. A., Biezen, E. et al. (2008), Predicting onset and dynamic behaviour of liquid loading gas wells, *in* 'SPE Annual Technical Conference and Exhibition', Society of Petroleum Engineers, Denver, Colorado, USA.
URL: *https://doi.org/10.2118/115567-MS*

Bendiksen, K. H., Maines, D., Moe, R. and Nuland, S. (1991), 'The dynamic two-fluid model olga: Theory and application', *SPE production engineering* **6**(02), 171–180.
URL: *https://doi.org/10.2118/19451-PA*

Chupin, G. (2003), An experimental investigation of multiphase gas-liquid pipe flow at low liquid loading, PhD thesis, Norwegian University of Science and Technology, Department of Energy and Process Technology.

Chupin, G., Hu, B., Haugset, T., Sagen, J. and Claudel, M. (2007), Integrated wellbore/reservoir model predicts flow transients in liquid-loaded gas wells, *in* 'SPE Annual Technical Conference and Exhibition', Society of Petroleum Engineers, Anaheim, California, U.S.A.
URL: *https://doi.org/10.2118/110461-MS*

Coleman, S. B., Clay, H. B., McCurdy, D. G. and Norris III, L. H. (1991), 'A new look at predicting gas-well load-up', *Journal of Petroleum Technology* **43**(03), 329–333.
URL: *https://doi.org/10.2118/20280-PA*

Diaz, M. J. (2016), Two-Phase Slug Flow Experiments with Viscous Liquids, PhD thesis, Norwegian University of Science and Technology, Department of Energy and Process Technology.

Duggan, J. O. (1961), 'Estimating flow rates required to keep gas wells unloaded', *Journal of Petroleum Technology* **13**(12), 1173–1176.
URL: *https://doi.org/10.2118/32-PA*

Dukler, A., Wicks, M. and Cleveland, R. (1964*a*), 'Frictional pressure drop in two-phase flow: A. a comparison of existing correlations for pressure loss and holdup', *AIChE Journal* **10**(1), 38–43.

Dukler, A., Wicks, M. and Cleveland, R. (1964*b*), 'Frictional pressure drop in two-phase flow: B. an approach through similarity analysis', *AIChE Journal* **10**(1), 44–51.

Enos, M. K. (2018), Evaluation of models to predict liquid loading in gas wells, Master's thesis, NTNU.

Experts, P. (2019), *Integrated Production Modelling - Online Manuals IPM 11.0*, version 15 edn, Petroleum Experts Limited.

Fernandez, J. J., Falcone, G., Teodoriu, C. et al. (2010), 'Design of a high-pressure research flow loop for the experimental investigation of liquid loading in gas wells', *SPE Projects, Facilities & Construction* **5**(02), 76–88.

Fiedler, S. and Auracher, H. (2004), 'Experimental and theoretical investigation of reflux condensation in an inclined small diameter tube', *International journal of heat and mass transfer* **47**(19-20), 4031–4043.
URL: *https://doi.org/10.1016/j.ijheatmasstransfer.2004.06.005*

Flanigan, O. (1958), 'Effect of uphill flow on pressure drop in design of two-phase gathering systems', *Oil and gas journal* **56**(10), 132.

Flores-Avila, F. S., Smith, J. R., Bourgoyne Jr, A. T. and Bourgoyne, D. A. (2002), Experimental evaluation of control fluid fallback during off-bottom well control: effect of deviation angle, *in* 'IADC/SPE Drilling Conference', Society of Petroleum Engineers, Dallas, Texas.
URL: *https://doi.org/10.2118/74568-MS*

Fore, L., Beus, S. and Bauer, R. (2000), 'Interfacial friction in gas–liquid annular flow: analogies to full and transition roughness', *International journal of multiphase flow* **26**(11), 1755–1769.
URL: *https://doi.org/10.1016/S0301-9322(99)00114-7*

Gokcal, B., Wang, Q., Zhang, H.-Q., Sarica, C. et al. (2008), 'Effects of high oil viscosity on oil/gas flow behavior in horizontal pipes', *SPE Projects, Facilities & Construction* **3**(02).
URL: *https://doi.org/10.2118/102727-PA*

Gray, H. (1978), *Vertical flow correlation in gas wells, user's manual for API 14B surface controlled subsurface safety valve sizing computer program, 2nd Edition*, American Petroleum Institute, Dallas, Texas.

Guner, M. (2012), Liquid loading of gas wells with deviation from 0° to 45°, Master's thesis, University of Tulsa.

Guner, M., Pereyra, E., Sarica, C., Torres, C. et al. (2015), An experimental study of low liquid loading in inclined pipes from 90° to 45°, *in* 'SPE Production and Operations Symposium', Society of Petroleum Engineers, Oklahoma City, USA.
URL: *https://doi.org/10.2118/173631-MS*

Guo, B., Ghalambor, A. and Xu, C. (2005), A systematic approach to predicting liquid loading in gas wells, *in* 'SPE Production and Operations Symposium', Society of Petroleum Engineers, Oklahoma City, Oklahoma.
URL: *https://doi.org/10.2118/94081-MS*

Hewitt, G., Lacey, P. and Nicholls, B. (1965), *Transitions in film flow in a vertical tube*, AERE, Chemical Division Harwell.

Jeyachandra, B. C., Sarica, C., Zhang, H.-q., Pereyra, E. J. et al. (2012), Effects of inclination on flow characteristics of high viscosity oil/gas two phase flow, *in* 'SPE Annual Technical Conference and Exhibition', Society of Petroleum Engineers, San

Antonio, Texas, USA.
URL: *https://doi.org/10.2118/159217-MS*

Johansen, M. (2006), An experimental study of the bubble propagation velocity in three-phase slug flow, PhD thesis, Norwegian University of Science and Technology, Department of Energy and Process Technology.

Jones, P. J. (1946), *Petroleum Production: The optimum rate of production*, Vol. 2, Reinhold Publishing Corporation.

Kelkar, M. G., Pereyra, E. J., Skopich, A., Sarica, C. et al. (2013), Pipe diameter effect on liquid loading in vertical gas wells, *in* 'SPE Production and Operations Symposium', Society of Petroleum Engineers, Oklahoma City, USA.
URL: *https://doi.org/10.2118/164477-MS*

Kokal, S. and Stanislav, J. (1989*a*), 'An experimental study of two-phase flow in slightly inclined pipes—i. flow patterns', *Chemical Engineering Science* **44**(3), 665–679.
URL: *https://doi.org/10.1016/0009-2509(89)85042-0*

Kokal, S. and Stanislav, J. (1989*b*), 'An experimental study of two-phase flow in slightly inclined pipes—ii. liquid holdup and pressure drop', *Chemical Engineering Science* **44**(3), 681–693.
URL: *https://doi.org/10.1016/0009-2509(89)85043-2*

Li, M., Lei, S. and Li, S. (2001), New view on continuous-removal liquids from gas wells, *in* 'SPE Permian Basin Oil and Gas Recovery Conference', Society of Petroleum Engineers, Midland, Texas.
URL: *https://doi.org/10.2118/70016-MS*

Luo, S., Kelkar, M., Pereyra, E., Sarica, C. et al. (2014), 'A new comprehensive model for predicting liquid loading in gas wells', *SPE Production & Operations* **29**(04), 337–349.
URL: *https://doi.org/10.2118/172501-PA*

Mandhane, J., Gregory, G. and Aziz, K. (1974), 'A flow pattern map for gas—liquid flow in horizontal pipes', *International Journal of Multiphase Flow* **1**(4), 537–553.
URL: *https://doi.org/10.1016/0301-9322(74)90006-8*

Nicholson, M., Aziz, K. and Gregory, G. (1978), 'Intermittent two phase flow in horizontal pipes: predictive models', *The Canadian Journal of chemical engineering* **56**(6), 653–663. Based on a paper presented at the 27th Canadian Chemical Engineering Conference, October 23–27, 1977; Calgary, Alberta.
URL: *https://doi.org/10.1002/cjce.5450560601*

Nosseir, M., Darwich, T., Sayyouh, M. and El Sallaly, M. (1997), A new approach for accurate prediction of loading in gas wells under different flowing conditions, *in* 'SPE Production Operations Symposium', Society of Petroleum Engineers, Oklahoma City, Oklahoma.
URL: *https://doi.org/10.2118/37408-MS*

Nymoen, T. (2017), Application of backpressure analysis to gas condensate systems, Master's thesis, Norwegian University of Technology and Science.

Oliemans, R., Pots, B. and Trompé, N. (1986), 'Modelling of annular dispersed two-phase flow in vertical pipes', *International journal of multiphase flow* **12**(5), 711–732.
URL: *https://doi.org/10.1016/0301-9322(86)90047-9*

Orkiszewski, J. (1967), 'Predicting two-phase pressure drops in vertical pipe', *Journal of Petroleum Technology* **19**(06), 829–838.
URL: *https://doi.org/10.2118/1546-PA*

Oudeman, P. (2007), On the flow performance of velocity strings to unload wet gas wells, *in* 'SPE Middle East Oil and Gas Show and Conference', Society of Petroleum Engineers, Manama, Bahrain.
URL: *https://doi.org/10.2118/104605-MS*

Paz, R. (1994), Film thickness distribution for annular flow in directional wells: horizontal to vertical, *in* 'SPE Annual Technical Conference and Exhibition', Society of Petroleum Engineers, New Orleans, Louisiana, pp. 257–272.
URL: *https://doi.org/10.2118/28541-MS*

Sarica, C., Yuan, G., Sutton, R. P. and Pereyra, E. J. (2013), An experimental study on liquid loading of vertical and deviated gas wells, *in* 'SPE Production and Operations Symposium', Society of Petroleum Engineers, Oklahoma City, USA.
URL: *https://doi.org/10.2118/164516-MS*

Shekhar, S., Kelkar, M., Hearn, W. J. and Hain, L. L. (2017), 'Improved prediction of liquid loading in gas wells', *SPE Production & Operations* **32**(4).
URL: *https://doi.org/10.2118/186088-PA*

Shoham, O. (1982), Flow Pattern Transition and Characterization in Gas-Liquid Two-Phase Flow in Inclined Pipes, PhD thesis, Tel - Aviv University, Israel.

Shoham, O. (2006), *Mechanistic modeling of gas-liquid two-phase flow in pipes*, Society of Petroleum Engineers Richardson, Texas.

Singh, G. and Griffith, P. (1970), 'Determination of the pressure drop optimum pipe size for a two-phase slug flow in an inclined pipe', *J. Engng Ind. Trans.* **92**(4), 717–729.
URL: *https://doi.org/10.1115/1.3427837*

Stanislav, J., Kokal, S. and Nicholson, M. (1986), 'Intermittent gas-liquid flow in upward inclined pipes', *International journal of multiphase flow* **12**(3), 325–335.
URL: *https://doi.org/10.1016/0301-9322(86)90011-X*

Sutton, R. P., Cox, S. A., Lea, J. F. and Rowlan, O. L. (2010), 'Guidelines for the proper application of critical velocity calculations', *SPE Production & Operations* **25**(02), 182–194.
URL: *https://doi.org/10.2118/120625-PA*

Taitel, Y., Barnea, D. and Dukler, A. (1980), 'Modelling flow pattern transitions for steady upward gas-liquid flow in vertical tubes', *AIChE Journal* **26**(3), 345–354.
URL: *https://doi.org/10.1002/aic.690260304*

Taitel, Y. and Dukler, A. (1976), 'A model for predicting flow regime transitions in hori-

zontal and near horizontal gas-liquid flow', *AIChE Journal* **22**(1), 47–55.
URL: *https://doi.org/10.1002/aic.690220105*

Turner, R., Hubbard, M. and Dukler, A. (1969), 'Analysis and prediction of minimum flow rate for the continuous removal of liquids from gas wells', *Journal of Petroleum Technology* **21**(11), 1–475.
URL: *https://doi.org/10.2118/2198-PA*

Van't Westende, J. M. C. (2008), Droplets in annular-dispersed gas-liquid pipe-flows, PhD thesis, Delft University of Technology, Netherlands.

Veeken, K., Hu, B. and Schiferli, W. (2010), 'Gas-well liquid-loading-field-data analysis and multiphase-flow modeling', *SPE Production & Operations* **25**(03), 275–284.
URL: *https://doi.org/10.2118/123657-PA*

Vitter Jr, A. (1942), Back-pressure tests on gas-condensate wells, *in* 'Drilling and Production Practice', American Petroleum Institute, New York, pp. 79–87.

Wallis, G. B. (1969), *One-dimensional two-phase flow*, McGraw-Hill, New York.

Waltrich, P. J., Posada, C., Martinez, J., Falcone, G. and Barbosa Jr., J. R. (2015), 'Experimental investigation on the prediction of liquid loading initiation in gas wells using a long vertical tube', *Journal of Natural Gas Science and Engineering* **26**, 1515–1529.
URL: *https://doi.org/10.1016/j.jngse.2015.06.023*

Wang, Y.-W., Zhang, S.-C., Jin, Y. and Chen, W.-B. (2010), 'A new calculation method for gas-well liquid loading capacity', *Journal of Hydrodynamics, Ser. B* **22**(6), 823–826.
URL: *https://doi.org/10.1016/S1001-6058(09)60122-0*

Wang, Z., Guo, L., Wu, W., Zhu, S. and Zhou, H. (2016), 'Experimental study on the critical gas velocity of liquid-loading onset in an inclined coiled tube', *Journal of Natural Gas Science and Engineering* **34**, 22–33.
URL: *https://doi.org/10.1016/j.jngse.2016.06.044*

Weisman, J. and Kang, S. (1981), 'Flow pattern transitions in vertical and upwardly inclined lines', *International Journal of Multiphase Flow* **7**(3), 271–291.
URL: *https://doi.org/10.1016/0301-9322(81)90022-7*

Yuan, G. (2011), Liquid loading of gas wells, Master's thesis, University of Tulsa.

Zabaras, G., Dukler, A. and Moalem-Maron, D. (1986), 'Vertical upward cocurrent gas-liquid annular flow', *AIChE journal* **32**(5), 829–843.
URL: *https://doi.org/10.1002/aic.690320513*

Zhou, D. and Yuan, H. (2009), New model for gas well loading prediction, *in* 'SPE Production and Operations Symposium', Society of Petroleum Engineers, Oklahoma City, Oklahoma.
URL: *https://doi.org/10.2118/120580-MS*

Appendix A

Experimental procedure

The experimental procedure prior and after any experiment do be performed at the multiphase laboratory at NTNU are presented in this appendix.

Start-up

1. Visual inspection of the flow loop, to ensure that all the valves are correctly connected.
2. Use the check list available in the lab to verify the position of each valve and to certify that the valves are connected according to the experiment to perform. The valves should be verified both both close to the meters and close to the pumps.
3. Set the desired inclination in the test section using the lift handle connected to the lift mechanism. Measure the inclination angle with the angle meter.
4. Mount the high-speed camera on the visualisation section and connect to the power source.
5. Start the air by slowly open the valve besides the large buffer tank (7 bar), allowing air to flow to the small buffer tank (4 bar). The desired water and/or oil pump must be selected. In case of using centrifugal pumps, the recommended operation frequency should be 30Hz and the maximum should be 45Hz.
6. Once everything is checked, open the air safety valve located close to the air control valves.
7. In the main computer launch the lABview Program to turn on the acquisition system for the instruments.
8. Connect the high-speed camera to the designated computer and launch the camera viewer program.

Daily Calibration

The daily calibrations were conducted as follows:

1. Clean the pressure taps and the impulse tubes to remove any purged liquid.
2. Check and if necessary, adjust the capacitance or conductance probes minimum and maximum values.
3. Start the water/oil pump and fill completely the test section. The choice of liquid used on the calibration depends on the experiments to be performed on the same day. Example if water will be the liquid phase on the scheduled experiments then calibration must be done with water.
4. Circulate the liquid in the test section for at least 15 minutes, or more if necessary, until steady-state conditions are reached.
5. Fill the impulsive tube with the liquid circulating in the test section. Make sure no bubbles are present.
6. Shut down the flow, by slowly decreasing the pump frequency is fully switched off. Simultaneously, close the control valves to avoid back-flow of the liquid.
7. Check and if necessary, adjust the probes maximum value.
8. Start logging the data for 2 minutes.
9. Use the logged pressure to check if the absolute pressures are reading according to the expected pressure calculated in Figure 3.7. Sometimes a trapped bubble in the pressure taps where the sensor is connected can lead to a wrong reading.
10. Empty the test section and sample the data again for 2 minutes.
11. Check if the differential pressure transmitter readings goes with the expected pressure calculated in Figure 3.8. Adjust the calibration range if necessary.

Shut-down

Similarly, the laboratory has a shut-down routine

1. Slowly stop the water/oil flow by reduce the frequency of the pump until the pumps are fully switched off.
2. Keep running the air flow to clean the test section and the flexible pipe.
3. Stop the air flow.
4. Close valve at the large buffer tank and the air safety valve, as well as all the valves in the mixing sections.
5. Write down activities and changes done during the day in the laboratory dossier.

Appendix B

Models derivations

In this appendix, computational details related to models used for flow pattern and pressure prediction in inclined section are presented. The model is otherwise presented and tested in Chapter 3 and 4.

The issues dealt with in this appendix are:

- Barnea (1986) model for determination annular to intermittent flow transition.
- Gray (1978) for pressure calculation.
- Development of a new model used on determination of annular to intermittent flow transition for the liquid loading onset predictions.

B.1 Barnea (1986) model for annular-intermittent flow transition

Barnea (1987) unified model is a mechanistic model developed with the propose of predicting flow pattern transition for the whole range of pipe inclination through operative equations and dimensionless maps, that incorporate the effect of flow rates, fluid properties, pipe size and pipe inclination. For each individual boundary a transition mechanism is presented, and a logical path is used for a systematic determination of the flow pattern, i.e., solving through a decision tree (Figure B.1).

As mentioned in Section 2.1 the thesis will focus on describing the transition mechanism behind the determination of annular-intermittent flow boundary and for a better understanding the published model described in Barnea (1986) were used.

Diverse mechanisms were suggested for annular to intermittent flow transition. Taitel et al. (1980) suggested that in order to maintain annular flow, the gas velocity must be large enough to lift the largest stable drop present in the gas core. Barnea et al. (1982*a*) adopted a different idea and suggested that the transition from annular to intermittent flow occurs when the liquid holdup is large enough to block the gas core, creating a stable slug. Later, Barnea (1986) define annular flow as gas flowing along the center of the pipe

and the liquid flowing as a film around the pipe walls, and that annular to intermittent transition would occurs when this characteristic structure no longer exists.

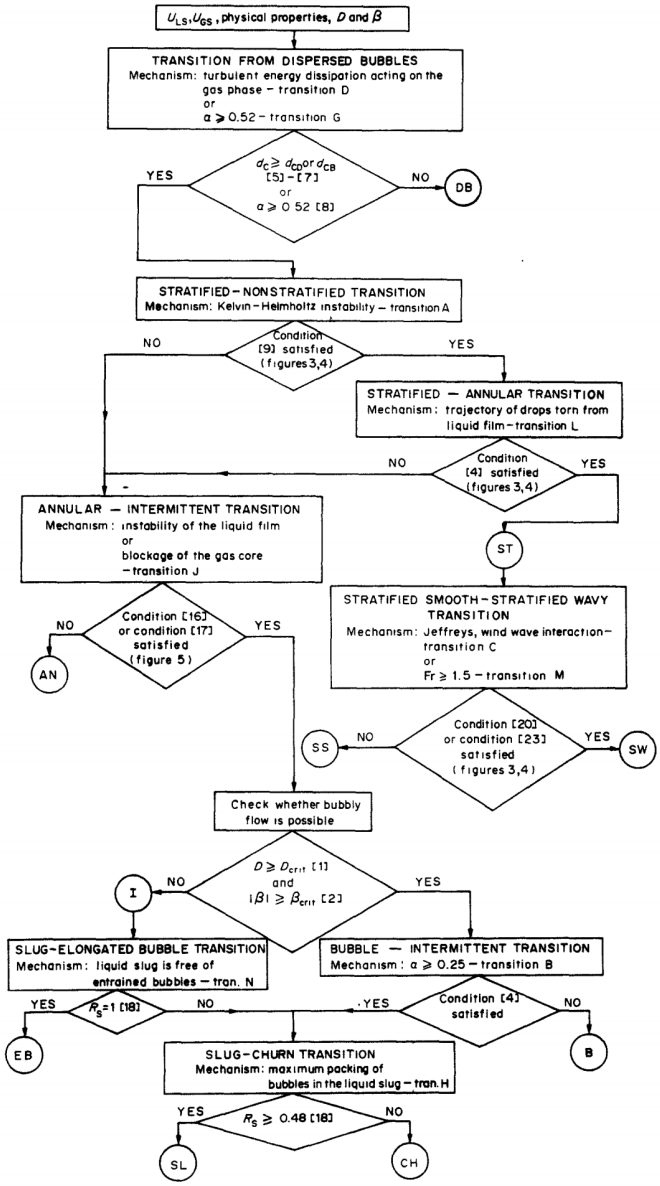

Figure B.1. Logic steps for flow pattern determination Barnea (1987)

Geometry of annular flow is presented in Figure B.2. The gas phase flow in the centre of the pipe while liquid phase as a film with a uniform thickness around the pipe wall. No liquid droplet in the gas core is assumed.

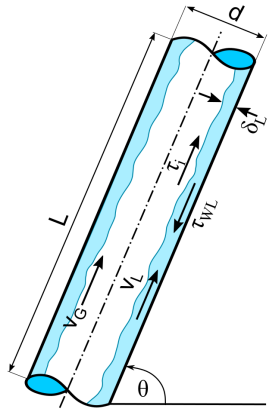

Figure B.2. Physical model for annular flow in an upward flow. Adapted from Shoham (2006)

Using the momentum balance for steady annular flow gives equation for:

Liquid film

$$-A_l\frac{dp}{dL}-\tau_{wl}S_l+\tau_iS_i-\rho_lA_lg\sin\theta=0 \tag{B.1}$$

and

Gas core

$$-A_g\frac{dp}{dL}-\tau_{wl}S_l-\rho_gA_gg\sin\theta=0 \tag{B.2}$$

where τ_i and τ_{wl} are the interfacial and wall shear stress, respectively, A_l and A_g are the cross-sectional area occupied by the liquid and gas phase, respectively, S_l and S_i are the perimeter over which τ_i and τ_{wl} act, respectively, ρ_l and ρ_g are liquid and gas densities, respectively. θ is the angle of inclination from the horizontal, g the gravitational acceleration, p is the static pressure and L the axial coordinate.

Simplifying the pressure gradient from both liquid and gas momentum equations yields the combined momentum (force) balance equation for liquid-gas two-phase for steady-state annular flow, as follows:

$$\tau_iS_i\left(\frac{1}{A_l}+\frac{1}{A_g}\right)-g(\rho_l-\rho_g)\sin\theta-\tau_{wl}\frac{S_l}{A_l}=0 \tag{B.3}$$

The wall shear stress of the liquid τ_{wl} is related to the liquid average axial velocity (v_l) by

$$\tau_{wl}=f_l\frac{\rho_l{v_l}^2}{2} \tag{B.4}$$

with the liquid/wall friction factor f_l evaluated from

$$f_l=C_l\left(\frac{\rho_lD_lv_l}{\mu_l}\right)^{-n} \tag{B.5}$$

where $D_l = 4A_l/S_l$ is the hydraulic diameter, ν_l is the liquid viscosity and C_l and n are constants in the friction factor correlation, where $C_l = 0.046$, $n = 0.2$ for turbulent liquid film and $C_l = 16$, $n = 1$ for laminar liquid film.

and the respective liquid velocity

$$v_l = \frac{v_{sl}A}{A_l} \tag{B.6}$$

Deriving the geometrical parameters based on uniform film thickness (δ) shown in Figure B.3, yield to Equation B.7:

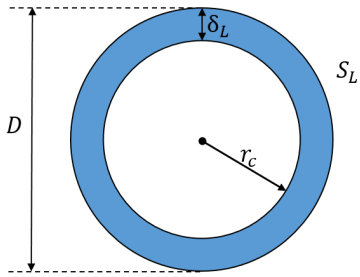

Figure B.3. Annular flow geometry for uniform film thickness

$$S_l = \pi D \qquad S_i = \pi(D - 2\delta) \qquad A_l = \pi(D\delta - \delta^2) \qquad A_g = \pi\Big(\frac{D}{2} - \delta\Big)^2 \tag{B.7}$$

Substituting the geometrical relationships and the liquid shear stress expression into Equation B.3 and rearranging for the interfacial shear stress yields:

$$\tau_i = g(\rho_l - \rho_g)D\sin\beta(\widetilde{\delta_l} - \widetilde{\delta_l}^2)(1 - 2\widetilde{\delta_l}) + \frac{1}{32}C_l\rho_l\left(\frac{D\rho_l}{\mu_l}\right)^{-n}(v_{sl})^{2-n}\left[\frac{(1 - 2\widetilde{\delta_l})}{(\widetilde{\delta_l} - \widetilde{\delta_l}^2)^2}\right] \tag{B.8}$$

Equation B.8 relates the required interfacial shear stress provided by the liquid phase to maintain the annular flow structure to the dimensionless film thickness ($\widetilde{\delta} = \delta/D$), for a given superficial liquid velocity v_{sl}. This relation for upward flow is shown in Figure B.4 for different values of liquid velocities. Note that $\widetilde{\tau_i}$ is the dimensionless interfacial shear stress given by

$$\widetilde{\tau_i} = \frac{\tau_i}{g(\rho_l - \rho_g)D} \tag{B.9}$$

The supplied interfacial shear stress provided by the gas phase for vertical upward flow as follow:

$$\tau_i = \frac{1}{2}f_i\frac{\rho_g v_{sg}^2}{(1 - 2\tilde{\delta}_l)^4} \tag{B.10}$$

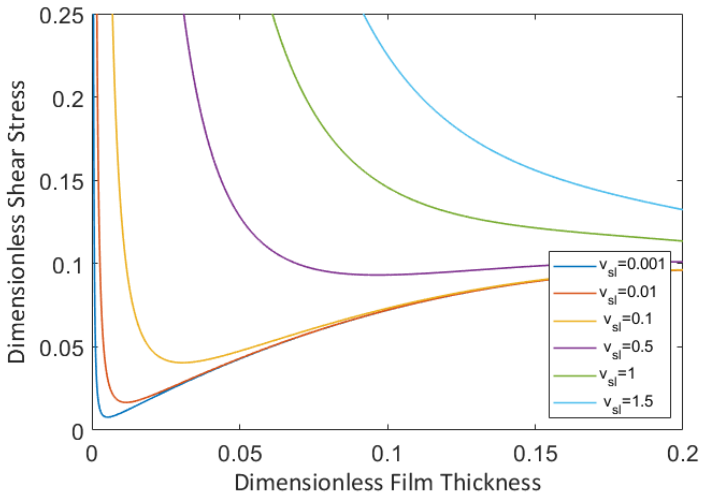

Figure B.4. Dimensionless interfacial shear stress at different liquid velocities

where the gas velocity in the core is given by

$$v_g = \frac{v_{sg}}{(1 - 2\widetilde{\delta_l})^2} \tag{B.11}$$

Barnea (1986) mentioned that the basic mechanism which determine the interfacial shear are not fully understood and the available relationships are largely empirical. Barnea then used an equation developed by Wallis (1969) to estimate the interfacial friction factor (f_i):

$$f_i = f_{sg}(1 + 300\tilde{\delta}_l) \tag{B.12}$$

where f_{sg} is the friction factor in the absence of the film, determined by:

$$f_{sg} = C_g \left(\frac{v_{sg} D \rho_g}{\mu_g} \right)^{-m} \tag{B.13}$$

where v_{sg} is gas superficial velocity, ν_g is the gas kinematic viscosity, $C_g = 0.046$, $m = 0.2$ for turbulent liquid film and $C_g = 16$, $m = 1$ for laminar liquid film.

Equation B.10 relates the provided interfacial shear stress to dimensionless film thickness for a given superficial gas velocity, v_{sg}. This relationship is given by the dashed line in Figure B.5.

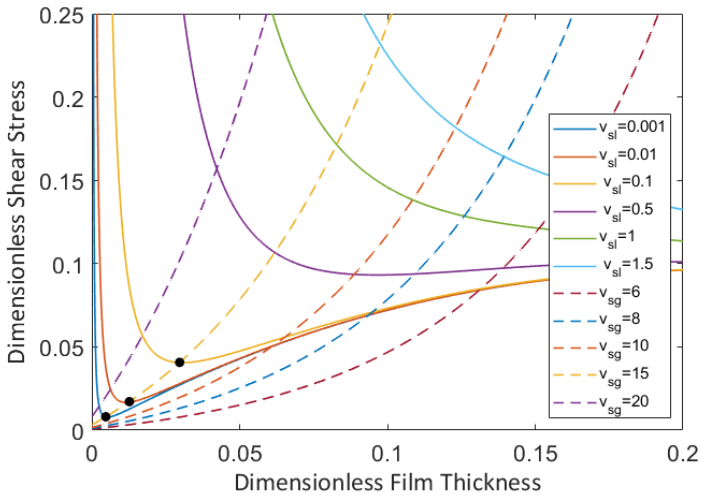

Figure B.5. Steady state solutions for vertical annular flow

For a given set of operational conditions, any intersection between the solid lines and the dashed line is a possible steady-state solution for annular flow.

Barnea (1986) mentioned that the transition from annular to intermittent flow occur if the gas core is blocked by the liquid promoting a change to slug flow. This blockage occurs due to two different mechanisms:

1. **The instability of annular flow configuration**

   In Figure B.4 the minimum velocity profile represents a sudden change in the superficial liquid velocity, indicating reversal of film. (Shekhar et al., 2017)

   The condition at the minimum points is obtained by differentiating Equation B.8 with respect to $\widetilde{\delta}_l$ and equating it to zero $\left(\frac{\partial \tau_i}{\partial \widetilde{\delta}_l} = 0\right)$, yielding

$$g(\rho_l - \rho_g) D \sin\beta \left[(1-2\widetilde{\delta}_l)^2 - 2(\widetilde{\delta}_l - \widetilde{\delta}_l^{\,2})\right] - \frac{1}{16} C_l \rho_l \left(\frac{D\rho_l}{\mu_l}\right)^{-n} (v_{Sl})^{2-n} \left[\frac{(\widetilde{\delta}_l - \widetilde{\delta}_l^{\,2}) + (1-2\widetilde{\delta}_l)^2}{(\widetilde{\delta}_l - \widetilde{\delta}_l^{\,2})^3}\right] = 0 \quad \text{(B.14)}$$

   Equation B.14 gives film thickness at the minimum of the curve, $\widetilde{\delta}_l$ for a given v_{sl}. Solving simultaneously Equations B.8 and B.10 with $\widetilde{\delta}_l$, that satisfies Equation B.14 yield the value of v_{sg} at the transition boundary. The black points in Figure B.5 represents the solutions at annular to slug low transition.

2. **Spontaneous blockage of the core due to wave growth on liquid film**

   Blockage of the gas core in annular flow may also occur when the supply of liquid in the film is large enough to provide a liquid bridge and create a stable slug, this may

happen at relatively higher liquid flow rates. The criteria for this transition is based on the minimum liquid holdup in a slug, $H_{LLS,MIN} = 0.48$. Taitel and Dukler (1976) presented a similar slug flow transition in pipelines, caused by blockage occurring when,

$$\frac{A_L}{AH_{LLS,MIN}} = \frac{H_L}{H_{LLS,MIN}} \geq 0.5 \tag{B.15}$$

$H_{LLS,MIN}$ corresponds to the liquid holdup in the slug only on the transition boundary to annular flow, and is not valid fully developed slug flow, away from the transition boundary. The Green point in Figure B.6 represents the final transition boundary given by

$$H_L \geq 0.24 \qquad or \qquad \widetilde{\delta_l} \geq 0.65 \tag{B.16}$$

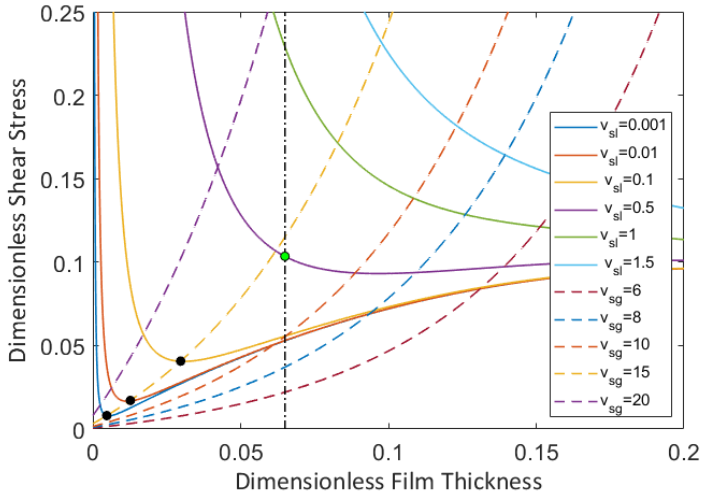

Figure B.6. Solution for liquid blockage of the core due to wave growth

In Figure B.6, combined criterion is shown, the minimum points (black) corresponding to the instability criteria and the criteria of wave growth and pipe blockage (green point) representing the existence of annular flow.

B.2 Gray correlation

The correlation is normally used to determine the pressure in a well at different depths when producing gas and liquids. Pressure gradient is determined as the sum of the pressure gradient originating from gravity, friction and acceleration Equation B.17 to Equation B.17 respectively,

$$\left(\frac{dp}{dx}\right)_G = \frac{g}{144g_c}(\alpha\rho_g + (1-\alpha)\rho_l) = \frac{g}{144g_c}\overline{\rho} \tag{B.17}$$

$$\left(\frac{dp}{dx}\right)_F = \frac{2f\rho_{NS}v_m^2}{144g_cD} \tag{B.18}$$

$$\left(\frac{dp}{dx}\right)_A = \rho_{NS}v_m\frac{dv_m}{dx} \tag{B.19}$$

Where α is the empirical in-situ volume fraction of gas, $\overline{\rho}$ is average density, ρ_{NS} is the no-slip density.

The acceleration term is usually neglected during the calculation. In Gray correlation liquid densities were taken to be independent of pressure and temperature. Another important assumption is that there is no solution condensate in the gas, meaning that all the condensate rate measured at the surface is constant. The in-situ volume fraction of gas (α) is calculated using the following equation

$$\alpha = \frac{1 - exp\left\{-2.314\left[N_V\left(1+\frac{205}{N_B}\right)\right]^B\right\}}{R+1} \tag{B.20}$$

Where: N_V, N_B, B and R are dimensionless parameters found from dimensionless analysis and laboratory tests.

The correlation is untested by the author for:

1. Flow velocities > 50 ft/sec;
2. Tubing size > 3.5 inches nominal, tested only for tubing ID 1.049 - 2.992 in
3. Condensate ratios > 50 bbl/MMcf;
4. Water ratios > 5 bbl/MMcf;

Gravity force
To determine the gravity force, the in-situ volume faction of gas α should be calculated. For this, four parameters were presented as mainly influence on the holdup in condensate wells:

$$N_V = \frac{\rho_{NS}^2V_m^4}{g\sigma(\rho_l - \rho_g)} \tag{B.21}$$

$$N_B = \frac{gD^2(\rho_l - \rho_g)}{\sigma} \tag{B.22}$$

$$R = \frac{v_{sl}}{v_{sg}} \tag{B.23}$$

$$B = 0.0814\left[1 - 0.0554ln\left\{1+\frac{730R}{R+1}\right\}\right] \tag{B.24}$$

In determining the above parameters the surface tension is required, approximation where then developed.Turner et al. (1969)

$$\sigma_c = 0.044 - 1.3 \times 10^{-4}(T - 460)\left(\frac{p_d - p}{p_d - 2120}\right)^{2.5} \tag{B.25}$$

$$\sigma_w = (2.115 - 0.119lnp)\left[0.174 - 2.09 \times 10^{-}4(t - 460)\right] \tag{B.26}$$

$$\sigma_m = \frac{q_c\sigma_c + 0.617q_w\sigma_w}{q_c + 0.617q_w} \tag{B.27}$$

Frictional force

The Gray correlation assumes that the effective roughness of the pipe *(r)* is dependent on the value of R. The conditions are as follow:

$$r = \begin{cases} r' = 28.5\dfrac{\tau}{\rho_m V_m^2} & R \geq 0.007 \\ r_g + R\dfrac{r' - r_g}{0.007} & R < 0.007 \end{cases}$$

The effective roughness must be larger than or equal to 2.77 $\times 10^{-5}$, where r_g is the dry hydraulic tubing roughness and Reynold's number is assumed to be 10^7. (Oudeman, 2007; Turner et al., 1969)

Note: The original publication contains a misprint (0.0007 instead of 0.007). Also, the surface tension is given in units of lb_f/s^2.

The friction factor can be determined using standing correlation. The no-slip density is then determined:

$$\rho_{NS} = \rho_l C_l + (1 - C_l)\rho_g \tag{B.28}$$

$$C_l = \frac{v_{sl}}{v_{sl} + v_{sg}} \tag{B.29}$$

B.3 New model proposed

In Section 2.2.2 was mentioned that Paz (1994) performed experimental investigation on two-phase annular flow on the effect of inclination angle on the liquid film thickness distribution the circumferential of the pipe. Figures B.7 to Figure B.11 show the fitting of the Paz (1994) measured data on the estimation of liquid area.

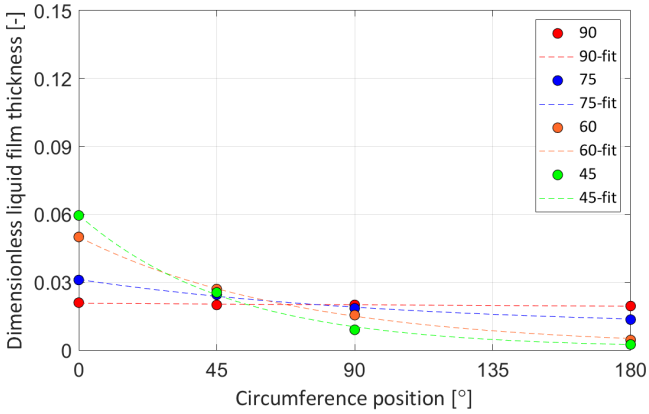

Figure B.7. Fitting Paz (1994) data (v_{sl}=0.012 m/s and v_{sg}=18.29 m/s)

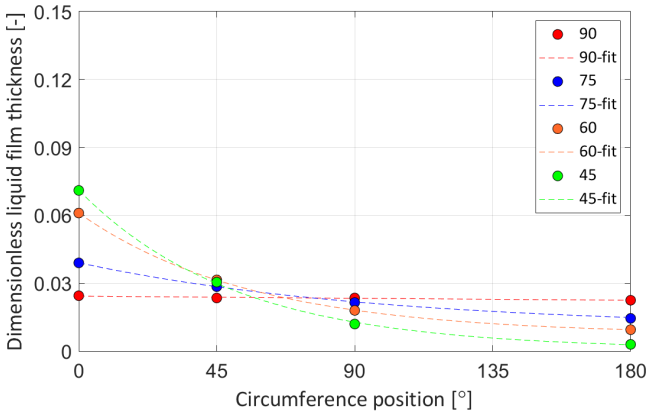

Figure B.8. Fitting Paz (1994) data (v_{sl}=0.024 m/s and v_{sg}=18.29 m/s)

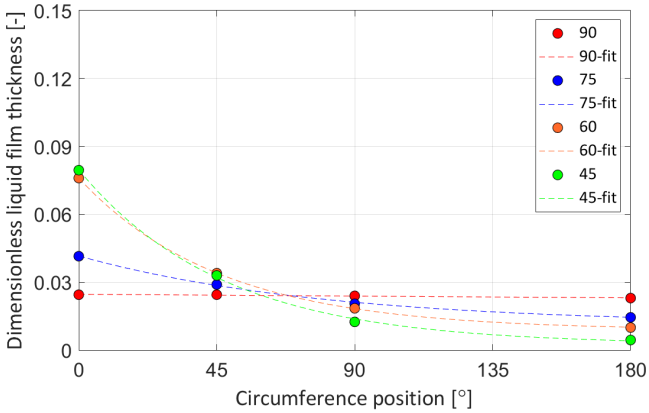

Figure B.9. Fitting Paz (1994) data (v_{sl}=0.031 m/s and v_{sg}=18.29 m/s)

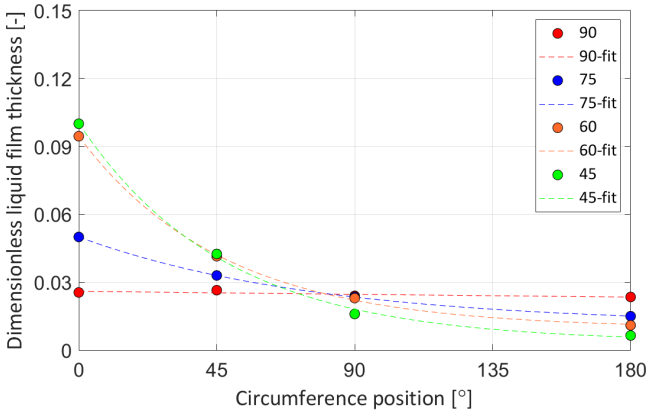

Figure B.10. Fitting Paz (1994) data (v_{sl}=0.046 m/s and v_{sg}=18.29 m/s)

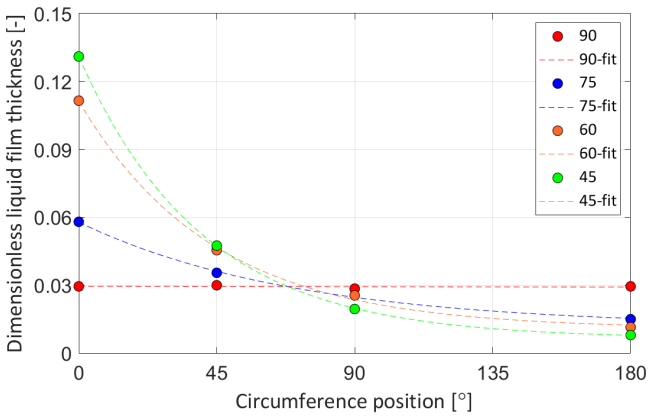

Figure B.11. Fitting Paz (1994) data (v_{sl}=0.061 m/s and v_{sg}=18.29 m/s)

B.4 Results

The models described on Section 2.2 were implemented using Matlab R2018a and run for the acquired data sets given in the measured results (Section 3.6). For each test case, the models were run to compute the annular-intermittent flow transition and critical gas velocity on the liquid loading onset.

Computations were further treated statistically. Experimental and calculated data were compared point by point. For each data point, an absolute error was determined according to:

$$err_{abs,X} = \left| \frac{X_{calc} - X_{meas}}{X_{meas}} \right| \tag{B.30}$$

where X stands for a physical variable critical gas velocity, X_{calc} is the model prediction value and X_{meas} is the experimental (measured) value.

Then a relative percent error was determined by

$$err_{rel,X} = \frac{100}{n} \sum_{1}^{n} err_{abs,i} \tag{B.31}$$

n is the number of data points in the data set considered.

B.4.1 Summary of the relative error presented in Section 4.2 and 4.3

Table B.1. Relative error summary for air-water system presented in Figure 4.5

	Pipe inclination					
Model	20°	30°	45°	60°	70°	78°
Barnea (1986)	11.66	22.49	10.25	10.43	17.69	23.79
Luo et al. (2014)	75.32	38.98	62.10	75.86	63.66	50.30
Shekhar et al. (2017)	42.54	11.11	20.88	23.13	21.40	15.42
Turner et al. (1969)	16.08	27.02	26.86	26.47	22.26	20.97
Belfroid et al. (2008)	11.28	25.32	18.51	17.89	16.80	20.88
OLGA	22.81	16.48	22.80	36.02	84.51	113.87

Table B.2. Relative error summary for air-Exxsol D80 system presented in Figure 4.8

	Pipe inclination		
Model	30°	45°	60°
Barnea (1986)	24.98	16.00	19.86
Luo et al. (2014)	37.90	45.93	87.54
Shekhar et al. (2017)	8.09	8.77	31.24
Turner et al. (1969)	38.70	45.53	34.23
Belfroid et al. (2008)	37.28	39.31	26.56
OLGA	16.88	35.51	42.44

Table B.3. Relative error summary for air-water system presented in Figure 4.13

	Pipe inclination					
Model	20°	30°	45°	60°	70°	78°
Barnea (1986)	10.26	21.21	8.26	6.88	15.04	20.71
Luo et al. (2014)	72.00	35.57	55.28	66.31	57.95	47.04
Shekhar et al. (2017)	39.69	7.64	17.79	19.67	18.92	10.56

Table B.4. Relative error summary for air-Exxsol D80 system presented in Figure 4.14

	Pipe inclination		
Model	30°	45°	60°
Barnea (1986)	22.91	18.77	18.25
Luo et al. (2014)	34.28	34.46	71.60
Shekhar et al. (2017)	5.67	3.47	23.72

Appendix C

Measured experimental data

In this appendix the acquired experimental data is presented, as well as the differential pressure transmitter signal showing their behaviour when different flow pattern was present in the test section.

C.1 Differential pressure transmitter and capacitance probes signal

In this section, differential pressure transmitter and capacitance probes signal for a given gas and liquid velocity and pipe inclination will be presented aiming to show how the pressure gradient behaviour changes according to the flow pattern.

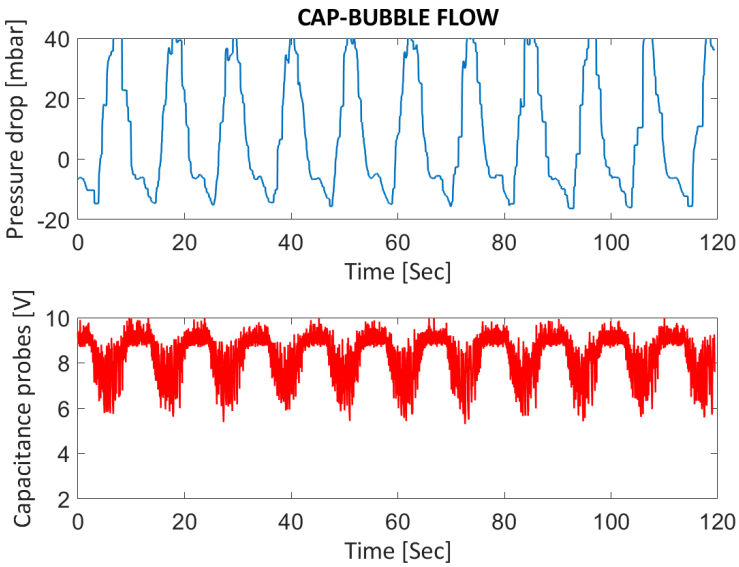

Figure C.1. Differential pressure transmitter and capacitance probes signal for v_{sl}=1 m/s, v_{sg}=0.57 m/s, $\theta = 60°$, showing Cap-bubble flow

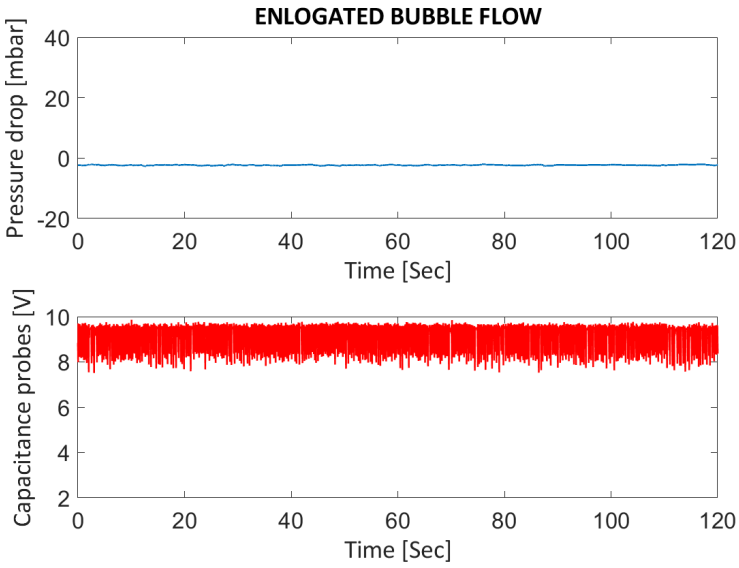

Figure C.2. Differential pressure transmitter and capacitance probes signal for v_{sl}=0.6 m/s, v_{sg}=0.58 m/s, $\theta = 20°$, showing Elongated-bubble flow

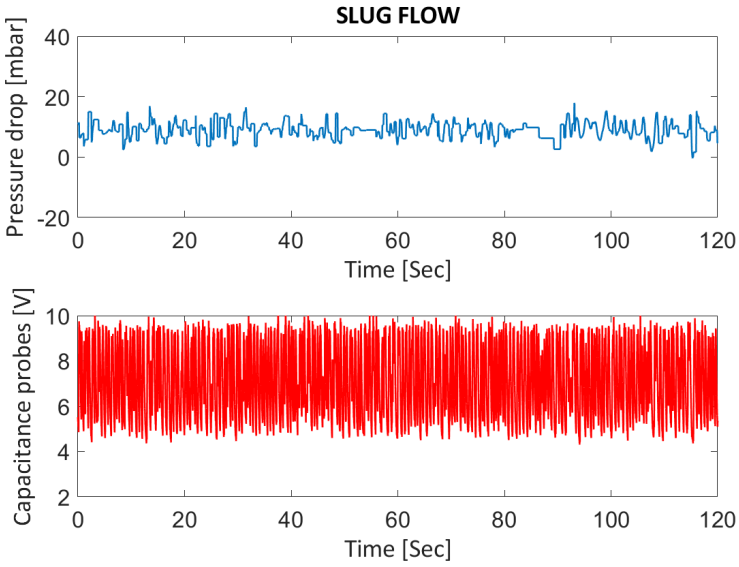

Figure C.3. Differential pressure transmitter and capacitance probes signal for v_{sl}=0.6 m/s, v_{sg}=1.07 m/s, $\theta = 20°$, showing Slug flow

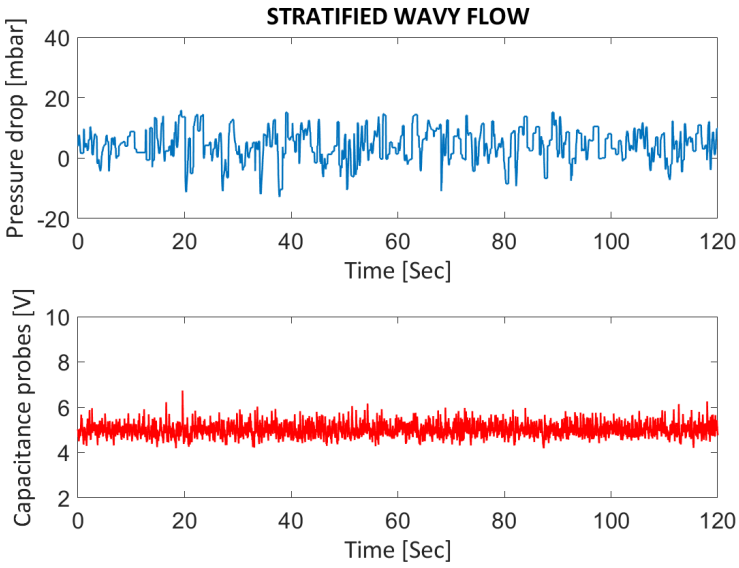

Figure C.4. Differential pressure transmitter and capacitance probes signal for v_{sl}=0.6 m/s, v_{sg}=17.72 m/s, $\theta = 20°$, showing Stratified-Wavy flow

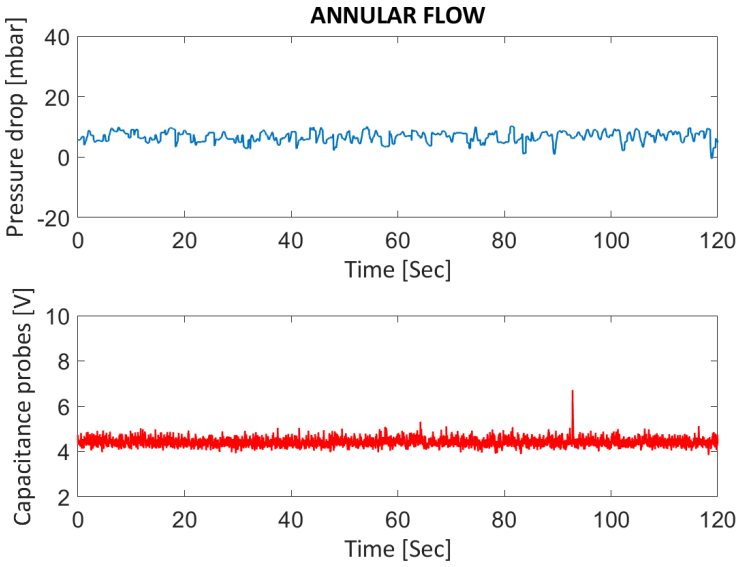

Figure C.5. Differential pressure transmitter and capacitance probes signal for v_{sl}=0.6 m/s, v_{sg}=31.68 m/s, $\theta = 20°$, showing Annular flow

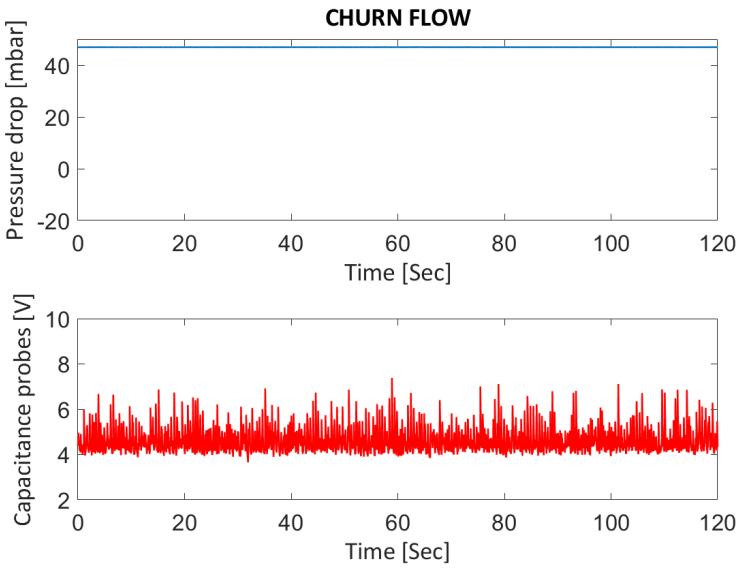

Figure C.6. Differential pressure transmitter and capacitance probes signal for v_{sl}=0.6 m/s, v_{sg}=12.22 m/s, $\theta = 70°$, showing Churn flow

C.2 Tabulated measured data

This appendix contains the following tabulated data:

- Inclination angle measured from horizontal;
- Superficial velocity of gas and liquid
- Temperature under which the experiment were performed;
- Measured pressure measure during experiment;
- Estimated liquid holdup;
- Identified flow regime.

The data were measured for air-water, air-Exxsol D80 and air-Mixed oil two-phase flow system.

In addition the appendix show the behaviour of the pressure gradient changes with inclinations and flow regime present in the test section.

C.2.1 Air-water system

Table C.1. Experimental data for air-mixed system in 60 mm inner diameter acrylic pipe

Exp	θ	$\mathbf{v}_{sg}$	$\mathbf{v}_{sl}$	**T**	**dp/dx**	$\mathbf{H}_L$	**FR**	**Exp**	θ	$\mathbf{v}_{sg}$	$\mathbf{v}_{sl}$	**T**	**dp/dx**	$\mathbf{H}_L$	**FR**
#	° FH	m/s	m/s	°C	Pa/m	[-]	[-]	#	° FH	m/s	m/s	°C	Pa/m	[-]	[-]
1	20	41.93	0.02	21.91	1010	0.012	AN	27	20	19.09	0.1	19.18	733	0.065	OLL
2	20	29.51	0.02	21.91	555	0.015	AN	28	20	14.01	0.1	22.54	747	0.094	SL
3	20	20.73	0.02	21.90	331	0.019	AN	29	20	10.93	0.1	19.20	784	0.105	SL
4	20	13.94	0.02	21.87	381	0.055	OLL	30	20	7.48	0.1	22.52	847	0.127	SL
5	20	7.50	0.02	21.84	548	0.080	SL	31	20	5.68	0.1	22.58	893	0.177	SL
6	20	5.66	0.02	21.78	555	0.080	SL	32	20	4.20	0.1	22.61	967	0.216	SL
7	20	4.13	0.02	21.77	577	0.094	SL	33	30	57.76	0.01	19.04	1464	0.011	AN
8	20	61.53	0.06	18.67	2470	0.011	AN	34	30	50.82	0.01	19.03	1172	0.011	AN
9	20	53.37	0.06	18.65	1998	0.012	AN	35	30	44.00	0.01	19.04	900	0.011	AN
10	20	47.96	0.06	18.61	1725	0.012	AN	36	30	36.26	0.01	19.05	645	0.012	AN
11	20	42.84	0.06	22.59	1399	0.017	AN	37	30	33.10	0.01	19.06	523	0.012	AN
12	20	36.09	0.06	18.64	1129	0.018	AN	38	30	29.92	0.01	19.09	439	0.012	AN
13	20	30.35	0.06	18.63	793	0.024	AN	39	30	27.06	0.01	19.08	361	0.012	AN
14	20	28.39	0.06	22.57	699	0.024	AN	40	30	23.69	0.01	19.13	291	0.013	AN
15	20	21.07	0.06	22.53	501	0.035	AN	41	30	21.57	0.01	19.12	254	0.013	AN
16	20	14.54	0.06	22.54	527	0.071	OLL	42	30	19.47	0.01	19.11	224	0.014	OLL
17	20	7.63	0.05	22.48	656	0.106	SL	43	30	16.99	0.01	19.07	294	0.022	SL
18	20	5.63	0.05	22.49	692	0.123	SL	44	30	13.88	0.01	19.12	528	0.047	SL
19	20	4.13	0.05	22.51	735	0.131	SL	45	30	10.77	0.01	19.09	571	0.057	SL
20	20	57.12	0.1	18.99	2710	0.012	AN	46	30	55.60	0.02	19.15	1616	0.011	AN
21	20	48.98	0.1	19.01	2230	0.014	AN	47	30	48.96	0.02	19.16	1348	0.011	AN
22	20	43.98	0.1	19.07	1883	0.016	AN	48	30	41.38	0.02	19.14	1043	0.012	AN
23	20	37.22	0.1	19.10	1443	0.022	AN	49	30	33.74	0.02	19.14	726	0.013	AN
24	20	28.35	0.1	19.14	975	0.036	AN	50	30	29.16	0.02	19.17	569	0.015	AN
25	20	23.95	0.1	19.17	872	0.048	AN	51	30	25.34	0.02	19.18	463	0.017	AN
26	20	21.44	0.1	22.56	782	0.060	AN	52	30	22.40	0.02	19.17	414	0.020	OLL

continued on next page

Table C.1. *(cont.)* Experimental data for air-water system in 60 mm inner diameter acrylic pipe

Exp	θ	v_{sg}	v_{sl}	**T**	**dp/dx**	$\mathbf{H}_L$	**FR**	**Exp**	θ	v_{sg}	v_{sl}	**T**	**dp/dx**	$\mathbf{H}_L$	**FR**
#	° FH	m/s	m/s	°C	Pa/m	[-]	[-]	#	° FH	m/s	m/s	°C	Pa/m	[-]	[-]
53	30	18.85	0.02	19.18	452	0.032	SL	80	30	29.65	0.2	19.17	1151	0.041	AN
54	30	14.87	0.02	19.21	643	0.052	SL	81	30	25.63	0.2	19.14	1088	0.058	OLL
55	30	7.31	0.02	19.21	642	0.086	SL	82	30	23.40	0.2	19.16	1132	0.069	SL
56	30	44.08	0.05	24.09	1522	0.013	AN	83	30	21.56	0.2	19.11	1125	0.074	SL
57	30	38.98	0.05	24.08	1253	0.014	AN	84	30	20.80	0.2	19.12	1173	0.079	SL
58	30	33.64	0.05	24.05	977	0.017	AN	85	30	20.07	0.2	19.12	1249	0.078	SL
59	30	28.97	0.05	24.05	751	0.020	AN	86	30	18.60	0.2	19.16	1199	0.088	SL
60	30	25.24	0.05	24.03	617	0.025	AN	87	30	16.67	0.2	19.16	1201	0.093	SL
61	30	23.32	0.05	24.05	582	0.028	OLL	88	30	13.81	0.2	19.14	1188	0.105	SL
62	30	21.68	0.05	24.15	583	0.032	SL	89	30	7.93	0.2	19.16	1202	0.128	SL
63	30	19.24	0.05	24.14	618	0.040	SL	90	45	57.71	0.01	19.58	1731	0.011	AN
64	30	17.20	0.05	24.10	691	0.054	SL	91	45	50.52	0.01	19.58	1440	0.011	AN
65	30	14.02	0.05	24.12	768	0.064	SL	92	45	43.93	0.01	19.64	1220	0.012	AN
66	30	58.77	0.1	19.23	2700	0.023	AN	93	45	37.43	0.01	19.63	1019	0.012	AN
67	30	51.70	0.1	19.23	2500	0.025	AN	94	45	31.71	0.01	19.68	814	0.013	AN
68	30	43.93	0.1	19.22	1920	0.027	AN	95	45	27.83	0.01	19.69	701	0.013	AN
69	30	37.24	0.1	19.21	1547	0.033	AN	96	45	25.69	0.01	19.68	643	0.013	AN
70	30	30.08	0.1	19.24	1034	0.040	AN	97	45	24.37	0.01	19.66	615	0.014	AN
71	30	25.32	0.1	19.24	854	0.051	OLL	98	45	23.43	0.01	19.68	588	0.014	AN
72	30	21.78	0.1	19.21	900	0.071	SL	99	45	20.97	0.01	19.69	561	0.015	AN
73	30	19.80	0.1	19.22	973	0.075	SL	100	45	19.80	0.01	19.70	557	0.017	OLL
74	30	16.16	0.1	19.20	985	0.089	SL	101	45	16.73	0.01	19.71	811	0.029	SL
75	30	8.50	0.1	19.21	1079	0.115	SL	102	45	15.22	0.01	19.73	922	0.041	SL
76	30	50.69	0.2	19.17	2787	0.017	AN	103	45	51.22	0.02	20.06	1654	0.011	AN
77	30	43.30	0.2	19.14	2094	0.022	AN	104	45	41.81	0.02	20.07	1318	0.012	AN
78	30	37.46	0.2	19.04	1699	0.028	AN	105	45	37.21	0.02	20.06	1165	0.013	AN
79	30	33.05	0.2	19.10	1374	0.036	AN	106	45	32.24	0.02	20.09	970	0.014	AN

continued on next page

Table C.1. *(cont.)* Experimental data for air-water system in 60 mm inner diameter acrylic pipe

Exp	θ	v_{sg}	v_{sl}	**T**	**dp/dx**	$\mathbf{H}_L$	**FR**	**Exp**	θ	v_{sg}	v_{sl}	**T**	**dp/dx**	$\mathbf{H}_L$	**FR**
#	° FH	m/s	m/s	°C	Pa/m	[-]	[-]	#	° FH	m/s	m/s	°C	Pa/m	[-]	[-]
107	45	28.07	0.02	20.10	841	0.016	AN	134	45	10.70	0.05	19.81	1260	0.077	SL
108	45	26.06	0.02	20.17	775	0.016	AN	135	45	50.02	0.1	20.21	2469	0.013	AN
109	45	24.63	0.02	20.19	729	0.017	AN	136	45	44.32	0.1	20.17	2294	0.016	AN
110	45	23.73	0.02	20.19	721	0.018	AN	137	45	40.96	0.10	20.19	2172	0.017	AN
111	45	21.46	0.02	20.25	713	0.022	OLL	138	45	37.74	0.10	20.18	1937	0.021	AN
112	45	20.36	0.02	20.25	747	0.026	SL	139	45	35.18	0.10	20.19	1735	0.023	AN
113	45	18.66	0.02	20.27	888	0.036	SL	140	45	33.18	0.10	20.20	1585	0.025	AN
114	45	17.31	0.02	20.27	964	0.042	SL	141	45	31.39	0.10	20.20	1445	0.027	AN
115	45	16.65	0.02	20.27	983	0.041	SL	142	45	29.39	0.10	20.21	1335	0.030	AN
116	45	12.02	0.02	20.29	1109	0.052	AN	143	45	28.17	0.10	20.23	1243	0.033	AN
117	45	6.75	0.02	20.28	1143	0.063	AN	144	45	26.95	0.10	20.24	1235	0.038	AN
118	45	49.69	0.05	19.88	2105	0.014	AN	145	45	24.76	0.10	20.26	1188	0.045	OLL
119	45	44.83	0.05	19.91	1970	0.016	AN	146	45	23.66	0.10	20.28	1278	0.051	SL
120	45	41.69	0.05	19.86	1832	0.016	AN	147	45	22.25	0.10	20.16	1375	0.057	SL
121	45	37.63	0.05	19.86	1619	0.019	AN	148	45	21.26	0.10	20.11	1404	0.062	SL
122	45	34.76	0.05	19.84	1420	0.021	AN	149	45	19.94	0.10	20.14	1370	0.062	SL
123	45	32.82	0.05	19.88	1331	0.022	AN	150	45	16.54	0.10	20.13	1432	0.070	SL
124	45	29.49	0.05	19.90	1173	0.025	AN	151	45	12.92	0.10	20.15	1549	0.077	SL
125	45	26.88	0.05	19.89	1025	0.030	AN	152	45	6.74	0.10	20.09	1610	0.097	SL
126	45	25.19	0.05	23.06	965	0.026	OLL	153	45	50.49	0.20	20.06	3048	0.009	AN
127	45	24.27	0.05	19.91	1029	0.039	SL	154	45	42.97	0.20	20.09	2560	0.015	AN
128	45	23.11	0.05	19.90	1118	0.043	SL	155	45	37.52	0.20	20.13	2312	0.024	AN
129	45	22.08	0.05	19.96	1172	0.047	SL	156	45	32.69	0.20	20.09	1803	0.031	AN
130	45	20.89	0.05	19.93	1229	0.055	SL	157	45	29.33	0.20	20.05	1597	0.039	SL
131	45	18.35	0.05	19.90	1230	0.059	SL	158	45	27.10	0.20	20.10	1599	0.049	SL
132	45	17.00	0.05	19.87	1251	0.064	SL	159	45	26.07	0.20	20.12	1519	0.052	SL
133	45	14.88	0.05	19.84	1246	0.069	SL	160	45	24.69	0.20	20.13	1477	0.053	OLL

continued on next page

Table C.1. *(cont.)* Experimental data for air-water system in 60 mm inner diameter acrylic pipe

Exp	θ	v_{sg}	v_{sl}	**T**	**dp/dx**	$\mathbf{H}_L$	**FR**	**Exp**	θ	v_{sg}	v_{sl}	**T**	**dp/dx**	$\mathbf{H}_L$	**FR**
#	° FH	m/s	m/s	°C	Pa/m	[-]	[-]	#	° FH	m/s	m/s	°C	Pa/m	[-]	[-]
161	45	23.40	0.20	20.14	1568	0.064	SL	188	60	24.48	0.02	19.88	535	0.018	AN
162	45	21.87	0.20	20.11	1650	0.069	SL	189	60	22.58	0.02	19.83	507	0.020	AN
163	45	20.71	0.20	20.09	1673	0.074	SL	190	60	21.72	0.02	19.84	496	0.021	OLL
164	45	19.46	0.20	20.07	1653	0.076	SL	191	60	20.72	0.02	19.82	503	0.023	SL
165	45	16.82	0.2	20.11	1724	0.082	SL	192	60	19.26	0.02	19.86	632	0.031	SL
166	45	14.69	0.2	20.12	1683	0.087	SL	193	60	17.87	0.02	19.86	740	0.033	SL
167	45	10.72	0.2	20.12	1934	0.100	SL	194	60	15.73	0.02	19.84	871	0.040	SL
168	60	49.59	0.01	19.83	1176	0.011	AN	195	60	12.65	0.02	19.82	1006	0.041	SL
169	60	41.55	0.01	19.85	930	0.012	AN	196	60	6.63	0.02	19.82	1297	0.058	SL
170	60	37.13	0.01	19.85	793	0.012	AN	197	60	55.41	0.05	20.19	2057	0.011	AN
171	60	30.87	0.01	19.87	594	0.013	AN	198	60	48.99	0.05	20.20	1766	0.012	AN
172	60	27.80	0.01	19.88	509	0.014	AN	199	60	42.69	0.05	20.19	1558	0.013	AN
173	60	25.00	0.01	19.88	432	0.014	AN	200	60	36.73	0.05	20.16	1288	0.015	AN
174	60	23.41	0.01	19.91	396	0.014	AN	201	60	30.50	0.05	20.16	993	0.019	AN
175	60	21.40	0.01	19.97	365	0.015	AN	202	60	27.09	0.05	20.16	841	0.022	AN
176	60	20.20	0.01	20.02	356	0.016	AN	203	60	23.70	0.05	20.20	763	0.032	OLL
177	60	19.48	0.01	20.02	356	0.017	OLL	204	60	22.54	0.05	20.23	886	0.040	SL
178	60	18.72	0.01	20.02	372	0.019	SL	205	60	21.68	0.05	20.21	971	0.046	SL
179	60	16.39	0.01	20.02	614	0.017	SL	206	60	18.93	0.05	20.25	1057	0.052	SL
180	60	12.03	0.01	20.04	953	0.034	SL	207	60	17.41	0.05	20.26	1100	0.056	SL
181	60	7.70	0.01	20.00	1111	0.039	SL	208	60	15.83	0.05	20.24	1142	0.061	SL
182	60	56.05	0.02	19.91	1592	0.011	AN	209	60	14.77	0.05	20.25	1161	0.060	SL
183	60	45.71	0.02	19.92	1204	0.012	AN	210	60	10.01	0.05	20.24	1330	0.069	SL
184	60	41.05	0.02	19.87	1056	0.012	AN	211	60	50.81	0.1	19.94	2620	0.013	AN
185	60	35.73	0.02	19.86	889	0.013	AN	212	60	44.19	0.1	19.98	2309	0.016	AN
186	60	30.50	0.02	19.89	721	0.015	AN	213	60	37.64	0.1	19.98	2066	0.022	AN
187	60	28.25	0.02	19.89	642	0.016	AN	214	60	35.22	0.1	20.00	1873	0.025	AN

continued on next page

Table C.1. *(cont.)* Experimental data for air-water system in 60 mm inner diameter acrylic pipe

Exp	θ	v_{sg}	v_{sl}	**T**	**dp/dx**	$\mathbf{H}_L$	**FR**	**Exp**	θ	v_{sg}	v_{sl}	**T**	**dp/dx**	$\mathbf{H}_L$	**FR**
#	° FH	m/s	m/s	°C	Pa/m	[-]	[-]	#	° FH	m/s	m/s	°C	Pa/m	[-]	[-]
215	60	32.89	0.1	19.96	1616	0.028	AN	242	70	33.04	0.01	20.94	830	0.013	AN
216	60	30.07	0.1	19.96	1409	0.030	AN	243	70	27.10	0.01	20.95	662	0.014	AN
217	60	28.90	0.1	19.96	1336	0.033	AN	244	70	23.76	0.01	20.97	553	0.014	AN
218	60	25.57	0.1	19.93	1214	0.047	OLL	245	70	21.12	0.01	20.94	536	0.016	AN
219	60	23.99	0.1	19.90	1275	0.055	SL	246	70	19.77	0.01	20.98	526	0.017	AN
220	60	23.15	0.1	19.87	1389	0.057	SL	247	70	18.11	0.01	20.97	528	0.020	OLL
221	60	20.86	0.1	19.89	1503	0.064	SL	248	70	16.88	0.01	20.99	621	0.025	SL
222	60	18.57	0.1	19.88	1573	0.075	SL	249	70	15.30	0.01	21.00	823	0.022	SL
223	60	15.81	0.1	19.90	1591	0.078	SL	250	70	10.87	0.01	20.99	1157	0.033	SL
224	60	9.11	0.1	19.94	1744	0.095	SL	251	70	5.51	0.01	20.99	1701	0.060	SL
225	60	51.42	0.2	20.22	3150	0.014	AN	252	70	56.60	0.02	20.60	1756	0.011	AN
226	60	42.56	0.2	20.19	2665	0.021	AN	253	70	49.37	0.02	20.60	1471	0.012	AN
227	60	36.32	0.2	20.18	2160	0.030	AN	254	70	43.60	0.02	20.63	1297	0.012	AN
228	60	29.64	0.2	20.18	1627	0.041	AN	255	70	37.41	0.02	20.58	1110	0.013	AN
229	60	25.77	0.2	20.17	1502	0.057	AN	256	70	34.11	0.02	20.60	1002	0.014	AN
230	60	24.86	0.2	20.19	1494	0.061	OLL	257	70	26.39	0.02	20.58	739	0.017	AN
231	60	23.27	0.2	20.19	1691	0.067	SL	258	70	23.60	0.02	20.57	677	0.019	AN
232	60	21.92	0.2	20.20	1737	0.072	SL	259	70	22.33	0.02	20.61	661	0.021	AN
233	60	21.27	0.2	20.25	1737	0.074	SL	260	70	21.32	0.02	20.60	643	0.022	AN
234	60	18.76	0.2	20.25	1805	0.086	SL	261	70	20.03	0.02	20.64	641	0.025	OLL
235	60	15.69	0.2	20.25	1806	0.091	SL	262	70	18.32	0.02	20.65	765	0.036	SL
236	60	12.15	0.2	20.26	1879	0.094	SL	263	70	16.22	0.02	20.69	938	0.036	SL
237	60	7.35	0.2	20.28	2051	0.115	SL	264	70	13.20	0.02	20.68	1089	0.044	SL
238	70	57.13	0.01	20.94	1651	0.011	AN	265	70	8.73	0.02	20.68	1477	0.066	SL
239	70	49.26	0.01	20.94	1338	0.011	AN	266	70	56.78	0.05	20.06	2343	0.011	AN
240	70	41.17	0.01	20.92	1076	0.012	AN	267	70	47.33	0.05	22.84	1964	0.012	AN
241	70	35.74	0.01	20.96	918	0.012	AN	268	70	41.03	0.05	22.82	1766	0.013	AN

continued on next page

Table C.1. *(cont.)* Experimental data for air-water system in 60 mm inner diameter acrylic pipe

Exp	θ	v_{sg}	v_{sl}	**T**	**dp/dx**	$\mathbf{H}_L$	**FR**	**Exp**	θ	v_{sg}	v_{sl}	**T**	**dp/dx**	$\mathbf{H}_L$	**FR**
#	° FH	m/s	m/s	°C	Pa/m	[-]	[-]	#	° FH	m/s	m/s	°C	Pa/m	[-]	[-]
269	70	36.41	0.05	22.79	1553	0.015	AN	296	70	37.08	0.2	20.64	2433	0.025	AN
270	70	29.42	0.05	22.82	1205	0.018	AN	297	70	32.88	0.2	20.70	1969	0.030	AN
271	70	28.34	0.05	22.04	1077	0.022	AN	298	70	28.74	0.2	20.69	1730	0.038	AN
272	70	24.18	0.05	22.40	920	0.025	OLL	299	70	23.72	0.2	20.72	1650	0.063	OLL
273	70	23.17	0.05	22.85	963	0.027	SL	300	70	22.08	0.2	20.66	1770	0.069	SL
274	70	22.60	0.05	22.32	1005	0.033	SL	301	70	19.71	0.2	20.69	1879	0.078	SL
275	70	20.89	0.05	22.81	1173	0.041	SL	302	70	17.83	0.20	20.64	1936	0.086	SL
276	70	19.76	0.05	22.81	1216	0.044	SL	303	70	16.05	0.20	20.62	2015	0.096	SL
277	70	17.97	0.05	22.79	1296	0.045	SL	304	70	12.33	0.20	20.58	2044	0.105	SL
278	70	16.16	0.05	22.81	1355	0.052	SL	305	70	4.43	0.20	20.64	2457	0.158	SL
279	70	13.17	0.05	22.77	1451	0.060	SL	306	78	45.47	0.01	22.60	1085	0.012	AN
280	70	10.86	0.05	22.75	1583	0.065	SL	307	78	39.17	0.01	22.58	886	0.012	AN
281	70	7.60	0.05	22.73	1801	0.081	SL	308	78	32.80	0.01	22.59	697	0.012	AN
282	70	57.12	0.1	20.33	2952	0.012	AN	309	78	29.45	0.01	22.66	591	0.013	AN
283	70	50.58	0.1	20.34	2607	0.013	AN	310	78	25.14	0.01	22.67	480	0.014	AN
284	70	43.42	0.1	20.32	2353	0.016	AN	311	78	22.80	0.01	22.58	438	0.014	AN
285	70	36.34	0.1	20.36	1978	0.021	AN	312	78	21.05	0.01	22.56	416	0.015	AN
286	70	28.11	0.1	20.36	1369	0.030	AN	313	78	18.78	0.01	22.59	376	0.017	AN
287	70	23.47	0.1	20.32	1283	0.051	OLL	314	78	16.45	0.01	22.58	363	0.019	OLL
288	70	21.60	0.1	20.28	1539	0.062	SL	315	78	15.47	0.01	22.64	372	0.021	SL
289	70	19.12	0.1	20.32	1615	0.069	SL	316	78	14.71	0.01	22.68	405	0.024	SL
290	70	15.65	0.1	20.34	1707	0.085	SL	317	78	11.92	0.01	22.72	687	0.022	SL
291	70	9.09	0.1	20.35	1868	0.105	SL	318	78	9.37	0.01	22.71	1003	0.023	SL
292	70	59.28	0.2	20.72	3634	0.012	AN	319	78	4.67	0.01	22.70	1866	0.068	SL
293	70	53.93	0.2	20.73	3343	0.013	AN	320	78	51.18	0.02	20.97	1356	0.010	AN
294	70	50.11	0.2	20.76	3094	0.014	AN	321	78	45.20	0.02	20.99	1142	0.010	AN
295	70	43.59	0.2	20.70	2688	0.018	AN	322	78	38.52	0.02	20.99	944	0.011	AN

continued on next page

Table C.1. *(cont.)* Experimental data for air-water system in 60 mm inner diameter acrylic pipe

Exp	θ	v_{sg}	v_{sl}	**T**	**dp/dx**	$\mathbf{H}_L$	**FR**	**Exp**	θ	v_{sg}	v_{sl}	**T**	**dp/dx**	$\mathbf{H}_L$	**FR**
#	° FH	m/s	m/s	°C	Pa/m	[-]	[-]	#	° FH	m/s	m/s	°C	Pa/m	[-]	[-]
323	78	32.81	0.02	21.02	776	0.012	AN	350	78	41.68	0.1	21.68	2142	0.014	AN
324	78	26.70	0.02	21.02	592	0.014	AN	351	78	37.75	0.1	21.70	1924	0.017	AN
325	78	24.55	0.02	21.04	534	0.015	AN	352	78	32.21	0.1	21.72	1515	0.020	AN
326	78	23.02	0.02	21.06	518	0.016	AN	353	78	26.13	0.1	21.70	1088	0.025	AN
327	78	21.70	0.02	21.05	506	0.017	AN	354	78	24.40	0.1	21.72	1008	0.028	OLL
328	78	20.32	0.02	20.98	459	0.018	AN	355	78	21.63	0.1	21.73	1076	0.043	SL
329	78	18.97	0.02	20.94	468	0.019	OLL	356	78	20.07	0.1	21.76	1089	0.054	SL
330	78	17.84	0.02	20.96	475	0.022	SL	357	78	19.15	0.1	22.17	1206	0.061	SL
331	78	16.52	0.02	20.97	473	0.026	SL	358	78	17.65	0.1	22.22	1303	0.067	SL
332	78	13.20	0.02	20.98	728	0.029	SL	359	78	16.22	0.1	22.32	1377	0.075	SL
333	78	7.03	0.02	21.00	1465	0.070	SL	360	78	12.06	0.1	22.41	1559	0.104	SL
334	78	2.58	0.02	21.03	2026	0.097	SL	361	78	10.12	0.1	22.44	1653	0.122	SL
335	78	50.41	0.05	20.92	1897	0.010	AN	362	78	6.55	0.1	22.48	1932	0.157	SL
336	78	42.70	0.05	21.07	1630	0.012	AN	363	78	51.33	0.2	22.45	3319	0.012	AN
337	78	37.63	0.05	21.19	1419	0.013	AN	364	78	41.10	0.2	22.40	2780	0.019	AN
338	78	33.24	0.05	21.24	1192	0.015	AN	365	78	37.88	0.2	22.40	2487	0.022	AN
339	78	27.21	0.05	21.24	911	0.019	AN	366	78	31.89	0.2	22.33	1996	0.028	AN
340	78	24.50	0.05	21.25	776	0.021	AN	367	78	27.15	0.2	22.33	1694	0.036	AN
341	78	21.94	0.05	21.25	767	0.027	OLL	368	78	24.49	0.2	22.40	1508	0.044	OLL
342	78	20.61	0.05	21.66	769	0.030	SL	369	78	21.63	0.2	22.40	1611	0.067	SL
343	78	19.23	0.05	21.49	818	0.039	SL	370	78	20.22	0.2	22.50	1711	0.079	SL
344	78	17.97	0.05	21.35	901	0.045	SL	371	78	18.59	0.2	22.50	1807	0.090	SL
345	78	16.50	0.05	21.31	978	0.050	SL	372	78	17.41	0.2	22.50	1882	0.099	SL
346	78	14.74	0.05	21.32	1045	0.058	SL	373	78	13.57	0.2	22.50	1974	0.127	SL
347	78	10.17	0.05	21.29	1349	0.087	SL	374	78	10.83	0.2	22.50	2004	0.143	SL
348	78	7.31	0.05	21.28	1661	0.117	SL	375	78	6.97	0.2	22.50	2256	0.168	SL
349	78	4.86	0.05	21.29	2004	0.118	SL	-	-	-	-	-	-	-	-

C.2.2 Air-Exxsol D80 system

Table C.2. Experimental data for air-Exxsol D80 system in 60 mm inner diameter acrylic pipe

Exp	θ	v_{sg}	v_{sl}	**T**	**dp/dx**	**FR**	**Exp**	θ	v_{sg}	v_{sl}	**T**	**dp/dx**	**FR**
#	° FH	m/s	m/s	°C	Pa/m	[-]	#	° FH	m/s	m/s	°C	Pa/m	[-]
1	30	50.48	0.02	23.91	1445	AN	24	30	20.57	0.05	21.02	447	SL
2	30	43.50	0.02	23.91	1167	AN	25	30	19.13	0.05	21.02	491	SL
3	30	41.22	0.02	23.90	1064	AN	26	30	17.79	0.05	21.05	505	SL
4	30	38.04	0.02	23.88	941	AN	27	30	16.06	0.05	21.06	504	SL
5	30	34.78	0.02	23.93	813	AN	28	30	9.80	0.05	21.06	532	SL
6	30	32.65	0.02	23.93	740	AN	29	30	46.81	0.1	24.64	1509	AN
7	30	29.21	0.02	23.91	610	AN	30	30	44.75	0.1	24.66	1478	AN
8	30	26.90	0.02	23.92	521	AN	31	30	41.72	0.1	24.61	1390	AN
9	30	25.04	0.02	23.94	446	AN	32	30	38.68	0.1	24.56	1247	AN
10	30	23.24	0.02	23.94	403	AN	34	30	31.72	0.1	24.61	910	AN
11	30	21.70	0.02	23.97	374	AN	35	30	28.80	0.1	24.59	760	AN
12	30	20.77	0.02	23.96	362	AN	36	30	26.83	0.1	24.53	665	AN
13	30	19.69	0.02	23.96	357	AN	37	30	24.06	0.1	24.56	530	AN
14	30	18.49	0.02	23.96	370	OLL	38	30	22.43	0.1	24.61	466	OLL
15	30	16.89	0.02	23.97	416	SL	39	30	21.23	0.1	24.61	481	SL
16	30	15.66	0.02	23.94	425	SL	40	30	20.00	0.1	24.59	519	SL
17	30	13.75	0.02	23.64	425	SL	41	30	18.62	0.1	24.53	562	SL
18	30	9.64	0.02	23.97	459	SL	42	30	17.47	0.1	24.60	624	SL
19	30	40.37	0.05	20.99	1159	AN	43	30	15.94	0.1	24.58	710	SL
20	30	33.37	0.05	21.01	851	AN	44	30	14.27	0.1	24.55	691	SL
21	30	27.77	0.05	21.01	628	AN	45	30	10.94	0.1	24.62	704	SL
22	30	24.08	0.05	21.01	485	AN	46	30	38.45	0.2	18.75	1461	AN
23	30	21.93	0.05	21.00	418	OLL	47	30	31.27	0.2	18.80	1028	AN

continued on next page

Table C.2. *(cont.)* Experimental data for air-Exxsol D80 system in 60 mm inner diameter acrylic pipe

Exp	θ	$\mathbf{v}_{sg}$	$\mathbf{v}_{sl}$	**T**	**dp/dx**	**FR**	**Exp**	θ	$\mathbf{v}_{sg}$	$\mathbf{v}_{sl}$	**T**	**dp/dx**	**FR**
#	° FH	m/s	m/s	°C	Pa/m	[-]	#	° FH	m/s	m/s	°C	Pa/m	[-]
48	30	24.27	0.2	18.81	685	AN	75	45	22.45	0.04	18.47	2017	SL
49	30	21.35	0.2	18.81	620	OLL	76	45	21.09	0.04	18.47	2047	SL
50	30	19.27	0.2	18.82	690	SL	77	45	19.65	0.04	18.46	2114	SL
51	30	17.21	0.2	18.84	848	SL	78	45	18.26	0.04	18.45	2127	SL
52	30	15.24	0.2	18.87	888	SL	79	45	16.63	0.04	18.46	2120	SL
53	30	13.49	0.2	18.94	890	SL	80	45	15.16	0.04	18.47	2112	SL
54	30	10.21	0.2	18.97	888	SL	81	45	11.01	0.04	18.41	2165	SL
55	30	8.15	0.2	19.06	941	SL	82	45	7.21	0.04	18.43	2247	SL
56	45	47.19	0.02	18.22	2807	AN	83	45	45.82	0.1	18.85	3041	AN
57	45	38.32	0.02	18.21	2453	AN	84	45	38.75	0.1	18.84	2750	AN
58	45	33.31	0.02	18.26	2228	AN	85	45	33.69	0.1	18.86	2511	AN
59	45	29.39	0.02	18.27	2091	AN	86	45	28.37	0.1	18.84	2287	AN
60	45	25.00	0.02	18.52	1973	AN	87	45	24.30	0.1	18.85	2127	OLL
61	45	21.96	0.02	18.48	1926	OLL	88	45	21.87	0.1	18.82	2162	SL
62	45	19.68	0.02	18.42	1958	SL	89	45	20.26	0.1	18.84	2208	SL
63	45	18.35	0.02	18.36	1980	SL	90	45	18.21	0.1	18.85	2256	SL
64	45	17.21	0.02	18.37	1972	SL	91	45	16.77	0.1	18.88	2230	SL
65	45	15.71	0.02	18.31	1978	SL	92	45	14.52	0.1	18.84	2226	SL
66	45	12.58	0.02	18.34	2071	SL	93	45	11.53	0.1	18.84	2286	SL
67	45	9.39	0.02	18.35	2103	SL	94	45	7.72	0.1	18.77	2332	SL
68	45	5.73	0.02	18.33	2252	SL	95	60	39.38	0.01	19.76	2606	AN
69	45	46.36	0.04	18.37	2881	AN	96	60	35.13	0.01	19.76	2441	AN
70	45	39.99	0.04	18.42	2601	AN	97	60	30.09	0.01	19.74	2259	AN
71	45	35.60	0.04	18.41	2425	AN	98	60	27.67	0.01	19.71	2193	AN
72	45	29.34	0.04	18.46	2162	AN	99	60	24.54	0.01	19.73	2103	AN
73	45	25.84	0.04	18.44	2091	AN	100	60	22.53	0.01	19.74	2050	AN
74	45	24.01	0.04	18.44	2007	OLL	101	60	19.96	0.01	19.75	1990	AN

continued on next page

Table C.2. *(cont.)* Experimental data for air-Exxsol D80 system in 60 mm inner diameter acrylic pipe

Exp	θ	$\mathbf{v}_{sg}$	$\mathbf{v}_{sl}$	**T**	**dp/dx**	**FR**	**Exp**	θ	$\mathbf{v}_{sg}$	$\mathbf{v}_{sl}$	**T**	**dp/dx**	**FR**
#	° FH	m/s	m/s	°C	Pa/m	[-]	#	° FH	m/s	m/s	°C	Pa/m	[-]
102	60	18.68	0.01	19.76	1959	AN	118	60	8.49	0.04	19.81	2430	SL
103	60	16.50	0.01	19.71	1912	AN	119	60	47.74	0.1	19.86	3484	AN
104	60	14.77	0.01	19.71	1865	OLL	120	60	41.64	0.1	19.85	3335	AN
105	60	12.06	0.01	19.71	1872	SL	121	60	37.96	0.1	19.87	3147	AN
106	60	8.49	0.01	19.69	1960	SL	122	60	33.30	0.1	19.88	2829	AN
107	60	47.33	0.04	19.72	3074	AN	123	60	28.05	0.1	19.87	2526	AN
108	60	38.58	0.04	19.73	2785	AN	124	60	25.97	0.1	19.88	2501	AN
109	60	31.27	0.04	19.73	2480	AN	125	60	24.29	0.1	19.87	2447	OLL
110	60	25.14	0.04	19.74	2251	AN	126	60	22.82	0.1	19.89	2530	SL
111	60	23.11	0.04	19.74	2222	AN	127	60	21.77	0.1	19.89	2563	SL
112	60	21.86	0.04	19.75	2216	OLL	128	60	19.57	0.1	19.89	2605	SL
113	60	20.19	0.04	19.76	2263	SL	129	60	17.53	0.1	19.90	2625	SL
114	60	18.72	0.04	19.76	2316	SL	130	60	16.46	0.1	19.92	2661	SL
115	60	16.89	0.04	19.77	2277	SL	131	60	14.59	0.1	19.93	2620	SL
116	60	15.40	0.04	19.78	2331	SL	132	60	9.70	0.1	19.92	2653	SL
117	60	12.48	0.04	19.80	2381	SL							

C.2.3 Air-mixed oil system

Table C.3. Experimental data for air-mixed oil flow in 60 mm inner diameter acrylic pipe

Exp	θ	v_{sg}	v_{sl}	**T**	**dp/dx**	$\mathbf{H_L}$	**FR**	**Exp**	θ	v_{sg}	v_{sl}	**T**	**dp/dx**	$\mathbf{H_L}$	**FR**
#	° FH	m/s	m/s	°C	Pa/m	[-]	[-]	#	° FH	m/s	m/s	°C	Pa/m	[-]	[-]
1	10	0.26	0.03	-	847	0.726	EB	27	10	32.08	0.52	-	2003	0.050	AN
2	10	0.58	0.03	-	639	0.562	EB	28	10	0.26	0.85	-	1762	0.965	EB
3	10	1.08	0.03	-	543	0.439	EB	29	10	0.58	0.85	-	1646	0.858	EB
4	10	2.29	0.03	-	476	0.358	SL	30	10	1.09	0.85	-	1574	0.745	SL
5	10	5.04	0.03	-	390	0.257	SL	31	10	2.32	0.85	-	1537	0.592	SL
6	10	18.44	0.03	-	424	0.098	SW	32	10	5.05	0.84	-	1848	0.446	SL
7	10	26.73	0.02	-	747	0.042	AN	33	10	5.06	0.77	-	1782	0.431	SL
8	10	36.39	0.04	-	967	0.054	AN	34	10	15.13	0.83	-	2427	0.200	SW
9	10	0.13	0.37	-	1454	0.965	EB	35	10	19.42	0.78	-	2357	0.166	SW
10	10	0.26	0.36	-	1317	0.891	EB	36	10	24.90	0.82	-	2650	0.119	SW
11	10	0.58	0.37	-	1135	0.745	EB	37	10	29.77	0.78	-	2688	0.095	AN
12	10	1.09	0.37	-	1026	0.634	EB	38	10	0.13	0.98	-	1868	1.007	EB
13	10	2.32	0.37	-	970	0.495	SL	39	10	0.25	0.98	-	1857	0.984	EB
14	10	5.42	0.37	19.80	1006	0.369	SL	40	10	0.57	0.98	-	1761	0.903	EB
15	10	10.89	0.35	20.53	991	0.173	SL	41	10	1.05	0.98	-	1713	0.793	SL
16	10	15.26	0.34	-	1194	0.150	SW	42	10	2.27	0.98	-	1715	0.635	SL
17	10	19.71	0.39	-	1446	0.119	SW	43	10	5.02	0.96	-	2125	0.492	SL
18	10	25.71	0.37	-	1373	0.060	AN	44	10	10.96	1.03	-	2596	0.252	SL
19	10	30.59	0.35	-	1327	0.038	AN	45	10	15.20	1.00	-	2676	0.210	SW
20	10	0.26	0.63	-	1570	0.944	EB	46	10	19.40	0.95	-	2676	0.171	SW
21	10	0.58	0.63	-	1429	0.815	EB	47	10	24.90	0.90	-	2710	0.131	SW
22	10	1.09	0.64	-	1333	0.696	EB	48	10	28.93	0.94	-	2714	0.112	SW
23	10	2.31	0.64	-	1266	0.557	SL	49	10	34.71	0.89	-	2714	0.092	SW
24	10	5.05	0.62	-	1364	0.418	SL	50	10	40.63	0.87	-	2714	0.061	AN
25	10	19.25	0.59	-	1932	0.161	SW	51	10	0.24	1.33	-	2122	0.997	EB
26	10	24.72	0.56	-	1939	0.105	SW	52	10	0.57	1.33	-	2108	0.943	EB

continued on next page

Table C.3. *(cont.)* Experimental data for air-mixed system in 60 mm inner diameter acrylic pipe

Exp	θ	v_{sg}	v_{sl}	**T**	**dp/dx**	$\mathbf{H_L}$	**FR**	**Exp**	θ	v_{sg}	v_{sl}	**T**	**dp/dx**	$\mathbf{H_L}$	**FR**
#	° FH	m/s	m/s	°C	Pa/m	[-]	[-]	#	° FH	m/s	m/s	°C	Pa/m	[-]	[-]
53	10	1.08	1.33	-	2102	0.849	EB	80	15	0.13	0.43	-	2158	0.979	EB
54	10	2.29	1.32	-	2231	0.705	SL	81	15	0.26	0.43	-	1955	0.908	EB
55	10	5.05	1.30	-	2799	0.544	SL	82	15	0.58	0.44	-	1676	0.772	EB
56	10	11.67	1.26	-	2712	0.256	SL	83	15	1.08	0.45	-	1475	0.657	SL
57	10	15.08	1.19	-	2714	0.225	SL	84	15	2.31	0.45	-	1300	0.508	SL
58	10	19.22	1.17	-	2714	0.194	SW	85	15	5.01	0.44	-	1280	0.368	SL
59	10	24.60	1.13	-	2714	0.161	SW	86	15	7.03	0.42	-	1554	0.271	SL
60	10	28.61	1.10	-	2714	0.153	SW	87	15	12.14	0.42	-	1421	0.191	SL
61	10	34.10	1.06	-	2714	0.147	AN	88	15	17.97	0.41	-	1816	0.164	SW
62	10	40.99	1.03	-	2714	0.061	AN	89	15	24.59	0.39	-	1664	0.108	SW
63	15	0.12	0.05	-	1730	0.892	EB	90	15	32.05	0.37	-	1761	0.061	SW
64	15	0.25	0.05	-	1333	0.736	EB	91	15	35.85	0.36	-	2093	0.046	AN
65	15	0.57	0.05	-	952	0.577	EB	92	15	0.13	0.59	-	2291	0.992	EB
66	15	1.06	0.05	-	796	0.467	SL	93	15	0.25	0.59	-	2141	0.946	EB
67	15	2.27	0.05	-	608	0.353	SL	94	15	0.58	0.60	-	1897	0.819	EB
68	15	5.02	0.05	-	491	0.239	SL	95	15	1.08	0.60	-	1708	0.695	SL
69	15	0.13	0.15	-	1850	0.928	EB	96	15	2.30	0.60	-	1505	0.548	SL
70	15	0.26	0.16	-	1557	0.823	EB	97	15	5.01	0.60	-	1654	0.394	SL
71	15	0.58	0.15	-	1174	0.650	SL	98	15	8.03	0.59	-	1908	0.276	SL
72	15	1.08	0.15	-	1020	0.546	SL	99	15	12.16	0.58	-	1947	0.223	SL
73	15	2.30	0.15	-	847	0.422	SL	100	15	17.75	0.56	-	2316	0.200	SL
74	15	5.02	0.15	-	762	0.299	SL	101	15	24.78	0.54	-	2074	0.139	SW
75	15	8.39	0.16	-	880	0.184	SL	102	15	32.14	0.50	-	2089	0.084	SW
76	15	12.38	0.16	-	860	0.162	SL	103	15	0.13	0.84	-	2468	0.995	EB
77	15	17.91	0.15	-	853	0.110	SW	104	15	0.25	0.85	-	2384	0.968	EB
78	15	24.77	0.14	-	1016	0.075	SW	105	15	0.58	0.85	-	2180	0.873	EB
79	15	32.13	0.12	-	1332	0.044	AN	106	15	1.08	0.85	-	2031	0.752	SL

continued on next page

Table C.3. *(cont.)* Experimental data for air-mixed system in 60 mm inner diameter acrylic pipe

Exp	θ	v_{sg}	v_{sl}	**T**	**dp/dx**	$\mathbf{H_L}$	**FR**	**Exp**	θ	v_{sg}	v_{sl}	**T**	**dp/dx**	$\mathbf{H_L}$	**FR**
#	° FH	m/s	m/s	°C	Pa/m	[-]	[-]	#	° FH	m/s	m/s	°C	Pa/m	[-]	[-]
107	15	2.30	0.85	-	1855	0.600	SL	134	15	24.38	1.13		3447	0.146	AN
108	15	5.01	0.85	-	2079	0.440	SL	135	20	0.14	0.07	18.68	2290	0.903	EB
109	15	9.07	0.83	-	2444	0.283	SL	136	20	0.27	0.08	18.70	1896	0.773	EB
110	15	12.44	0.86	-	2666	0.251	SL	137	20	0.62	0.10	18.72	1599	0.618	SL
111	15	17.75	0.83	-	2846	0.221	SL	138	20	1.15	0.11	18.76	1565	0.509	SL
112	15	24.67	0.77	-	2746	0.133	AN	139	20	2.45	0.11	18.89	1535	0.391	SL
113	15	32.14	0.77	-	3029	0.117	AN	140	20	5.38	0.11	18.95	1523	0.257	SL
114	15	0.13	1.05	-	2595	0.998	EB	141	20	0.13	0.17	-	2461	0.946	EB
115	15	0.26	1.05	-	2559	0.976	EB	142	20	0.25	0.18	-	2114	0.853	EB
116	15	0.58	1.06	-	2400	0.904	EB	143	20	0.58	0.19	-	1720	0.690	EB
117	15	1.08	1.06	-	2286	0.783	SL	144	20	1.07	0.19	-	1629	0.588	SL
118	15	2.30	1.06	-	2190	0.627	SL	145	20	2.30	0.20	-	1547	0.455	SL
119	15	5.01	1.05	-	2476	0.462	SL	146	20	5.02	0.20	-	1523	0.319	SL
120	15	6.91	1.05	-	2840	0.342	SL	147	20	8.85	0.18	22.75	1210	0.204	SL
121	15	12.40	1.02	-	3019	0.248	SL	148	20	12.44	0.18	-	1101	0.181	SL
122	15	17.73	0.95	-	3046	0.208	SL	149	20	17.76	0.17	-	1005	0.130	SW
123	15	24.45	0.91	-	3156	0.140	AN	150	20	24.60	0.16	-	1175	0.091	SW
124	15	31.84	0.84	-	3311	0.118	AN	151	20	32.14	0.15	-	1503	0.056	AN
125	15	0.13	1.31	-	2757	0.999	EB	152	20	0.13	0.41	-	2647	0.985	EB
126	15	0.26	1.32	-	2764	0.976	EB	153	20	0.25	0.41	-	2438	0.918	EB
127	15	0.58	1.32	-	2677	0.921	EB	154	20	0.58	0.42	-	2188	0.783	EB
128	15	1.07	1.32	-	2589	0.828	SL	155	20	1.06	0.43	-	1996	0.667	EB
129	15	2.28	1.31	-	2624	0.666	SL	156	20	2.27	0.43	-	1734	0.526	SL
130	15	5.01	1.30	-	2983	0.503	SL	157	20	5.02	0.43	-	1682	0.380	SL
131	15	7.11	1.28	-	3274	0.381	SL	158	20	8.87	0.44	-	1711	0.247	SL
132	15	12.10	1.21		3331	0.276	AN	159	20	12.47	0.43	-	1585	0.198	SL
133	15	17.80	1.18		3423	0.216	AN	160	20	17.76	0.42	-	1822	0.163	SW

continued on next page

Table C.3. *(cont.)* Experimental data for air-mixed system in 60 mm inner diameter acrylic pipe

Exp	θ	v_{sg}	v_{sl}	**T**	**dp/dx**	$\mathbf{H_L}$	**FR**	**Exp**	θ	v_{sg}	v_{sl}	**T**	**dp/dx**	$\mathbf{H_L}$	**FR**
#	° FH	m/s	m/s	°C	Pa/m	[-]	[-]	#	° FH	m/s	m/s	°C	Pa/m	[-]	[-]
161	20	24.60	0.40	-	1844	0.117	SW	188	20	1.08	1.04	-	2824	0.790	SL
162	20	32.23	0.37	-	1830	0.070	AN	189	20	2.29	1.04	-	2652	0.631	SL
163	20	0.13	0.59	-	2961	0.996	EB	190	20	5.01	1.03	-	2802	0.459	SL
164	20	0.26	0.59	-	2778	0.957	EB	191	20	6.91	1.03	-	3093	0.298	SL
165	20	0.58	0.60	-	2473	0.842	EB	192	20	11.86	1.01	-	3226	0.218	SL
166	20	1.07	0.61	-	2260	0.723	SL	193	20	17.68	0.95	-	3388	0.177	SW
167	20	2.29	0.61	-	2030	0.574	SL	194	20	24.40	0.89	-	3228	0.133	AN
168	20	5.09	0.61	-	2043	0.417	SL	195	20	31.74	0.84	-	3354	0.097	AN
169	20	6.91	0.61	-	2060	0.299	SL	196	20	0.13	1.30	-	3418	1.000	EB
170	20	12.41	0.60	-	2109	0.225	SL	197	20	0.25	1.30	-	3412	0.983	EB
171	20	17.72	0.58	-	2547	0.200	SW	198	20	0.58	1.30	-	3284	0.931	EB
172	20	24.76	0.55	-	2306	0.150	SW	199	20	1.07	1.30	-	3147	0.837	EB
173	20	31.68	0.56	-	2395	0.108	AN	200	20	2.27	1.30	-	3087	0.675	SL
174	20	0.13	0.83	-	3134	0.996	EB	201	20	5.01	1.29	-	3391	0.508	SL
175	20	0.26	0.83	-	3026	0.969	EB	202	20	7.12	1.28	-	3692	0.321	SL
176	20	0.58	0.84	-	2768	0.876	EB	203	20	11.92	1.22	-	3799	0.231	SL
177	20	1.07	0.84	-	2559	0.758	SL	204	20	17.55	1.16	-	3829	0.178	AN
178	20	2.30	0.85	-	2342	0.603	SL	205	20	24.80	1.12	-	3963	0.142	AN
179	20	5.01	0.84	-	2440	0.435	SL	206	20	31.36	1.06	-	4119	0.110	AN
180	20	6.92	0.85	-	2662	0.286	SL	207	25	0.13	0.14	-	2954	0.91	EB
181	20	12.36	0.83	-	2837	0.207	SL	208	25	0.26	0.14	-	2523	0.81	EB
182	20	17.64	0.79	-	3045	0.176	SW	209	25	0.58	0.15	-	2006	0.65	EB
183	20	24.56	0.73	-	2773	0.126	AN	210	25	1.07	0.15	-	1736	0.53	EB
184	20	31.51	0.69	-	2797	0.081	AN	211	25	2.28	0.16	-	1416	0.38	SL
185	20	0.13	1.03	-	3258	0.999	EB	212	25	5.03	0.16	-	1095	0.24	SL
186	20	0.25	1.03	-	3199	0.976	EB	213	25	6.92	0.16	-	1237	0.20	SL
187	20	0.58	1.04	-	2991	0.901	EB	214	25	12.03	0.16	-	1099	0.16	SL

continued on next page

Table C.3. *(cont.)* Experimental data for air-mixed system in 60 mm inner diameter acrylic pipe

Exp	θ	v_{sg}	v_{sl}	**T**	**dp/dx**	$\mathbf{H}_L$	**FR**	**Exp**	θ	v_{sg}	v_{sl}	**T**	**dp/dx**	$\mathbf{H}_L$	**FR**
#	° FH	m/s	m/s	°C	Pa/m	[-]	[-]	#	° FH	m/s	m/s	°C	Pa/m	[-]	[-]
215	25	17.70	0.15	-	1069	0.114	SL	242	25	0.57	0.84	-	3242	0.886	EB
216	25	24.60	0.15	-	1182	0.079	AN	243	25	1.07	0.84	-	2954	0.770	EB
217	25	32.42	0.13	-	1456	0.049	AN	244	25	2.29	0.85	-	2654	0.593	SL
218	25	0.13	0.36	-	3253	0.950	EB	245	25	5.04	0.84	-	2593	0.422	SL
219	25	0.25	0.36	-	2953	0.895	EB	246	25	6.93	0.83	-	2798	0.322	SL
220	25	0.57	0.37	-	2512	0.763	EB	247	25	12.00	0.82	-	2909	0.250	SL
221	25	1.07	0.38	-	2208	0.635	EB	248	25	17.59	0.79	-	3202	0.216	SL
222	25	2.29	0.39	-	1802	0.455	SL	249	25	24.27	0.74	-	2973	0.170	AN
223	25	5.03	0.39	-	1658	0.324	SL	250	25	31.85	0.72	-	3061	0.119	AN
224	25	6.90	0.40	-	1762	0.261	SL	251	25	0.13	1.03	-	3884	0.998	EB
225	25	12.09	0.39	-	1700	0.197	SL	252	25	0.25	1.03	-	3779	0.981	EB
226	25	17.51	0.38	-	1575	0.139	SL	253	25	0.57	1.04	-	3527	0.922	EB
227	25	24.70	0.36	-	1676	0.096	AN	254	25	1.07	1.04	-	3282	0.823	EB
228	25	31.94	0.34	-	1794	0.059	AN	255	25	2.29	1.05	-	3018	0.647	SL
229	25	0.13	0.60	-	3519	0.990	EB	256	25	5.04	1.04	-	3066	0.467	SL
230	25	0.25	0.61	-	3307	0.953	EB	257	25	8.48	1.01	-	3289	0.323	SL
231	25	0.57	0.62	-	2937	0.847	EB	258	25	12.74	0.98	-	3403	0.259	SL
232	25	1.08	0.63	-	2641	0.718	EB	259	25	17.85	0.93	-	3591	0.223	SL
233	25	2.29	0.64	-	2280	0.530	SL	260	25	24.44	0.88	-	3446	0.180	AN
234	25	5.04	0.64	-	2204	0.381	SL	261	25	31.94	0.84	-	3564	0.140	AN
235	25	7.13	0.63	-	2356	0.291	SL	262	25	0.13	1.15	-	3902	0.997	EB
236	25	12.31	0.62	-	2248	0.209	SL	263	25	0.25	1.21	-	3916	0.984	EB
237	25	17.66	0.60	-	2638	0.186	SL	264	25	0.58	1.20	-	3716	0.935	EB
238	25	24.28	0.58	-	2536	0.148	AN	265	25	1.07	1.27	-	3582	0.861	EB
239	25	31.63	0.54	-	2459	0.093	AN	266	25	2.29	1.27	-	3386	0.698	EB
240	25	0.13	0.82	-	3707	0.993	EB	267	25	5.03	1.25	-	3514	0.509	SL
241	25	0.26	0.83	-	3544	0.968	EB	268	30	0.14	0.11	22.91	3525	0.919	EB

continued on next page

Table C.3. *(cont.)* Experimental data for air-mixed system in 60 mm inner diameter acrylic pipe

Exp	θ	v_{sg}	v_{sl}	**T**	**dp/dx**	$\mathbf{H}_L$	**FR**	**Exp**	θ	v_{sg}	v_{sl}	**T**	**dp/dx**	$\mathbf{H}_L$	**FR**
#	° FH	m/s	m/s	°C	Pa/m	[-]	[-]	#	° FH	m/s	m/s	°C	Pa/m	[-]	[-]
269	30	0.27	0.12	22.88	2922	0.807	EB	296	30	6.97	0.45	22.81	2173	0.246	SL
270	30	0.63	0.13	22.89	2331	0.646	EB	297	30	12.30	0.45	22.80	2058	0.186	SL
271	30	1.16	0.13	22.90	2028	0.527	EB	298	30	17.67	0.44	22.79	1939	0.131	SL
272	30	2.47	0.14	22.91	1601	0.359	SL	299	30	24.41	0.42	22.79	2119	0.097	AN
273	30	5.45	0.14	22.90	1391	0.232	SL	300	30	31.91	0.39	22.78	2039	0.057	AN
274	30	9.64	0.14	22.71	1421	0.153	SL	301	30	0.14	0.59	22.76	4065	0.984	EB
275	30	14.55	0.14	22.80	1299	0.126	SL	302	30	0.28	0.60	22.76	3852	0.950	EB
276	30	20.55	0.14	22.84	1252	0.090	SL	303	30	0.63	0.62	22.76	3395	0.850	EB
277	30	26.69	0.13	22.87	1355	0.066	AN	304	30	1.17	0.63	22.75	3062	0.725	EB
278	30	31.64	0.12	22.90	1475	0.044	AN	305	30	2.50	0.64	22.75	2651	0.537	SL
279	30	0.14	0.17	22.68	3611	0.930	EB	306	30	5.45	0.64	22.75	2507	0.384	SL
280	30	0.28	0.18	22.69	3084	0.839	EB	307	30	7.14	0.63	22.75	2515	0.282	SL
281	30	0.63	0.18	22.70	2476	0.673	EB	308	30	11.95	0.63	22.74	2455	0.204	SL
282	30	1.17	0.19	22.73	2113	0.549	EB	309	30	17.66	0.60	22.74	2757	0.170	SL
283	30	2.50	0.19	22.74	1752	0.388	SL	310	30	24.34	0.57	22.73	2804	0.139	AN
284	30	5.46	0.20	22.76	1467	0.248	SL	311	30	31.59	0.54	22.72	2605	0.088	AN
285	30	7.01	0.20	22.77	1541	0.197	SL	312	30	0.13	0.90	22.69	4360	0.996	EB
286	30	12.07	0.19	22.77	1462	0.151	SL	313	30	0.26	0.90	22.68	4199	0.971	EB
287	30	17.72	0.19	22.76	1315	0.103	SL	314	30	0.59	0.91	22.68	3847	0.898	EB
288	30	24.49	0.19	22.78	1351	0.068	AN	315	30	1.11	0.92	22.68	3514	0.785	EB
289	30	31.90	0.18	22.78	1719	0.045	AN	316	30	2.37	0.92	22.67	3156	0.605	SL
290	30	0.14	0.42	22.83	3853	0.963	EB	317	30	5.23	0.92	22.67	3029	0.424	SL
291	30	0.27	0.43	22.82	3544	0.917	EB	318	30	6.90	0.91	22.65	3215	0.321	SL
292	30	0.63	0.44	22.82	3063	0.792	EB	319	30	12.36	0.87	22.65	3291	0.212	SL
293	30	1.17	0.45	22.80	2714	0.660	EB	320	30	17.47	0.83	22.65	3584	0.193	SL
294	30	2.49	0.46	22.09	2246	0.471	SL	321	30	24.18	0.80	22.64	3393	0.152	AN
295	30	5.44	0.46	22.81	2044	0.331	SL	322	30	31.50	0.73	22.62	3294	0.107	AN

continued on next page

Table C.3. *(cont.)* Experimental data for air-mixed system in 60 mm inner diameter acrylic pipe

Exp	θ	v_{sg}	v_{sl}	**T**	**dp/dx**	$\mathbf{H}_L$	**FR**	**Exp**	θ	v_{sg}	v_{sl}	**T**	**dp/dx**	$\mathbf{H}_L$	**FR**
#	° FH	m/s	m/s	°C	Pa/m	[-]	[-]	#	° FH	m/s	m/s	°C	Pa/m	[-]	[-]
323	30	0.10	1.05	22.79	4473	1.001	EB	350	45	5.02	0.45	-	3018	0.316	SL
324	30	0.20	1.05	22.82	4341	0.984	EB	351	45	6.90	0.45	-	3019	0.246	SL
325	30	0.46	1.06	22.84	4045	0.925	EB	352	45	12.14	0.44	-	3000	0.184	SL
326	30	0.88	1.07	22.85	3729	0.826	EB	353	45	17.64	0.43	-	2929	0.138	SL
327	30	1.90	1.07	22.87	3443	0.650	SL	354	45	24.47	0.41	-	2913	0.099	AN
328	30	4.37	1.06	22.88	3429	0.455	SL	355	45	31.91	0.38	-	2905	0.067	AN
329	30	6.92	1.27	23.07	4143	0.376	SL	356	45	0.13	0.61	-	5675	0.985	CB
330	30	12.21	1.20	23.07	4237	0.272	SL	357	45	0.25	0.61	-	5406	0.957	CB
331	30	17.65	1.15	23.07	4390	0.221	SL	358	45	0.57	0.63	-	5012	0.880	CB
332	30	24.20	1.12	23.08	4464	0.179	AN	359	45	1.07	0.65	-	4281	0.758	SL
333	30	32.03	1.07	23.10	4679	0.163	AN	360	45	2.28	0.67	-	3634	0.567	SL
334	45	0.14	0.12		5357	0.961	CB	361	45	5.03	0.67	-	3329	0.390	SL
335	45	0.27	0.13	-	4684	0.882	CB	362	45	6.90	0.67	-	3434	0.302	SL
336	45	0.60	0.14	-	3669	0.715	CB	363	45	12.20	0.66	-	3310	0.214	SL
337	45	1.13	0.15	-	3154	0.577	SL	364	45	17.55	0.64	-	3260	0.169	SL
338	45	2.40	0.16	-	2924	0.398	SL	365	45	24.37	0.62	-	3728	0.146	AN
339	45	5.30	0.16	-	2906	0.252	SL	366	45	31.80	0.59	-	3655	0.105	AN
340	45	7.33	0.16	-	2905	0.190	SL	367	45	0.13	0.82	-	5891	0.993	CB
341	45	12.26	0.16	-	2904	0.146	SL	368	45	0.25	0.83	-	5630	0.967	CB
342	45	17.75	0.16	-	2904	0.110	SL	369	45	0.57	0.84	-	5227	0.903	CB
343	45	24.56	0.15	-	2904	0.079	AN	370	45	1.07	0.85	-	4654	0.791	CB
344	45	32.06	0.14	-	2904	0.053	AN	371	45	2.29	0.87	-	4071	0.609	SL
345	45	0.13	0.36	-	5467	0.954	CB	372	45	5.02	0.87	-	3757	0.416	SL
346	45	0.25	0.39	-	5191	0.914	CB	373	45	6.90	0.86	-	3866	0.316	SL
347	45	0.57	0.41	-	4549	0.804	CB	374	45	12.06	0.84	-	3742	0.221	SL
348	45	1.07	0.43	-	3764	0.660	SL	375	45	17.62	0.79	-	4001	0.177	SL
349	45	2.28	0.44	-	3162	0.472	SL	376	45	24.38	0.75	-	4370	0.155	AN

continued on next page

Table C.3. *(cont.)* Experimental data for air-mixed system in 60 mm inner diameter acrylic pipe

Exp	θ	v_{sg}	v_{sl}	**T**	**dp/dx**	$\mathbf{H_L}$	**FR**	**Exp**	θ	v_{sg}	v_{sl}	**T**	**dp/dx**	$\mathbf{H_L}$	**FR**
#	° FH	m/s	m/s	°C	Pa/m	[-]	[-]	#	° FH	m/s	m/s	°C	Pa/m	[-]	[-]
377	45	31.38	0.73	-	4263	0.121	AN	404	60	24.36	0.19	-	4213	0.104	AN
378	45	0.13	1.07	-	6128	0.999	CB	405	60	31.81	0.18	-	4213	0.070	AN
379	45	0.25	1.07	-	5903	0.981	CB	406	60	0.13	0.29	-	6800	0.983	CB
380	45	0.57	1.08	-	5565	0.930	CB	407	60	0.25	0.31	-	6523	0.944	CB
381	45	1.07	1.09	-	5070	0.845	CB	408	60	0.57	0.34	-	5999	0.850	CB
382	45	2.29	1.10	-	4540	0.672	SL	409	60	1.07	0.38	-	4762	0.697	CB
383	45	5.03	1.10	-	4314	0.471	SL	410	60	2.28	0.41	-	4214	0.511	SL
384	45	7.01	1.08	-	4471	0.350	SL	411	60	5.01	0.43	-	4213	0.346	SL
385	45	12.04	1.03	-	4371	0.257	SL	412	60	6.91	0.43	-	4213	0.271	SL
386	45	17.55	0.98	-	4745	0.215	SL	413	60	11.96	0.42	-	4213	0.208	SL
387	45	24.28	0.95	-	5208	0.183	AN	414	60	17.68	0.41	-	4213	0.161	SL
388	45	31.47	0.91	-	5011	0.152	AN	415	60	24.52	0.39	-	4213	0.119	AN
389	45	0.12	1.24	-	6268	1.003	CB	416	60	31.89	0.36	-	4213	0.087	AN
390	45	0.24	1.26	-	6116	0.989	CB	417	60	0.13	0.62	-	7028	0.990	CB
391	45	0.57	1.22	-	5760	0.941	CB	418	60	0.25	0.64	-	6677	0.962	CB
392	45	1.07	1.27	-	5367	0.874	SL	419	60	0.57	0.65	-	6328	0.898	CB
393	45	2.28	1.28	-	4921	0.707	SL	420	60	1.07	0.67	-	5843	0.804	CB
394	45	5.02	1.28	-	4714	0.497	SL	421	60	2.27	0.71	-	4335	0.589	SL
395	60	0.14	0.11	-	6586	0.962	CB	422	60	5.01	0.73	-	4247	0.398	SL
396	60	0.26	0.13	-	6079	0.920	CB	423	60	7.15	0.72	-	4265	0.309	SL
397	60	0.60	0.16	-	4984	0.745	CB	424	60	12.10	0.71	-	4232	0.233	SL
398	60	1.13	0.17	-	4236	0.603	SL	425	60	17.45	0.69	-	4237	0.190	SL
399	60	2.41	0.19	-	4213	0.415	SL	426	60	24.33	0.62	-	4275	0.160	SL
400	60	5.28	0.20	-	4213	0.286	SL	427	60	31.78	0.62	-	4341	0.124	AN
401	60	6.94	0.21	-	4213	0.215	SL	428	60	0.13	0.80	-	7114	0.993	CB
402	60	12.05	0.20	-	4213	0.170	SL	429	60	0.25	0.82	-	6837	0.972	CB
403	60	17.62	0.20	-	4213	0.140	SL	430	60	0.57	0.83	-	6331	0.912	CB

continued on next page

Table C.3. *(cont.)* Experimental data for air-mixed system in 60 mm inner diameter acrylic pipe

Exp	θ	v_{sg}	v_{sl}	**T**	**dp/dx**	$\mathbf{H}_L$	**FR**	**Exp**	θ	v_{sg}	v_{sl}	**T**	**dp/dx**	$\mathbf{H}_L$	**FR**
#	° FH	m/s	m/s	°C	Pa/m	[-]	[-]	#	° FH	m/s	m/s	°C	Pa/m	[-]	[-]
431	60	1.06	0.85	-	6002	0.831	CB	458	70	0.57	0.15	-	-	0.665	CB
432	60	2.29	0.88	-	4646	0.620	SL	459	70	1.04	0.16	-	-	0.494	SL
433	60	5.02	0.89	-	4366	0.431	SL	460	70	2.24	0.18	-	-	0.299	SL
434	60	7.31	0.88	-	4338	0.337	SL	461	70	5.00	0.19	-	-	0.162	SL
435	60	12.00	0.87	-	4321	0.253	SL	462	70	5.05	0.19	-	-	0.136	SL
436	60	17.34	0.83	-	4409	0.207	SL	463	70	8.62	0.19	-	-	0.085	CH
437	60	24.05	0.79	-	4771	0.173	SL	464	70	13.76	0.19	-	-	0.061	CH
438	60	31.65	0.73	-	5043	0.145	AN	465	70	17.95	0.19	-	-	0.052	AN
439	60	0.13	1.03	-	7315	0.988	CB	466	70	25.01	0.18	-	-	0.036	AN
440	60	0.25	1.03	-	7033	0.968	CB	467	70	34.01	0.17	-	-	0.025	AN
441	60	0.57	1.04	-	6604	0.918	CB	468	70	0.13	0.25	-	7372	0.949	CB
442	60	1.07	1.05	-	6257	0.836	CB	469	70	0.57	0.34	-	6383	0.794	CB
443	60	2.28	1.08	-	5097	0.648	SL	470	70	1.06	0.34	-	-	0.590	SL
444	60	5.02	1.08	-	4702	0.454	SL	471	70	2.25	0.37	-	-	0.362	SL
445	60	7.14	1.07	-	4702	0.350	SL	472	70	5.01	0.39	-	-	0.203	SL
446	60	12.34	1.03	-	4604	0.260	SL	473	70	6.35	0.38	-	-	0.150	SL
447	60	17.41	0.97	-	4838	0.212	SL	474	70	9.87	0.38	-	-	0.108	CH
448	60	25.82	0.91	-	5765	0.176	SL	475	70	13.88	0.38	-	-	0.084	CH
449	60	30.86	0.89	-	6071	0.161	AN	476	70	17.95	0.37	-	-	0.069	CH
450	60	0.13	1.21	-	7487	0.998	CB	477	70	24.72	0.35	-	-	0.049	AN
451	60	0.25	1.22	-	7260	0.983	CB	478	70	30.56	0.34	-	-	0.037	AN
452	60	0.57	1.24	-	6838	0.941	CB	479	70	0.13	0.56	-	7315	0.957	CB
453	60	1.07	1.24	-	6424	0.868	CB	480	70	0.26	0.57	-	7231	0.929	CB
454	60	2.28	1.26	-	5515	0.693	SL	481	70	0.58	0.60	-	6779	0.841	CB
455	60	5.02	1.26	-	5132	0.485	SL	482	70	1.08	0.62	-	6311	0.706	CB
456	70	0.12	0.10	-	7194	0.951	CB	483	70	2.28	0.67		-	0.460	SL
457	70	0.25	0.13	-	6270	0.858	CB	484	70	5.02	0.69		-	0.267	SL

continued on next page

Table C.3. *(cont.)* Experimental data for air-mixed system in 60 mm inner diameter acrylic pipe

Exp	θ	v_{sg}	v_{sl}	**T**	**dp/dx**	$\mathbf{H}_L$	**FR**	**Exp**	θ	v_{sg}	v_{sl}	**T**	**dp/dx**	$\mathbf{H}_L$	**FR**
#	° FH	m/s	m/s	°C	Pa/m	[-]	[-]	#	° FH	m/s	m/s	°C	Pa/m	[-]	[-]
485	70	5.68	0.69	-	-	0.208	SL	512	70	12.34	1.14	-	4845	0.153	SL
486	70	9.74	0.68	-	-	0.140	CH	513	70	17.88	1.10	-	5328	0.117	CH
487	70	14.93	0.66	-	-	0.098	CH	514	70	24.93	1.06	-	7046	0.103	CH
488	70	20.49	0.62	-	-	0.075	CH	515	70	31.77	1.01	-	7319	0.085	AN
489	70	28.13	0.61	-	-	0.060	AN	516	70	36.14	1.02	-	7547	0.082	AN
490	70	31.47	0.59		-	0.050	AN	517	78	0.13	0.11	-	7704	0.866	CB
491	70	0.10	0.91	-	7733	0.966	CB	518	78	0.26	0.13	-	6814	0.782	CB
492	70	0.20	0.92	-	7231	0.938	CB	519	78	0.58	0.15	-	5373	0.596	CB
493	70	0.45	0.93	-	6985	0.870	CB	520	78	1.06	0.17	-	5136	0.418	SL
494	70	0.85	0.94	-	6615	0.772	CB	521	78	2.27	0.19	-	5136	0.243	SL
495	70	1.86	0.97	-	-	0.529	SL	522	78	5.02	0.20	-	5136	0.146	SL
496	70	4.22	0.98	-	-	0.303	SL	523	78	7.82	0.20	-	5136	0.092	SL
497	70	5.20	0.97	-	-	0.259	SL	524	78	12.17	0.20	-	5136	0.065	CH
498	70	7.48	0.96	-	-	0.192	SL	525	78	18.03	0.19	-	5136	0.048	CH
499	70	12.22	0.93	-	-	0.127	CH	526	78	25.14	0.18	-	5136	0.033	AN
500	70	17.82	0.86	-	-	0.091	CH	527	78	29.70	0.18	-	5136	0.028	AN
501	70	24.95	0.81	-	-	0.073	CH	528	78	0.13	0.26	-	7670	0.877	CB
502	70	32.00	0.78	-	5028	0.057	AN	529	78	0.25	0.28	-	7447	0.829	CB
503	70	36.58	0.78	-	5040	0.065	AN	530	78	0.57	0.33	-	6986	0.718	CB
504	70	0.13	1.20	-	7174	0.977	CB	531	78	1.06	0.37	-	5340	0.534	CB
505	70	0.25	1.20	-	7660	0.955	CB	532	78	2.26	0.41	-	5136	0.319	SL
506	70	0.58	1.21	-	7211	0.904	CB	533	78	5.02	0.43	-	5136	0.183	SL
507	70	1.07	1.22	-	6740	0.817	CB	534	78	7.39	0.45	-	5136	0.124	SL
508	70	2.29	1.24	-	4812	0.600	SL	535	78	12.15	0.44	-	5136	0.085	CH
509	70	5.04	1.25	-	-	0.368	SL	536	78	17.91	0.42	-	5136	0.064	CH
510	70	5.95	1.23	-	-	0.283	SL	537	78	24.92	0.39	-	5136	0.046	AN
511	70	8.08	1.21	-	-	0.218	SL	538	78	32.26	0.36	-	5136	0.034	AN

continued on next page

Table C.3. *(cont.)* Experimental data for air-mixed system in 60 mm inner diameter acrylic pipe

Exp	θ	v_{sg}	v_{sl}	**T**	**dp/dx**	$\mathbf{H}_L$	**FR**	**Exp**	θ	v_{sg}	v_{sl}	**T**	**dp/dx**	$\mathbf{H}_L$	**FR**
#	° FH	m/s	m/s	°C	Pa/m	[-]	[-]	#	° FH	m/s	m/s	°C	Pa/m	[-]	[-]
539	78	0.13	0.55	-	8332	0.911	CB	557	78	12.07	0.87	-	-	0.096	CH
540	78	0.25	0.56	-	7560	0.879	CB	558	78	17.59	0.80	-	-	0.065	CH
541	78	0.57	0.58	-	7161	0.794	CB	559	78	24.47	0.75	-	-	0.045	AN
542	78	1.06	0.61	-	6464	0.664	CB	560	78	31.08	0.71	-	-	0.027	AN
543	78	2.26	0.67	-	5136	0.425	SL	561	78	0.13	1.19	-	-	-	CB
544	78	5.03	0.69	-	5136	0.254	SL	562	78	0.26	1.19	-	-	-	CB
545	78	7.81	0.68	-	5136	0.155	SL	563	78	0.58	1.20	-	-	-	CB
546	78	12.10	0.67	-	5136	0.112	SL	564	78	1.08	1.21	-	-	-	CB
547	78	17.80	0.65	-	5136	0.085	CH	565	78	2.30	1.24	-	-	-	SL
548	78	24.87	0.61	-	5136	0.073	AN	566	78	5.04	1.24	-	-	-	SL
549	78	30.70	0.57	-	5136	0.071	AN	567	78	7.41	1.22	-	-	-	SL
550	78	0.14	0.84	-	7931	0.856	CB	568	78	11.98	1.14	-	-	-	CH
551	78	0.26	0.85	-	7671	0.818	CB	569	78	17.50	1.08	-	-	-	CH
552	78	0.58	0.86	-	7320	0.740	CB	570	78	24.25	1.03	-	-	-	CH
553	78	1.07	0.88	-	6767	0.635	CB	571	78	31.24	1.00	-	-	-	AN
554	78	2.29	0.91	-	5136	0.409	SL								
555	78	5.02	0.92	-	-	0.232	SL								
556	78	7.34	0.92	-	-	0.147	SL								

Appendix D

Published Papers

Applicability of Models for Liquid Loading Prediction in Gas Wells. SPE Europec- 81st EAGE Conference and Exhibition; 2019
Is not included due to copyright
available at https://doi.org/10.2118/195466-MS

Experimental investigation of two-phase flow regime in an inclined pipe

C Vieira, M Kallager, M Vassmyr, N La Forgia, Z Yang
Norwegian University of Science and Technology, Norway

ABSTRACT

Experiments were performed with propose of mapping the flow patterns in two-phase flow in an upward inclinable 60 mm ID and 6 m long Plexiglas pipe. Air and viscous oil were used as working fluids and degree of inclination changed from 10 º to 78 º. Measurements includes pressure drop. Flow regime were recorded with high speed video cameras. Experimental results were compared with existing models by Barnea (1987) and with a commercial dynamic multiphase flow simulator (OLGA7.3®). Predictions with unified model had acceptable agreement with experimental data.

1. INTRODUCTION

The need of understanding two-phase gas-liquid flow has been increasing in the recent years, as well as the need of a technical solution for handling and controlling the flow behaviour. A correct prediction of multiphase flow dynamics is critical for the design of pipelines for deep-water riser and production tubing in offshore oil and gas field development, where parameters as pressure drop and liquid holdup are strongly dependent on the flow pattern. Generally, flow pattern in gas-liquid system can exist in a wide variety of forms, depending on the flow rate, physical properties of the phases, the geometry and inclination of the tube (McQuillan and Whalley, 1985).

For several years, extensive research on multiphase flow has been conducted. Most of these were aiming to either horizontal or flow in vertical pipe, since such pipe geometry and topology are quite common. Nowadays, exploration into deep-water and development of horizontal well drilling make it more actual for the pipe or flow channel with inclination between 10 º to 85 º, little information on the flow in pipe with such inclination angle range is available.

Diverse classification of the flow pattern in the conduit exit, most of them based on individual interpretation of visual observation of the fluid distribution within the pipe flow (Barnea et al., 1980a). This has been a disadvantage in the industry, due to different visual interpretations reported under identical flow conditions. Therefore, many researches have proposed to classify the flow pattern quantitatively. Considerable numbers of correlation to predict the flow pattern, pressure drop and liquid holdup in either horizontal and vertical flow are available, but these correlations have not been satisfactory when applied to inclined flow. Beggs and Brill (1973) developed a model for predicting pressure gradient from correlation of liquid holdup and friction factor for two-phase flow in pipe at all angles for many flow conditions. Gould et al. (1974) presented a model to predict pressure distribution through vertical, horizontal and 45 º inclined pipe.

Taitel and Dukler (1976) proposed a physical model that predicts the flow regime transitions in horizontal and near horizontal gas-liquid flow. Barnea et al. (1985) reported experimental data on flow pattern transitions for upwards flow of air-water in pipes having 0 to 90 ^{o} of inclination. Later Barnea (1987) proposed a unified model to predict the steady-state transition boundaries for the whole range of pipe inclination for gas-liquid system. The model is an extension of the suggested model by Barnea (1986) were the transition from annular to intermittent flow and from dispersed flow were suggested and previously published models as Barnea et al. (1982a), Barnea et al. (1982b), (1980b) and Barnea et al. (1985).

Zhang et al. (2003a) presented a unified model which predicts the flow pattern transition, pressure gradient, liquid holdup and slug characteristics in gas-liquid flow for all inclination angle (±90 ^{o} from horizontal). The validation of the model were presented by Zhang et al. (2003b) were extensive experimental data acquired with different pipe geometry and fluid properties were used. Gokcal et al. (2008) experimentally studied the effect of high viscosity liquid on the flow pattern for oil-gas flow in horizontal pipe and later on Jeyachandra et al. (2012) extended the study using slightly inclined pipe (± 2 ^{o}). They reported flow pattern and pressure drop, the results were then used to evaluate different flow pattern maps, model and two-phase flow correlation. There is variety of measuring techniques used in two-phase of which only few are used directly for flow pattern as void fraction fluctuation measurements, pressure gradient oscillations and conducted/capacitance probe techniques (Barnea et al., 1980a).

From the literature survey on two-phase gas-liquid flow in inclined pipes, it can be concluded that most of the experiment data available for comparing with existing correlations come from air-water solution as test fluids. Moreover, the data with viscous liquid phase and inclined pipe is limited. The first objective of this study was to obtain reliable data for the flow pattern identification having gas and viscous liquid system for inclination-angle range of $10^{o} \leq \theta \geq 78^{o}$ from horizontal. Next, the performance of flow pattern using Barnea (1987) model and Multiphase flow simulator by SPT-Group (OLGA®7.3-hereafter referred to as OLGA) is evaluated using the data acquired in the experimental part of the study. Barnea (1987) model was selected to evaluate if the model is applicable for more viscous fluid since it was developed based on experimental data for air-water flow system.

2. EXPERIMENTAL SET UP AND PROCEDURE

2.1 Test Section

Experiments were carried out at the Multiphase Flow Laboratory at NTNU, which consists of several flexible test sections used for diverse proposed. The facility used comprised of a 6-m long, 60-mm ID transparent acrylic pipe for better visualisation. Inclination angles can be changed from 10 ^{o} to 78 ^{o} from horizontal. There were limitations on the variation of inclination range due to safety issues during the experiments. The inclined setup has two possible mixture sections. One is located before the test section where gas and liquid flow simultaneously through a flexible pipe and the other where each fluid is mixed at the test section inlet separately. The second mixture section were preferred in present investigation to prevent instabilities prior to the test section, which can be caused if the mixing occurs several meters before the test section. The two-phase flow propagates through the test section to a separator at the top of the pipe where the air is vented to the atmosphere and the liquid drained to a main storage separator. The schematic of the facility is given in Fig. 1.

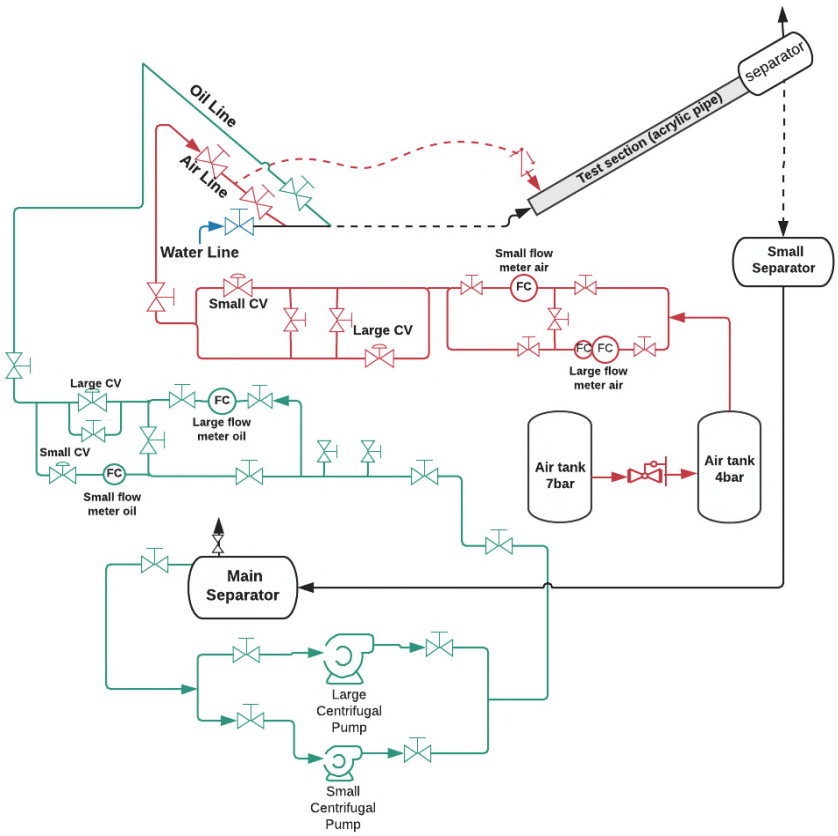

Fig. 1 Schematic of the test facility

2.2 Fluid system

Experiments were carried out using compressed air as gas phase and oil as liquid phase. Air is supplied at 7 bar by the pressurized air network of the university and reduced to operational pressure of 4 bar. Oil is supplied through an oil line by centrifugal pump and is storage with water separated by gravity in the main separator located in the basement. Fluid flow rate were measured by mean of Coriolis meter. The properties of the fluids at 20 °C and 1 atm are given in Table 1.

Table 1. Fluid properties

Physical property	Air	Oil
Density, $kg.m^{-3}$	1.22	840
Viscosity, cP	0.018	25

2.3 Pressure gradient

Pressure gradient is calculated from the measure pressure of two pressure cells and two absolute pressure that were connected along the test section.

2.4 Experimental test matrix

The flow pattern in two-phase flow system depends on the geometry, physical properties and superficial velocities of the fluids. Effect of inclination angle on the flow patterns was the interest on this study. For every inclination 10 °, 15 °, 20 °, 25 °, 30 °, 45 °, 60 °, 70 °

and 78 ^{o} (from horizontal), different combination of superficial liquid and gas velocity (v_{sl} and v_{sg}) varied from 0.1 m/s to 1.2 m/s and 0.04 m/s to 10 m/s, respectively were used. The limits of v_{sl} were due to the accuracy of the flow meter and the centrifugal pump operation limits. In the case of air, the lower limit was due to accuracy of flow meter, while the higher was set after few experiments to verify at which velocity annular flow was identified.

2.5 Flow regime visualisation and characterisation

Flow regimes were identified by visual inspection, pictures and video were recorded using, three synchronised cameras installed in the test section. The camera was a Basler acA640 with the maximum resolution of 659x494 pixels in black and white. The videos were recorded at 120 frames per second and simultaneously acquired using a program written in LabVIEW2013® for the acquisition system. Stratified wavy (SW), elongated bubble (EB), cap bubble (CB), slug (SL), churn (CH) and annular (AN) flow pattern were observed. Dispersed bubble (DB) flow could not be observed due to limitations of oil flow rate during the experiments. Experimentally the identification if either the flow was annular, churn or stratified wavy by visual inspection was quite challenging, thus may have led to a poor flow pattern characterisation. Long time on the observations was considered and the most dominant flow regime over the time was classified as the final flow regime.

3. RESULTS AND DISCUSSION

In this section, experimental flow pattern observations were compared with predictions of Barnea (1987) model and simulations results from OLGA (Fig. 2 to Fig. 10). Pressure gradient were only compared with OLGA results, since the unified model is basically a set of equations and criteria solved for superficial velocities, void fraction and pipe geometry having no relation with pressure drop.

3.1 Flow pattern comparison

Barnea (1987) developed a model with the purpose of predicting flow pattern transition boundaries for the whole range of pipe inclination through operative equations and dimensionless maps, that incorporate the effect of flow rates, fluid properties, pipe size and pipe inclination. In Barnea et al. (1985) the classification of two-phase were defined into four main regions: stratified that was subdivide into *stratified smooth* and *stratified wavy;* Intermittent with *elongated, slug* and *churn flow*; annular with *annular* and *annular wavy* and dispersed bubble region.

Besides the flow pattern transition predicted through theoretical model, dynamic multiphase flow as OLGA are also used with the same proposed. Bendiksen et al. (1991) mentioned that flow regime transition identification in OLGA, is basic two flow regime classes distributed and separated. The distributed is where the contribution of bubble and slug flow are present, while separated including stratified and annular flow. In total, OLGA distinguish between four flow regimes: *stratified*, *bubble*, *slug* and *annular*. It should be mentioned that the stratified flow is classified either as smooth of wavy.

For all the inclination stratified smooth pattern were not experimentally observed neither predicted through unified model nor OLGA simulation. In Barnea et al. (1985) this flow pattern could be observed only for inclination angles less than 0.25 ^{o}. Dispersed flow was not achieved in the experiments due to limitation on the liquid flow rate, which was confirmed with the theoretical transition line (DB-SL) located above the maximum superficial velocity of the liquid used in the experiments.

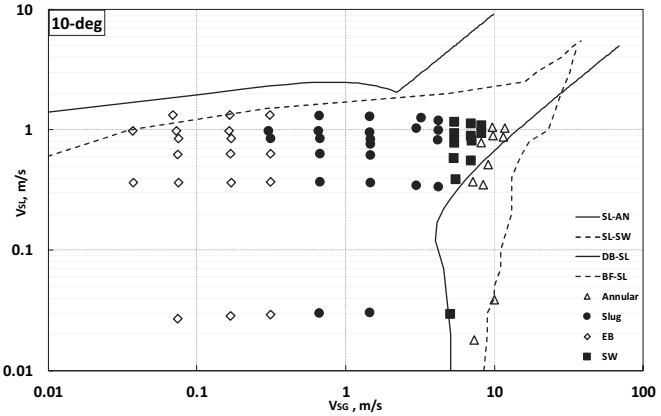

Fig. 2 Flow pattern map 10º upward, 6 cm pipe: ─ Barnea (1987) model; --- OLGA simulation

Fig. 5 - Fig. 10 stratified wavy flow was not identified. However, a transition boundary for SW predicted from Barnea (1987) was expected to appear at inclination angles below 20 º, which could not be observed due to the lower liquid flow rates used in the model compared with the experiments. On the other hand, the transition boundary from slug to stratified wavy (SL-SW) predicted in OLGA was identified in most of the inclination except in Fig. 8 to Fig. 10. Experimentally elongated bubble flow region reduces with increasing inclination angle and cap bubble appears for inclinations above 30 º. Similar condition as observed in Barnea et al. (1985) and Barnea (1987) where the elongated bubble disappeared at angles above 30 º for upward inclined pipe and dispersed bubble flow take place. Due to the gas phase inlet location on the test section, cap bubble pattern was identified instead of dispersed bubble. Considering that, small bubbles of air injected in the system were flowing on the top of the pipe section creating a cap bubble flow.

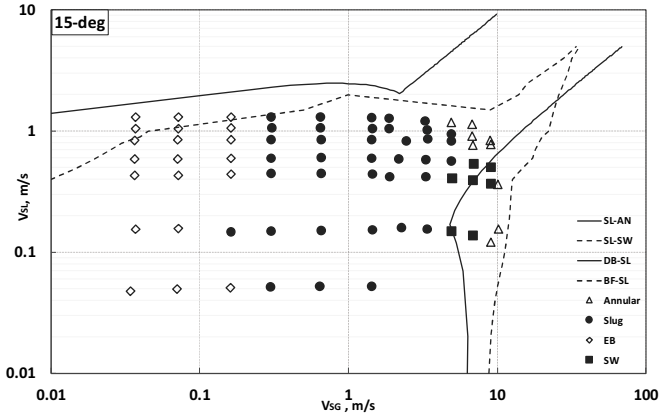

Fig. 3 Flow pattern map 15º upward, 6 cm pipe: ─ Barnea (1987) model; --- OLGA simulation

Bubble-slug transition curve (BF-SL) predicted from the model represented better the experimental data for inclinations angles above 60 º. The criteria set by the unified model used in this transition were not met for inclination angles 10 º and 15 º. In OLGA, bubble-slug transition curve moves to the right down when the inclination angle increase, hence

the experimental bubble flow region in better represented for inclination above 30°. This conclusion was based on the fact that, cap bubble and elongated bubble exists in the bubble flow region. Churn flow in the experimental data has a similar behaviour as the one verified by Barnea et al. (1985) where the first appearance of this pattern occurred at 70° inclination (Fig. 9). In Barnea et al. (1985) the range of v_{sl} at which the churn flow appeared increase with the pipe diameter, thus it was possible to observe this pattern for the velocities used in the experiment.

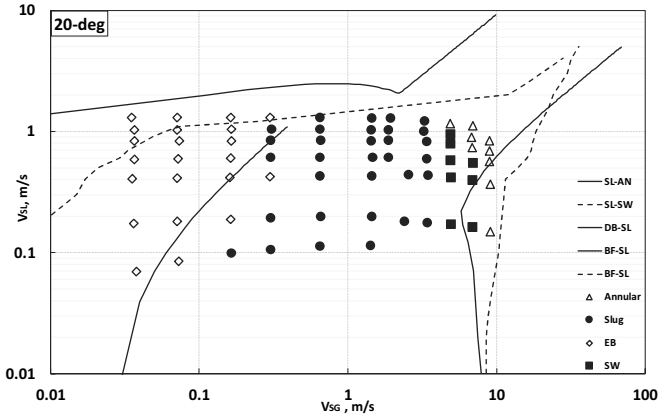

Fig. 4 Flow pattern map 20° upward, 6 cm pipe: ─ Barnea (1987) model; --- OLGA simulation

Slug-annular transition curve (SL-AN) in both theoretical and simulations predictions occurred at higher gas flow rates compared with the experiments. In OLGA, annular flow transitions for 10° inclination were observed for v_{sg} around 200 m/s. The required gas flow rate for annular flow to be seen, decreases as the angle increases around 50 m/s for 70° inclination. Thus, no SL-AN transition was observed for inclination angle below 60°.

It should be mentioned that different naming between annular wavy and stratified wavy, the stratified-annular transition was not clear, which mean that experimentally flow pattern could be misinterpreted.

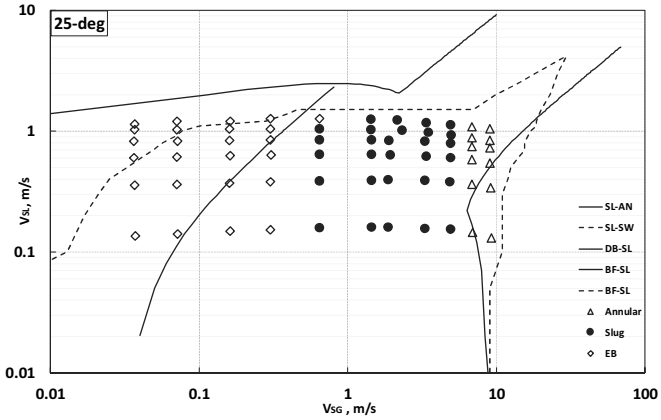

Fig. 5 Flow pattern map 25° upward, 6 cm pipe: ─ Barnea (1987) model; --- OLGA simulation

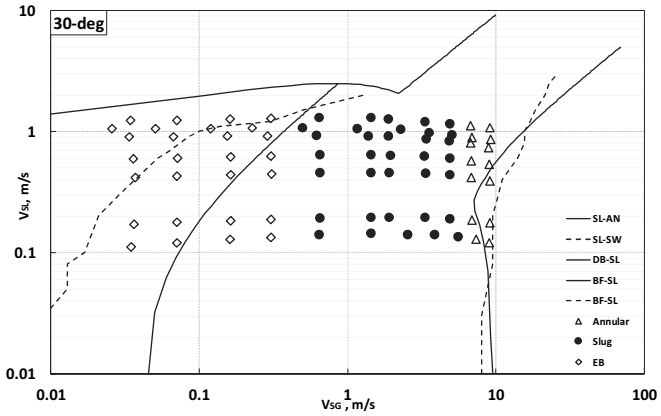

Fig. 6 Flow pattern map 30° upward, 6 cm pipe: ─ Barnea (1987) model; --- OLGA simulation

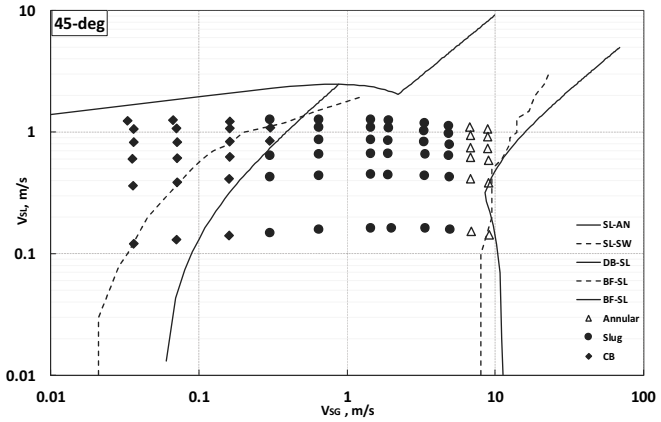

Fig. 7 Flow pattern map 45° upward, 6 cm pipe: ─ Barnea (1987) model; --- OLGA simulation

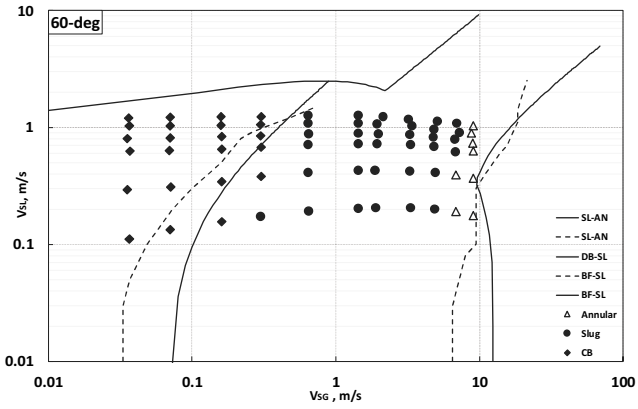

Fig. 8 Flow pattern map 60° upward, 6 cm pipe: ─ Barnea (1987) model; --- OLGA simulation

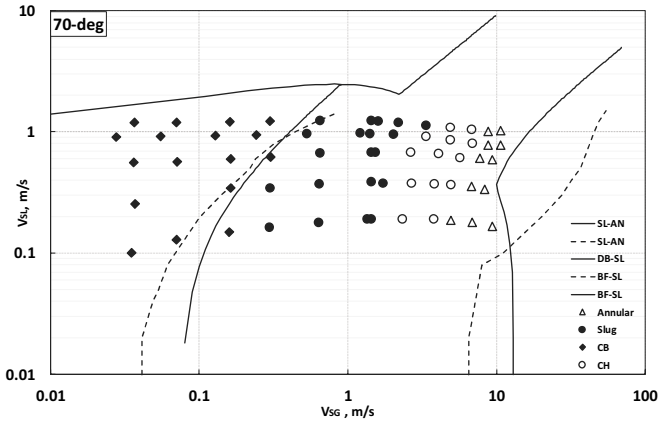

Fig. 9 Flow pattern map 70° upward, 6 cm pipe: ─ Barnea (1987) model; --- OLGA simulation

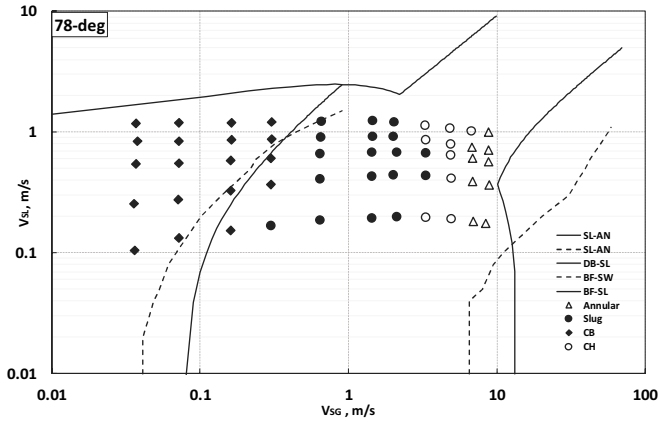

Fig. 10 Flow pattern map 78° upward, 6 cm pipe: ─ Barnea (1987) model; --- OLGA simulation

3.2 Pressure gradient and liquid holdup

This section presents the pressure drop from experimental results compared to OLGA simulations results. Pressure drop in two-phase is more complicated and difficult to predict compared to single phase. Beggs and Brill (1973) developed and equation for the pressure drop when gas, liquid or both are flowing in a pipe. They also mentioned that in directional wells pressure are usually determined from vertical flow correlations.

In Fig. 11 to Fig. 15 total pressure drop versus superficial gas velocities given a constant superficial liquid velocity for different inclination are shown. Overall, it was observed that the pressure drop response changed with the flow pattern present in the test section and the inclination angles. Experimentally, two differential pressure transducers were used to measure the pressure drop in the test section. The output pressure signal (from LabVIEW®) was then processed and corrected for non-zero value at zero flow, during calibration.

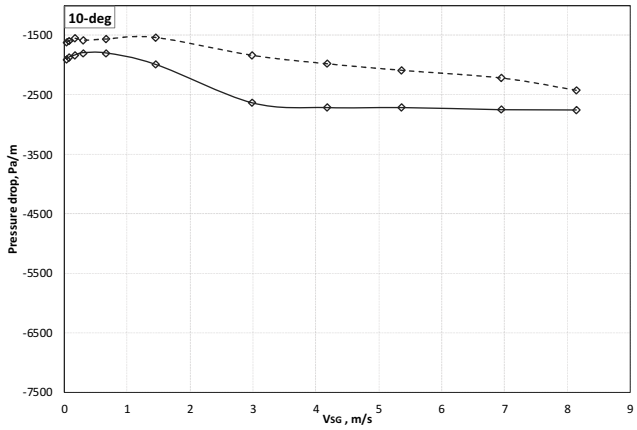

Fig. 11 Pressure drop 10° upward, Usl = 1m/s: ─ experimental data; --- OLGA simulation

On Fig. 11 to Fig. 15 it was observed that the total pressure drop reached a minimum point for lower gas flow rates and a further increase in gas flow rates resulted in larger pressure drop for all inclinations. In the area of high gas flow rates, the frictional losses are more dominant. Although OLGA and experiments data show the same trends, the lines for total pressure gradients deviates a lot, especially for high gas flow rates when the inclination angle increases.

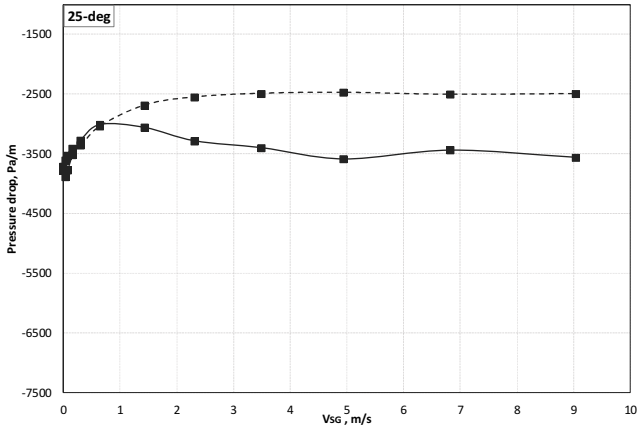

Fig. 12 Pressure drop 25° upward, Usl = 1m/s: ─ experimental data; --- OLGA simulation

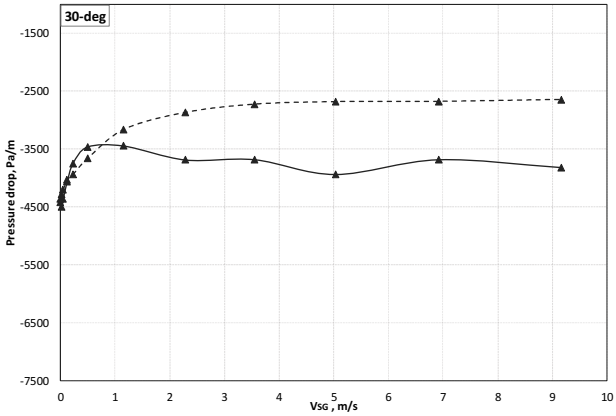

Fig. 13 Pressure drop 30° upward, Usl = 1m/s: ─ experimental data; --- OLGA simulation

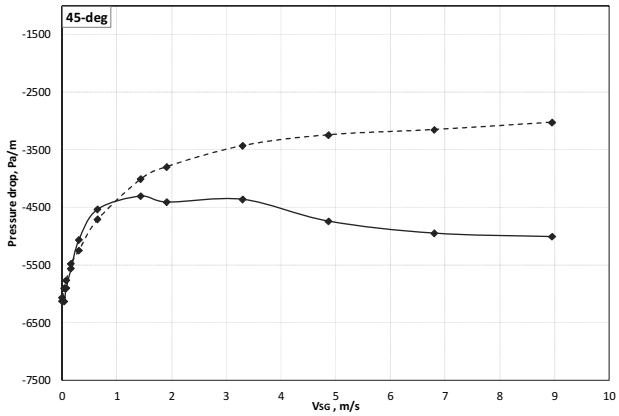

Fig. 14 Pressure drop 45° upward, Usl = 1m/s: ─ experimental data; --- OLGA simulation

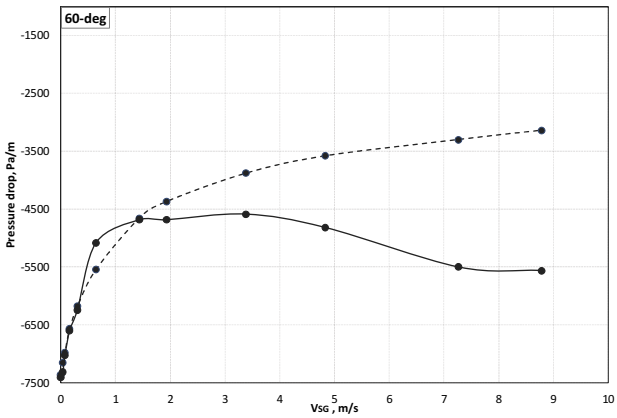

Fig. 15 Pressure drop 60° upward, Usl = 1m/s: ─ experimental data; --- OLGA simulation

4. SUMMARY AND CONCLUSION

Experimental results were collected for two-phase flow air-oil system 60 mm ID upward inclined pipe and flow patterns were identified. Experimental flow pattern were then compared with flow pattern predicted using Barnea (1987) model and multiphase flow simulator. Experimentally, the flow regime consisted of stratified wavy at 10°- 20°, churn flow at 70°-78°, while bubble flow (elongated bubble and cap bubble), slug and annular flow were observed for the entire range of inclination. A comprehensive conclusion of the experimental study was that variation on the inclination angle had a major effect on the flow pattern. Comparison of experimental flow pattern with Barnea (1987) model indicated that the unified model, which was obtain based on two-phase air-water to predict flow patterns, shows a good agreement with the experimental measurements. Most of the flow pattern regions defined by Barnea et al. (1980a), Barnea et al. (1980b), Barnea et al. (1985) and Barnea (1987) were observed also in our study.

In general, flow pattern prediction in OLGA was not in successful agreement with the measured data. OLGA patterns were sufficient similar for the slug flow at 70°-78°, but failed on the slug-annular transition flow for the same inclination. Experimental results for pressure drop were also compared with the simulation results. It was shown total pressure gradient measured agreed quite well on the behaviour with the predictions in OLGA for the tested inclination angles.

Future work is focusing on evaluating Barnea (1987) model on two-phase flow system with viscous liquid for vertical and horizontal geometries.

REFERENCES

Barnea, D. 1986. Transition from annular flow and from dispersed bubble flow—unified models for the whole range of pipe inclinations. *International journal of multiphase flow,* 12**,** 733-744.

Barnea, D. 1987. A unified model for predicting flow-pattern transitions for the whole range of pipe inclinations. *International Journal of Multiphase Flow,* 13**,** 1-12.

Barnea, D., Shoham, O. & Taitel, Y. 1980a. Flow pattern characterization in two phase flow by electrical conductance probe. *International Journal of Multiphase Flow,* 6**,** 387-397.

Barnea, D., Shoham, O. & Taitel, Y. 1982a. Flow pattern transition for downward inclined two phase flow; horizontal to vertical. *Chemical Engineering Science,* 37**,** 735-740.

Barnea, D., Shoham, O. & Taitel, Y. 1982b. Flow pattern transition for vertical downward two phase flow. *Chemical Engineering Science,* 37**,** 741-744.

Barnea, D., Shoham, O., Taitel, Y. & Dukler, A. E. 1980b. Flow pattern transition for gas-liquid flow in horizontal and inclined pipes. Comparison of experimental data with theory. *International Journal of Multiphase Flow,* 6**,** 217-225.

Barnea, D., Shoham, O., Taitel, Y. & Dukler, A. E. 1985. Gas-liquid flow in inclined tubes: flow pattern transitions for upward flow. *Chemical Engineering Science,* 40**,** 131-136.

Beggs, D. H. & Brill, J. P. 1973. A study of two-phase flow in inclined pipes. *Journal of Petroleum technology,* 25**,** 607-617.

Bendiksen, K. H., Maines, D., Moe, R. & Nuland, S. 1991. The dynamic two-fluid model OLGA: Theory and application. *SPE production engineering,* 6**,** 171-180.

Gokcal, B., Wang, Q., Zhang, H.-Q. & Sarica, C. 2008. Effects of High Oil Viscosity on Oil/Gas Flow Behavior in Horizontal Pipes.

Gould, T. L., Tek, M. R. & Katz, D. L. 1974. Two-phase flow through vertical, inclined, or curved pipe. *Journal of Petroleum Technology,* 26**,** 915-926.

Jeyachandra, B. C., Sarica, C., Zhang, H. & Pereyra, E. J. Effects of Inclination on Flow Characteristics of High Viscosity Oil/Gas Two Phase Flow. SPE Annual Technical Conference and Exhibition, 2012. Society of Petroleum Engineers.

Mcquillan, K. & Whalley, P. 1985. Flow patterns in vertical two-phase flow. *International Journal of Multiphase Flow,* 11**,** 161-175.

Taitel, Y. & Dukler, A. 1976. A model for predicting flow regime transitions in horizontal and near horizontal gas liquid flow. *AIChE Journal,* 22**,** 47-55.

Zhang, H., Wang, Q., Sarica, C. & Brill, J. P. 2003a. Unified model for gas-liquid pipe flow via slug dynamics-part 1: Model development. *Transactions-american society of mechanical engineers journal of energy resources technology,* 125**,** 266-273.

Zhang, H., Wang, Q., Sarica, C. & Brill, J. P. 2003b. Unified Model for Gas-Liquid Pipe Flow via Slug Dynamics—Part 2: Model Validation. *Transactions-american society of mechanical engineers journal of energy resources technology* 125**,** 274-283.

Effect of droplet entrainment in liquid loading prediction

Cleide Vieira and Milan Stanko
Norwegian University of Science and Technology, Norway

ABSTRACT
The present work investigate the effect of droplets entrainment on critical gas velocity, using the liquid film reversal model from Barnea (1986), Luo et al. (2014) and Shekhar et al. (2017). Especial attention was given to the onset of liquid loading in gas well. Experimental and field data were considered for model evaluation. Field data were taken from published data (Turner et al., 1969, Belfroid et al., 2008 and Veeken et al., 2010). Experiments were performed at the multiphase laboratory (EPT-NTNU) in an upward inclinable pipe. The test section was 6 m long and 60 mm ID. Inclination angles varied from 30° to 70° from horizontal. The fluids used were air and water. Measurements included fluid velocities and reversal point. High-speed video cameras were used to record the flow regime transition (slug to annular) present in the system. Prediction using the film reversal models revealed that the model over-estimate the critical gas velocity compared to results where entrainment is neglected.

1 INTRODUCTION

Most gas wells produce liquid as co-produced fluid during well production. Liquid flows along with the gas core as droplets or liquid film on the tubing wall. At the beginning of the production, the gas rate is sufficient to carry all the produced fluid to the surface. However, the declining on the reservoir pressure, the gas production rate decreases until the current gas velocity is insufficient to lift the liquid to the surface. Once this condition is establish, fraction of the liquid starts to flow counter-current to the gas core and accumulates at the bottom of the well, creating a static column of liquid. This accumulation causes backpressure against the formation, which affect the production capacity of the well, making the well produce at unstable flow condition. If the well keep producing at unstable condition, it may lead to a premature abandonment of the well or in some case to wrong well test calculations due to slugging or churning of the liquid.

Several models were proposed to predict the inception of liquid loading in gas wells. Most models are based on two physical models for liquid removal in gas well first proposed by Turner et al. (1969):

Droplet model – the liquid is transported as droplets that entrained in the high velocity gas core.

Liquid film reversal model – the liquids transported as film moving along the walls of the pipe.

Although the two models are probably in continuous exchange between the gas core and liquid film, they are threated separately. Turner et al. (1969) stated that the droplet model predict liquid loading better. They concluded that there exists a minimum gas velocity required to remove the largest drops. The proposed equation was adjusted 20 percent to insure match with field data. Many researches, such Coleman et al. (1991), Nosseir et al. (1997), Li et al. (2001), Guo et al. (2005), Belfroid et al. (2008) and Veeken et al. (2010) made refinements and modifications to the Turner droplet model to better match different

set of data, with various degrees of success. Even though the droplet model is simple, easy to use and tune, there are some field and experimental evidence that shows limited predictability.

Different from the droplet model, the liquid film reversal model assumes that the liquid loading occurs when the liquid film along the pipe wall, can no longer be lifted to the surface. It has been extensively used and associated to flow pattern transition from annular to intermittent flow. Barnea (1986) proposed a unified model that predicts flow pattern transition for the whole range of pipe inclination for gas-liquid system. In the model, the transition from annular to intermittent flow is assumed to exist due to liquid film instabilities and gas core blockage. Luo et al. (2014) proposed a new model based on the Barnea (1986) model showing a better prediction result over droplet model. In the model they used Fore et al. (2000) equation instead of Wallis (1969) equation for the interfacial friction factor calculations and introduced a new equation for film thickness around the pipe. Barnea (1986) model the film thickness around the circumferential position of the pipe is assumed to be constant. However, studies done by Paz (1994) show that the liquid film structure and thickness varied with pipe inclination. With the change in inclination from vertical to horizontal. The film thickness at the top became thinner, and thicker at the bottom part of the pipe. The film thickness variation also resulted in variation of the deposition and entrainments rate (Shoham, 2006).

Chen et al. (2016) proposed a new model based on force balance of the liquid film and gas core. They developed a correlation term to compare the new model with the widely used Turner et al. (1969) model and evaluate the model using field data from Belfroid et al. (2008). They concluded that the prediction results from the new model had an improvement over the Turner model and for matching the Belfroid et al. data.

Riza et al. (2016), unlike other models, often used the wellhead flow conditions. They predicted flow regime across the entire production tubing to determine where the liquid loading initiates. Through field data, they observed that onset of liquid loading was more likely to occur at the bottom of the well. Shekhar et al. (2017) proposed an improved model for the prediction of onset of liquid loading in inclined pipes, based on the idea of Luo et al. (2014). They assumed a non-uniform film thickness and developed a new correlation for the interfacial friction factor. The model was compared with experimental data, shoving a great improvement over droplet model and the Luo et al. (2014) model.

A literature review revelled that all the film reversal models were developed based on the assumption that liquid in the well is transported in the form of film, neglecting the droplets entrainment in the gas core. This assumption can overestimate the film thickness and therefore the critical gas velocity calculations. To evaluate the effect of droplet entrainment in the liquid film the field data from Turner et al. (1969), Belfroid et al. (2008), Veeken et al. (2010) and experimental data were used. To account the fraction of liquid droplet entering in the gas core (E), empirical correlation developed from a regression analyse proposed by Oliemans et al. (1986) were used:

$$\frac{E}{1-E} = 10^{-2.52}\rho_L^{1.08}\rho_G^{0.18}\mu_L^{0.27}\mu_G^{0.28}\sigma^{-1.80}D^{1.72}v_{sL}^{0.70}v_{sG}^{1.44}g^{0.46} \qquad (1)$$

Film liquid models from Barnea (1986), Luo et al. (2014) and Shekhar et al. (2017) were preferred to be evaluated in this study, since they are widely used to estimate the annular – intermittent flow-transition for inclined pipes and for critical gas velocity prediction in gas wells.

2 EXPERIMENTAL SET UP

The experiments were carried out for two-phase flow using a 60 mm ID, 6 m long transparent acrylic pipe for visualisation. The test section was supported on a steel beam connected to a lift mechanism designed to vary angles of inclination. Experiments were performed with upward inclination angles of 30°, 45°, 60°and 70°. The phases are measured separately using a Coriolis and vortex flow meter. They entered the test section through a mixing tee at the bottom, flow through the pipe and separated primarily at the top where the gas phase was vented to the atmosphere and liquid phase was recirculated back to the main separator located in the basement. Compressed air, supplied by the university network, and water (ρ_w=998kg/m^3,σ=0.06N/m at 20°C and 1 atm) were used as test fluids. The water was stored with oil in the main separator. The surface tension of water appear to be lower than pure water (typically 0.072N/m), probably due to contamination by surface active agents coming from either the oil or small amounts of organisms living in the water. Further details of the experimental facility can be found in Vieira et al. (2018).

Preliminary tests were performed for each selected inclination in order to define the experimental matrix that covers annular to intermittent flow where liquid loading is expected to occur. Superficial gas and liquid velocities ranged from 55 to 5 m/s, and 0.01 to 0.2 m/s respectively. A high speed camera (GoPro Hero 6 Black®) was installed in the test section; videos supported the observed reversed point (onset liquid loading).

3 MODEL VALIDATION

Experimental data and field data from Turner et al. (1969), Belfroid et al. (2008) and Veeken et al. (2010) were used to confirm the ability of the liquid film models to predict the onset of liquid loading, assuming droplet entrainment in the gas core.

In addition to validate the models, a percentage deviation (ε) was calculated, using the following equation (2).

$$\varepsilon(\%) = \frac{1}{N}\frac{100}{\sum\left(\frac{v_{sg,model} - v_{sg,observed}}{v_{sg,model}}\right)} \quad (2)$$

If $\varepsilon > 0$ the predicted critical gas velocity is higher than the observed, else $\varepsilon < 0$ the prediction values are lower. Therefore, if the deviation approaches zero it means there is a perfect match between the calculated and observed critical gas velocity.

3.1 Experimental data

The effect of droplet entrainment on critical gas velocity for predicting the onset of liquid loading was studied by considering four different inclination angles. For each inclination angle, five superficial liquid velocities, and for each liquid velocity, 14 superficial gas velocities were tested. Thus, significant amount of data points were collected. Experimental data points were subdivided into two groups; *Unloaded* in the case annular flow was observed and *loaded* for intermittent flow (see **Fig. 1**).

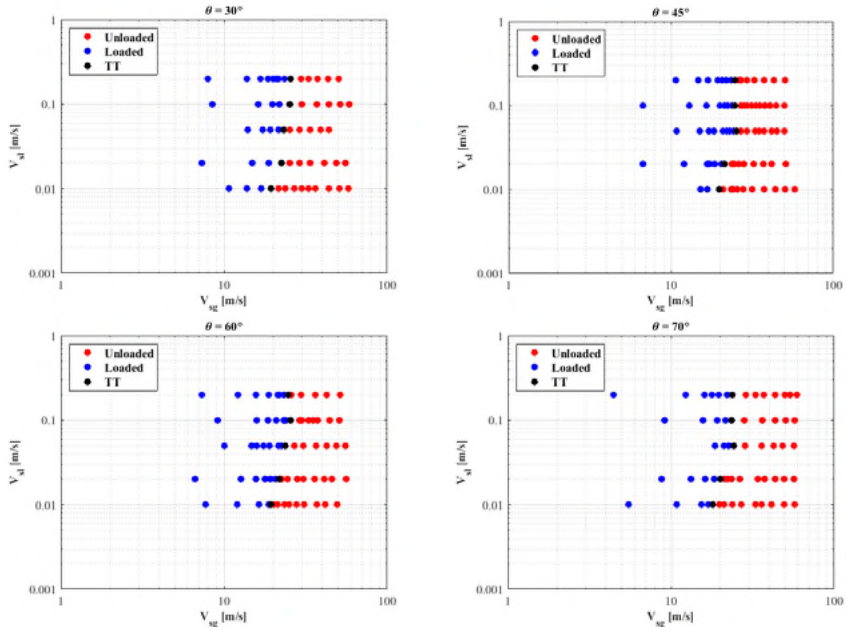

Fig. 1 Experimental data for air-water system at STP for different inclinations

A *true transition point (TT)* was calculated by averaging the last loaded two point (right-most blue point) and the first unloaded (red) for each superficial liquid velocity.

In **Fig. 2** through **Fig. 5**, true transition points represent the critical gas velocity values ($v_{sg,critical}$) and continuous and dashed line represent the liquid film models, assuming no entrainment in the gas core.

It can be observed from **Fig. 2** that the Shekhar et al. model has a better approximation with the TT points than the two other models. However, in **Fig. 3**,Fig**.** 4 andFig**.** 5 the transition line is best predicted by Barnea model.

The similarity of both models on high inclination is due to the fact that the film thickness distribution around the inner pipe is almost constant. Thus, Shekhar et al. (2017) approaches Barnea (1986) model. Barnea assumes constant film thickness for all inclination angles.

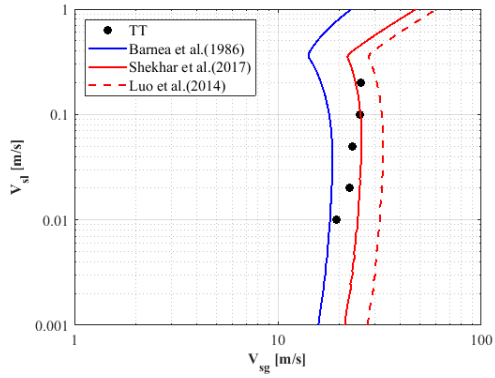

Fig. 2 Experimental data for air-water system at STP for 30-degree inclination angle

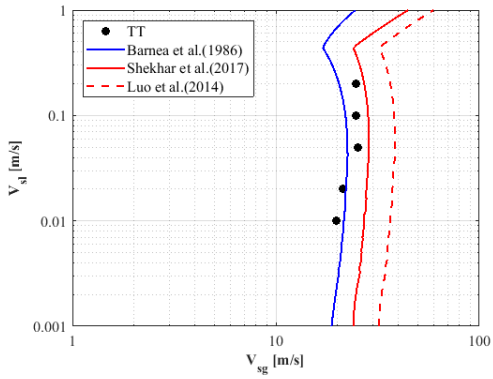

Fig. 3 Experimental data for air-water system at STP for 45-degree inclination angle

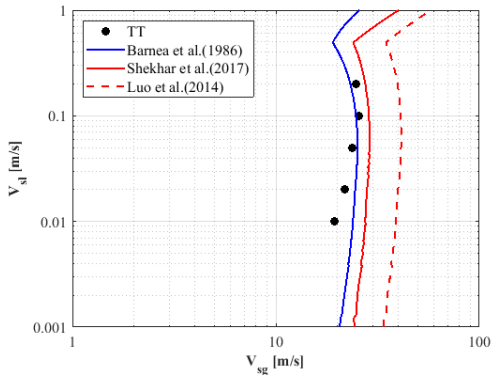

Fig. 4 Experimental data for air-water system at STP for 60-degree inclination angle

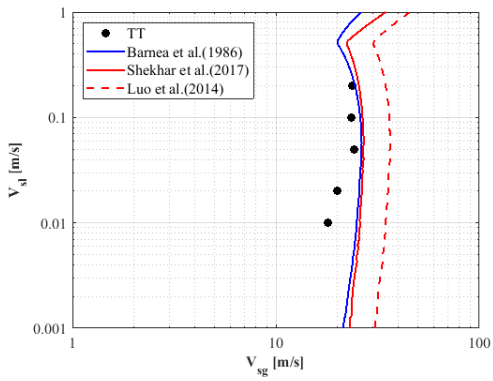

Fig. 5 Experimental data for air-water system at STP for 70-degree inclination angle

Overall, it is observed that the model proposed by Luo et al. (2014) over estimate the transition of annular to intermittent flow for all the inclination. Predictions of $v_{sg,critical}$ using

the liquid film models, assuming droplet entrainment were also performed and compared with the laboratorial data, and the was presented as a percentage. In **Fig. 6** it can be observed that the prediction of critical gas velocities with droplet entrainment present slight better results in general.

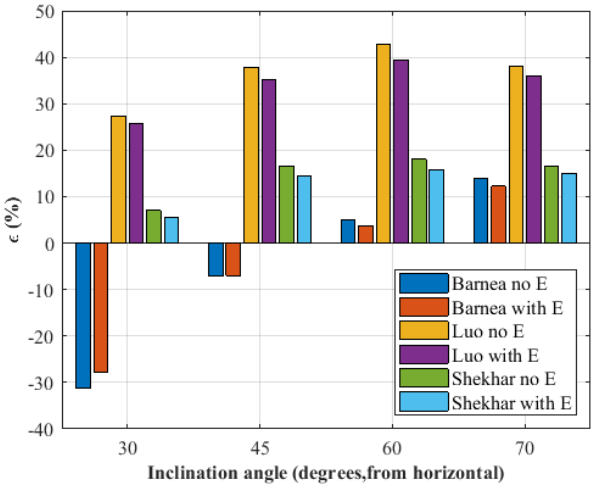

Fig. 6 Deviation for all the models prediction with and without entrainment for the laboratory data

Barnea, 1986 model for lower inclination present negative deviation meaning that model predicted much lower velocities at which liquid loading occurs. This may also be, because of the film thickness that was considered constant in the model.

Values not lower that 10% of deviation were not observed through the experimental data comparison with the models, due to the fact that transition point were not always very clear, which mean that experimentally the transition could be misinterpreted.

3.2 Field data

Three different set of field data were used to evaluate the importance of droplet entrainment during the prediction of onset of liquid loading. **Veeken et al. (2010)** published 67 gas wells from North Sea that were starting to experience liquid loading. The gas wells had from 2-6 inches of tubing diameter and included vertical and inclined pipe geometry (0 to 64° inclination angles from vertical). The liquids produced were condensate and water. Liquid gas ratio was assumed to be 5 bb/MMcf in the calculation as recommended by Luo et al. (2014). Veeken et al. (2010) reported the gas rate after the onset of liquid loading, which means that all the data should be located sight above the 45° line (loaded region) in the plot of calculated critical gas velocity ($v_{sgc,model}$) and the observed gas velocity ($v_{sgc,observed}$).

Fig. 7 to **Fig. 9** observed gas velocities of Veeken et al., 2010 were compared with critical gas velocities predicted by Barnea (1986), Luo et al. (2014) and Shekhar et al. (2017) models, with and without droplet entrainment. It can be seen that most of the wells are in the loaded region for both cases. It is also observed that when droplet entrainment are considered for the critical gas velocity calculation most of the points on the graphs are close to the 45° line, suggesting that the well have just started to load.

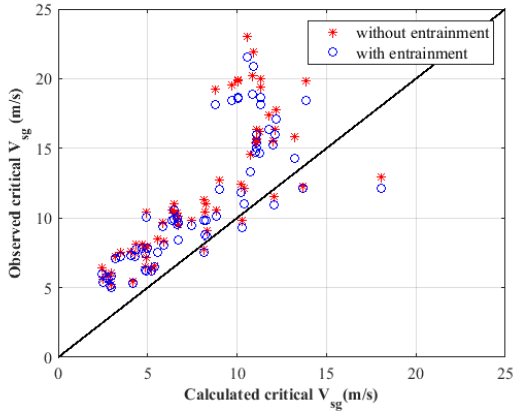

Fig. 7 Veeken et al. (2010) data vs Barnea (1986) model prediction

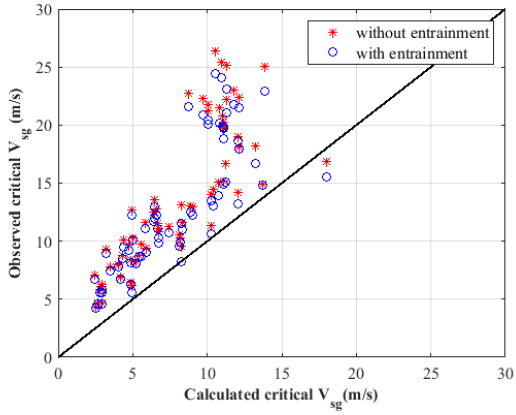

Fig. 8 Veeken et al. (2010) data vs Luo et al. (2014) model prediction

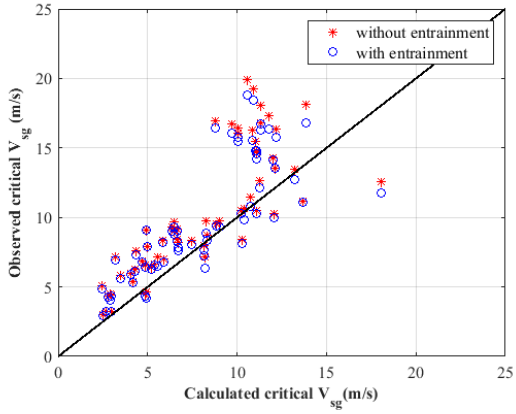

Fig. 9 Veeken et al. (2010) data vs Shekhar et al. (2017) model prediction

For an ideal model, the points have to be slight above the 45° line and the percentage deviation should be positive and close to zero. From **Table 1** result, it is clear that Shekhar et al., 2017 model, assuming entrainment presents best result, although the number of well predicted correct is the same.

Table 1.Critical gas velocity prediction for Veeken et al. (2010) data

	Without Entrainment		With Entrainment	
Model	Number of well predicted	ε(%)	Number of well predicted	ε(%)
Barnea (1986)	62/67	32.40	62/67	28.49
Luo et al. (2014)	66/67	40.78	65/67	37.35
Shekhar et al. (2017)	57/67	19.94	54/67	16.71

Belfroid et al. (2008) published data for two gas wells, both had a deviation of 40 degree. One well had 0.112 m for the tubing diameter and observed critical gas rate of 90 000 Sm^3/d, and the other 0.074 m for the tubing size and 45 000 Sm^3/d for critical gas rate. For both well sufficient data were shared, which made possible the calculation. Since the well were also reported at critical condition, the predicted results is expected to be above the 45°-line, which can be seen in **Fig. 10**. The same as Veeken et al. data, **Table 2** shows that critical gas velocity prediction assuming droplet entrainment present improved having a positive and small value for the perceptual deviation.

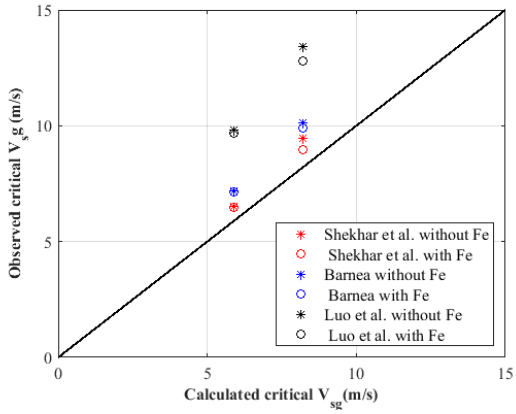

Fig. 10 Belfroid et al. (2008) data vs liquid film models prediction

Table 2.Critical gas velocity prediction for Belfroid et al. (2008) data

	Without Entrainment		With Entrainment	
Model	Number of well predicted	ε(%)	Number of well predicted	ε(%)
Barnea (1986)	2/2	18.58	2/2	17.32
Luo et al. (2014)	2/2	39.42	2/2	37.42
Shekhar et al. (2017)	2/2	11.41	2/2	8.72

Turner et al. (1969) presented data for 90 gas wells, where 37 were experiencing liquid loading and 53 were producing at stable conditions (unloaded). All the wells were reported as vertical (0° inclination angle).

From **Fig. 11** to **Fig**. 13, observed critical gas velocity is compared with the calculated critical gas velocity using the model with and without entrainment. When the calculated velocity is higher than the observed the well is consider loaded. If the calculated velocity is, lower than the observed the well is defined as unloaded. In case the well is unloaded the data point should be located slight below the 45° line in the plot. It can be that for Turner et al., 1969 data, droplet entrainment does not influence the prediction of critical gas velocity. Shoham (2006) mentioned that the film thickness variation changes the variation of the deposition and entrainment rate. Since the published well present vertical geometry, film thickness was considered constant.

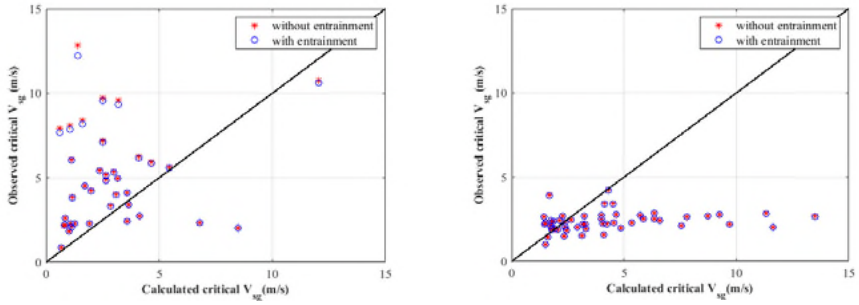

a. Loaded wells b. Unloaded wells

Fig. 11 Turner et al. (1969) data vs Barnea (1986) model prediction

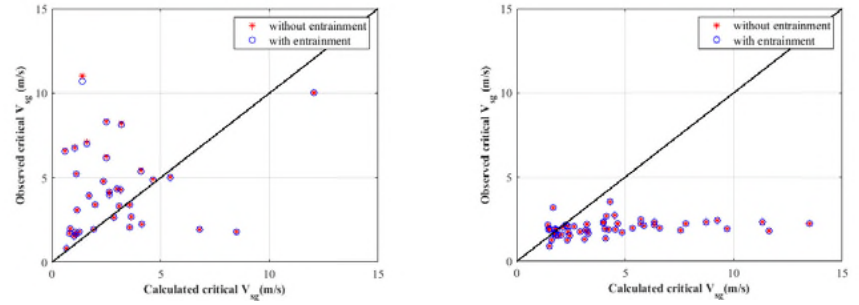

a. Loaded wells b. Unloaded wells

Fig. 12 Turner et al. (1969) data vs Luo et al. (2014) model prediction

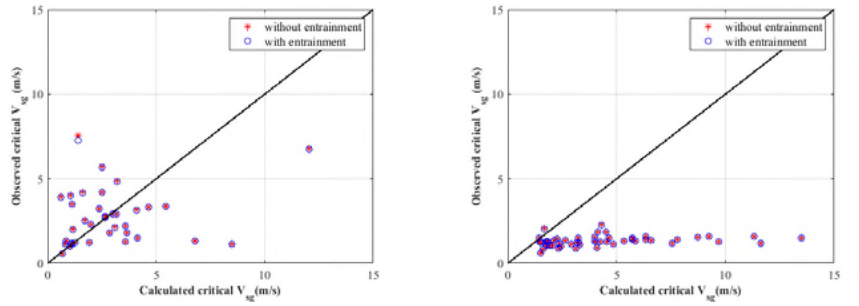

a. Loaded wells b. Unloaded wells

Fig. 13 Turner et al. (1969) data vs Shekhar et al. (2017) model prediction

For all the model the prediction of unloaded well is accurate i.e., the data points are located below the 45° line. However, the percentage deviation calculated is high in the case of Luo et al. (2014) and Shekhar et al. (2017) as shown in **Table 3**. Although the film thickness correlation introduced in both model to account the effect of inclination do not have any effect, the interfacial friction factor used in the model overestimate the critical gas velocity in vertical gas wells. On the other hand Barnea (1986) model shows better prediction in both number of well and percentage deviation.

Table 3.Critical gas velocity prediction for Turner et al. (1969) data

Well at loaded condition				
Model	Without Entrainment		With Entrainment	
	Number of well predicted	ε(%)	Number of well predicted	ε(%)
Barnea (1986)	31/37	26.01	31/37	25.65
Luo et al. (2014)	28/37	12.16	28/37	12.02
Shekhar et al. (2017)	20/37	-33.82	20/37	-33.97
Well at unloaded condition				
Barnea (1986)	41/53	-82.06	40/53	-82.28
Luo et al. (2014)	46/53	-114.56	46/53	-114.49
Shekhar et al. (2017)	51/53	-216.08	51/53	-216.17

4 CONCLUSION

In the study, field and experimental data were compared with liquid film model, used to predict critical gas velocity in gas well. The proposed liquid film model assumes no entrainment of droplets in the gas core. Therefore, the present work was performed to verify the effect of entrainment on the liquid film model when critical gas velocity is predicted.

A comprehensive conclusion based on the data comparison with the models was that droplet entrainment had an effect on the accuracy of critical gas velocity predictions for the onset liquid loading.

Overall, Luo et al. (2014) model over estimates the transition from annular to intermittent flow for all cases studied.

The liquid film model of Barnea (1986) model was developed to predict the transition of annular to intermittent flow transition in both vertical and deviated pipe. However, in most of the case showed not be better than Shekhar et al. (2017) model, due to the assumption that the film thickness is constant for all pipe inclinations.

In the case of gas wells with vertical geometry, droplet entrainment does not have any effect on the critical gas velocity prediction. The film thickness is constant at such geometry and the variation of the deposition or entrainment rate in the gas core is negligible. Luo et al. (2014) and Shekhar et al. (2017) showed not to be a good model to be used when the well is vertical in case accurate critical gas velocity is crucial.

5 ACKNOLOGMENTS

The author would like to thank Masolwa Kasongi Enos for his help on the collection of literature data. In particular, we would like to thank Professor Ole Nydal from NTNU for making available the Multiphase laboratory.

6 NOMENCLATURE

ID	pipe inner diameter (m)
E	entrainment fraction(-)
g	gravitational acceleration (m^2/s)
N	number of points or wells.
v_{sg}	superficial gas velocity (m/s)
v_{sgc}	critical gas velocity (m/s)
v_{sl}	superficial liquid velocity (m/s)
θ	Angle of inclination from horizontal (degrees)
$\mu_{g,l}$	gas, liquid viscosity (Pa.s)
$\rho_{g,l}$	gas, liquid density (kg/m^3)
σ	surface tension (N/m)

7 REFERENCES

Barnea, D. 1986. Transition from annular flow and from dispersed bubble flow—unified models for the whole range of pipe inclinations. *International journal of multiphase flow,* 12**,** 733-744DOI: https://doi.org/10.1016/0301-9322(86)90048-0.

Belfroid, S., Schiferli, W., Alberts, G., Veeken, C. A. & Biezen, E. Predicting onset and dynamic behaviour of liquid loading gas wells. SPE Annual Technical Conference and Exhibition, 2008. Society of Petroleum Engineers, DOI: https://doi.org/10.2118/115567-MS.

Chen, D., Yao, Y., Fu, G., Meng, H. & Xie, S. 2016. A new model for predicting liquid loading in deviated gas wells. *Journal of Natural Gas Science and Engineering,* 34**,** 178-184DOI: https://doi.org/10.1016/j.jngse.2016.06.063.

Coleman, S. B., Clay, H. B., Mccurdy, D. G. & Norris Iii, L. H. 1991. A new look at predicting gas-well load-up. *Journal of Petroleum Technology,* 43**,** 329-333DOI: https://doi.org/10.2118/20280-PA.

Fore, L., Beus, S. & Bauer, R. J. I. J. O. M. F. 2000. Interfacial friction in gas–liquid annular flow: analogies to full and transition roughness. 26**,** 1755-1769DOI: https://doi.org/10.1016/S0301-9322(99)00114-7.

Guo, B., Ghalambor, A. & Xu, C. A systematic approach to predicting liquid loading in gas wells. SPE Production Operations Symposium, 2005. Society of Petroleum Engineers, DOI: https://doi.org/10.2118/94081-PA.

Li, M., Lei, S. & Li, S. 2001. New View on Continuous-removal Liquids from Gas Wells. *SPE Permian Basin Oil and Gas Recovery Conference.* Midland, Texas: Society of Petroleum Engineers.

Luo, S., Kelkar, M., Pereyra, E. & Sarica, C. 2014. A new comprehensive model for predicting liquid loading in gas wells. *SPE Production & Operations,* 29**,** 337-349DOI: https://doi.org/10.2118/172501-PA.

Nosseir, M., Darwich, T., Sayyouh, M. & El Sallaly, M. A new approach for accurate prediction of loading in gas wells under different flowing conditions. SPE Production Operations Symposium, 1997. Society of Petroleum Engineers, DOI: https://doi.org/10.2118/66540-PA.

Oliemans, R., Pots, B. & Trompe, N. J. I. J. O. M. F. 1986. Modelling of annular dispersed two-phase flow in vertical pipes. 12**,** 711-732DOI: https://doi.org/10.1016/0301-9322(86)90047-9.

Paz, R. J. 1994. Film Thickness Distribution for Annular Flow in Directional Wells: Horizontal to Vertical. *SPE Annual Technical Conference and Exhibition.* New Orleans, Louisiana: Society of Petroleum Engineers.

Riza, M. F., Hasan, A. R. & Kabir, C. S. 2016. A Pragmatic Approach to Understanding Liquid Loading in Gas Wells. *SPE Production & Operations,* 31**,** 185-196DOI: https://doi.org/10.2118/170583-MS.

Shekhar, S., Kelkar, M., Hearn, W. J. & Hain, L. L. 2017. Improved Prediction of Liquid Loading In Gas Wells. *SPE Production & Operations,* DOI: https://doi.org/10.2118/186088-PA.

Shoham, O. 2006. *Mechanistic modeling of gas-liquid two-phase flow in pipes,* Richardson, Tex Society of Petroleum Engineers

Turner, R., Hubbard, M. & Dukler, A. 1969. Analysis and prediction of minimum flow rate for the continuous removal of liquids from gas wells. *Journal of Petroleum Technology,* 21**,** 1,475-1,482DOI: https://doi.org/10.2118/2198-PA.

Veeken, K., Hu, B. & Schiferli, W. 2010. Gas-Well Liquid-Loading-Field-Data Analysis and Multiphase-Flow Modeling. *Spe Production & Operations,* 25**,** 275-284DOI: https://doi.org/10.2118/123657-PA.

Vieira, C., Kallager, M., Vassmyr, M., La Forgia, N. & Yang, Z. 2018. Experimental investigation of two-phase flow regime in an inclined pipe. *11th North American Conference on Multiphase Production Technology.* Banff, Canada: BHR Group.

Wallis, G. B. 1969. *One-dimensional two-phase flow,* New York, McGraw-Hill.